

---

Theses and Dissertations

---

Fall 2010

# Measuring and modeling the anisotropic, nonlinear and hysteretic behavior of woven fabrics

Robert W. Williams  
*University of Iowa*

Copyright 2010 Robert W. Williams

This dissertation is available at Iowa Research Online: <https://ir.uiowa.edu/etd/907>

---

## Recommended Citation

Williams, Robert W.. "Measuring and modeling the anisotropic, nonlinear and hysteretic behavior of woven fabrics." PhD (Doctor of Philosophy) thesis, University of Iowa, 2010.  
<https://ir.uiowa.edu/etd/907>. <https://doi.org/10.17077/etd.ulx80lo7>

---

Follow this and additional works at: <https://ir.uiowa.edu/etd>



Part of the [Civil and Environmental Engineering Commons](#)

MEASURING AND MODELING THE ANISOTROPIC, NONLINEAR  
AND HYSTERETIC BEHAVIOR OF WOVEN FABRICS

by

Robert W. Williams

An Abstract

Of a thesis submitted in partial fulfillment  
of the requirements for the Doctor of  
Philosophy degree in Civil and Environmental Engineering  
in the Graduate College of  
The University of Iowa

December 2010

Thesis Supervisor: Professor Colby C. Swan

## ABSTRACT

The computational modeling of clothing has received increasing attention since the late 1980's with the desire to study and animate clothing-wearer interactions. Within a clothing modeling framework, it is necessary to model the mechanical behavior of woven fabrics. An important aspect of modeling the mechanics of woven fabrics is capturing realistic stress-strain behaviors which are invariably anisotropic, nonlinear, and hysteretic in that they feature irrecoverable deformation when loadings are removed from the fabric. The objective of this research is to develop a fabric constitutive model that captures the primary features of anisotropy, nonlinearity, and hysteresis, and that can be easily implemented in a nonlinear, large deformation shell finite element framework for general clothing-wearer interaction modeling.

To achieve the objective, biaxial responses of four different woven fabrics were experimentally measured under a battery of load-unload uniaxial stress tests performed in the fabrics' warp, weft, and bias  $45^\circ$  directions. Axial deformations were measured precisely using LVDTs, and transverse deformations were measured less precisely using photogrammetric methods. Such measurements yielded insight on the different fabrics' membrane properties such as nonlinear Young's moduli in the warp and weft directions, shear moduli, and Poisson's ratios. These membrane behaviors were captured in an incremental constitutive model that uses polynomial fitting of a fabric's loading warp and weft Young's moduli, and polynomial fitting of the membrane shear modulus. Measured membrane Poisson's ratios of the different fabrics were found to be asymmetrical and highly variable between fabric types. All of these effects were integrated in a nonsymmetrical incremental constitutive model that relates Piola-Kirchhoff stress to Green-Lagrangian strain.

For numerical implementation in a shell finite element framework, the woven fabric's warp and weft directions relative to an individual element's lamina coordinate

system are specified in the undeformed configuration of the fabric and are denoted as the local material coordinate system. As the fabric undergoes arbitrary deformations, the local Piola-Kirchoff stress, the Green-Lagrange strain, and its increment at a point in the fabric are transformed to the material coordinate system in which the stress is updated. The updated state of Piola-Kirchoff stress in the material coordinate system is then rotated back into the local lamina coordinate system for usage in finite element force and stiffness calculations.

This new realistic material model for woven fabrics is successfully implemented and tested in a variety of computations such as simulation of quasi-static material tests, and dynamic fabric “drape” and “poke” tests.

Abstract Approved: \_\_\_\_\_  
Thesis Supervisor  
\_\_\_\_\_  
Title and Department  
\_\_\_\_\_  
Date

MEASURING AND MODELING THE ANISOTROPIC, NONLINEAR  
AND HYSTERETIC BEHAVIOR OF WOVEN FABRICS

by

Robert W. Williams

A thesis submitted in partial fulfillment  
of the requirements for the Doctor of  
Philosophy degree in Civil and Environmental Engineering  
in the Graduate College of  
The University of Iowa

December 2010

Thesis Supervisor: Professor Colby C. Swan

Copyright by  
ROBERT W. WILLIAMS  
2010  
All Rights Reserved

Graduate College  
The University of Iowa  
Iowa City, Iowa

CERTIFICATE OF APPROVAL

---

PH.D. THESIS

---

This is to certify that the Ph.D. thesis of

Robert W. Williams

has been approved by the Examining Committee  
for the thesis requirement for the Doctor of Philosophy  
degree in Civil and Environmental Engineering at the December 2010  
graduation.

Thesis Committee: \_\_\_\_\_  
Colby C. Swan, Thesis Supervisor

\_\_\_\_\_  
M. Asghar Bhatti

\_\_\_\_\_  
Jia Lu

\_\_\_\_\_  
Sharif Rahman

\_\_\_\_\_  
Salam Rahmatalla

To My Mom and Dad



## ABSTRACT

The computational modeling of clothing has received increasing attention since the late 1980's with the desire to study and animate clothing-wearer interactions. Within a clothing modeling framework, it is necessary to model the mechanical behavior of woven fabrics. An important aspect of modeling the mechanics of woven fabrics is capturing realistic stress-strain behaviors which are invariably anisotropic, nonlinear, and hysteretic in that they feature irrecoverable deformation when loadings are removed from the fabric. The objective of this research is to develop a fabric constitutive model that captures the primary features of anisotropy, nonlinearity, and hysteresis, and that can be easily implemented in a nonlinear, large deformation shell finite element framework for general clothing-wearer interaction modeling.

To achieve the objective, biaxial responses of four different woven fabrics were experimentally measured under a battery of load-unload uniaxial stress tests performed in the fabrics' warp, weft, and bias  $45^\circ$  directions. Axial deformations were measured precisely using LVDTs, and transverse deformations were measured less precisely using photogrammetric methods. Such measurements yielded insight on the different fabrics' membrane properties such as nonlinear Young's moduli in the warp and weft directions, shear moduli, and Poisson's ratios. These membrane behaviors were captured in an incremental constitutive model that uses polynomial fitting of a fabric's loading warp and weft Young's moduli, and polynomial fitting of the membrane shear modulus. Measured membrane Poisson's ratios of the different fabrics were found to be asymmetrical and highly variable between fabric types. All of these effects were integrated in a nonsymmetrical incremental constitutive model that relates Piola-Kirchhoff stress to Green-Lagrangian strain.

For numerical implementation in a shell finite element framework, the woven fabric's warp and weft directions relative to an individual element's lamina coordinate

system are specified in the undeformed configuration of the fabric and are denoted as the local material coordinate system. As the fabric undergoes arbitrary deformations, the local Piola-Kirchoff stress, the Green-Lagrange strain, and its increment at a point in the fabric are transformed to the material coordinate system in which the stress is updated. The updated state of Piola-Kirchoff stress in the material coordinate system is then rotated back into the local lamina coordinate system for usage in finite element force and stiffness calculations.

This new realistic material model for woven fabrics is successfully implemented and tested in a variety of computations such as simulation of quasi-static material tests, and dynamic fabric “drape” and “poke” tests.

## TABLE OF CONTENTS

LIST OF TABLES .....	vii
LIST OF FIGURES .....	viii
LIST OF BOXES .....	xiv
CHAPTER 1. INTRODUCTION .....	1
1.1 Motivation.....	1
1.2 Objectives and Organization.....	4
CHAPTER 2. WOVEN FABRIC STRUCTURES .....	6
2.1 Fibers .....	7
2.2 Yarns.....	11
2.3 Fabrics.....	13
2.4 Summary.....	20
CHAPTER 3. EXPERIMENTAL METHODS .....	21
3.1 Objectives .....	22
3.2 Specimen Preparation .....	25
3.3 Fabric Tests, Procedures, and Results .....	26
3.3.1 Fabric Thickness and Density .....	26
3.3.2 In-plane Tensile Behavior .....	28
3.3.3 Poisson's Ratios.....	43
3.3.4 In-plane Shear Behavior .....	64
3.4 Summary of Measured Fabric Behaviors .....	77
CHAPTER 4. REVIEW OF FABRIC CONSTITUTIVE MODELS .....	78
4.1 Yarn Models .....	78
4.2 Particle-Spring Models .....	84
4.3 Continuum Models .....	86
4.4 Discussion.....	92
CHAPTER 5. FINITE ELEMENT BACKGROUND.....	95
5.1 Problem Statement.....	95
5.2 Coordinate Systems .....	98
5.3 Shell Geometry and Kinematics .....	100
5.4 Explicit Linearized Kinematics .....	105
5.5 Force Vectors and Tangential Matrices.....	106
5.6 Solution Algorithms.....	109
CHAPTER 6. INCREMENTAL CONSTITUTIVE MODEL FOR FABRICS .....	111
6.1 Initial Computations .....	112
6.2 Global to Material Frame Transformations .....	113
6.3 Construction of Moduli.....	115

6.3.1 Axial Moduli .....	116
6.3.2 Off-diagonal Moduli.....	119
6.3.3 Shear Moduli .....	120
6.4 Stress Update .....	122
6.5 Material to Global Frame Transformations .....	123
6.6 Summary of Fabric Model.....	124
<b>CHAPTER 7. MODEL VERIFICATION AND APPLICATIONS .....</b>	<b>127</b>
7.1 Material Parameters .....	127
7.1.1 Axial Moduli .....	127
7.1.2 Shear Moduli .....	132
7.2 Verification of Fabric Model.....	137
7.2.1 Axial Tests in Warp and Weft Directions .....	137
7.2.2 Bias and Simple Shear Tests .....	149
7.3 Applications .....	160
7.3.1 Biaxial Strain .....	160
7.3.2 Draping Fabric From Four Corners.....	162
7.3.3 Poking Fabric.....	163
7.4 Discussion.....	169
<b>CHAPTER 8. CONCLUSION AND FUTURE WORK .....</b>	<b>176</b>
8.1 Conclusion .....	176
8.2 Future Work.....	178
<b>REFERENCES .....</b>	<b>179</b>
<b>APPENDIX A.....</b>	<b>184</b>

## LIST OF TABLES

Table 2.1. Typical fiber size and length.....	9
Table 2.2. Tensile properties of common fibers. ....	11
Table 3.1. Parameters measured by KES-F system. ....	21
Table 3.2. Parameters measured by FAST system. ....	22
Table 3.3. Density and thickness data for tested fabrics.....	28
Table 3.4. Maximum displacement for single-cycle tensile tests. ....	36
Table 7.1. Tensile loading and unloading moduli for the four tested fabrics (tensor notation). ....	132
Table 7.2. Average Poisson's ratios and mass densities for the four tested fabrics. ....	132
Table 7.3. In-plane loading and unloading shear moduli for the four tested fabrics. ....	136
Table 7.4. Upper bound for modified Poisson's ratios for Duck and Muslin.....	142
Table 7.5. Estimates of the constant shear modulus using Kilby's equation and the corresponding estimate from the present approach. ....	171

## LIST OF FIGURES

Figure 1-1. Examples of the uses of virtual clothing: (a) computer animation, (b) virtual clothing design, and (c) clothing-wearer interaction. ....	2
Figure 2-1. Different hierarchical length scales that comprise functional fabric garments. ....	6
Figure 2-2. SEM photographs of (a) natural and (b) man-made fibers. ....	8
Figure 2-3. Typical weaving loom. ....	14
Figure 2-4. Common weave patterns: (a) plain, (b) twill, (c) satin, and (d) basket. ....	14
Figure 2-5. Yarn crimp in two different weave patterns: (a) plain and (b) satin. ....	16
Figure 2-6. Peirce’s basic yarn geometry in a plain weave. ....	16
Figure 2-7. Idealization of fabric behavior due to (a) stretching where region <i>A</i> exhibits decrimping of the yarns until they lock as shown in (b) at which the material properties of the yarns dominate and a stiffer response is experienced in region <i>B</i> . Region <i>C</i> shows the hysteresis upon unloading. ....	17
Figure 2-8. Idealization of fabric behavior (a) due to shearing. In region <i>D</i> , the shear angle is governed by friction resisting rotation. Slippage and bending of the yarns at the yarn intersection occurs in region <i>E</i> , and shear force increases rapidly in region <i>F</i> due to yarn jamming, shown in (b). ....	18
Figure 2-9. Idealization of fabric behavior due to bending where frictional constraints at yarn intersections account for behavior in region <i>G</i> , and free elastic bending occurs in region <i>H</i> once the frictional constraints are overcome. ....	19
Figure 3-1. Cotton-polyester blend: (a) macroscopic and (b) SEM photographs. ....	23
Figure 3-2. Cotton duck: (a) macroscopic and (b) SEM photographs. ....	24
Figure 3-3. Cotton muslin: (a) macroscopic and (b) SEM photographs. ....	24
Figure 3-4. Cotton denim: (a) macroscopic and (b) SEM photographs. ....	25
Figure 3-5. Woven fabric samples. (a) Sample preparation, (b) definition of middle region, (c) orientation of specimens, and (d) completed specimens. ....	26
Figure 3-6. Test method for determining fabric thickness using two acrylic plates and a digital caliper. ....	27
Figure 3-7. Experimental pin grips (a) without and (b) with fabric specimen loaded. ....	29

Figure 3-8. Experimental setup: (a) photograph and (b) schematic including MTS load frame, secondary monitor, and digital camera. ....	30
Figure 3-9. Experimental data for cotton-polyester blend from three monotonic tests in the warp direction and three monotonic tests in the weft direction. ....	32
Figure 3-10. Experimental data for cotton duck from three monotonic tests in the warp direction and three monotonic tests in the weft direction. ....	33
Figure 3-11. Experimental data for cotton muslin from three monotonic tests in the warp direction and three monotonic tests in the weft direction. ....	34
Figure 3-12. Experimental data for cotton denim from three monotonic tests in the warp direction and three monotonic tests in the weft direction. ....	35
Figure 3-13. Experimental load/unload data for cotton-polyester blend from multiple single-cycle tests in the warp and weft directions. ....	37
Figure 3-14. Experimental load/unload data for cotton duck from multiple single-cycle tests in the warp and weft directions. ....	38
Figure 3-15. Experimental load/unload data for cotton muslin from multiple single-cycle tests in the warp and weft directions. ....	39
Figure 3-16. Experimental load/unload data for cotton denim from multiple single-cycle tests in the warp and weft directions. ....	40
Figure 3-17. End of test cycle showing the resulting gap between the bottom pin and the specimen due to permanent deformation in the fabric. ....	41
Figure 3-18. Strain rate comparison for cotton-polyester blend loaded in the warp direction. ....	42
Figure 3-19. Load/unload cyclic behavior of a cotton-polyester blend specimen under force control in the warp direction. ....	43
Figure 3-20. Measuring longitudinal and transverse strains in order to determine Poisson's ratio. ....	45
Figure 3-21. Poisson's ratios found using lateral strain as a function of longitudinal strain for the warp monotonic specimen 01 of cotton-polyester blend. ....	46
Figure 3-22. Poisson's ratios found using lateral strain as a function of longitudinal strain for the warp monotonic specimen 02 of cotton-polyester blend. ....	46
Figure 3-23. Poisson's ratios found using lateral strain as a function of longitudinal strain for the warp monotonic specimen 03 of cotton-polyester blend. ....	47
Figure 3-24. Poisson's ratios found using lateral strain as a function of longitudinal strain for the weft monotonic specimen 04 of cotton-polyester blend. ....	47
Figure 3-25. Poisson's ratios found using lateral strain as a function of longitudinal strain for the weft monotonic specimen 05 of cotton-polyester blend. ....	48

Figure 3-26. Poisson's ratios found using lateral strain as a function of longitudinal strain for the weft monotonic specimen 06 of cotton-polyester blend.....	48
Figure 3-27. Poisson's ratios found using lateral strain as a function of longitudinal strain for the warp monotonic specimen 01 of cotton duck.....	49
Figure 3-28. Poisson's ratios found using lateral strain as a function of longitudinal strain for the warp monotonic specimen 02 of cotton duck.....	50
Figure 3-29. Poisson's ratios found using lateral strain as a function of longitudinal strain for the warp monotonic specimen 03 of cotton duck.....	50
Figure 3-30. Poisson's ratios found using lateral strain as a function of longitudinal strain for the weft monotonic specimen 04 of cotton duck.....	51
Figure 3-31. Poisson's ratios found using lateral strain as a function of longitudinal strain for the weft monotonic specimen 05 of cotton duck.....	51
Figure 3-32. Poisson's ratios found using lateral strain as a function of longitudinal strain for the weft monotonic specimen 06 of cotton duck.....	52
Figure 3-33. Poisson's ratios found using lateral strain as a function of longitudinal strain for the warp monotonic specimen 01 of cotton muslin.....	53
Figure 3-34. Poisson's ratios found using lateral strain as a function of longitudinal strain for the warp monotonic specimen 02 of cotton muslin.....	53
Figure 3-35. Poisson's ratios found using lateral strain as a function of longitudinal strain for the warp monotonic specimen 03 of cotton muslin.....	54
Figure 3-36. Poisson's ratios found using lateral strain as a function of longitudinal strain for the weft monotonic specimen 04 of cotton muslin.....	54
Figure 3-37. Poisson's ratios found using lateral strain as a function of longitudinal strain for the weft monotonic specimen 05 of cotton muslin.....	55
Figure 3-38. Poisson's ratios found using lateral strain as a function of longitudinal strain for the weft monotonic specimen 06 of cotton muslin.....	55
Figure 3-39. Poisson's ratios found using lateral strain as a function of longitudinal strain for the warp monotonic specimen 01 of cotton denim.....	56
Figure 3-40. Poisson's ratios found using lateral strain as a function of longitudinal strain for the warp monotonic specimen 02 of cotton denim.....	57
Figure 3-41. Poisson's ratios found using lateral strain as a function of longitudinal strain for the warp monotonic specimen 03 of cotton denim.....	57
Figure 3-42. Poisson's ratios found using lateral strain as a function of longitudinal strain for the weft monotonic specimen 04 of cotton denim. ....	58
Figure 3-43. Poisson's ratios found using lateral strain as a function of longitudinal strain for the weft monotonic specimen 05 of cotton denim. ....	58



Figure 3-44. Poisson's ratios found using lateral strain as a function of longitudinal strain for the weft monotonic specimen 06 of cotton denim. ....	59
Figure 3-45. Close-up of scale showing pixels using <i>Adobe Photoshop CS4</i> . ....	61
Figure 3-46. Screenshot of <i>Adobe Photoshop CS4</i> showing an individual pixel used for subsequent measurements. ....	62
Figure 3-47. Measurements using "ruler tool" in <i>Photoshop</i> . ....	63
Figure 3-48. Chart showing the strain results for a muslin weft specimen using both <i>AutoCAD</i> and <i>Photoshop</i> . ....	63
Figure 3-49. Common types of tests for determining shear properties of woven fabrics: (a) KES-F shear test, (b) picture frame test, and (c) bias extension test. ....	65
Figure 3-50. Shear deformation of an element. ....	67
Figure 3-51. Transformation of stress tensor from original coordinate system to a rotated coordinate system. ....	68
Figure 3-52. Deformation zones for a bias extension test: (I) no significant deformation, (II) mixed shearing and extension, and (III) shearing. ....	70
Figure 3-53. Schematic showing dimensions of the reference configuration and those of the deformed configuration at time $t$ . ....	71
Figure 3-54. Photograph of bias 45 specimen showing dimensions. ....	72
Figure 3-55. Measured stretch ratios for warp and weft yarns of cotton-polyester blend fabric during bias tension tests. ....	73
Figure 3-56. Measured stretch ratios for warp and weft yarns of cotton duck fabric during bias tension tests. ....	73
Figure 3-57. Measured stretch ratios for warp and weft yarns of cotton muslin fabric during bias tension tests. ....	74
Figure 3-58. Measured stretch ratios for warp and weft yarns of cotton denim fabric during bias tension tests. ....	74
Figure 3-59. Measured shear stress-shear strain data for cotton-polyester blend. ....	75
Figure 3-60. Measured shear stress-shear strain data for cotton duck. ....	75
Figure 3-61. Measured shear stress-shear strain data for cotton muslin. ....	76
Figure 3-62. Measured shear stress-shear strain data for cotton denim. ....	76
Figure 4-1. Yarn interaction: (a) the crossover point of two yarns and (b) the corresponding stretches and forces during loading. ....	80

Figure 4-2. Comparison of Kawabata <i>et al's</i> theory for a plain-weave cotton fabric versus experimental data for (a) uniform biaxial tension and (b) strip biaxial tension.....	81
Figure 4-3. Yarn shear interaction: (a) the original configuration of a crossover point of two yarns and (b) the resulting deformation due to a shear load. ....	82
Figure 4-4. Comparison of Kawabata <i>et al's</i> theory for a plain-weave cotton fabric versus experimental data for (a) uniaxial tension and (b) shear.....	83
Figure 4-5. Comparison between hysteretic model and experimental data. ....	84
Figure 4-6. Example of a particle-spring model for a plain-weave fabric showing three types of springs.....	85
Figure 4-7. Homogenization of (a) a fabric of woven yarns to (b) a corresponding anisotropic continua. ....	86
Figure 4-8. Animation of simulated fabric drape by Chen and Govindaraj. ....	88
Figure 4-9. Comparison of (a) uniaxial warp/weft results and (b) bias 45° results for a woven composite fabric. In both cases, moduli are developed by fitting a curve to the experimental data. ....	90
Figure 4-10. Comparison of biaxial response of experiments and model. Initially, behavior is controlled by the rubber matrix, resulting in very low stress. As the load is taken up by the yarns, stress increases rapidly until it yields, where plastic behavior dominates.....	92
Figure 4-11. Comparison of SVK and experimental results for a monotonic uniaxial stress tensile test in the warp and weft directions for cotton-polyester blend fabric. ....	94
Figure 5-1. Geometric description of the shell element.....	100
Figure 5-2. Finite rotation of a vector $\mathbf{r}$ about the axis $\hat{\mathbf{e}}_1$ . ....	102
Figure 6-1. Model of a sleeve at (a) the original configuration and (b) the current configuration in relation to a global coordinate Cartesian coordinate system.....	112
Figure 6-2. General orientation of the warp and weft material directors $\mathbf{g}_1$ , $\mathbf{g}_2$ , and $\mathbf{g}_3$ relative to the lamina coordinates of the shell element. ....	114
Figure 6-3. Comparison of $C_{21}^{n+1}$ and $C_{12}^{n+1}$ for cotton-polyester blend subjected to monotonic loading (uniaxial stress) using curve fit. ....	120
Figure 6-4. Typical fabric behavior due to shear and different locations of values of $E_5^*$ depending on the cyclic loading. ....	122
Figure 7-1. Curve fitting the loading and unloading behavior in order to determine tensile parameters in the warp and weft directions for cotton-polyester blend. ....	128

Figure 7-2. Curve fitting the loading and unloading behavior in order to determine tensile parameters in the warp and weft directions for cotton duck. ....	129
Figure 7-3. Curve fitting the loading and unloading behavior in order to determine tensile parameters in the warp and weft directions for cotton muslin. ....	130
Figure 7-4. Curve fitting the loading and unloading behavior in order to determine tensile parameters in the warp and weft directions for cotton denim. ....	131
Figure 7-5. Curve fit of shear stress-strain data for loading and unloading behavior from representative cotton-polyester bias-45 test. ....	133
Figure 7-6. Curve fit of shear stress-strain data for loading and unloading behavior from representative cotton duck bias-45 test. ....	134
Figure 7-7. Curve fit of shear stress-strain data for loading and unloading behavior from representative cotton muslin bias-45 test. ....	135
Figure 7-8. Curve fit of shear stress-strain data for loading and unloading behavior from representative cotton denim bias-45 test. ....	136
Figure 7-9. Snapshots of cyclic simulation in the warp direction of cotton-polyester blend at (a) the initial configuration, (b) the maximum displacement, and (c) the compressive buckling instability upon unloading. ....	138
Figure 7-10. Comparison of computational and experimental results for cyclic uniaxial stress tensile tests loaded in the warp, weft and bias 45 directions for cotton-polyester blend fabric. ....	140
Figure 7-11. Comparison of computational and experimental results for cyclic uniaxial stress tensile tests loaded in the warp, weft and bias 45 directions for cotton denim fabric. ....	141
Figure 7-12. Comparison of computational and experimental results for cyclic uniaxial stress tensile tests loaded in the warp, weft and bias 45 directions for cotton duck fabric. The model results without an asterisk are for a single-element simulation and the model results with the asterisk are the 27 element simulation with modified Poisson's ratios. ....	143
Figure 7-13. Comparison of computational and experimental results for cyclic uniaxial stress tensile tests loaded in the warp, weft and bias 45 directions for cotton muslin fabric. The model results without an asterisk are for a single-element simulation and the model results with the asterisk are the 27 element simulation with modified Poisson's ratios. ....	144
Figure 7-14. Comparison of the computational and experimental transverse strains as a function of loading strain for cotton-polyester blend fabric. ....	145
Figure 7-15. Comparison of the computational and experimental transverse strains as a function of loading strain for cotton denim fabric. ....	146

Figure 7-16. Comparison of the computational and experimental transverse strains as a function of loading strain for cotton duck fabric. The model results without an asterisk are for a single-element simulation and the model results with the asterisk are the 27 element simulation with modified Poisson's ratios. ....	147
Figure 7-17. Comparison of the computational and experimental transverse strains as a function of loading strain for cotton muslin fabric. The model results without an asterisk are for a single-element simulation and the model results with the asterisk are the 27 element simulation with modified Poisson's ratios. ....	148
Figure 7-18. Uniaxial stress loading, unloading and reloading of a cotton-polyester blend fabric in the warp direction. ....	149
Figure 7-19. Snapshots of cyclic simulation in the bias 45 direction of cotton-polyester blend at (a) the initial configuration, (b) the maximum displacement, and (c) unloading. ....	151
Figure 7-20. Comparison of the fabric model results of a bias 45 tension test to the experimental data for cotton-polyester blend. ....	152
Figure 7-21. Comparison of the fabric model results of a bias 45 tension test to the experimental data for cotton denim. ....	153
Figure 7-22. Comparison of the fabric model results of a bias 45 tension test to the experimental data for cotton duck. ....	154
Figure 7-23. Comparison of the fabric model results of a bias 45 tension test to the experimental data for cotton muslin. ....	155
Figure 7-24. Experimental and computational uniaxial stress results for cotton-polyester blend for warp yarn orientations of 30° and 60° to the loading direction. ....	156
Figure 7-25. Experimental and computational uniaxial stress results for cotton denim for warp yarn orientations of 30° and 60° to the loading direction. ....	157
Figure 7-26. Simulation results showing non-uniform behavior at (a) the beginning and (b) near the maximum displacement for cotton-polyester blend with the warp yarn oriented 30° to the loading direction. ....	158
Figure 7-27. Modeling the shear stress and strain behavior of a cotton-polyester blend fabric subjected to a cyclic simple shear test. ....	159
Figure 7-28. Modeling the shear stress and strain behavior of a cotton-polyester blend fabric subjected to a simple shear test where the specimen is loaded, unloaded and then reloaded. ....	160
Figure 7-29. Computational results for 1:1 biaxial strain of cotton-polyester blend. ....	161
Figure 7-30. Computational results for 1:1 biaxial strain of cotton denim. ....	162

Figure 7-31. The dynamics response of a cotton-polyester blend fabric falling with gravity but pinned at the four corners at (a) 0.0 seconds, (b) 0.1 seconds, (c) 0.2 seconds, (d) 0.3 seconds, (e) 0.4 seconds, and (f) 0.5 seconds.....	163
Figure 7-32. Original configuration of a square cotton-polyester blend fabric. The elements in the blue square are displaced in the z-direction. The stress-strain data for the SVK model and the present model are compared for the elements highlighted in red.....	164
Figure 7-33. The dynamics response of a cotton-polyester blend fabric poke test using the SVK model at (a) 0.0 seconds, (b) 0.15 seconds, (c) 0.25 seconds, (d) 0.35 seconds, and (e) 0.50 seconds.....	166
Figure 7-34. The dynamics response of a cotton-polyester blend fabric poke test using the present fabric model at (a) 0.0 seconds, (b) 0.15 seconds, (c) 0.25 seconds, (d) 0.35 seconds, and (e) 0.50 seconds.....	167
Figure 7-35. Poke test stress-strain results for element 207. ....	168
Figure 7-36. Poke test stress-strain results for element 271. ....	169
Figure 7-37. Comparison of experimental, SVK and the present fabric model results in the warp and weft directions for cotton-polyester blend.....	173
Figure A-1. Uniaxial tensile test schematic. ....	185

## LIST OF BOXES

Box 5-1: Newton's Method .....	109
Box 5-2: Newmark's Method .....	110
Box 6-1: Algorithm for Fabric Model with Incremental Loading and Unloading .....	124
Box 6-2: Routine for the computation of consistent tangent operator .....	125

## CHAPTER1. INTRODUCTION

### 1.1 Motivation

In today's digital world, it is commonplace to see clothed virtual humans, or avatars, which must interact with their surrounding environment. As part of this digital realm, the computational modeling of clothing has seen increased attention since the late 1980's when Terzopoulus *et al* developed continuum-based models that allowed for dynamic simulations of elastic [4] and inelastic [5] materials for a variety of loadings. From a modeling perspective, clothing is treated as a layered shell consisting of multiple plies of fabric. As the human body moves, the clothing is subjected to a variety of deformations such as stretching, shearing and bending, all of which occur concurrently [6]. As is shown in Figure 1-1, the motivation for such clothing modeling is quite varied, ranging from computer animation to virtual fashion design to the study of the how clothing interacts with the wearer, the latter being of particular interest for this research. Noting the limited number and subjectivity of available approaches for studying the mechanical performance of protective clothing, Man and Swan [3, 7, 8] developed an analysis framework that aimed to quantify the effects that a garment of a particular fabric, size, and fit had on the mobility, dexterity and range-of-motion of a virtual human in order to better understand the clothing-wearer interaction problem. Their framework separates the clothing-wearer interaction problem into three main areas: (1) finite element modeling of fabric garments; (2) human modeling; and (3) contact interactions between the clothing and the body and self-contact of the clothing.

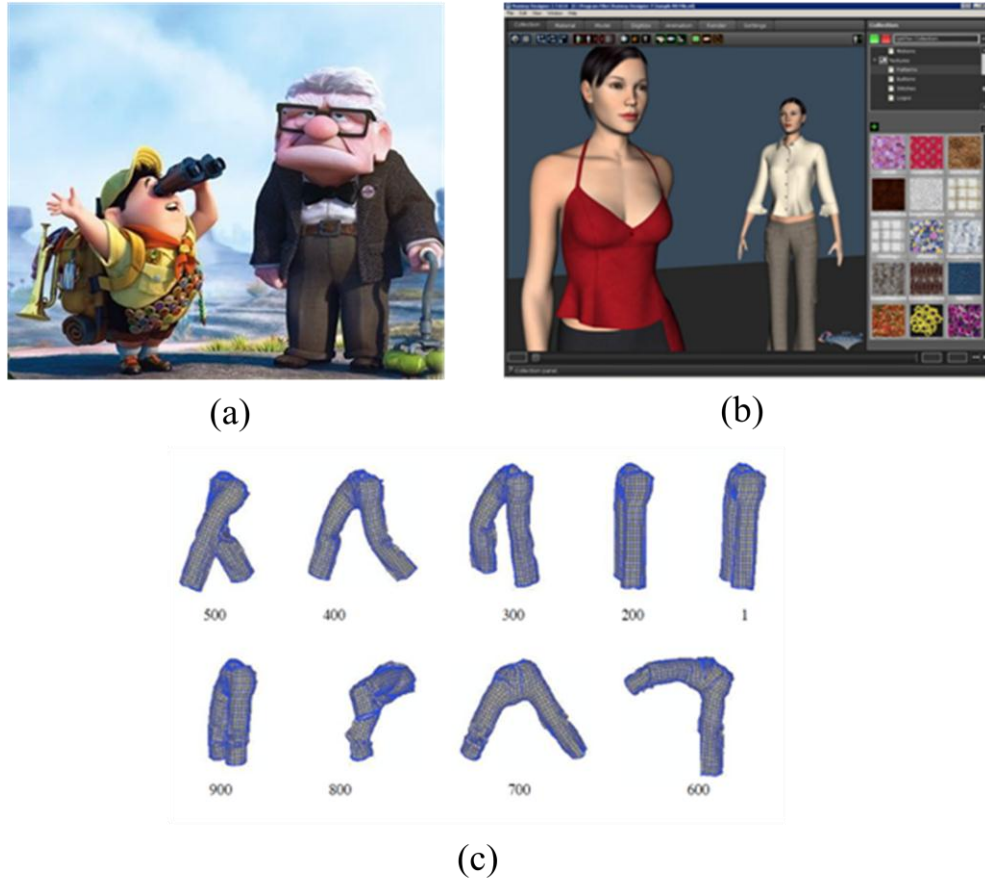


Figure 1-1. Examples of the uses of virtual clothing: (a) computer animation [1], (b) virtual clothing design [2], and (c) clothing-wearer interaction [3].

In regards to fabric modeling, House and Breen [9], Choi and Ko [10] and Hearle [11] note that in the computer graphics industry, visual realism takes precedence over mechanical realism, and that in order to quantify performance and compare to real cloth, special attention must be paid to the physical properties of fabrics in developing new constitutive models. While the mechanical behavior of fabrics is highly nonlinear, anisotropic and hysteretic [12], many authors, such as [3, 13-17], have assumed linear elastic behavior. Constitutive models that include only linear elastic deformation suffice for quasi-static models such as fabric draping where deformations are small and only the load due to gravity is considered; however, for realistic clothing simulations, the



constitutive model needs to account for a wide range of loadings induced from the movement of the virtual human and various forms of contact and should include nonlinear mechanical behavior [10, 18].

In addition to material non-linearity, the type of deformation (i.e. linear or nonlinear geometric assumptions) is also an issue. Since this research concerns itself with clothing-wearer interaction, it is important to have an idea of the maximum strains to which the clothing is subjected. In an effort to understand the relationship between fabric stretch and anthropometric requirements, Kirk and Imbrahim [19] determined that convex regions of high curvature such as the knees, seat, back and elbows, are the critical strain areas of the body. Of these, the front of the knee and the outside of the elbows exhibited the largest amounts of biaxial stretch, which have an absolute maximum fabric stretch of about 52%, if garment slip is neglected and the fabric is snug against the skin. Another study by Bassett *et al* [20] note that tensile strains in most woven garments are small, but that stretch and knitted fabrics can experience tensile strains up to 25%; and loosely woven shirt fabrics can undergo shear angles up to 0.5 radians ( $\sim 30^\circ$ ). As the strains in the previous studies are quite substantial, a large deformation approach is justified in developing constitutive models for fabric.

Thus, there is a need for a constitutive model that exhibits the complex behavior of fabrics while undergoing large deformations. While a model that includes these features will enhance the physical realism of clothing animations, Hearle [11] notes that the inherent difficulty has led many researchers to “retreat”. With that being stated, the motivation for this research is to develop a new fabric constitutive model that exhibits the nonlinear, anisotropic, and hysteretic behavior that can then be implemented in whole body shell finite-element clothing simulations as part of the Man and Swan’s framework.

## 1.2 Objectives and Organization

The purpose of this research is to develop a new constitutive model that closely matches the phenomenological response of fabrics under a variety of loadings and that will aid in the clothing-wearer interaction study. While there are numerous types of fabrics (i.e. woven, nonwoven, knit), the research here is focused on plain-woven fabrics. To this end, the following objectives are declared: (1) use available experimental procedures to study the behavior of a variety of woven fabrics as a continuum and glean appropriate physical parameters from the data for use in the constitutive model; (2) develop an constitutive model that features incremental loading and unloading, thereby capturing the nonlinear, anisotropic and hysteretic behavior (further discussed in the next chapter) and employ it in a shell finite element analysis; (3) compare results from the finite element model to experimental data; and (4) employ the constitutive model in a dynamic shell finite element simulation. While a few nonlinear and anisotropic constitutive models exist for woven fabrics, the current research: (1) addresses the symmetry assumption of orthotropic fabric models; (2) develops a novel approach for shear parameter estimation for large deformations; and (3) includes the hysteresis exhibited by fabrics when being unloaded.

This dissertation is organized as follows. The physical structure of woven textiles and common behavior is presented and common terminology is presented in Chapter 2. Chapter 3 introduces the experimental procedures used to study fabric behavior and experimental data is generated that is later used to determine appropriate material parameters. In Chapter 4, different types of models for predicting the behavior of woven fabrics are summarized and reviewed. Chapter 5 reviews the geometrically nonlinear shell finite element used in the clothing-wearer interaction study. An incrementally elastic constitutive model that is anisotropic, nonlinear and includes hysteresis is developed in Chapter 6 and the results of which are compared to experimental data. The incremental model is verified with experimental data and applied to some biaxial and

dynamic tests in Chapter 7. Finally, the dissertation is summarized and future work is proposed in Chapter 8.

## CHAPTER 2. WOVEN FABRIC STRUCTURES

Fabric, or textile, garments are inherently hierarchical structural systems, an example of which is shown in Figure 2-1. At the smallest length scale are microscopic fibers, which are combined to make larger yarns that can then be woven into a bolt of fabric made up of repeating structural patterns that depend on the type of weave. Using patterns, woven fabrics can then be cut and sewn into garments that exhibit complex behavior. In this chapter, woven textiles are described on the fiber, yarn and fabric scales and common textile terminology is defined from an engineering perspective. From a mechanical perspective, it will be shown how the properties of one length scale affect the properties of the next larger length scale.

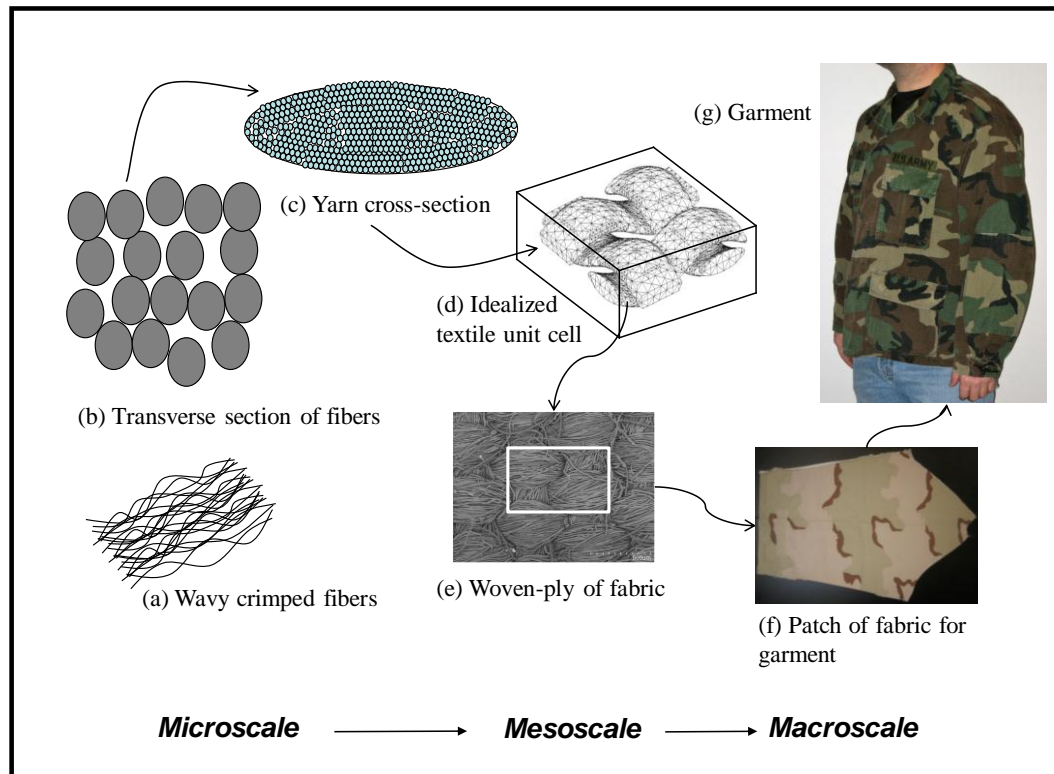


Figure 2-1. Different hierarchical length scales that comprise functional fabric garments.

## 2.1 Fibers

Although it can be hard to distinguish individual fibers with the naked eye, the characteristics of each type of fiber greatly affect the ultimate behavior of the final textile product via strength, friction, weight, and permeability. Fibers are broken down into two main categories: natural and man-made. Natural fibers are those that are a product of agriculture and include such protein-based fibers like silk and wool, and cellulose-based fibers such as cotton and linen [21]. All natural fibers are characterized as having a large variability in size, length, shape, and number of imperfections with the exception of silk, which is an extruded protein fiber that is chemically and structurally uniform. Man-made fibers are engineered materials that can be produced from a variety of sources and techniques. They are typically manufactured by extruding a chemical compound into continuous filaments that can be optimized for particular shape, size and performance criteria. Due to the nature of man-made fibers, there are several sub-categories that consist of specialty fiber types that are usually patented by the manufacturer (i.e. Coolmax® polyester, Lycra™ spandex, and Kevlar® aramid). Figure 2-2 shows two images from a scanning electron microscope (SEM). The image on the left is a close-up of the cotton fibers that make up the exterior of cotton-polyester blend yarns showing the variability of natural fibers, while the image on the right shows man-made fibers that are formed into a non-woven mat.

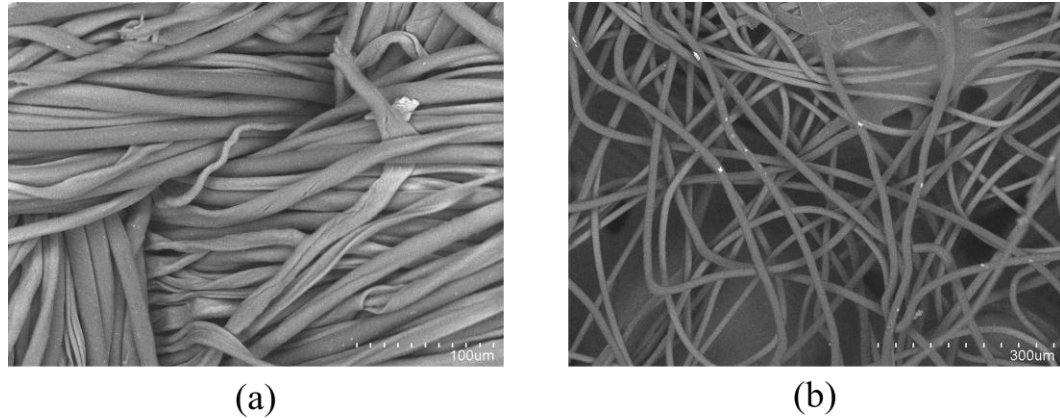


Figure 2-2. SEM photographs of (a) natural and (b) man-made fibers.

The macroscopic features of fibers include size, length, density, and crimp while the microscopic features include its microstructure [6, 22, 23]. These are described as follows:

**Fiber size** is also known as diameter or fineness. It can either be specified in terms of its actual diameter, or in terms of *linear density*. The actual diameter is usually measured using units of *microns* ( $\mu\text{m}$ ). Linear density is the weight per unit length, where the less the fiber weighs, the finer it is. Common units are *denier*, which is the mass in grams of 9000 meters of a fiber; and *tex*, which is the mass in grams of 1000 meters of a fiber. One tex is one-ninth of one denier. Denier is the typical unit in the US, while tex is more common in Europe. Typical fiber sizes are listed in Table 2.1.

**Fiber length** is important in the translation of fiber strength to yarn strength, for which longer fibers are preferred. Textile fibers are considered either *staple* length (2 to 46 cm – most natural fibers) or *filament* length (infinite length – silk and man-made fibers). Typical fiber lengths are listed in Table 2.1.

**Density** is the ratio of mass to unit volume. For fibers, density is usually expressed as grams per cubic centimeter, or g/cc. Another common term to describe a fiber is *specific gravity*, which is the ratio of the fiber's density to the density of an equal volume of water at 4°C.

**Fiber crimp** includes waves, bends, twists and curls in individual fibers and is expressed as crimps per unit length. Fibers can be linear or can exhibit 2-D or 3-D crimp (many natural fibers). Typically, the more crimp a fiber has the more that fiber can elongate. An extensive review of fiber crimp may be found in [24].

**Microstructure** of a fiber includes the cross-sectional shape (i.e. round, triangular, flat, dog-bone, and kidney-bean); and the surface (i.e. smooth, serrated, scaly, and convoluted).

Table 2.1. Typical fiber size and length [22, 23]

<i>Fiber Type</i>	<i>Diameter(<math>\mu\text{m}</math>)</i>	<i>Linear Density (DPF<sup>†</sup>)</i>	<i>Typical Length</i>
Cotton	12-20	1.5	0.32-6.35 cm
Wool	14-45	4	5-12 cm
Silk	12-30	1	~300 m
Polyester	12-25	2	any

<sup>†</sup>Denier per filament.

All of these factors have a great affect on the mechanical behavior of the fibers. Tensile tests show that fibers exhibit a viscoelastic load response that typically includes work-hardening. The strength of fibers can be greatly influenced by time (rate of loading and the fibers load history), temperature and moisture. The surfaces of fibers also dictate the amount of friction present as the fibers are spun into yarns, which influences yarn

strength, elongation and abrasion resistance among other properties [21, 23]. Mechanical properties of fibers are described as follows:

**Tensile strength** is the tensile stress, or force per area, required to cause a material to fail. Cross-sectional area of a fiber is difficult to determine, therefore fiber strength is measured relative to the linear density and is referred to as *tenacity*. Common units for tenacity are grams per denier, or gpd. The tenacity can be affected by the presence of moisture as some fibers might be stronger when wet while others may be stronger when dry.

**Elongation** is the stretching of a fiber under a tensile force and is expressed as a percentage of the original length. The published values of elongation are actually the breaking elongation which is the elongation at failure.

**Elastic recovery** is a measure of how much of the original length is recovered after a particular stretch is applied and released.

**Elastic modulus** is the ratio of stress to strain in the elastic range of a fiber.

**Resiliency** is the ability of a fiber to return to its initial position after being bent, twisted or compressed.

Table 2.2 contains these mechanical properties for some common natural and man-made fibers.



Table 2.2. Tensile properties of common fibers [21, 25].

<i>Property</i>	<i>Cotton</i>	<i>Wool</i>	<i>Silk</i>	<i>Rayon</i> <sup>†</sup>	<i>Nylon</i> <sup>†</sup>	<i>Polyester</i> <sup>†</sup>
<b>Tenacity</b> (gpd) <sup>‡</sup>						
Standard	3.0-4.9	1.0-1.7	2.4-5.1	1.9-2.3	4.0-7.2	2.8-5.6
Wet	3.3-5.4	0.9-1.4	1.8-4.0	1.0-1.4	3.7-6.2	2.8-5.6
<b>Breaking Elongation</b> (%)						
Standard	3-7	25-35	10-25	20-25	17-45	24-42
Wet		25-50		24-29	20-47	24-42
<b>Elastic Recovery</b> (%)	74 at 2% 45 at 5%	99 at 2% 63 at 20%	92 at 2% 51 at 10%	NA	98-100 at 1-10%	76 at 3%
<b>Specific Gravity</b>	1.54	1.30	1.34	1.52	1.14	1.38
<b>Tensile Strength</b> (ksi)	59.5-97.0	16.5-28.0	38.5-88.0	NA	73.0-100.0	50.0-99.0
<b>Average Elastic Modulus</b> (gpd) <sup>‡</sup>	60-70	4.5	60-116	NA	18-23	10-30

<sup>†</sup>Filament length/regular tenacity    <sup>‡</sup> grams per denier

## 2.2 Yarns

Bundles of fibers are usually combined to produce larger yarns that are more suitable for working into the various types of fabrics. Staple fibers, such as most natural fibers, are typically combined by *spinning*, which uses three main mechanisms to make a yarn: *drafting*, *fiber coherence* and *winding* [21, 23]. In drafting, fibers are slid over one another without stretching them in order to reduce the fiber strands into the desired yarn size. In fiber coherence, cohesive forces are introduced by such methods as twisting, winding, or adhesive bonding to hold the fibers together, utilizing the microstructure of the fibers, which are responsible for the strength of the overall yarn. Finally, in winding, the continuous yarn is wound onto a bobbin or cone with particular attention paid to yarn

tension and appearance. Due to the small cross-sectional area in relation to their extreme length, filament fibers, such as silk and man-made fibers, are usually combined into *producer's yarns* by twisting together the requisite number of fibers to produce the desired yarn size. Producer's yarns can then be twisted into even larger yarns at textile mills for the appropriate application. For clarification, in the composite textile industry, textiles can be manufactured using yarns, as are described here, or with *roving*, which are similar but instead of the fibers being twisted together, the fibers are aligned.

Like individual fibers, yarns are classified according to their size and density. *Yarn number* and *count* refer to the relationship between yarn weight and length. There are two common systems used in the textile industry: the *direct yarn number* and the *indirect yarn number*. The direct yarn number is the mass per unit length system and is derived from the fact that the heavier the yarn, the greater the mass per unit length. The direct yarn number uses units of tex or denier and is more conducive to the metric measurement system where the length is in meters and the mass in grams. The indirect yarn number is the length per unit weight and uses units of various *counts* and is typically used where the British Standard form of measurement is dominant where length is in yards and weight is in pounds (i.e. cotton with a count of 840 means that a pound of yarn is 840 yards long) [21, 25].

The mechanical properties of yarns are dependent on the stress-strain properties of the fibers, the inter-fiber friction and the compressive properties of the fiber mass. Fiber stress-strain relationships usually focus on the tensile behavior, described in the previous section, which can be tested on several individual fibers and then averaged. Simple expressions to estimate the yarn specific stress and yarn elastic modulus from the fiber properties are given, respectively, as:

$$\sigma_y = E_f \varepsilon_y \cos^2 \alpha \quad (2.1)$$

$$E_y = E_f \cos^2 \alpha \quad (2.2)$$

where  $\alpha$  is the angle between the orientation of the fiber and the axis of the yarn [26].

Fibers and yarns buckle easily in compression due to the long and slender geometry; therefore, only very small strain elasticity is considered when compressive forces are present. Bending, shear and torsional behavior relate to yarn flexibility. Frictional forces are introduced as fibers move relative to one another as a load is applied to the yarn. This is most apparent in staple yarns where there is more slippage due to the fibers being discontinuous. Compression of the fiber mass is how much a yarn can compact laterally when loaded, which has an effect on the slippage of fibers. It is regarded as a function of fiber crimp, density, orientation and packing [23].

### 2.3 Fabrics

Fabrics are the primary materials that are used to fabricate garments and other textiles. While fabrics can be woven, braided, knitted or non-woven, the emphasis in this research is on woven fabrics made up of two families of yarns: the *warp* and the *weft*. Warp yarns are those that run the length of the fabric, usually longitudinally between beams on a loom. Weft yarns, sometimes referred to as fill yarns, run transversely to the warp yarns. In the weaving process, a *loom* is used where the weft yarn is attached to a shuttle that is sent back and forth across the warp yarns that raise or lower at various intervals to create a weave pattern as shown in Figure 2-3. Figure 2-4 shows four common weave patterns. From left to right, they are plain, twill, satin and basket weaves.

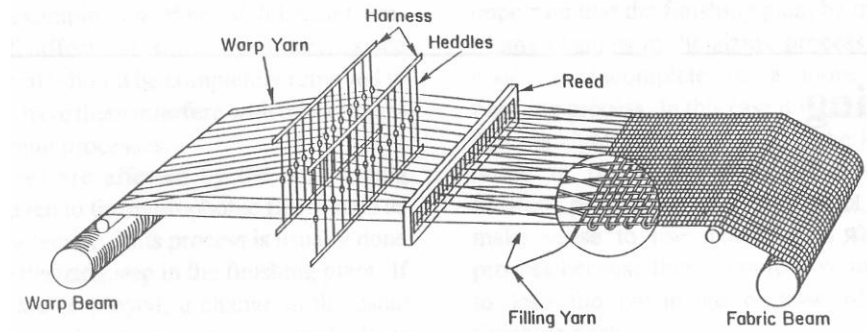


Figure 2-3. Typical weaving loom [21].

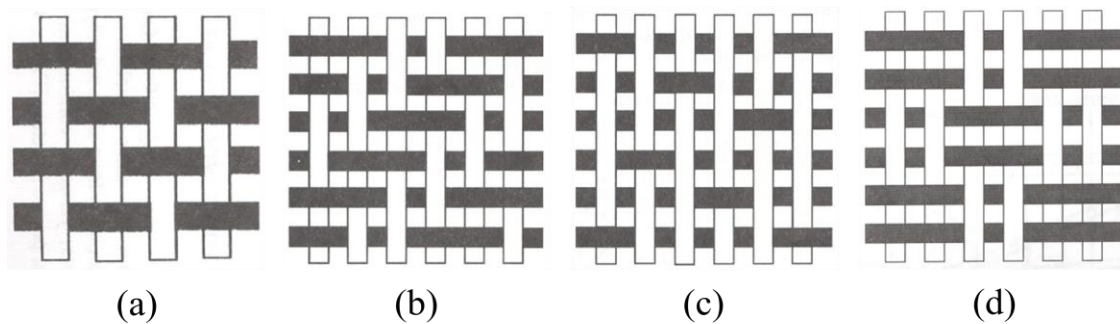


Figure 2-4. Common weave patterns: (a) plain, (b) twill, (c) satin, and (d) basket [21].

The most general terms in which a fabric's mechanical properties are described in the textile community are: *drape*, which is the manner in which a fabric bends over and conforms to three-dimensional forms; *elasticity*, the ability of a material to recover its original dimensions and shape after the removal of load; *elongation*, the ability of a fiber to be stretched; *modulus*, the resistance to strain from stress to which a fabric is exposed; and *resiliency*, the ability of a textile to return to its original shape after bending, twisting, compressing, or a combination of loads [6]. Fabric mechanical properties are governed by the yarn mechanical properties and other geometric considerations such as the *yarn count*, *degree of thread packing* within the structure, weave pattern, as well as the yarn

crimp. The yarns are the source of a fabric's strength. In a weave pattern having two families of yarns in orthogonal directions, the properties will be anisotropic with relatively high strength and stiffness in either yarn direction and much lower strength and stiffness at intermediate angles. Yarn count is the number of warp or weft yarns per inch. In principle, the higher the yarn count, the more dense the fabric, and the lower the count, the more open space will exist between yarns. In other words, for a given material, a fabric with a higher yarn count will be stronger than one with a lower count. Yarn count can also be described in terms of *ends* and *picks*; where ends refer to warp yarns and picks refer to weft yarns. If the yarn count is the same for warp and weft yarns, the weave is said to be *balanced*, meaning that the strength properties in either principle direction are the same. The degree of thread packing is similar to the yarn count in that it measures the density of a fabric where the higher the density, the stronger the fabric. Degree of thread packing also allows the *porosity*, or amount of open space, in the fabric to be calculated.

Finally, the weave pattern and yarn crimp have a large influence on the behavior of fabrics. The fact that fabrics consist of interlacing families of yarns that are woven together means that either the warp, weft, or usually both yarns assume a "wavy" shape in order to be accommodated within the fabric such as in Figure 2-5. Yarn crimp results in changes in the fabric geometry as it is loaded and unloaded which can have advantageous or adverse effects on properties such as elongation, breaking strength, tear strength, energy absorption and crease resistance. The weave pattern has a large influence on the yarn crimp. As shown in Figure 2-5, a plain weave has more crimp than a satin weave, meaning that there will be substantially more elongation in the plain weave. Basic yarn crimp geometry is shown in Figure 2-6, where  $p$  is the warp or weft thread spacing,  $d$  is the diameter of a warp or weft yarn,  $D$  is the sum of the diameters for the warp and weft yarns,  $L$  is the yarn length,  $h$  is the crimp height, and  $\alpha$  is the crimp angle [27].

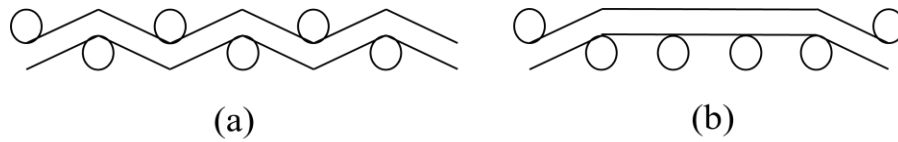


Figure 2-5. Yarn crimp in two different weave patterns: (a) plain and (b) satin.

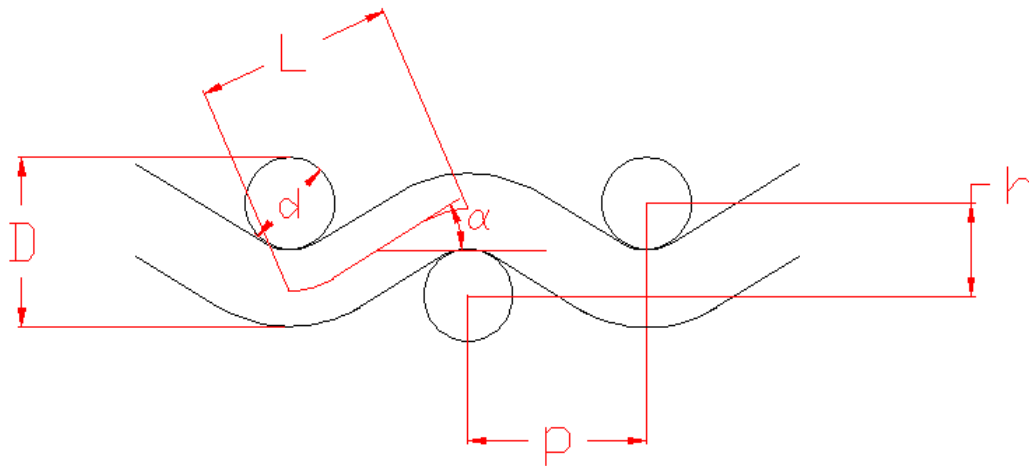


Figure 2-6. Peirce's basic yarn geometry in a plain weave [27].

Stretching occurs under tensile loads exerted on the fabric. Fabrics are able to support only small compressive forces before they buckle. Figure 2-7(a) shows typical non-linear tensile behavior of fabrics. Initially, the behavior is from the result of inter-fiber friction, inter-yarn friction and decrimping of the yarns, which results in compound behavior that exhibits relatively high elongation, though the overall tensile stress remains quite small, as shown as region A. Decrimping is the straightening of a yarn when under tensile load. Due to the interaction between the two families of yarns, when one family is under tensile load, its yarn crimp will decrease in amplitude while the other family's yarn crimp will increase in amplitude. After the fibers and yarns reconfigure/compact,

decrimping of the yarns become dominant until they reach a point of yarn lock shown in Figure 2-7(b), at which point the contact forces between the intersecting yarns become high enough where they can no longer move relative to one another. After the yarn lock occurs, the rest of the behavior is dominated by the mechanical properties of the constituents, shown in region *B*. The recovery of the fabric as it is unloaded exhibits hysteresis due to energy dissipation and residual friction between fibers and yarns, shown in region *C*. Hysteresis in this context is defined as the permanent set, or deformation, resulting of the loading history [9, 12]. Further, if the weave is unbalanced for a specific fabric, the tensile properties are generally different in the warp and weft directions leading to anisotropy of the material [12, 23].

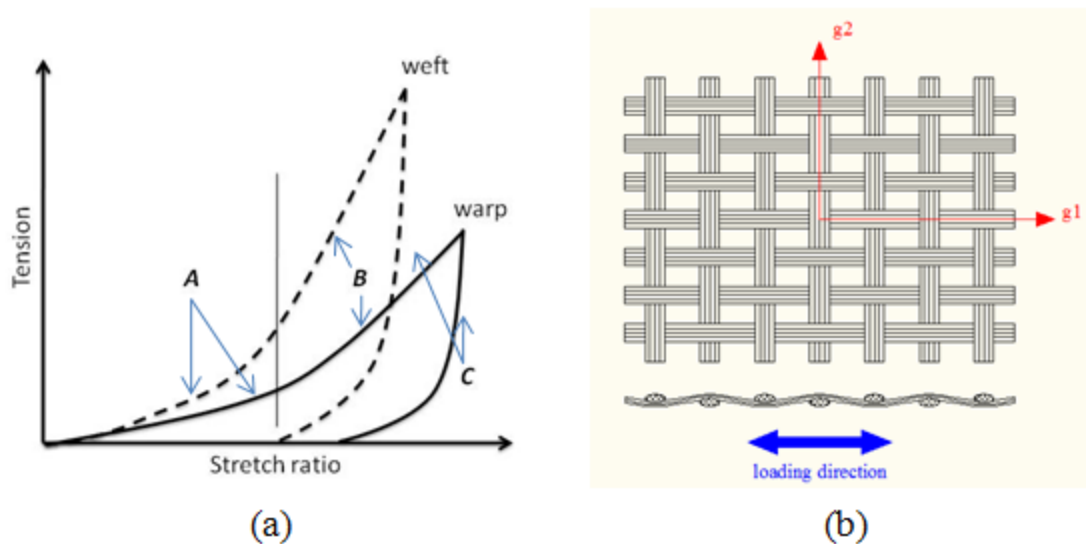


Figure 2-7. Idealization of fabric behavior due to (a) stretching where region *A* exhibits decrimping of the yarns until they lock as shown in (b) at which the material properties of the yarns dominate and a stiffer response is experienced in region *B*. Region *C* shows the hysteresis upon unloading.

Shear behavior is also highly non-linear. Resistance to shear deformation is low compared to the deformation in tension because there is slippage of fibers and yarns at

yarn intersections. In region *D* of Figure 2-8(a), the deformation is governed by frictional forces that are resisting the relative rotation of the yarns and the elastic bending deformation of the yarns. Shear deformation in region *E* is due to the slippage and bending of the yarns at the yarn intersection. Shear forces in region *F* increase rapidly due to the jamming, also known as shear lock, of the yarns, shown in Figure 2-8(b). Due to the presence of friction between fibers and yarns, hysteresis is also present with a decreasing shear angle [12, 23].

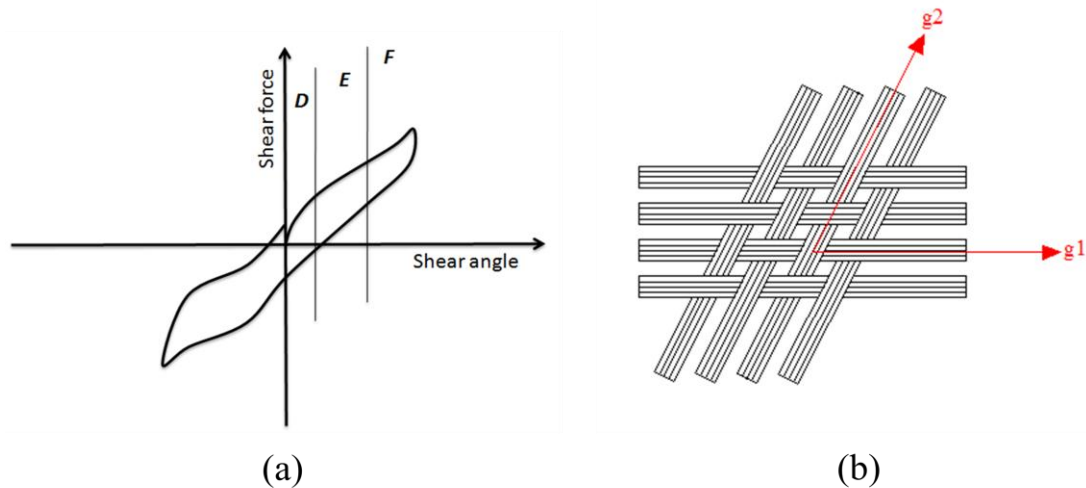


Figure 2-8. Idealization of fabric behavior (a) due to shearing [23]. In region *D*, the shear angle is governed by friction resisting rotation. Slippage and bending of the yarns at the yarn intersection occurs in region *E*, and shear force increases rapidly in region *F* due to yarn jamming, shown in (b).

The ability for fabrics to buckle gracefully in rounded folds when subjected to bending moments allow for them to be draped over any object. The bending rigidity is typically less than 1/100 of the tensile rigidity of the same fabric [12]. Figure 2-9 shows initial bending in region *G* that is governed by a frictional restraint produced mainly by contact forces at the yarn intersections. Once the friction is overcome, free elastic



bending occurs as shown in region  $H$ . Again, due to inter-fiber and inter-yarn friction, bending behavior also exhibits hysteresis [23].

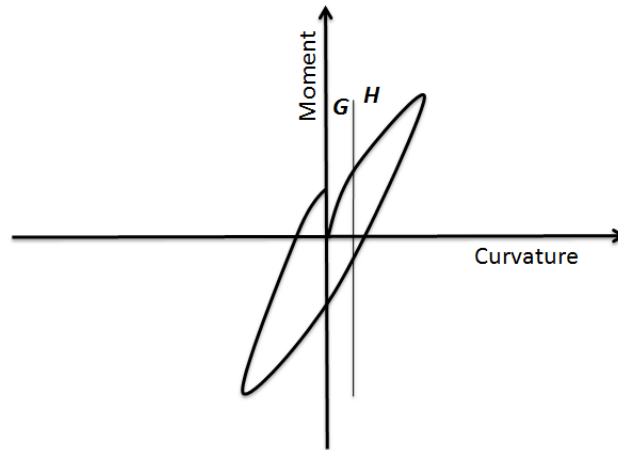


Figure 2-9. Idealization of fabric behavior due to bending where frictional constraints at yarn intersections account for behavior in region  $G$ , and free elastic bending occurs in region  $H$  once the frictional constraints are overcome [23].

In general, tensile behaviors of fabric are dependent on end and pick density (the number of warp or weft yarns per unit length), weave crimp, and yarn linear density, which affects fiber extension and yarn compression. A rough estimate of the tensile strength and stiffness of a fabric may be found by multiplying the strength or stiffness of a fiber by the volume fraction of the fibers in the fabric for a given yarn direction:

$$\begin{aligned}\sigma_{fabric} &= \phi \sigma_{fiber} \\ E_{fabric} &= \phi E_{fiber} .\end{aligned}\tag{2.1}$$

$$\phi = \frac{V_{fiber}}{V_{fabric}}$$

For example, if it is known that the fabric is a balanced weave, one can assume that 50% of the yarns run in the warp direction and 50% of the yarns run in the weft direction. If the volume fraction of the fibers in the yarn is known, then the strength and stiffness

found using (2.1) can be used as a reality check for measured values. Bending behavior is dependent on fabric thickness, weight per unit area, weave crimp, and yarn density. However, it has been found that such structural variables have much less influence on the shear behavior, which is dependent on the resistance to rotation between the two families of yarns [26, 28].

#### 2.4 Summary

The aim of this chapter was to introduce the structural hierarchy that makes up a woven fabric, each level's characteristics, and some of the terminology used in the textile field. The behavior of woven fabrics relate directly to the material properties of the fibers via complex structural interactions at both the yarn and fiber scales. This results in complex behavior that is anisotropic, nonlinear, and shows irrecoverable deformation, or hysteresis, when loaded in tension, shear and bending.

### CHAPTER 3. EXPERIMENTAL METHODS

In the textile community, many researchers use one of two common systems of experimental testing to obtain relevant material parameters: the *Kawabata Evaluation System* (KES-F), which measures the parameters listed in Table 3.1; or the *Fabric Assurance by Simple Testing* (FAST) system, which measures the parameters listed in Table 3.2 [12]. Both systems are able to provide a wide variety of parameters relating to the various forms of deformation of fabrics [12]. While the parameters determined by either the KES or FAST tests are conducive for analytical yarn models, trying to incorporate them into an anisotropic continuum model is much more difficult [29]. For this reason, more traditional structural material testing methods are used in this research to develop appropriate material parameters for various fabrics samples.

Table 3.1. Parameters measured by KES-F system [12].

<b>Property</b>	<b>Symbol</b>	<b>Parameter Measured</b>
<i>Tensile</i>	<i>EMT</i>	<i>Extensibility</i>
	<i>LT</i>	<i>Linearity of the tensile load-extension curve</i>
	<i>WT</i>	<i>Tensile energy per unit area</i>
	<i>RT</i>	<i>Tensile resilience</i>
<i>Shear</i>	<i>G</i>	<i>Shear rigidity</i>
	<i>2HG</i>	<i>Shear hysteresis (width of loop at <math>\pm 0.5^\circ</math> shear angle)</i>
	<i>2HG5</i>	<i>Shear hysteresis (width of loop at <math>\pm 5^\circ</math> shear angle)</i>
<i>Bending</i>	<i>B</i>	<i>Bending rigidity</i>
	<i>2HB</i>	<i>Bending hysteresis (width of loop at <math>\pm 0.5 \text{ cm}^{-1}</math> curvature)</i>
<i>Surface</i>	<i>MIU</i>	<i>Coefficient of fabric surface friction</i>
	<i>MMD</i>	<i>Mean deviation of MIU</i>
	<i>SMD</i>	<i>Geometric roughness</i>
<i>Compression</i>	<i>LC</i>	<i>Linearity of compression-thickness curve</i>
	<i>WC</i>	<i>Compression energy per unit area</i>

Table 3.1. Continued

	<i>RC</i>	<i>Compression resilience</i>
<i>Thickness</i>	<i>T</i>	<i>Fabric thickness</i>
<i>Weight</i>	<i>W</i>	<i>Fabric weight per unit area</i>

---

Table 3.2. Parameters measured by FAST system [12].

<b>Property</b>	<b>Symbol</b>	<b>Parameters Measured</b>
<i>Tensile</i>	<i>E5</i>	<i>Extension at 5N/m</i>
	<i>E20</i>	<i>Extension at 20 N/m</i>
	<i>E100</i>	<i>Extension at 100 N/m</i>
	<i>EB5</i>	<i>Bias extension</i>
<i>Shear</i>	<i>G</i>	<i>Shear rigidity</i>
<i>Bending</i>	<i>C</i>	<i>Bending length</i>
	<i>B</i>	<i>Bending rigidity</i>
<i>Compression</i>	<i>T2</i>	<i>Thickness at 2 gf/cm<sup>2</sup></i>
	<i>T100</i>	<i>Thickness at 100 gf/cm<sup>2</sup></i>
	<i>ST</i>	<i>Surface thickness</i>
	<i>STR</i>	<i>Released surface thickness</i>
<i>Dimensional stability</i>	<i>RS</i>	<i>Relaxed shrinkage</i>
	<i>RC</i>	<i>Hygral expansion</i>
<i>Derived parameter</i>	<i>F</i>	<i>Formability</i>

---

### 3.1 Objectives

A series of experimental tests were carried out in this research to become familiar with the behavior of a four different woven fabrics: Cotton-polyester blend, cotton duck, cotton muslin, and cotton denim; which are shown in Figures 3-1 through 3-4, respectively. Cotton-polyester blend fabric is commonly used for military battle dress uniforms (BDUs) and has an unbalanced plain weave architecture that includes periodic larger yarns that help retard fabric tearing. The yarns themselves are made up of a

polyester core with a cotton fiber exterior. Cotton duck, also known as duck canvas, is a tightly woven heavyweight fabric that has an unbalanced  $2\times 1$  basket weave, meaning that two yarns run together side-by-side in the warp direction with only one yarn in the weft. Cotton muslin is a loosely, plain woven medium-weight fabric made up of white or unbleached cotton yarns. Denim is a yarn-dyed cotton fabric that has twill weave architecture. Denim usually has a blue dyed warp yarn, while the weft yarn is white [6]. Various tests, including uniaxial tensile tests were performed in three different orientations of the warp fiber direction with respect to the load direction:  $0^\circ$ ,  $45^\circ$  and  $90^\circ$ . Objectives of these tests were to generate stress and strain data in order to investigate the tensile and shear behavior.

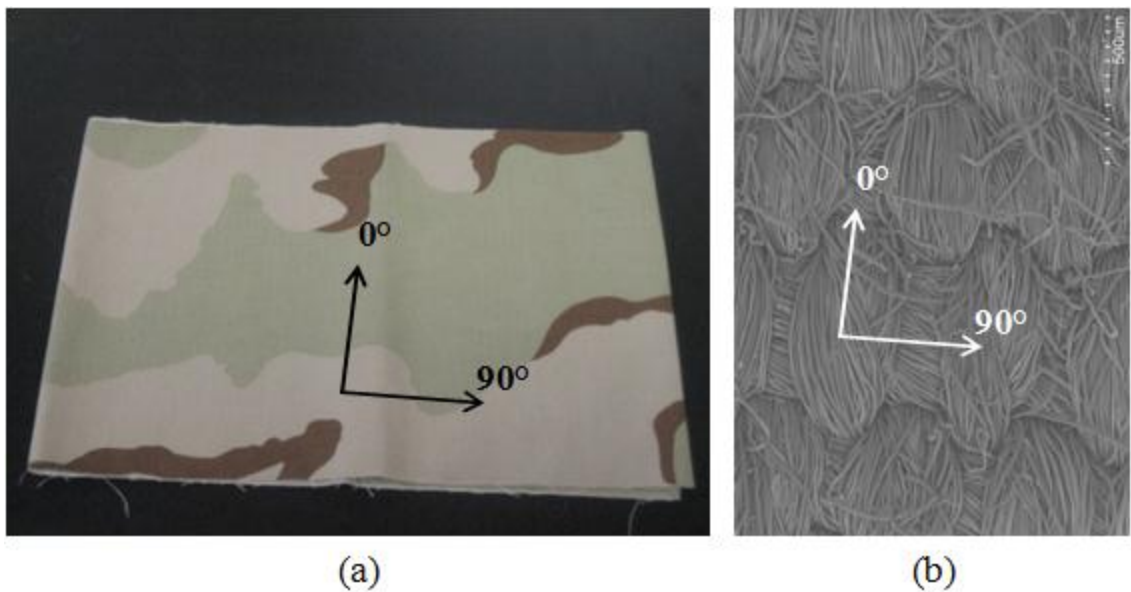


Figure 3-1. Cotton-polyester blend: (a) macroscopic and (b) SEM photographs.

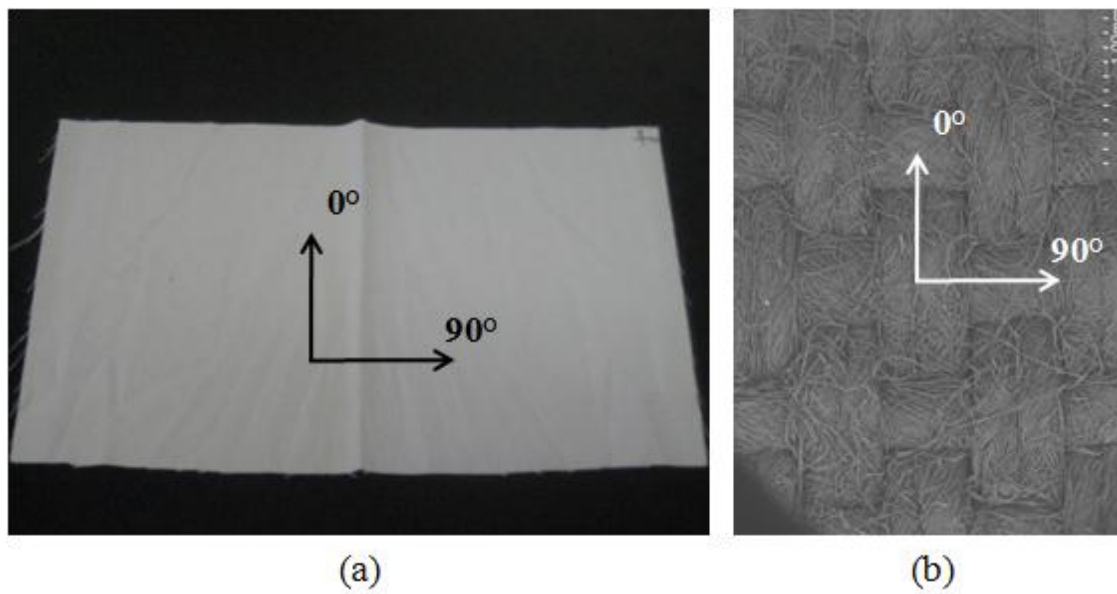


Figure 3-2. Cotton duck: (a) macroscopic and (b) SEM photographs.

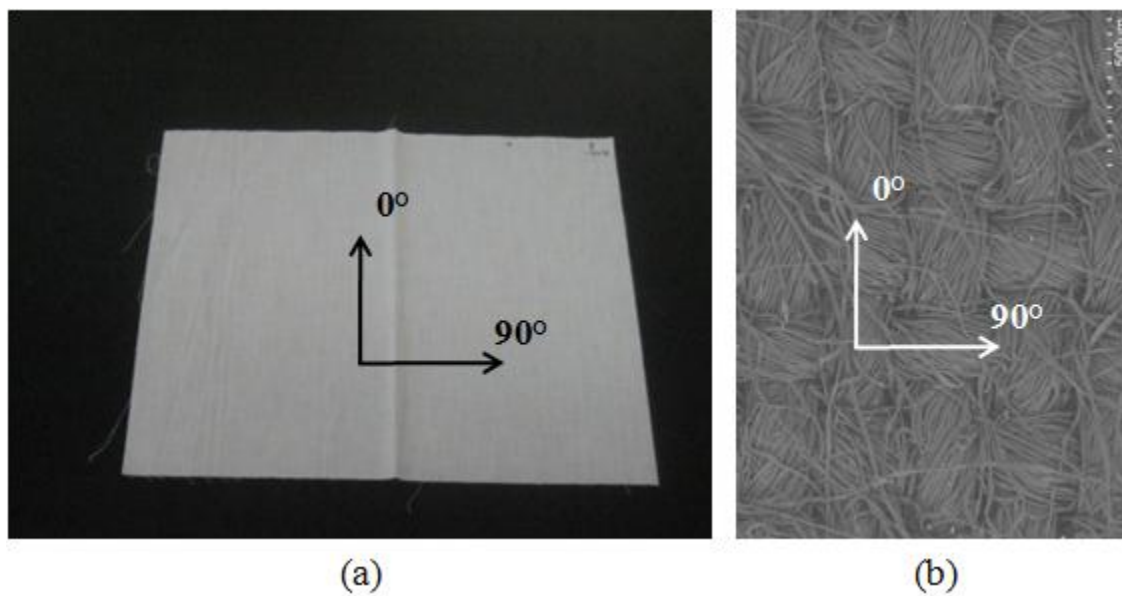


Figure 3-3. Cotton muslin: (a) macroscopic and (b) SEM photographs.

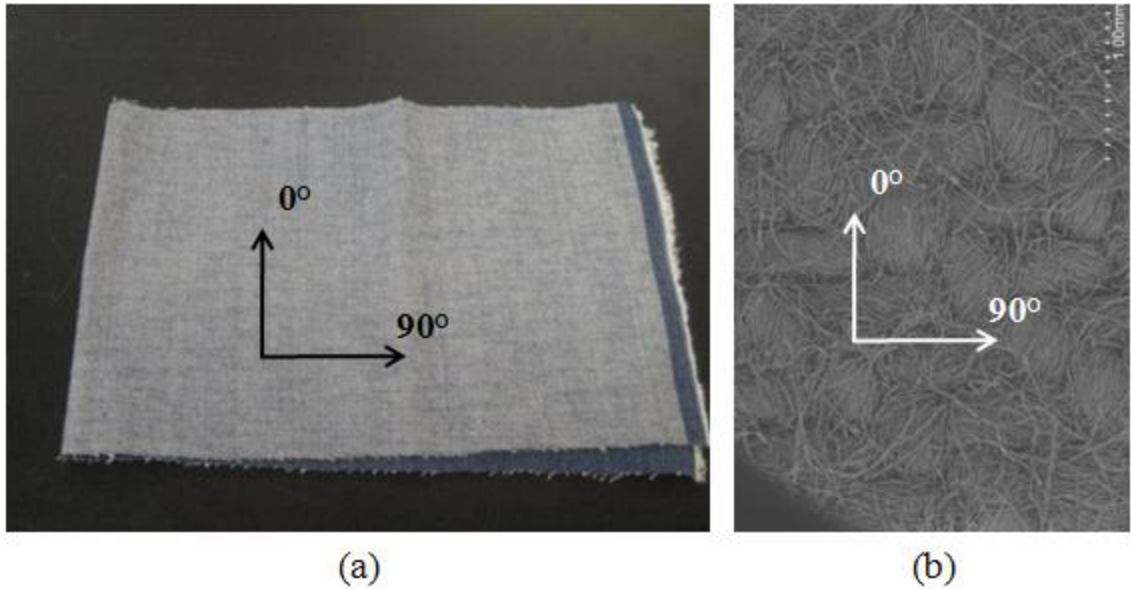


Figure 3-4. Cotton denim: (a) macroscopic and (b) SEM photographs.

### 3.2 Specimen Preparation

Test specimens are cut from the middle region of a swath of fabric using a rotary cutting tool and a measuring guide (Figure 3-5a). The middle region is defined here as being the area of the fabric that is at least 10% of the total bolt width away from either selvage [25] to ensure uniformity of the weave structure (Figure 3-5b). The longitudinal axis of the specimens included three different orientations:  $0^\circ$ ,  $45^\circ$  and  $90^\circ$  (Figure 3-5c). Based upon guidelines from ASTM D5035-95 [30], specimens are cut so that the starting geometry is 1.0 inch wide and approximately 7.5 inches long. Using a sewing machine, the specimens are finished by being sewn into loops that are 6.75 inches in circumference (Figure 3-5d), so that they may be used with our gripping method, described later.

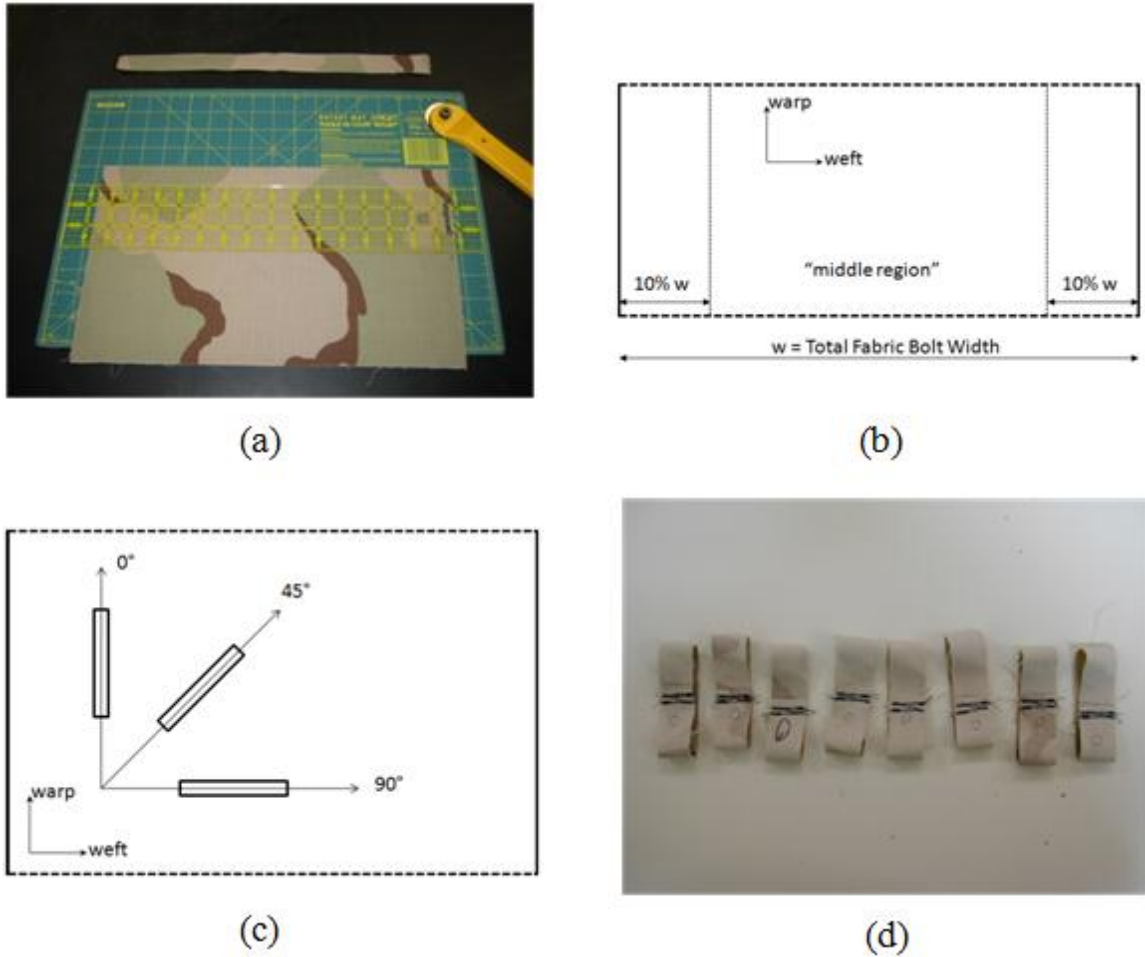


Figure 3-5. Woven fabric samples. (a) Sample preparation, (b) definition of middle region, (c) orientation of specimens, and (d) completed specimens.

### 3.3 Fabric Tests, Procedures, and Results

#### 3.3.1 Fabric Thickness and Density

The fabric thickness is measured using a procedure based upon ASTM D1777 [31] using several specimens of each fabric. Each specimen is placed between two thin acrylic plates with a minimal applied compressive pressure. Using a digital caliper, the fabric thickness is determined by subtracting the thickness of the two plates with the



specimen between them by the thickness of only the two plates, shown in Figure 3-6.

The average thicknesses of the tested fabrics are listed in Table 3-3.

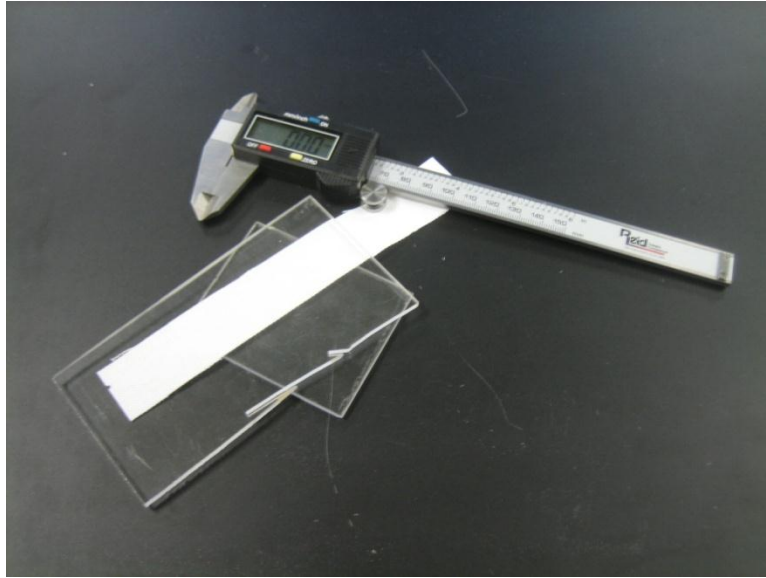


Figure 3-6. Test method for determining fabric thickness using two acrylic plates and a digital caliper.

The fabric density is found using the aforementioned fabric thickness and the mass per unit area, which is determined using ASTM D3776-Option C [32]. The density is then found by dividing the average mass per unit area by the corresponding fabric thickness. The mass densities for the four fabrics are presented in Table 3-3.

Table 3.3. Density and thickness data for tested fabrics.

<b>Fabric</b>	<b>Label</b>	<b>Material</b>	<b>Weave</b>	<b>Thickness, mm</b>	<b>Mass per Unit Area, g/m<sup>2</sup></b>	<b>Mass Density kg/m<sup>3</sup></b>
Blend	CRS8	Cotton/Poly	Plain	0.38	230	590
Duck	WD10	Cotton	Basket	0.62	290	470
Denim	BD11	Cotton	Twill	1.12	390	350
Muslin	WM12	Cotton	Plain	0.28	100	370

### 3.3.2 In-plane Tensile Behavior

#### Experimental Setup

Uniaxial and biaxial extension tests are the most common methods to determine tensile moduli for fabrics in the warp and weft directions. While the presence of transverse loadings has been shown to have a large effect on the apparent stiffness of fabric in the longitudinal direction due to decrimping [33, 34] and would have a significant effect on the apparent Poisson's ratio [35], the tests conducted for this research are limited to uniaxial tests. Many researchers, including [17, 29, 36, 37], have utilized uniaxial tests; and two ASTM standards [38, 39] are available for determining the breaking force and elongation of textile fabrics. For these tests, a gripping method similar to the one used by [40, 41] is employed where fabric specimen loops are loaded into the grips around the two stainless steel pins shown in Figure 3-7a.

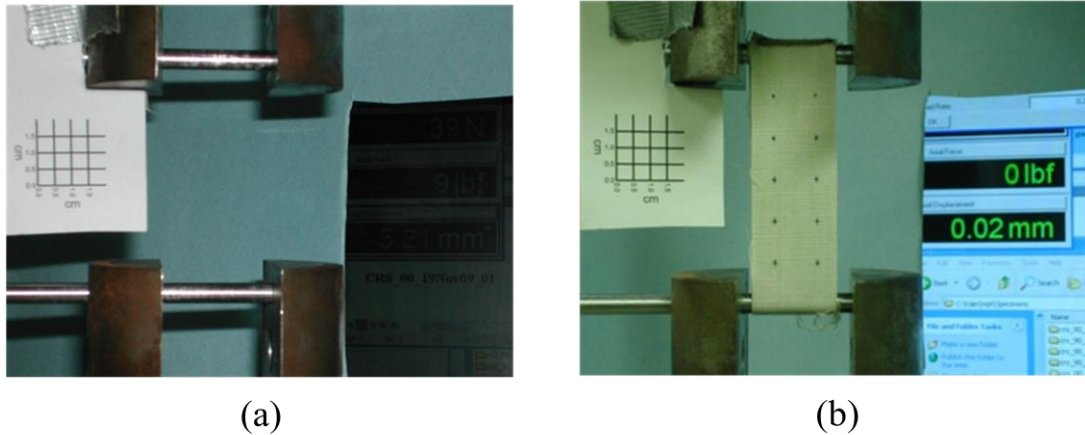
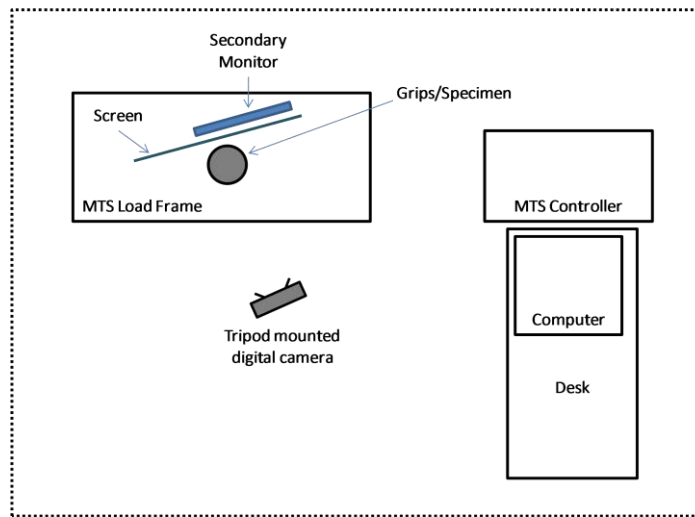


Figure 3-7. Experimental pin grips (a) without and (b) with fabric specimen loaded.

In order to determine the tensile behavior of the fabric in the warp and weft directions, specimens were loaded into the two grips shown in Figure 3-7b, so that the gage length between the centers of the pins was 3.0 inches and that the specimens were taut but with negligible pre-stress. A *MTS*<sup>®</sup> servo-hydraulic load frame with *Multi-Purpose Testware*<sup>™</sup> software was used for all mechanical tests. Monotonic and cyclic tests for each orientation were carried out in displacement control, where force was measured using a load cell mounted on the load frame and the displacement was measured using the internal LVDT connected to the actuator. Tests were carried out at  $20^{\circ} \pm 3^{\circ}\text{C}$  and  $50\% \pm 5\% \text{RH}$ . The strain rate for each test was 0.003 /s. Photographs using a *Canon PowerShot SD400* digital camera were taken during tests to help determine local longitudinal and transverse strains. The full experimental setup is shown in Figure 3-8.



(a)



(b)

Figure 3-8. Experimental setup: (a) photograph and (b) schematic including MTS load frame, secondary monitor, and digital camera.

Upon completion of each test, *Microsoft Excel* was used to convert the uniaxial force and displacement data into the corresponding components of 2nd Piola-Kirchhoff stress and Green-Lagrange strain using the following equations [42]:

$$S_{ii}(t) = \frac{P(t)}{A_0 \left[ 1 + \frac{l(t) - l_0}{l_0} \right]} \quad (3.1)$$

$$E_{ii}(t) = \left( \frac{l(t) - l_0}{l_0} \right) + \frac{1}{2} \left( \frac{l(t) - l_0}{l_0} \right)^2 \quad (3.2)$$

where  $S_{ii}$  is the tensile stress in the loading direction in MPa,  $P(t)$  is the force at time  $t$  in N,  $A_0$  is the initial cross-sectional area of each fabric in  $\text{mm}^2$ ,  $E_{ii}$  is the tensile strain in the loading direction,  $l(t)$  is the displacement at time  $t$  in mm and  $l_0$  is the original gage length in mm, and  $ii$  is the either the warp (11) or weft direction (22) with no summation implied. A derivation of Equations (3.1) and (3.2) can be found in Appendix A. It is noted here that the experimental measurements are limited to the plane of the fabric and therefore the out-of-plane deformation is neglected.

The specimens in the monotonic tests were loaded until failure. The results of the monotonic tests for cotton-polyester blend are shown in Figure 3-9 and show the typical nonlinear fabric behavior caused by decrimping of the yarns as well as anisotropy between the warp and weft yarn directions. The fabric shows higher ultimate strength in the warp direction, but a stiffer response in the weft direction. The strain-to-failure in the warp direction is roughly twice that of the weft direction. Both directions also show apparent yielding behavior before the eventual failure. Figure 3-10 shows the results for cotton duck, where it is noted that both warp and weft directions show similar strain-to-failure, however, the ultimate strength in the warp direction is about twice that of the weft. The results for cotton muslin, shown in Figure 3-11, exhibit the highest degree of anisotropy of the tested fabrics, which is interesting since they are considered balanced weaves. The strength and stiffness in the warp direction are much greater than those of the weft, though the weft direction exhibits a much greater strain-to-failure. Finally, the results for cotton denim, shown in Figure 3-12, show that the ultimate strength in the

warp and weft directions is roughly equal, though the strain-to-failure in the warp direction is more than twice that of the weft.

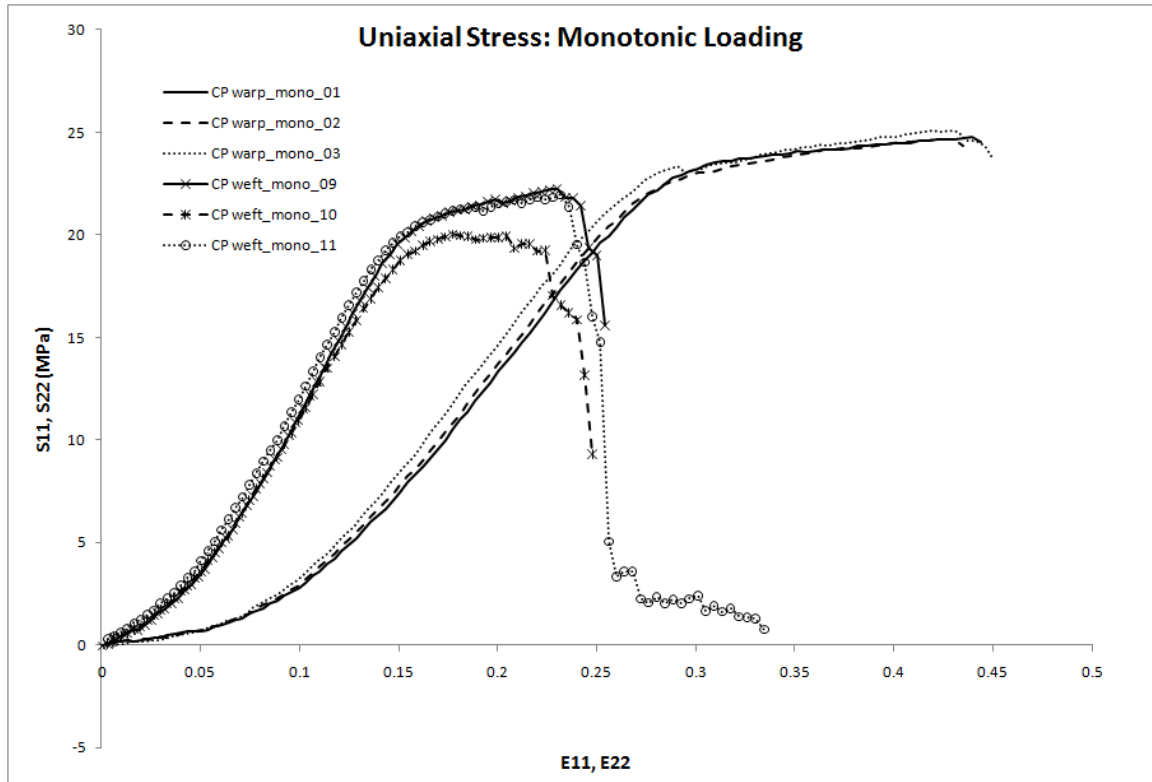


Figure 3-9. Experimental data for cotton-polyester blend from three monotonic tests in the warp direction and three monotonic tests in the weft direction.

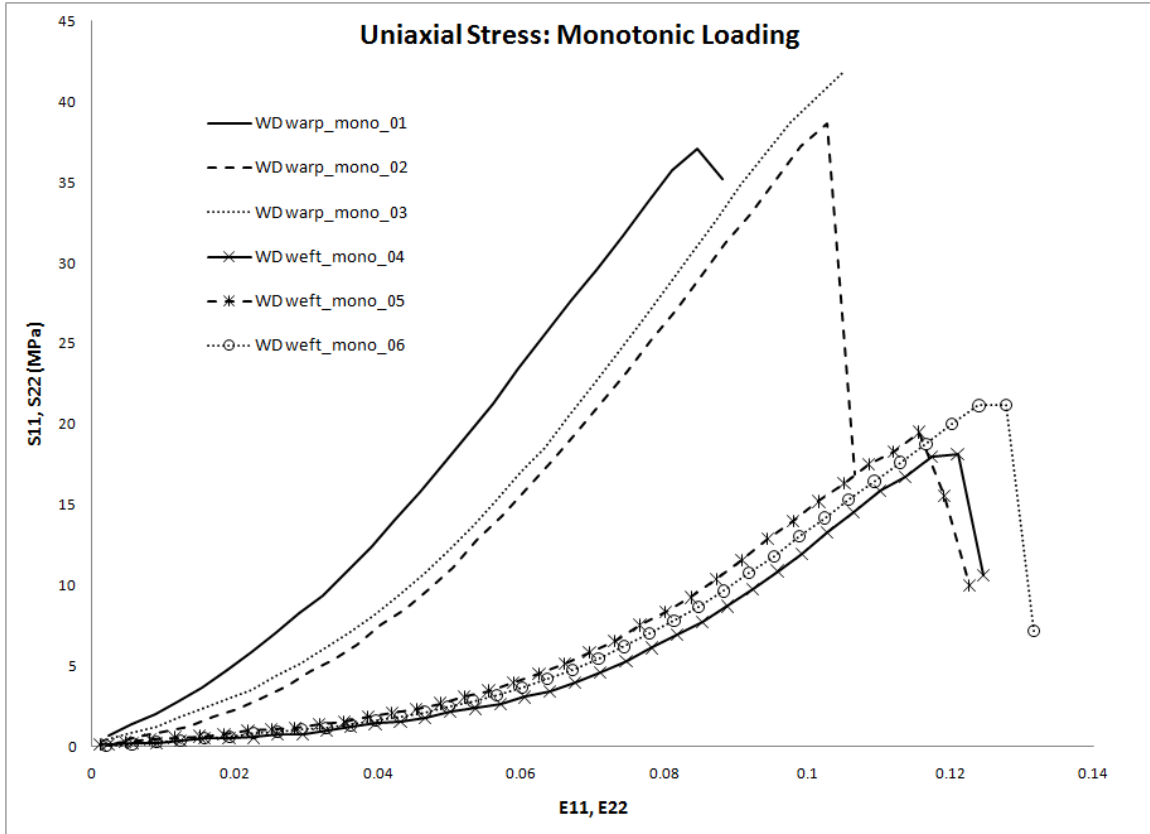


Figure 3-10. Experimental data for cotton duck from three monotonic tests in the warp direction and three monotonic tests in the weft direction.

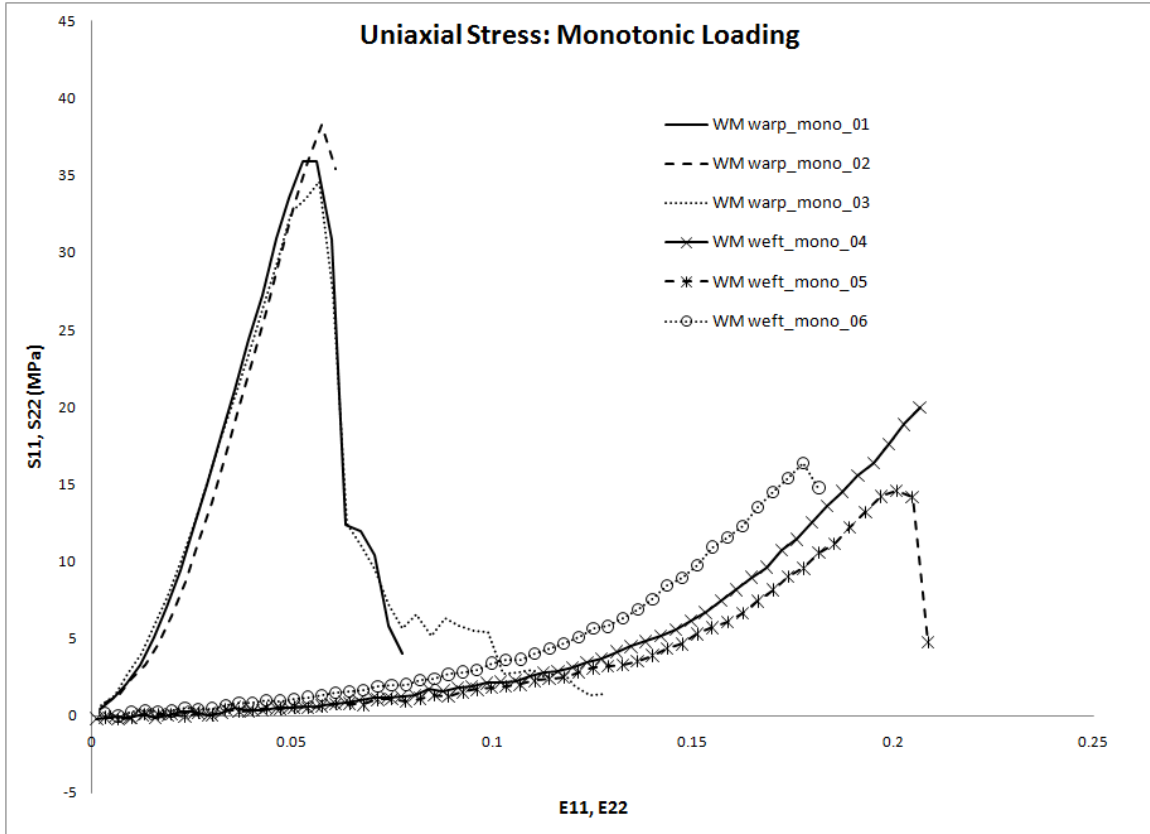


Figure 3-11. Experimental data for cotton muslin from three monotonic tests in the warp direction and three monotonic tests in the weft direction.



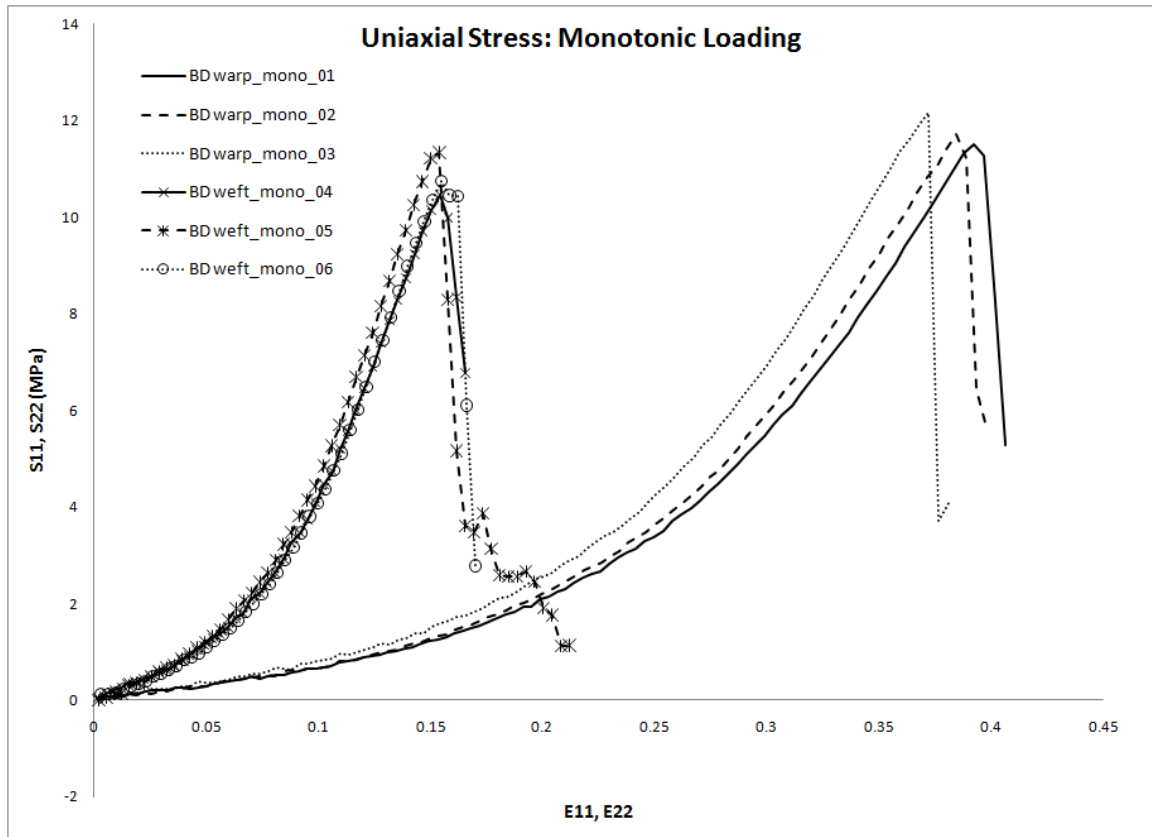


Figure 3-12. Experimental data for cotton denim from three monotonic tests in the warp direction and three monotonic tests in the weft direction.

For cyclic tests, the tensile strain amplitude is selected from monotonic results as a strain that just precedes yielding or breakage of the fabric. The corresponding displacements are found from the strain values and are listed in Table 3.4. The test program was modified to load the specimen in displacement control until the maximum displacement was reached, after which, the specimen was then unloaded at the same strain rate until the displacement reaches zero. Figures 3-13 through 3-16 display the stress-strain results for single-cycle tests, and feature nonlinear decrimping, anisotropy, as well as hysteresis upon unloading. Here, hysteresis refers to the partial recovery of deformation upon unloading and is characterized by a steep slope from the point of unloading, which gradually decreases as some crimp is recovered and the specimen loses

contact with the pin grip (Figure 3-17). Earlier tests using wedge grips instead of pins exhibited similar hysteresis, where instead of losing contact, the specimen buckled due to residual deformation.

Table 3.4. Maximum displacement for single-cycle tensile tests.

<b>Fabric</b>	<b>Warp Displacement, mm</b>	<b>Weft Displacement, mm</b>
C/P Ripstop	18.0	10.0
Cotton Denim	20.0	9.00
Cotton Duck	6.00	7.00
Cotton Muslin	3.00	10.0

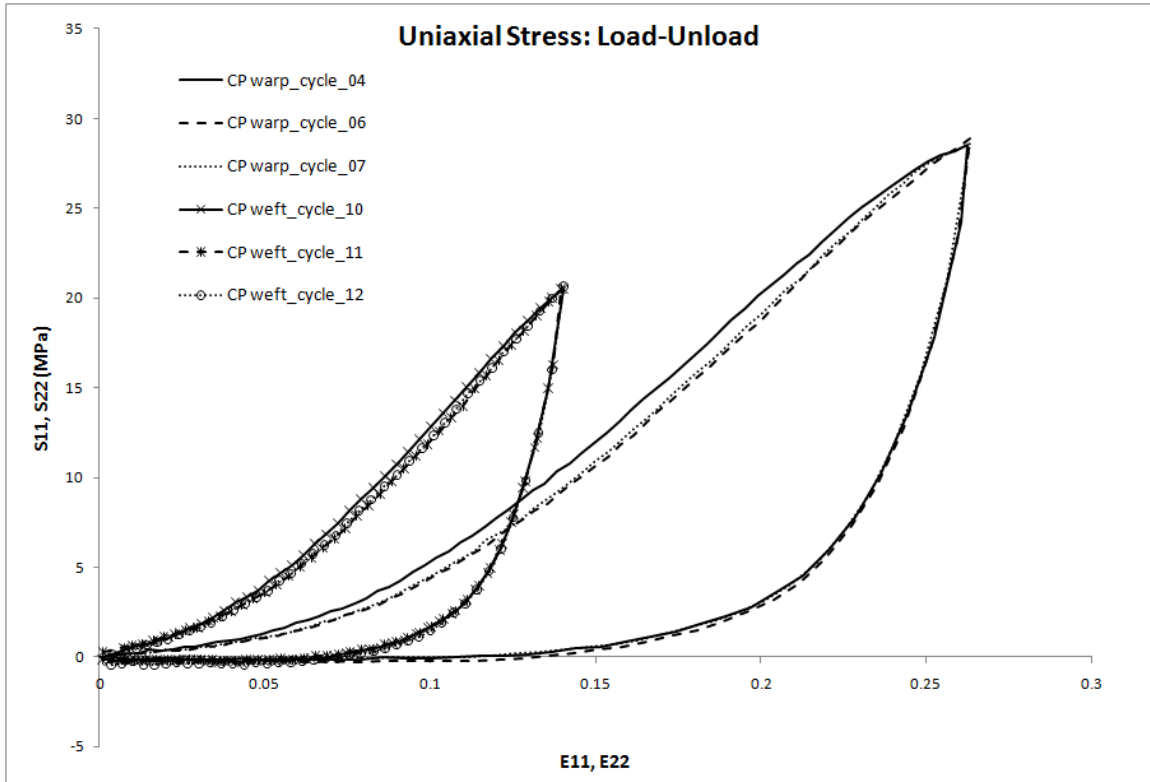


Figure 3-13. Experimental load/unload data for cotton-polyester blend from multiple single-cycle tests in the warp and weft directions.

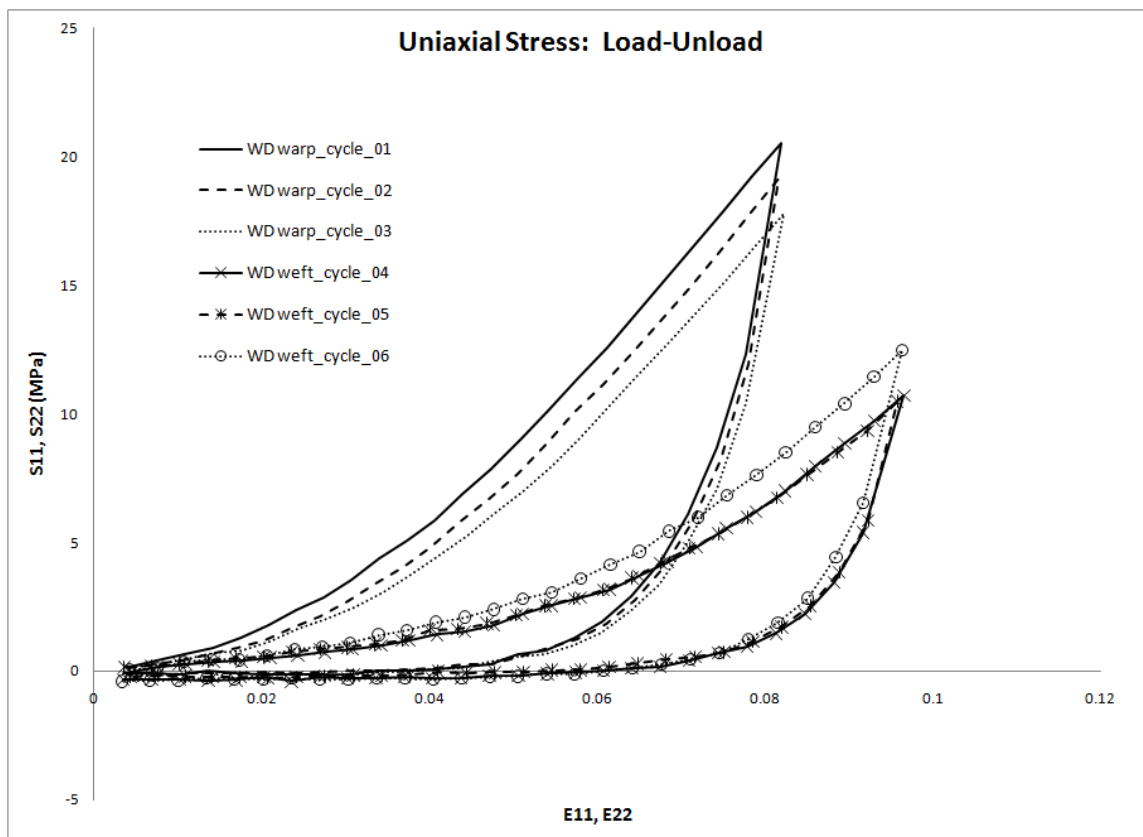


Figure 3-14. Experimental load/unload data for cotton duck from multiple single-cycle tests in the warp and weft directions.

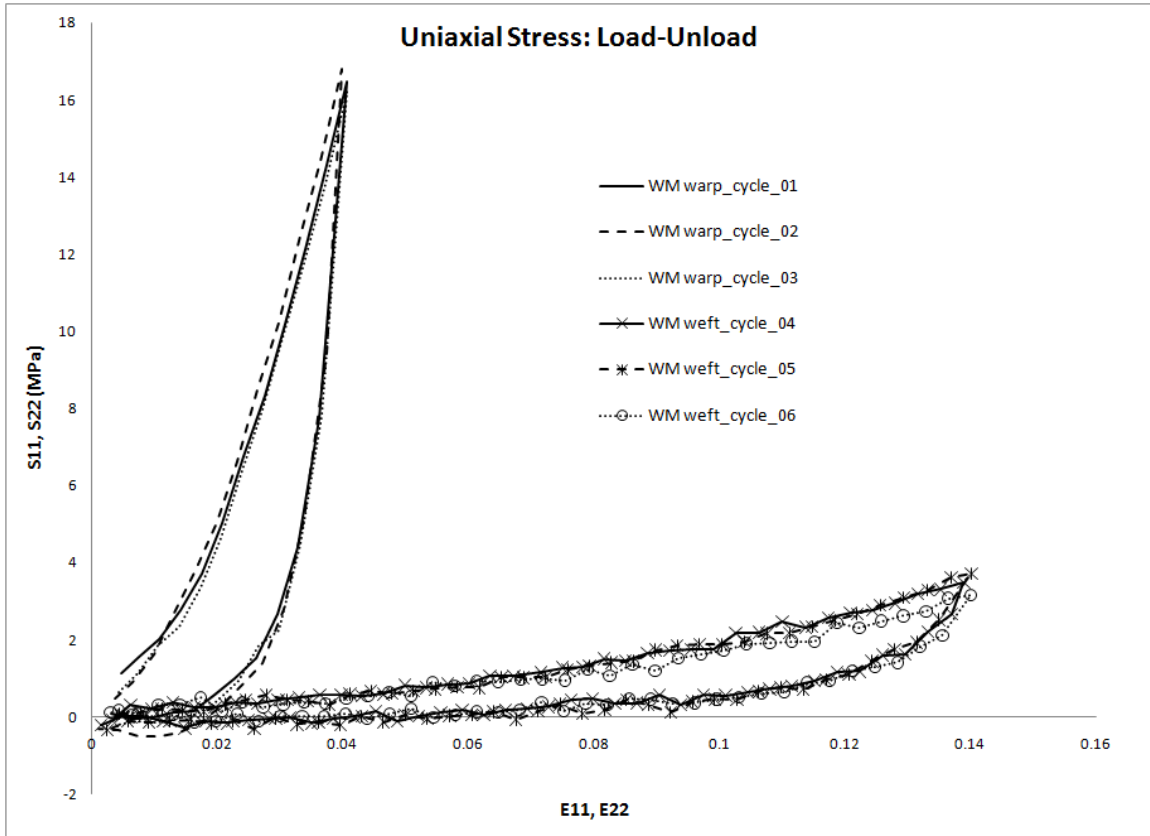


Figure 3-15. Experimental load/unload data for cotton muslin from multiple single-cycle tests in the warp and weft directions.

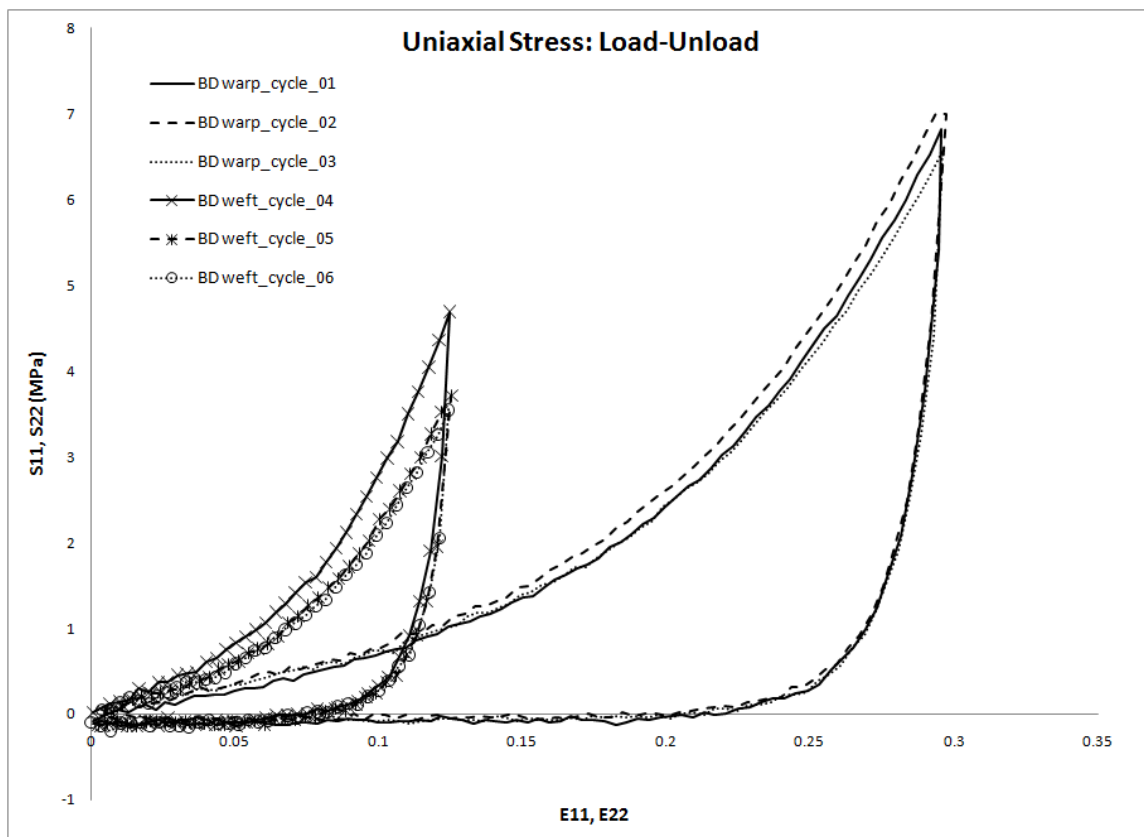


Figure 3-16. Experimental load/unload data for cotton denim from multiple single-cycle tests in the warp and weft directions.

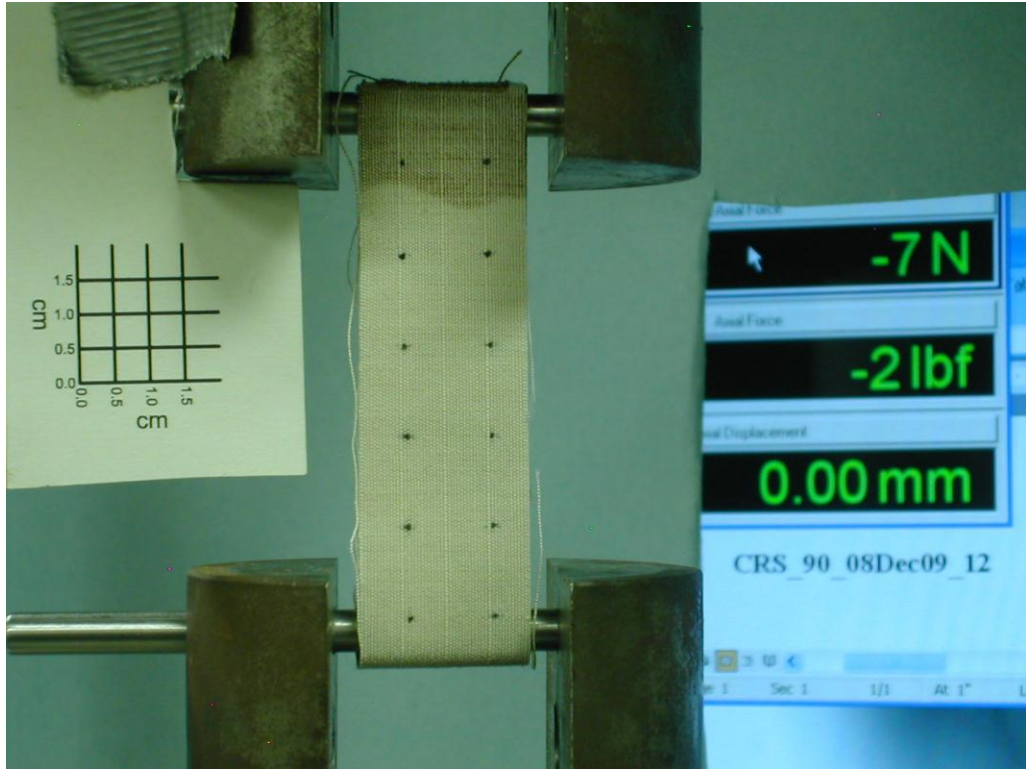


Figure 3-17. End of test cycle showing the resulting gap between the bottom pin and the specimen due to permanent deformation in the fabric.

To test the effect of different strain rates, cotton-polyester blend warp specimens were loaded at three additional strain rates:  $1.31 \times 10^{-3}$  /s,  $1.31 \times 10^{-2}$  /s, and  $1.31 \times 10^{-1}$  /s. The results, shown in Figure 3-18, exhibit very little difference in the higher two strain rates with the slower strain rate giving slightly smaller stress values. For this research, the strain rate is assumed to have little effect on the stress-strain results.

In addition to the battery of displacement control tests, some tests cycled in force control were performed. Figure 3-19 shows one such test of cotton-polyester blend loaded in the warp direction. As the fabric is unloaded and subsequently reloaded, it follows a similar path that that is much steeper and more linear than the original loading path. Once the fabric is loaded past a point of virgin strain, it continues on a trend that is

consistent with the original nonlinear loading path. The figure also shows that multiple cycles exhibit hysteresis loops.

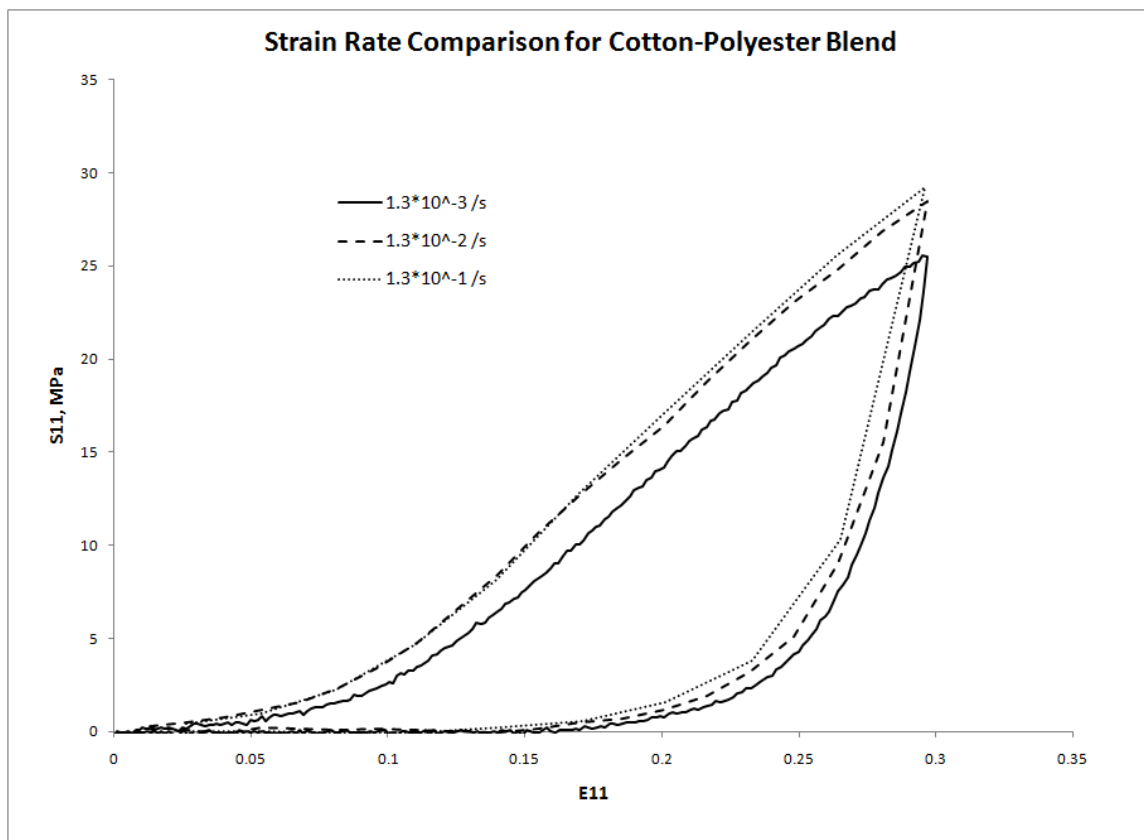


Figure 3-18. Strain rate comparison for cotton-polyester blend loaded in the warp direction.



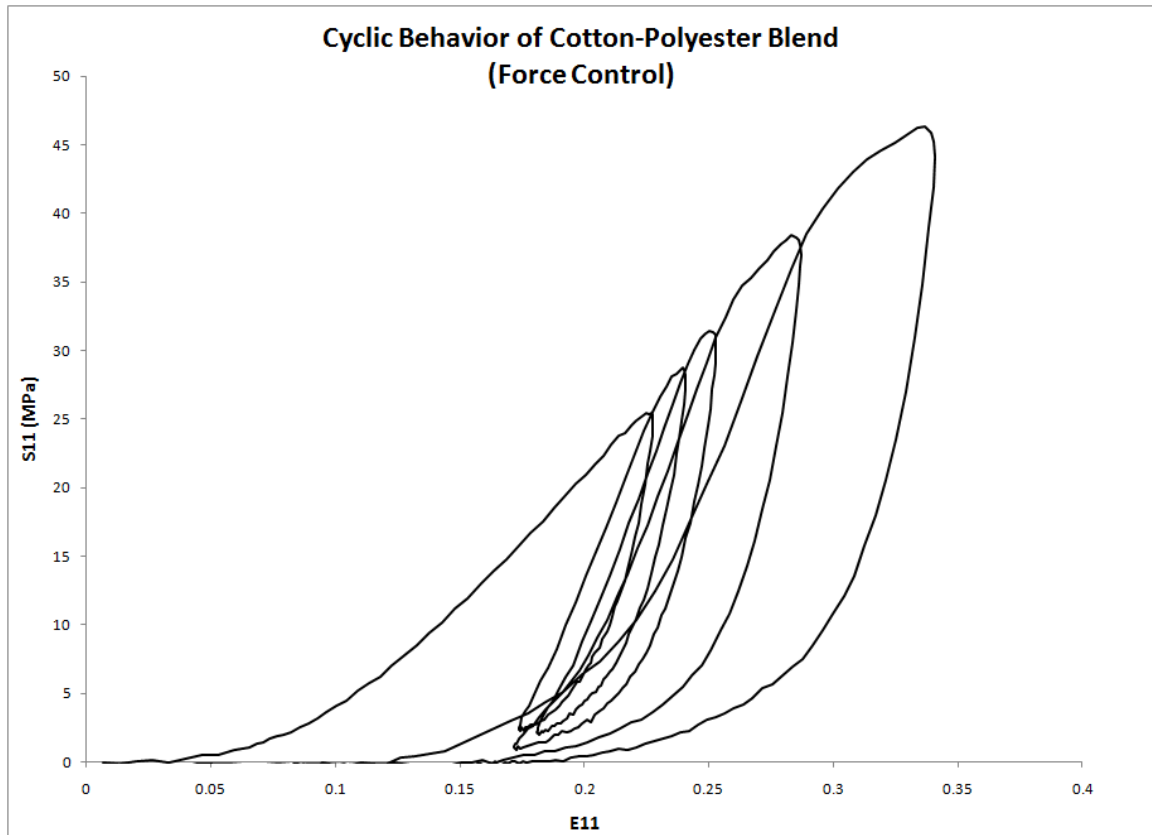


Figure 3-19. Load/unload cyclic behavior of a cotton-polyester blend specimen under force control in the warp direction.

### 3.3.3 Poisson's Ratios

Like conventional homogenous materials such as metals and plastics, a fabric stretched uniaxially in either the warp or weft direction will feature a corresponding contraction in the lateral direction, even though there is no external loading in that direction. However, unlike homogenous materials, this *apparent* Poisson's ratio is a result of geometrical changes due to the crimp interchange [41]. In order to determine the apparent Poisson's ratios of the fabric, an experimental setup similar to the one used by Bruniaux *et al* [29] was utilized in which a digital camera is used to determine longitudinal and transverse strains as a fabric specimen is loaded in uniaxial tension. As

an extension of their technique, we use a grid of dots to determine the Poisson's ratios throughout the gage length of the specimen as shown in Figure 3-17.

### 3.3.3.1 Experimental Procedure

As a specimen is loaded in uniaxial stress, a series of digital photos is taken, capturing the displacements of each dot. Each series of photos is then imported into *AutoCAD*<sup>®</sup> and scaled according to the dimensions of the known scale in the photo. The dots are connected to create several rectangles. The stretch and contraction of the respective sides of each rectangle are measured as shown in Figure 3-20, and the corresponding Green-Lagrange strains are calculated according to (3.2). Using the total Green-Lagrange strain, the Poisson's ratios for each box are then computed using

$$\nu_{II} = -\frac{E_{JJ}}{E_{II}} \text{ (repeated index not summed)} \quad (3.3)$$

where  $I$  is the loading direction and  $J$  is the transverse direction. Secant values of strain (total strain) are used, since the results are more stable.

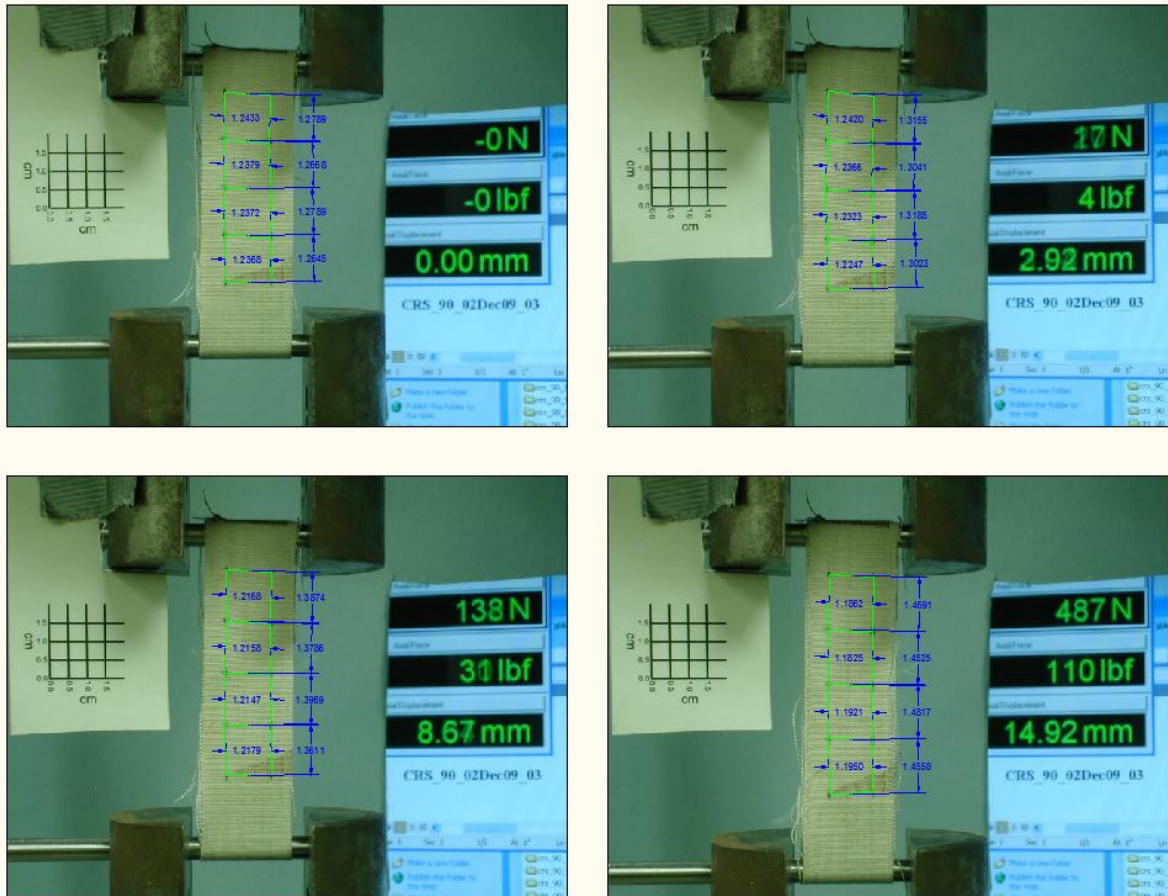


Figure 3-20. Measuring longitudinal and transverse strains in order to determine Poisson's ratio.

Figures 3-21 through 3-26 show for each box, how the lateral strain varies as a function of longitudinal loading strain for cotton-polyester blend fabric when loaded in the warp or weft directions. Linear trend lines were fit through the origin for each specimen. Averaging the absolute values for each slope, the Poisson's ratios for cotton-polyester blend were found to be:  $\nu_{12} = 0.25$  and  $\nu_{21} = 0.42$ .

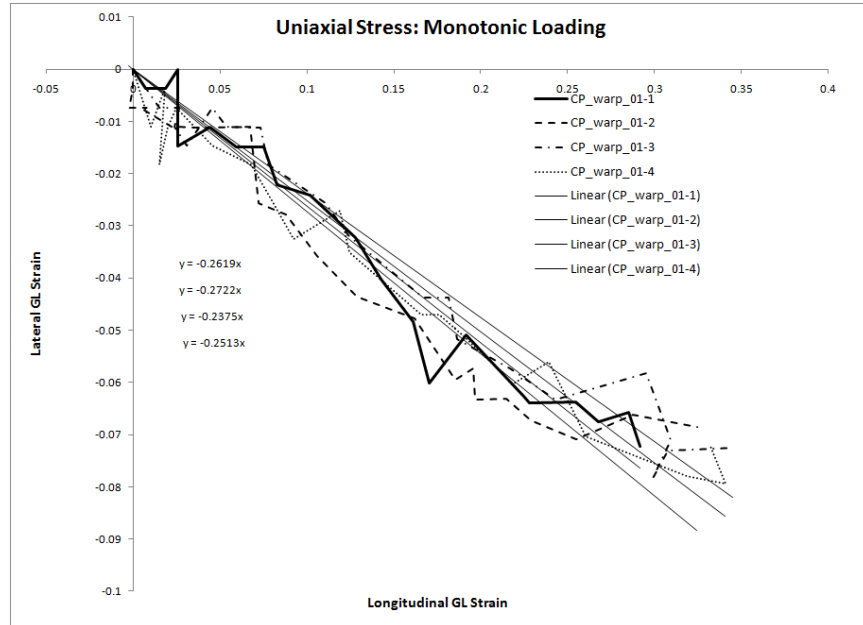


Figure 3-21. Poisson's ratios found using lateral strain as a function of longitudinal strain for the warp monotonic specimen 01 of cotton-polyester blend.

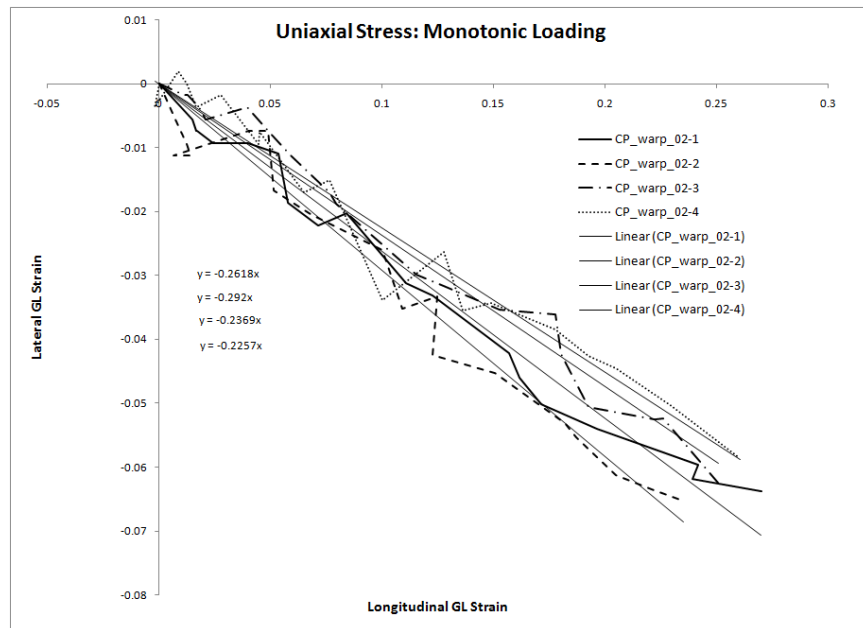


Figure 3-22. Poisson's ratios found using lateral strain as a function of longitudinal strain for the warp monotonic specimen 02 of cotton-polyester blend.

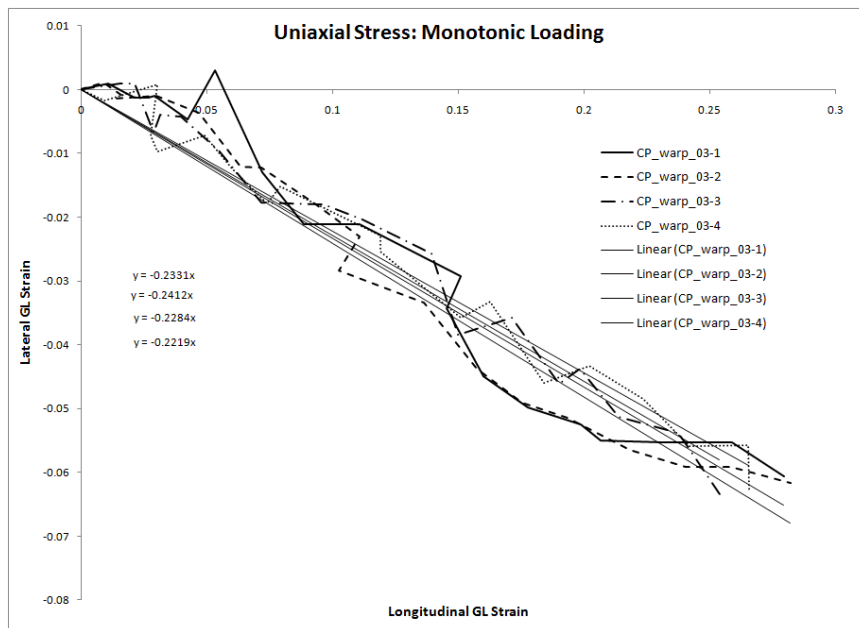


Figure 3-23. Poisson's ratios found using lateral strain as a function of longitudinal strain for the warp monotonic specimen 03 of cotton-polyester blend.

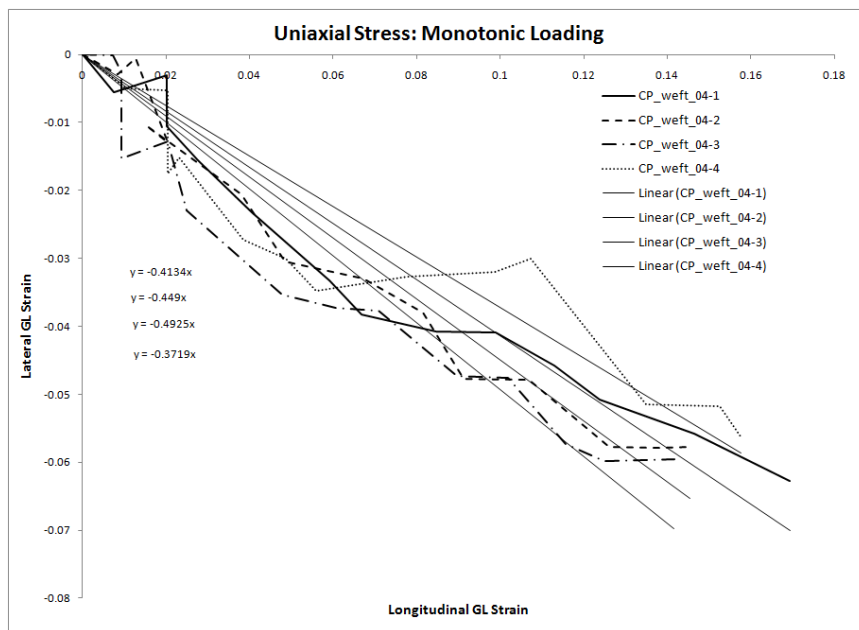


Figure 3-24. Poisson's ratios found using lateral strain as a function of longitudinal strain for the weft monotonic specimen 04 of cotton-polyester blend.

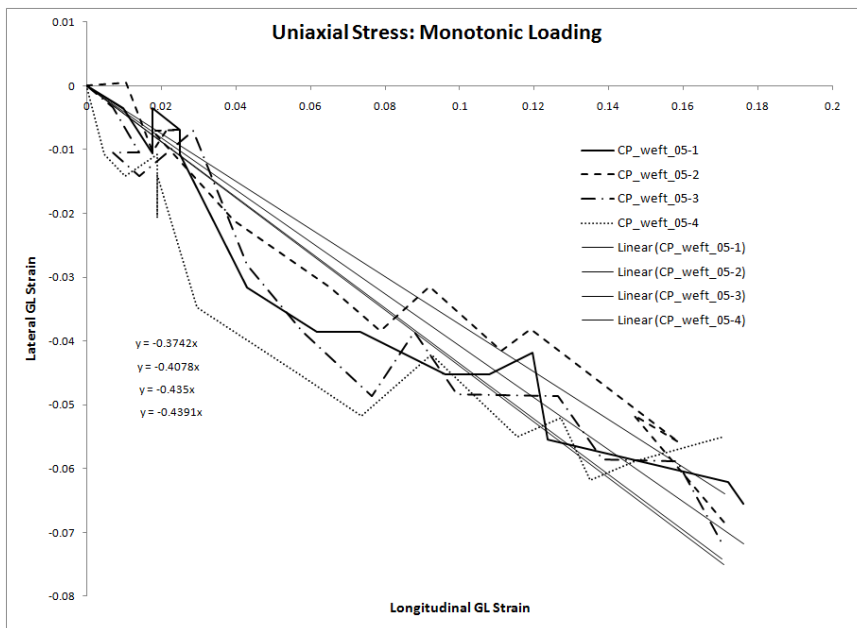


Figure 3-25. Poisson's ratios found using lateral strain as a function of longitudinal strain for the weft monotonic specimen 05 of cotton-polyester blend.

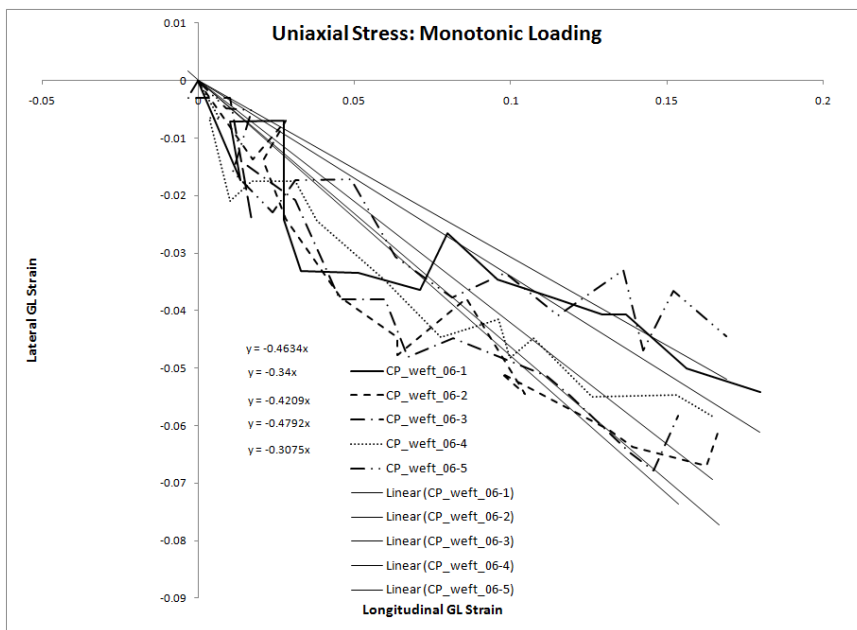


Figure 3-26. Poisson's ratios found using lateral strain as a function of longitudinal strain for the weft monotonic specimen 06 of cotton-polyester blend.

Figures 3-27 through 3-32 show for each box, how the lateral strain varies as a function of longitudinal loading strain for cotton-polyester blend fabric when loaded in the warp or weft directions. Linear trend lines were fit through the origin for each specimen. Averaging the absolute values for each slope, the Poisson's ratios for cotton duck were found to be:  $\nu_{12} = 0.99$  and  $\nu_{21} = 0.68$ .

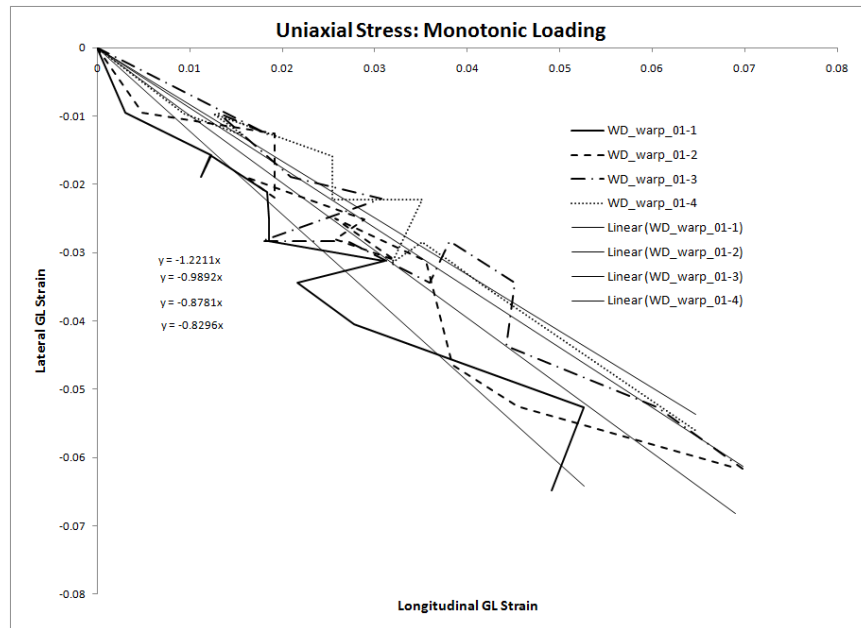


Figure 3-27. Poisson's ratios found using lateral strain as a function of longitudinal strain for the warp monotonic specimen 01 of cotton duck.

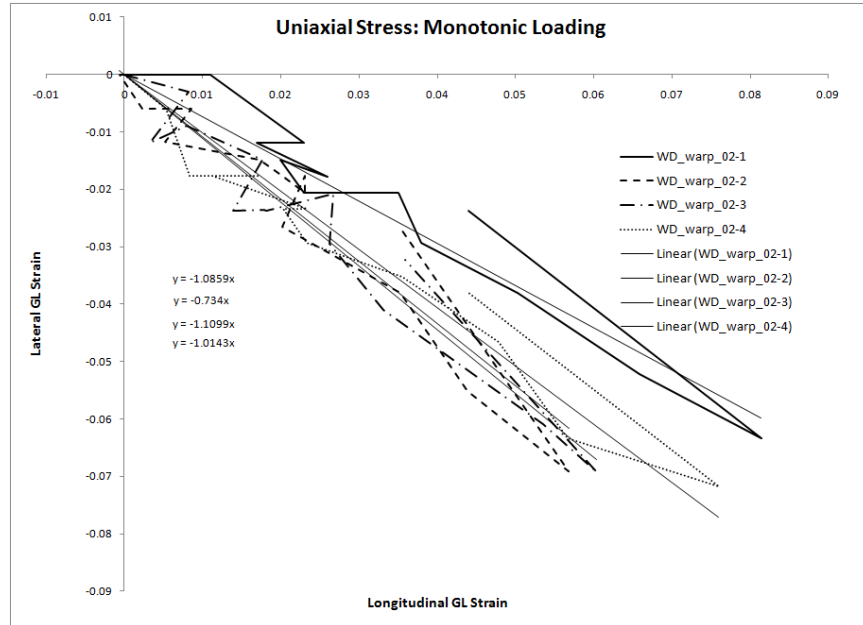


Figure 3-28. Poisson's ratios found using lateral strain as a function of longitudinal strain for the warp monotonic specimen 02 of cotton duck.

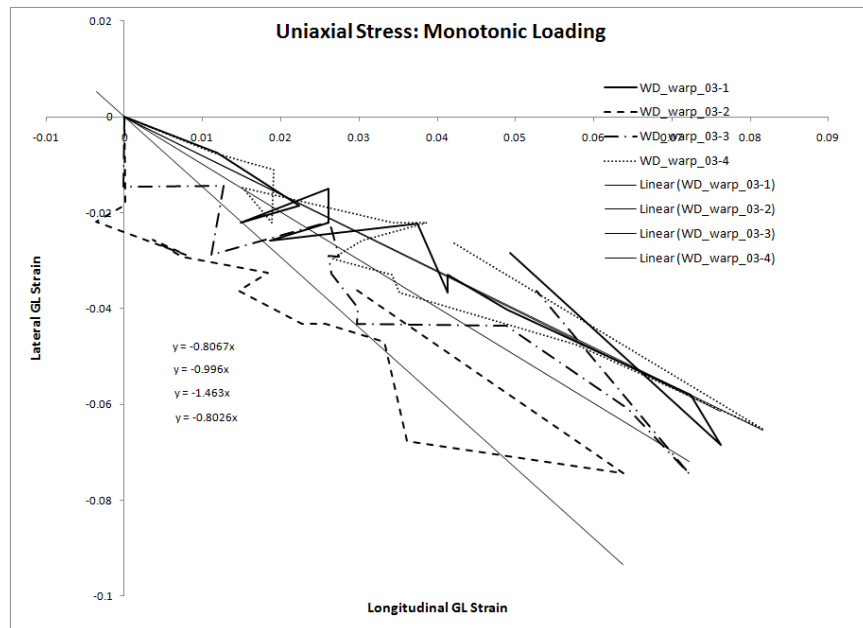


Figure 3-29. Poisson's ratios found using lateral strain as a function of longitudinal strain for the warp monotonic specimen 03 of cotton duck.



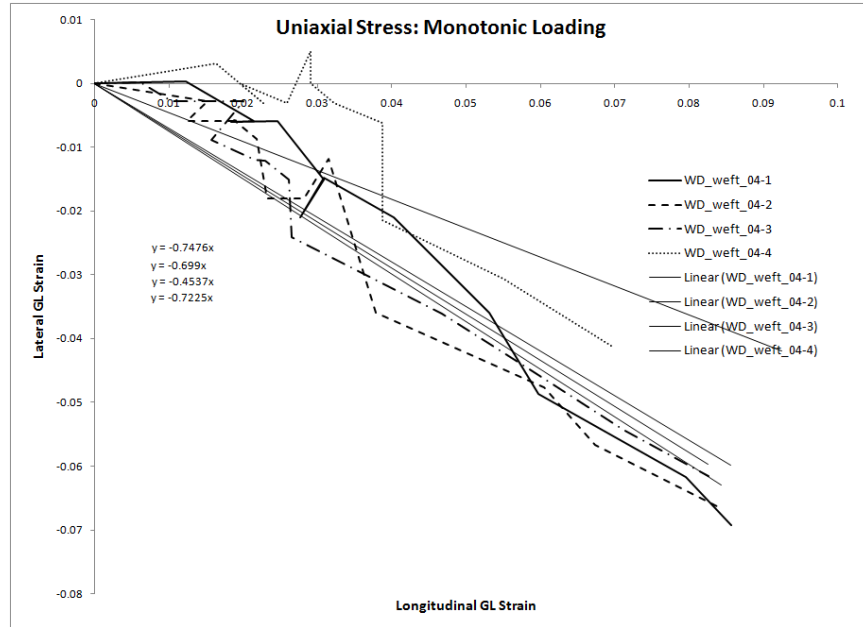


Figure 3-30. Poisson's ratios found using lateral strain as a function of longitudinal strain for the weft monotonic specimen 04 of cotton duck.

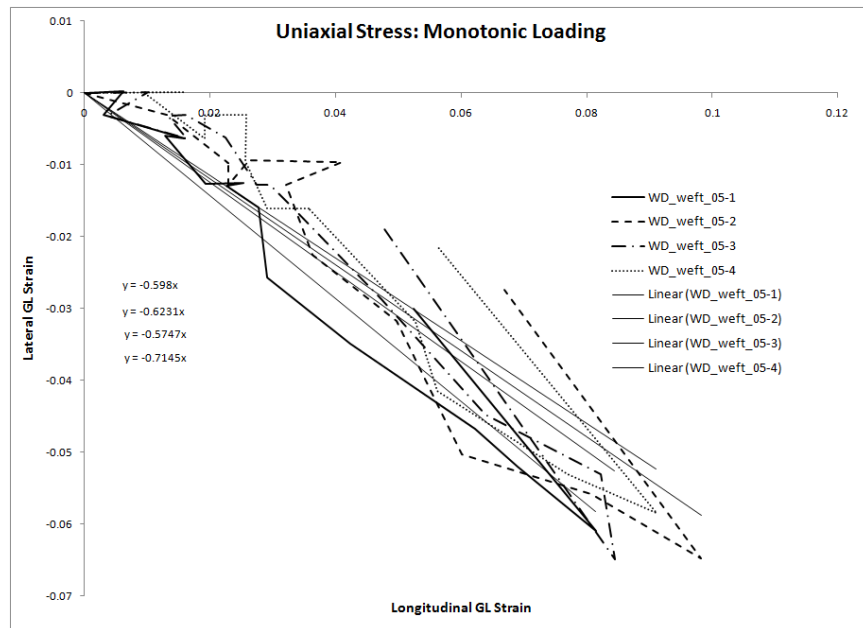


Figure 3-31. Poisson's ratios found using lateral strain as a function of longitudinal strain for the weft monotonic specimen 05 of cotton duck.

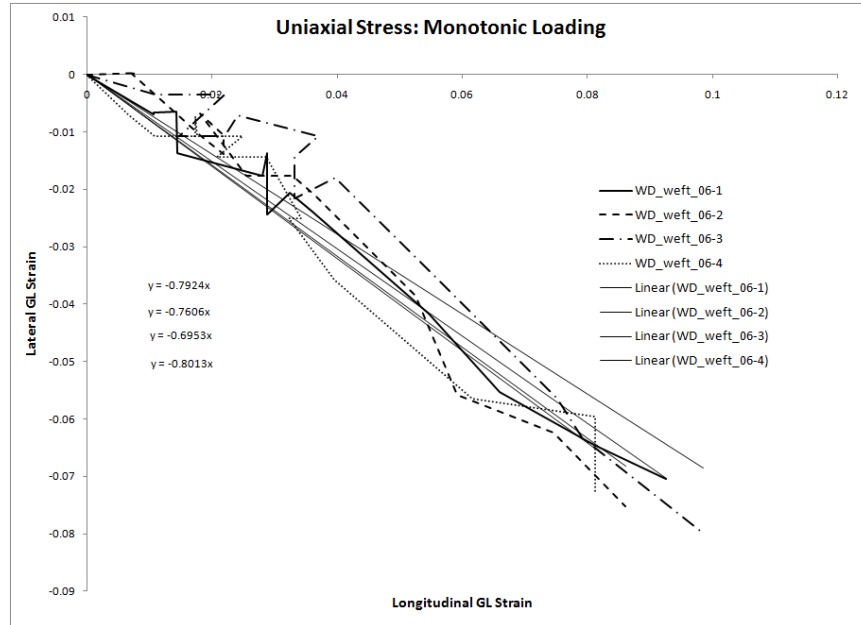


Figure 3-32. Poisson's ratios found using lateral strain as a function of longitudinal strain for the weft monotonic specimen 06 of cotton duck.

Figures 3-33 through 3-38 show for each box, how the lateral strain varies as a function of longitudinal loading strain for cotton-polyester blend fabric when loaded in the warp or weft directions. Linear trend lines were fit through the origin for each specimen. Averaging the absolute values for each slope, the Poisson's ratios for cotton muslin were found to be:  $\nu_{12} = 2.04$  and  $\nu_{21} = 0.41$ .

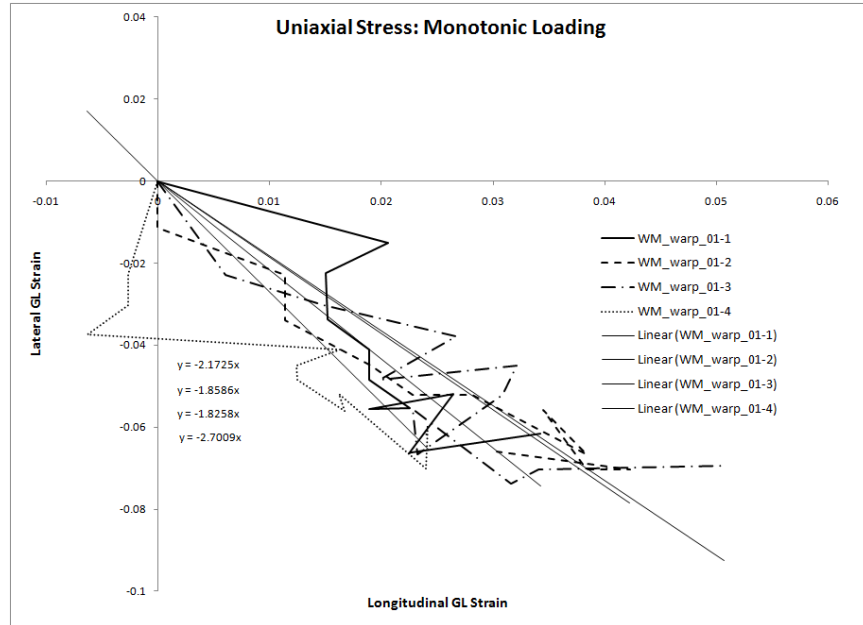


Figure 3-33. Poisson's ratios found using lateral strain as a function of longitudinal strain for the warp monotonic specimen 01 of cotton muslin.

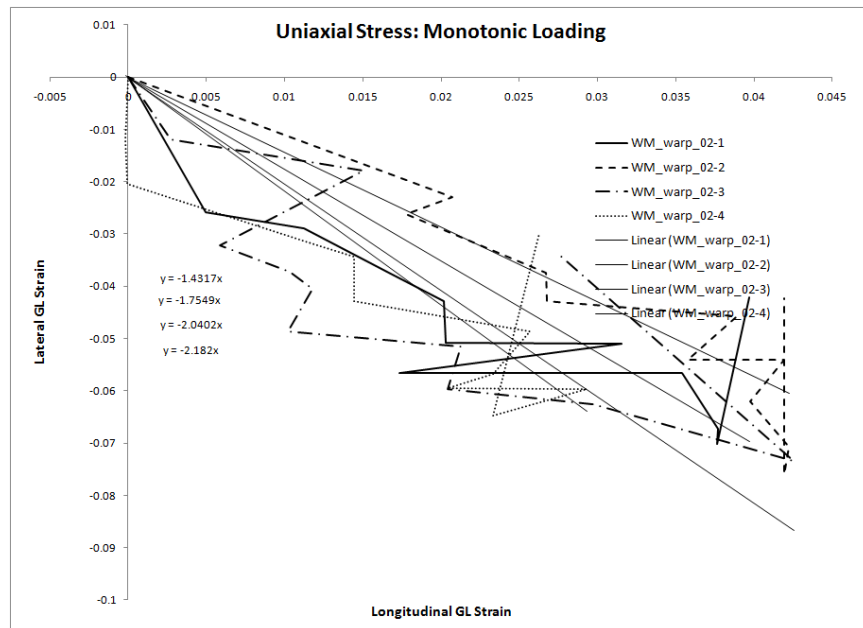


Figure 3-34. Poisson's ratios found using lateral strain as a function of longitudinal strain for the warp monotonic specimen 02 of cotton muslin.

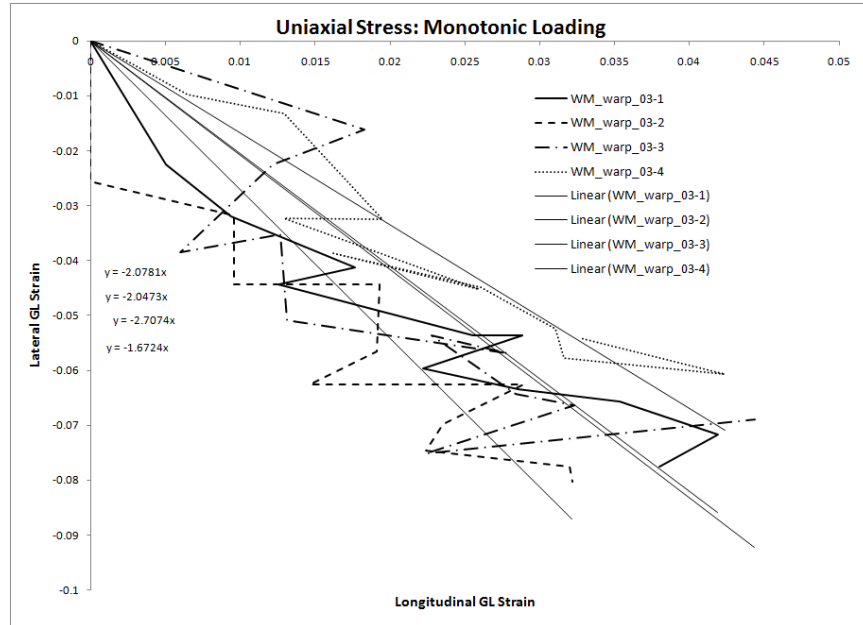


Figure 3-35. Poisson's ratios found using lateral strain as a function of longitudinal strain for the warp monotonic specimen 03 of cotton muslin.

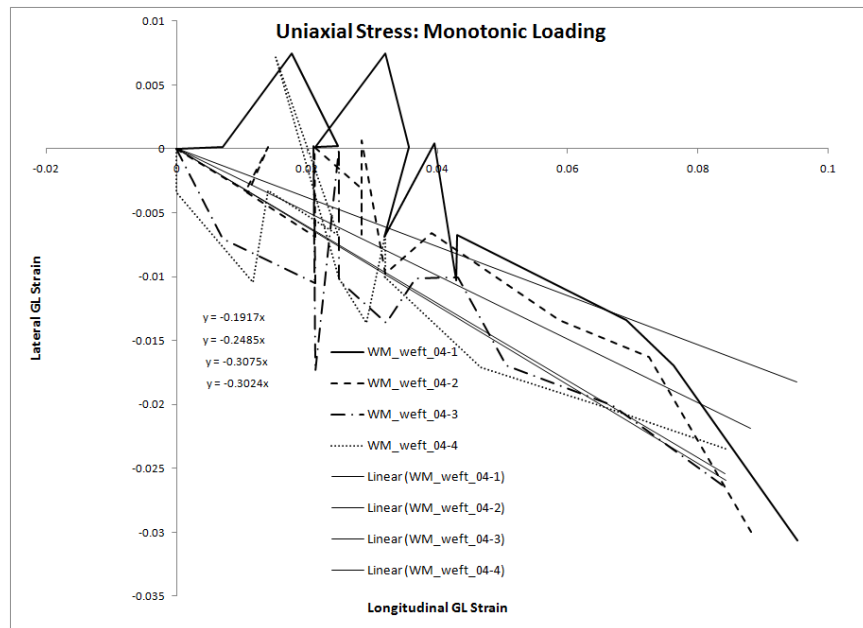


Figure 3-36. Poisson's ratios found using lateral strain as a function of longitudinal strain for the weft monotonic specimen 04 of cotton muslin.

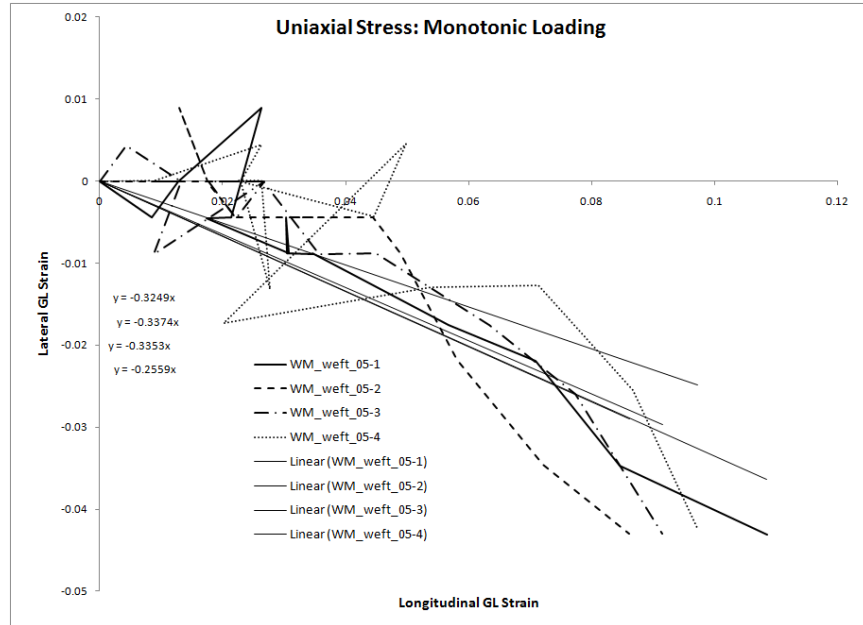


Figure 3-37. Poisson's ratios found using lateral strain as a function of longitudinal strain for the weft monotonic specimen 05 of cotton muslin.

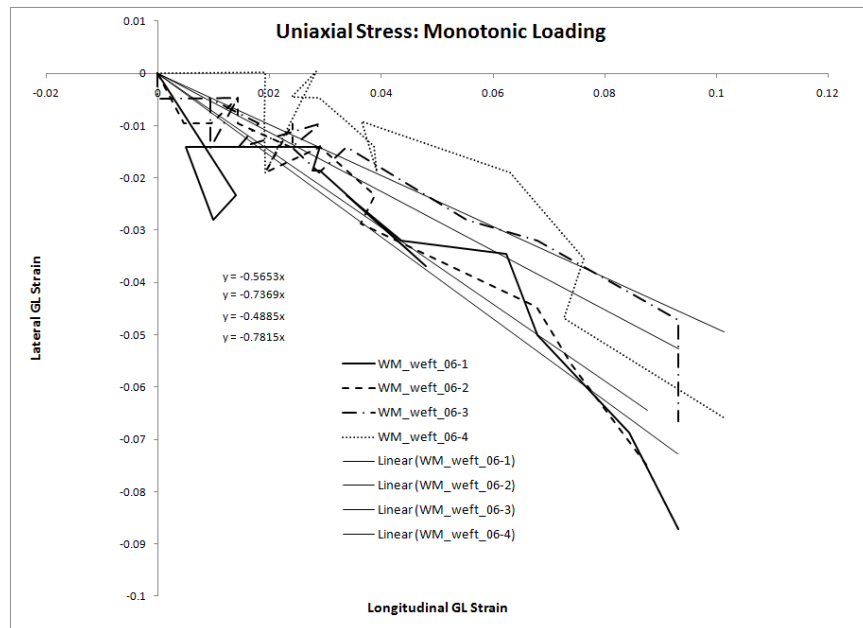


Figure 3-38. Poisson's ratios found using lateral strain as a function of longitudinal strain for the weft monotonic specimen 06 of cotton muslin.

Figures 3-39 through 3-44 show for each box, how the lateral strain varies as a function of longitudinal loading strain for cotton-polyester blend fabric when loaded in the warp or weft directions. Linear trend lines were fit through the origin for each specimen. Averaging the absolute values for each slope, the Poisson's ratios for cotton denim were found to be:  $\nu_{12} = 0.12$  and  $\nu_{21} = 0.22$ .

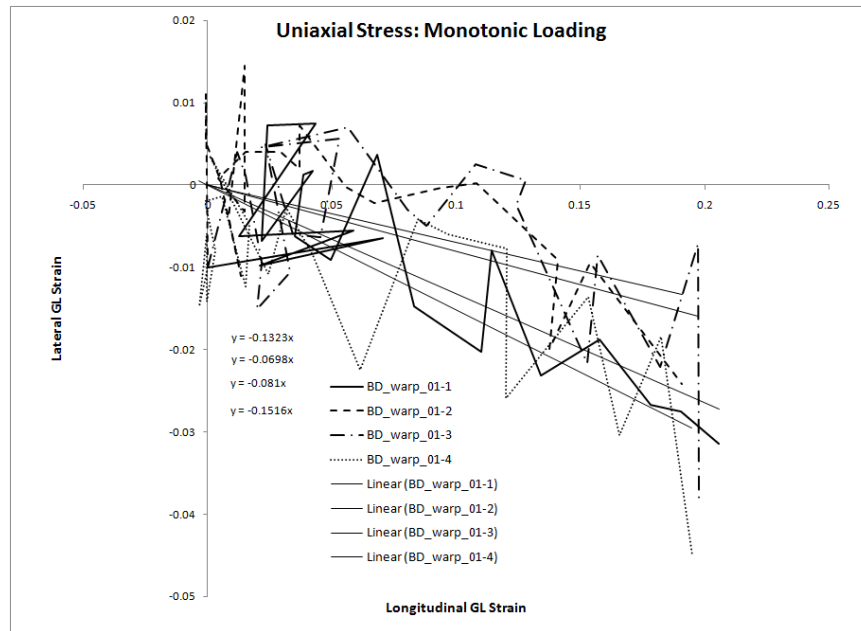


Figure 3-39. Poisson's ratios found using lateral strain as a function of longitudinal strain for the warp monotonic specimen 01 of cotton denim.

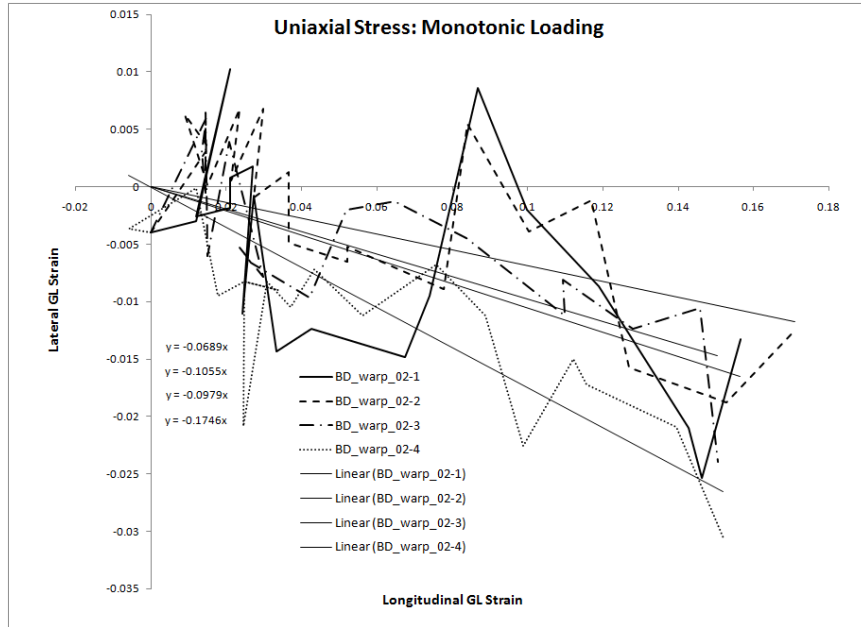


Figure 3-40. Poisson's ratios found using lateral strain as a function of longitudinal strain for the warp monotonic specimen 02 of cotton denim.

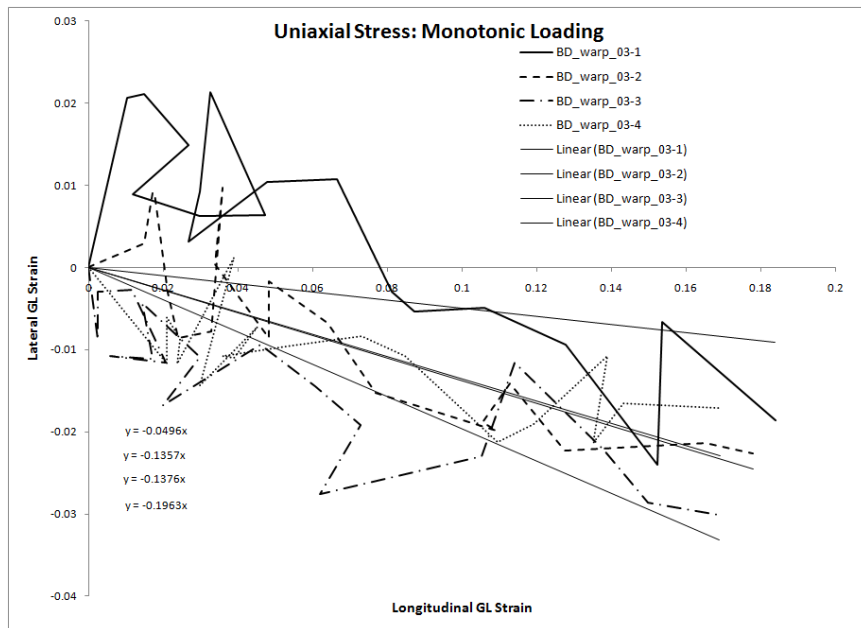


Figure 3-41. Poisson's ratios found using lateral strain as a function of longitudinal strain for the warp monotonic specimen 03 of cotton denim.

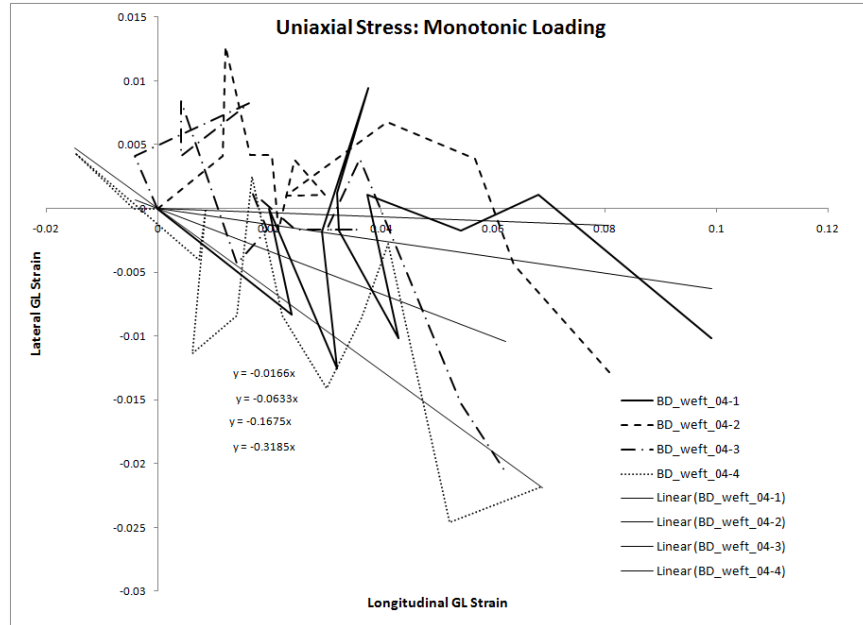


Figure 3-42. Poisson's ratios found using lateral strain as a function of longitudinal strain for the weft monotonic specimen 04 of cotton denim.

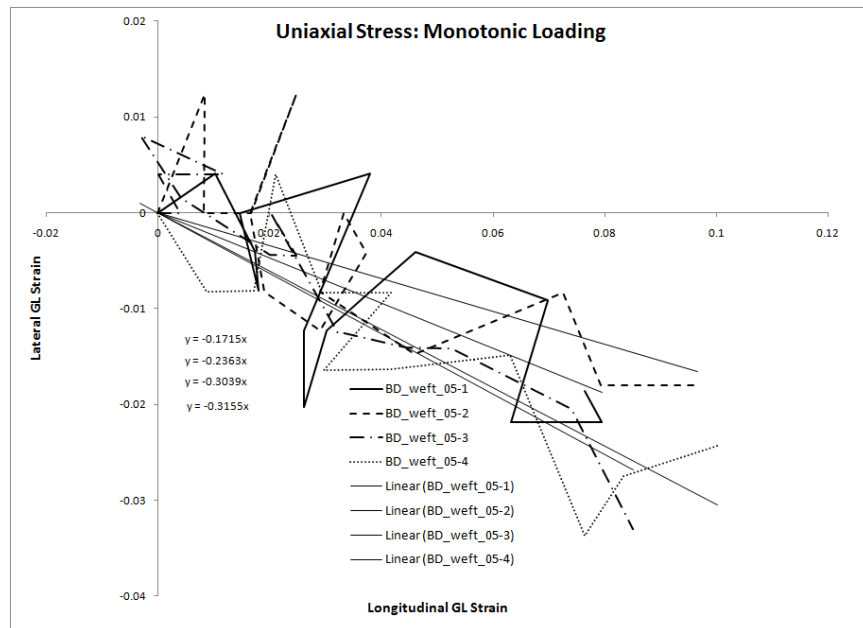


Figure 3-43. Poisson's ratios found using lateral strain as a function of longitudinal strain for the weft monotonic specimen 05 of cotton denim.



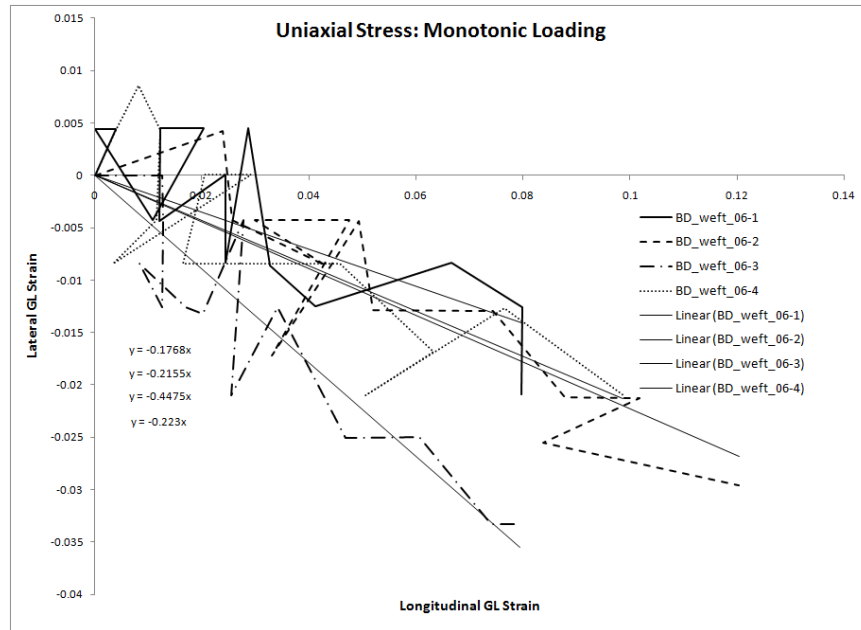


Figure 3-44. Poisson's ratios found using lateral strain as a function of longitudinal strain for the weft monotonic specimen 06 of cotton denim.

The Poisson's ratios for the duck and muslin fabrics are noticeably very large. For isotropic elastic materials, the Poisson's ratio must be between -1 and 0.5. Sun *et al* [35] state that the Poisson's ratios for fabrics are very different than those for conventional engineering materials and can have some peculiar values. They developed a model based upon weave geometry and found that yarn spacing and yarn diameter have significant influence on the Poisson's ratios. The high values found here are related to the weaving process. For example, muslin has very different behavior in the warp and weft directions although the weave is considered "balanced". While the weave geometry was not investigated for this research, it is inferred that one yarn direction must have more crimp than the other. As the yarn with more crimp is loaded, the crimp is transferred to the "free" yarn (without load) such that the latter yarn is able to contract a considerable amount. Further, the experimental procedures used in this research only consider membrane strains of the continuum. Measuring the deformations in the

through-thickness direction and computing the corresponding Poisson's ratios could provide more insight into the high Poisson's ratios in the plane of the fabric.

### 3.3.3.2 Experimental Verification

The use of photographs to determine physical dimensions is an experimental method called *photogrammetry*. There are several sources of error associated with the experimental procedure including: (1) random errors due to slight movements of the camera setup during testing; (2) random errors in the placement of nodes, or points, in AutoCAD; and (3) systematic errors due to the limited resolution of the digital photographs. Here, the effect the errors have on the results is discussed and reconciled.

The resolution of the digital photographs is determined by the number of pixels the camera is able to capture and process. The camera used for these experiments was a *Canon PowerShot SD400* which produces images consisting of 5.0 megapixels. The physical dimensions of the fabric specimens that are represented by individual pixels is a function of the object distance (the distance between the fabric and the camera) as well as any associated camera parameters such as zoom. The experimental setup used for this research has the camera located approximately 55 centimeters from the fabric specimen along with a 3.0x digital zoom to ensure that the entire fabric specimen was visible throughout testing. Using *Adobe Photoshop CS4*, the setup just described yields approximately 101 pixels per centimeter (shown in Figure 3-45), which translates to the height and width of a pixel being about 0.0099 centimeters.

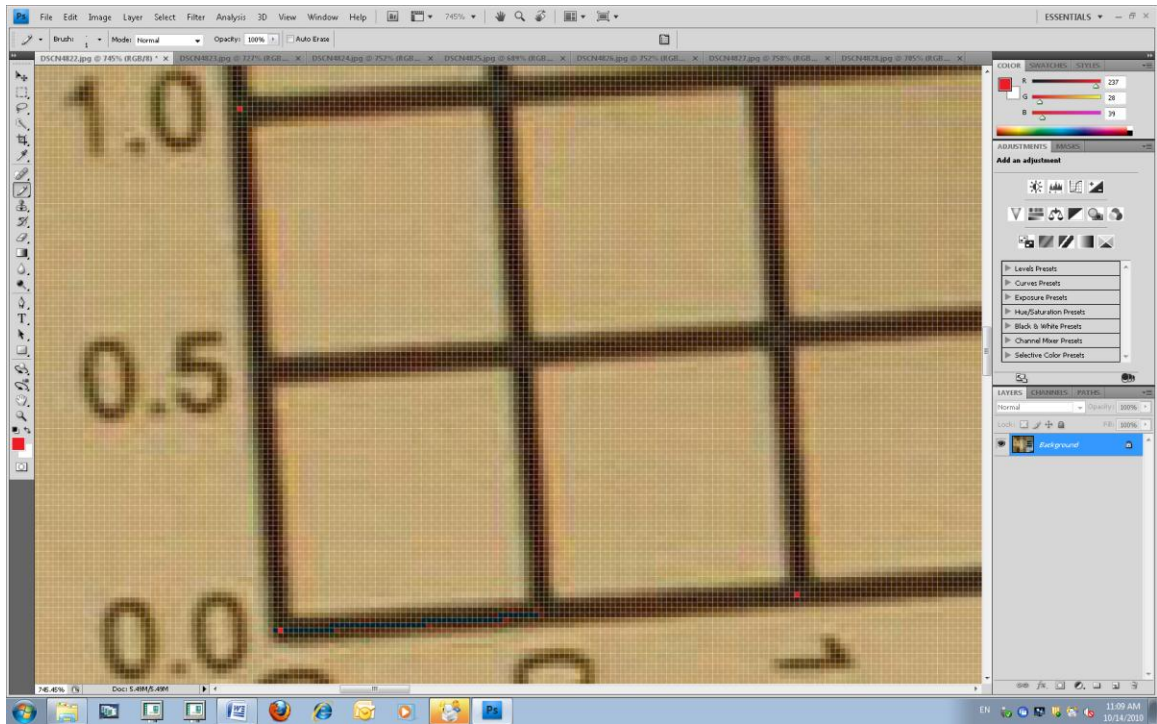


Figure 3-45. Close-up of scale showing pixels using *Adobe Photoshop CS4*.

As is shown in the previous subsection, several of the strain measurements found using *AutoCAD* exhibit significant noise due to the error associated with the placement of the node. It was found that *AutoCAD* has a few limitations when attempting to zoom in on the photograph to place individual nodes including a limit as to how far one can zoom in and see individual pixels, and an inherent “snapping” when trying to place a node. In order to verify the experimental procedure and the subsequent results, measurements for a representative fabric specimen were also made using *Adobe Photoshop CS4*. Using *Photoshop*, it was possible to zoom in and choose individual pixels for each fabric dot throughout the series of photographs, as shown in Figure 3-46. Using the ruler tool (shown in Figure 3-47), measurements were made to determine the stretching and contracting between respective dots, which were, for each photograph, adjusted by dividing the measured number of pixels between dots by the respective number of pixels

per centimeter. The resulting displacements (now in units of centimeters) were converted to longitudinal strains in the loading direction and the corresponding lateral strains. The results found using *Photoshop* for a muslin weft specimen were plotted against the results found using *AutoCAD* and are shown in Figure 3-48. It was concluded that the results using the two different software packages show a similar signal-to-noise ratio and in order to produce more precise data, one should use a camera with higher resolution and a better marker system.

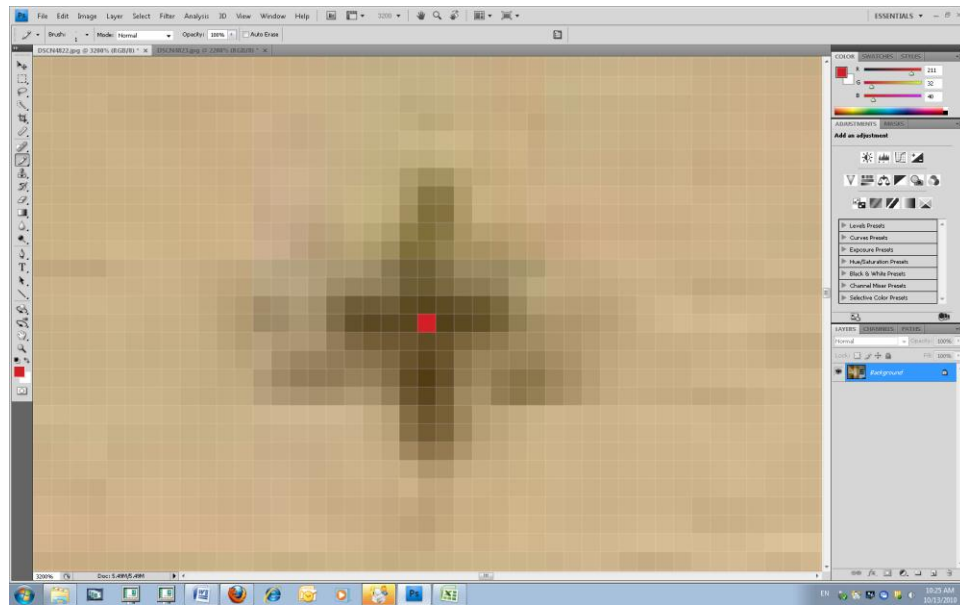


Figure 3-46. Screenshot of *Adobe Photoshop CS4* showing an individual pixel used for subsequent measurements.

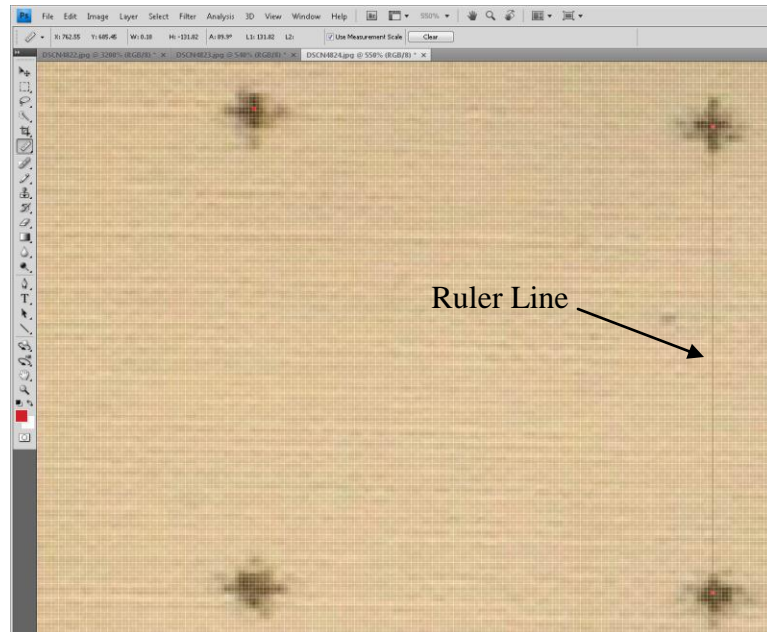


Figure 3-47. Measurements using "ruler tool" in *Photoshop*.

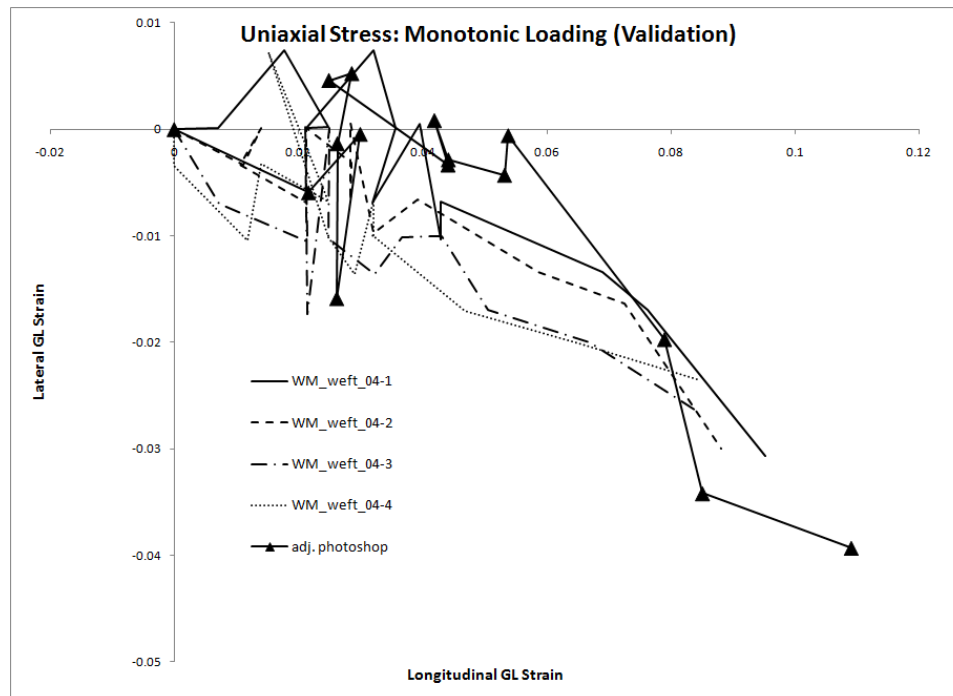


Figure 3-48. Chart showing the strain results for a muslin weft specimen using both *AutoCAD* and *Photoshop*.

### 3.3.4 In-plane Shear Behavior

The ability of a woven fabric to easily drape over objects in complex shapes is a result of its shear rigidity being much lower than its tensile rigidity [12]. Shear behavior of fabrics consists of several modes of deformation, including deformation due to rigid intersections of yarns when the shear force is too small to overcome friction, yarn slippage when the shear force overcomes friction, elastic deformation when slipping is complete, and yarn jamming [43]. In terms of shear rigidity, Kilby [41] notes that the shear modulus,  $G$ , is usually much less than the tensile moduli in either the warp or weft directions; and yet will have a significant contribution to the effective moduli in orientations other than the warp and weft. There are three main types of experimental tests that researchers have used to determine shear behavior: the pure-shear test such as the KES-F shear test [44], the picture-frame test [45], and the bias extension test [37] as shown in Figure 3-49. Using the bias extension test, many researchers such as [17, 46-48] have used the work of Kilby [41] to estimate the shear modulus in the plane of the fabric by measuring the linear elastic moduli and the Poisson's ratios in the warp and weft direction, the tensile modulus determined from a uniaxial stress test in the bias  $45^\circ$  direction and the equation:

$$G_{12} = \frac{1}{\frac{4}{E_{45^\circ}} - \frac{1}{E_1} - \frac{1}{E_2} + \left( \frac{\nu_{21}}{E_1} + \frac{\nu_{12}}{E_2} \right)} \quad (3.4)$$

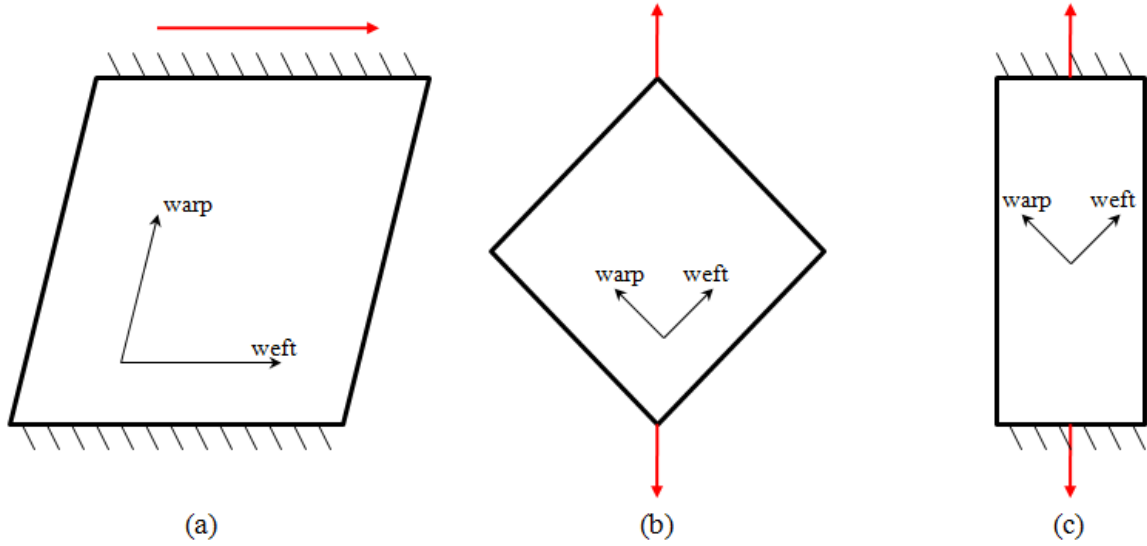


Figure 3-49. Common types of tests for determining shear properties of woven fabrics: (a) KES-F shear test, (b) picture frame test, and (c) bias extension test.

For this research, the bias extension test is used to establish the shear properties of fabrics. Differing from previous approaches that utilize linear approximations based on the Kilby approach, we adopt a new approach using large deformation continuum mechanics. In order to compute the shear strain, we begin with the deformation of an infinitesimal line element  $dX_R$  into  $dx_i$ , as follows:

$$dx_i = \frac{\partial x_i}{\partial X_R} dX_R = F_{iR} dX_R, \quad (3.5)$$

where  $F_{iR}$  is the deformation gradient. The Green-Lagrange strain tensor is defined as

$$E_{RS} = \frac{\partial x_k}{\partial X_R} \frac{\partial x_k}{\partial X_S} - \delta_{RS} = F_{kR} F_{kS} - \delta_{RS} = C_{RS} - \delta_{RS}, \quad (3.6)$$

where  $C_{RS}$  is the right Cauchy-Green deformation tensor and  $\delta_{RS}$  is the Kronecker delta.

For the physical interpretation of in-plane shear, consider two differential line elements  $dX_R^{(1)}$  and  $dX_R^{(2)}$  which deform into  $dx_i^{(1)}$  and  $dx_i^{(2)}$  as shown in Figure 3-50, where  $dS$  and  $ds$  are the lengths of the line elements, and  $\Phi$  and  $\phi$  are the angles between the

differential line elements before and after deformation, respectively. The unit vectors of the line element directions before and after deformation are defined, respectively, as

$$N_R = \frac{dX_R}{dS}, n_i = \frac{dx_i}{ds}, \quad (3.7)$$

and the stretch ratio is

$$\lambda = \frac{ds}{dS}. \quad (3.8)$$

Following the derivation found in [49], the off-diagonal terms of the Green-Lagrange strain tensor can be expressed as

$$\cos \phi = \frac{2E_{IJ} N_I^{(1)} N_J^{(2)} + \cos \Phi}{\lambda_1 \lambda_2}. \quad (3.9)$$

If the two differential line elements are initially orthogonal,  $\Phi = 90^\circ$ , equation (3.9) is simplified to

$$\cos \phi_{12} = \frac{2E_{12}}{\lambda_1 \lambda_2}. \quad (3.10)$$

Rearranging terms, an expression for in-plane shear strain is now defined as

$$E_{12} = \frac{\lambda_1 \lambda_2 \cos \phi_{12}}{2}. \quad (3.11)$$



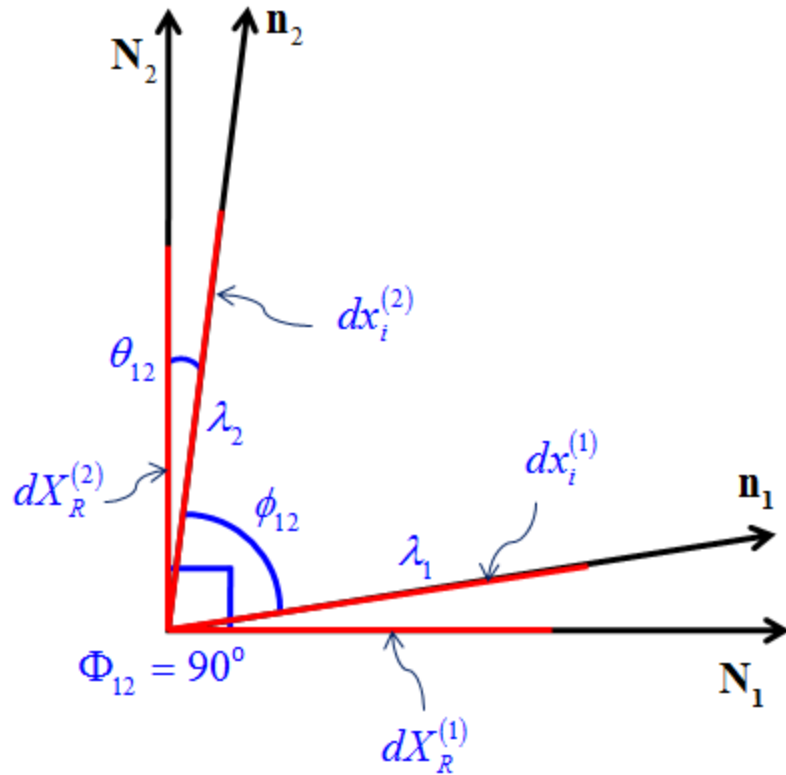


Figure 3-50. Shear deformation of an element.

For the bias 45 extension tests, the applied stress (3.1) is in the loading direction. In order to determine the shear stress causing rotation of the line elements/yarns, the 2PK stress tensor must be transformed from the original coordinate system  $X_R$  ( $R = 1,2,3$ ) to a material coordinate system  $\hat{X}_R$  that is aligned with the original yarn directions, which are rotated counterclockwise by  $45^\circ$ , as shown in Figure 3-51. Vectors and tensors in this rotated coordinate system are denoted with a “^” (hat). The stress tensor is transformed according to

$$\hat{S}_{IJ} = Q_{MI} Q_{NJ} S_{MN} \quad (3.12)$$

where

$$Q_{MI} = \cos(X_M, \hat{X}_I). \quad (3.13)$$

The resulting stress tensor is

$$\hat{S}_{IJ} = \begin{bmatrix} \frac{S_{22}}{2} & \frac{S_{22}}{2} & 0 \\ \frac{S_{22}}{2} & \frac{S_{22}}{2} & 0 \\ 0 & 0 & 0 \end{bmatrix}, \quad (3.14)$$

which leads to an in-plane shear stress of

$$\hat{S}_{12} = \frac{1}{2} \left[ \frac{P(t)}{A_0 \left( 1 + \frac{\Delta l(t)}{l_0} \right)} \right] \quad (3.15)$$

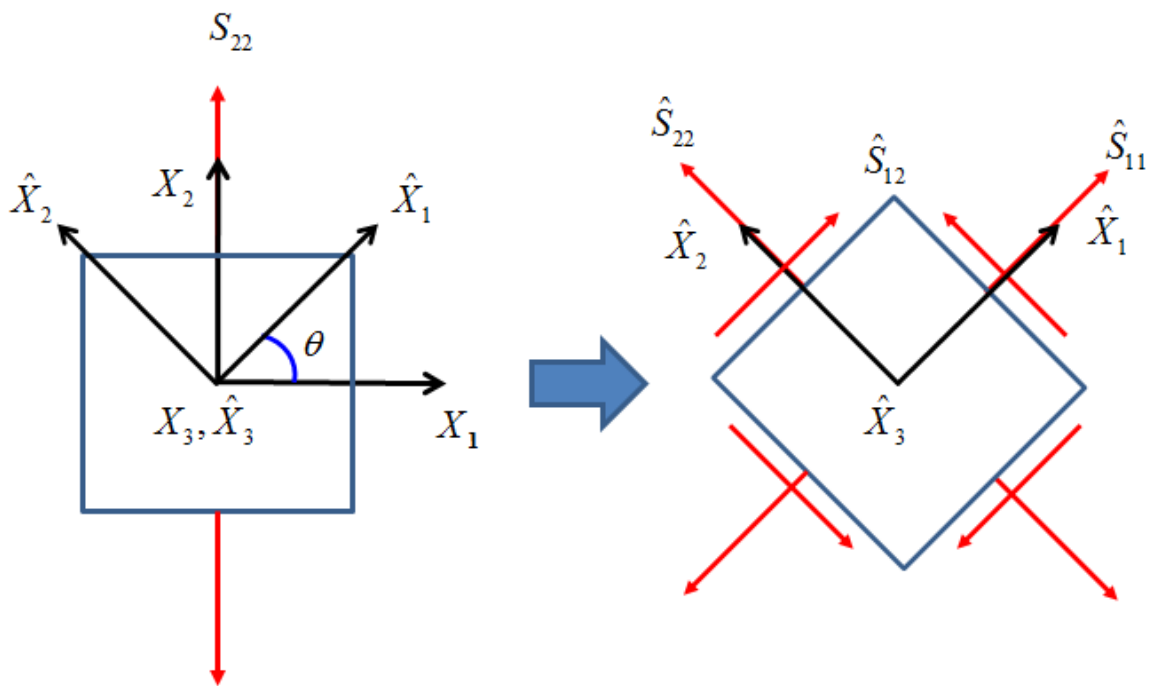


Figure 3-51. Transformation of stress tensor from original coordinate system to a rotated coordinate system.

During the bias 45 extension test, there are three distinct zones where different deformation modes occur as shown in Figure 3-52. Identified by Sidhu *et al.* [50], these are: zone I near the specimen grips where there is no significant deformation; zone II, which frames the center region of the specimen and includes a mixture of extension and shearing; and the middle region, zone III, where the deformation is dominated by shear. The bias 45 extension tests performed for this research follow a similar experimental procedure as that of the uniaxial tension tests, the main differences being the orientation of the yarns and the markings on the front of the specimen. As shown in Figure 3-53, two line elements are marked that correspond with a warp and weft yarn, respectively. The specimens were loaded at a strain rate of 0.003 /s until the total displacement of the ram was 20.00 mm at which point unloading took place until the displacement of the ram was 0.00 mm. During the experimental test, a series of digital photos are taken for both loading and unloading of the specimen. These photos are then imported into AutoCAD and scaled to the reference grid. For each photo, the length of each line element is used to determine the corresponding stretch ratio [Eqn. (3.8)], and the angle between them,  $\phi_{12}$ , is recorded, as shown in Figure 3-54. As the yarns and their coordinates axes are rotated 45° from the global coordinate system, the shear strain expression (3.11) is modified by including the “hat” notation to denote the rotated coordinate system:

$$\hat{E}_{12} = \frac{\lambda_1 \lambda_2 \cos \phi_{12}}{2} . \quad (3.16)$$

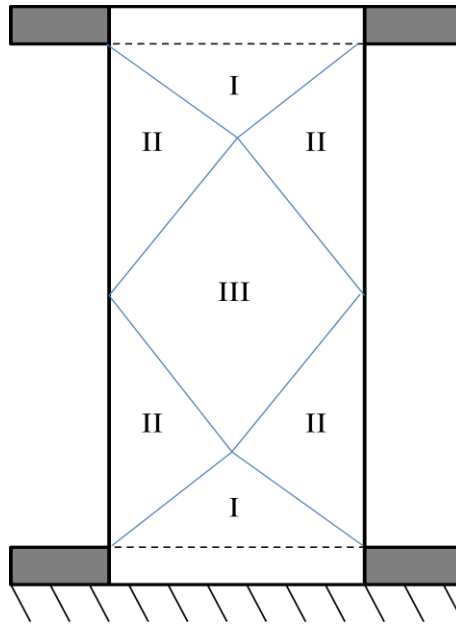


Figure 3-52. Deformation zones for a bias extension test: (I) no significant deformation, (II) mixed shearing and extension, and (III) shearing [50].

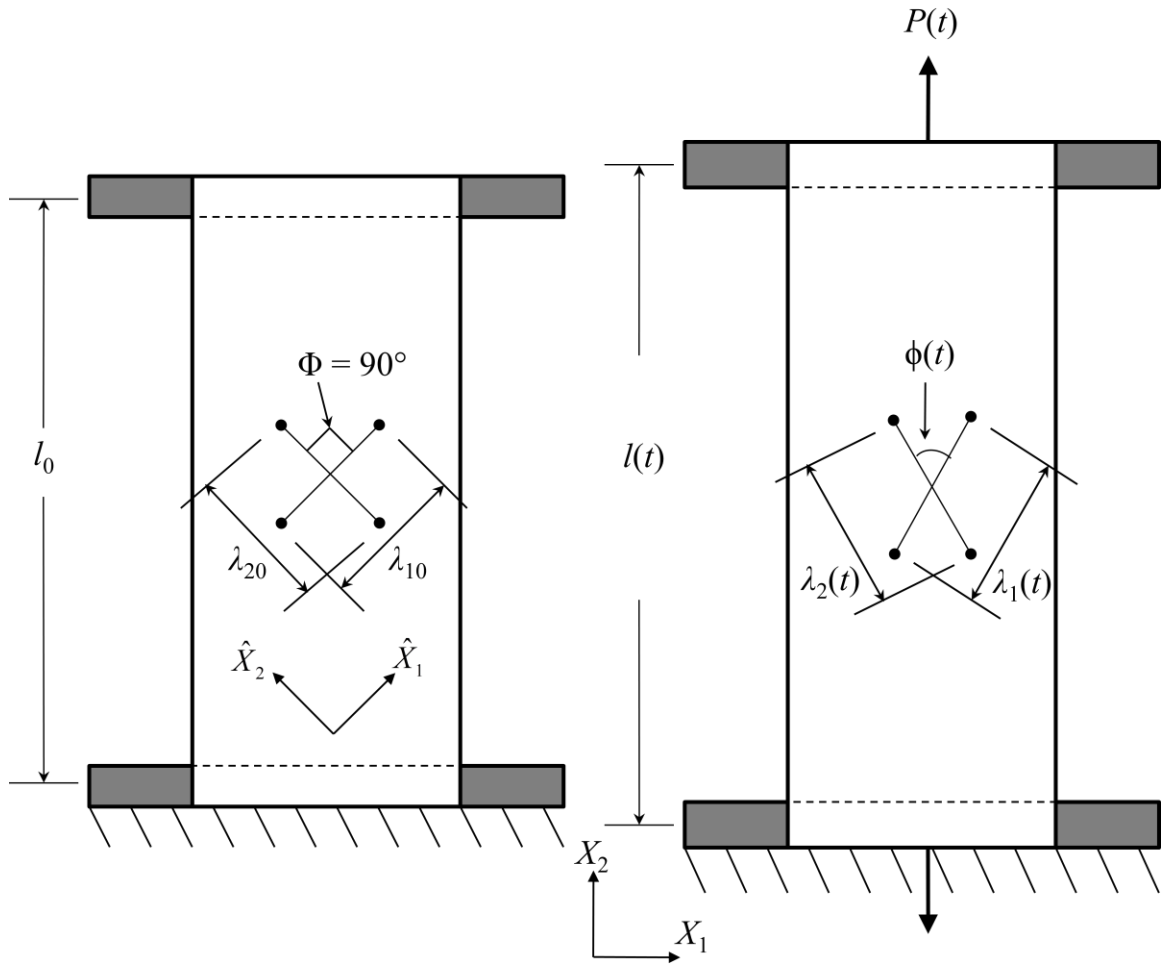


Figure 3-53. Schematic showing dimensions of the reference configuration and those of the deformed configuration at time  $t$ .

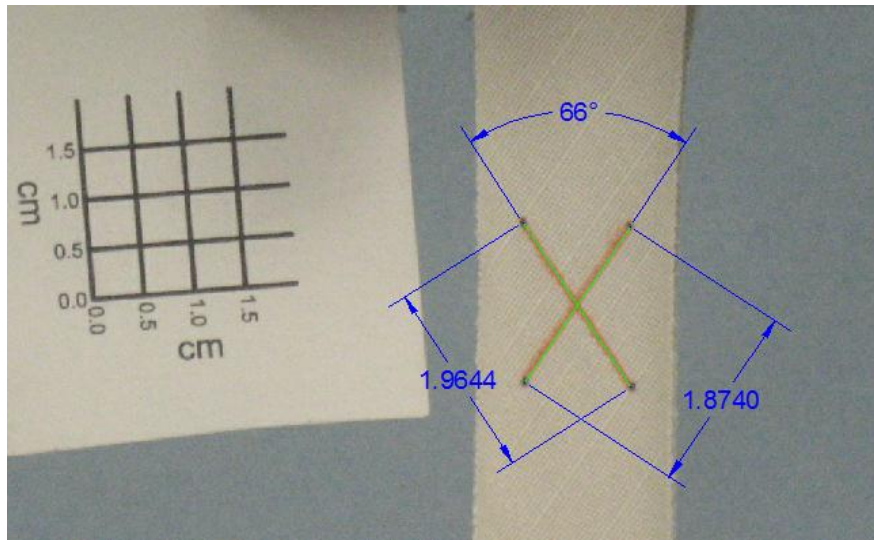


Figure 3-54. Photograph of bias 45 specimen showing dimensions.

Yarn stretches and the angle between the two yarns were determined from the digital photographs. It was found that stretch ratios in the warp and weft yarns for each fabric, shown in Figures 3-55 through 3-58, deviated little from 1.0, which the maximum for all fabrics 1.06. This affirms the assumption that the deformation in the center of the specimen is dominated by pure shear. The shear strain was determined from equation (3.16) and the shear stress by equation (3.15) and the force data from file and plots of the shear stress-shear strain relationship for each fabric were created. To be consistent with engineering strain, the plots are a function of twice the shear strain, or  $2E_{12}$ . Data for all tested fabrics exhibit the expected nonlinear behavior with hysteresis as shown in Figures 3-59 through 3-62.

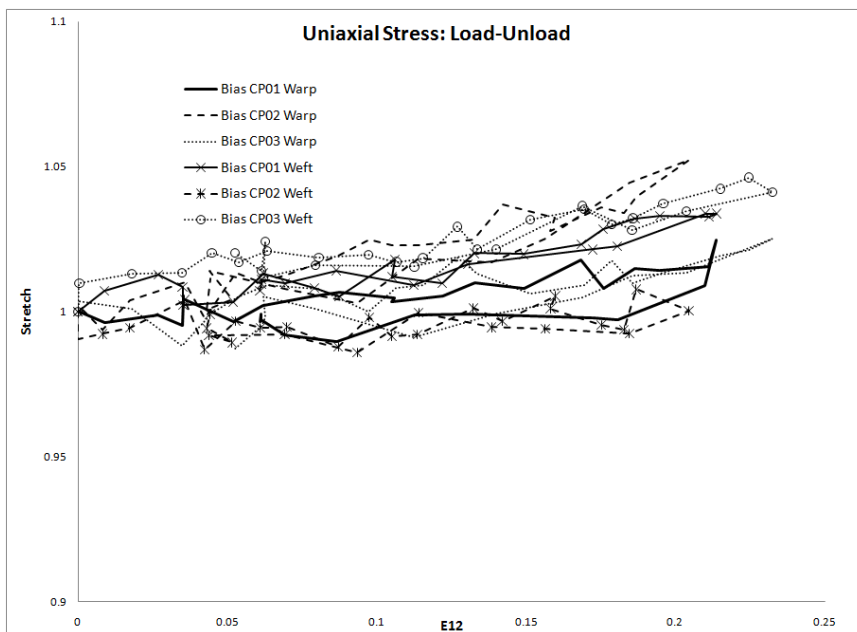


Figure 3-55. Measured stretch ratios for warp and weft yarns of cotton-polyester blend fabric during bias tension tests.

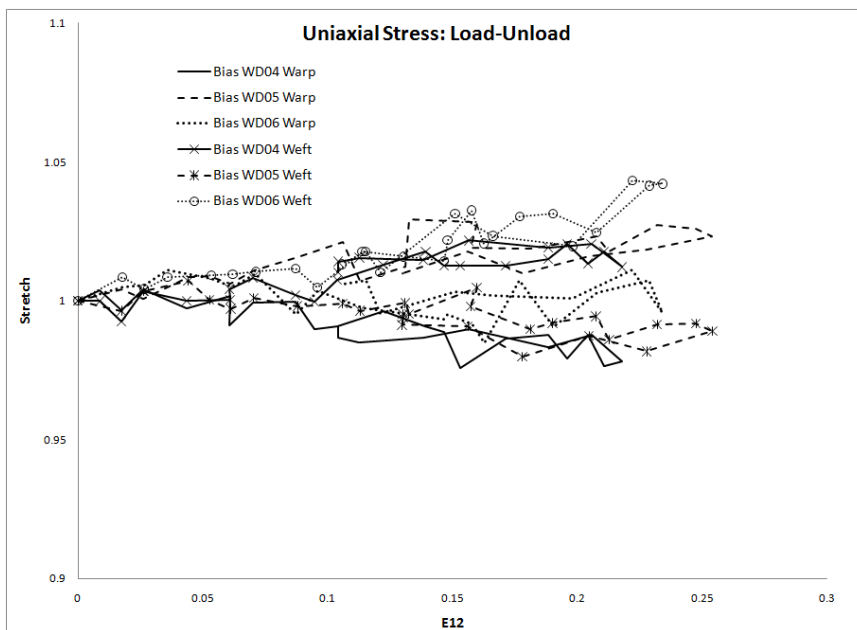


Figure 3-56. Measured stretch ratios for warp and weft yarns of cotton duck fabric during bias tension tests.

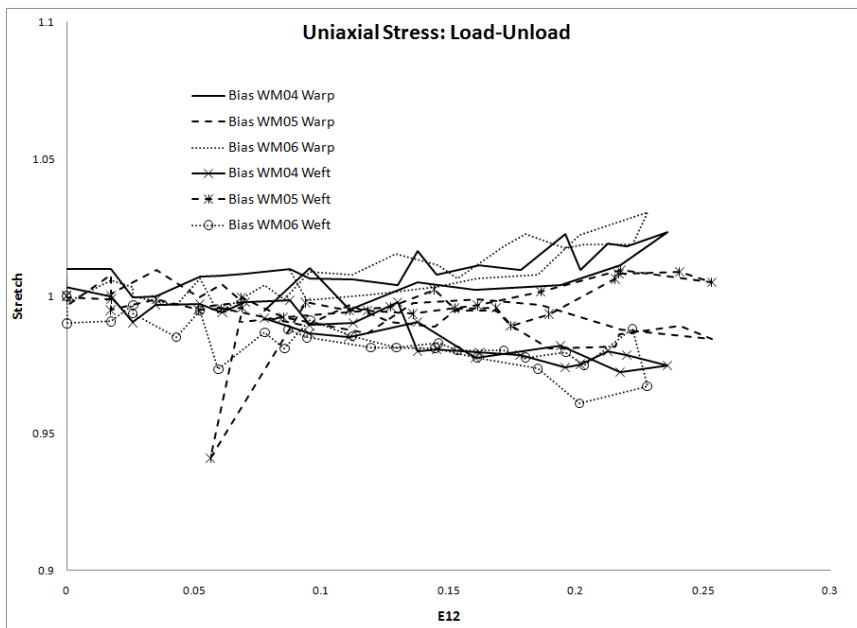


Figure 3-57. Measured stretch ratios for warp and weft yarns of cotton muslin fabric during bias tension tests.

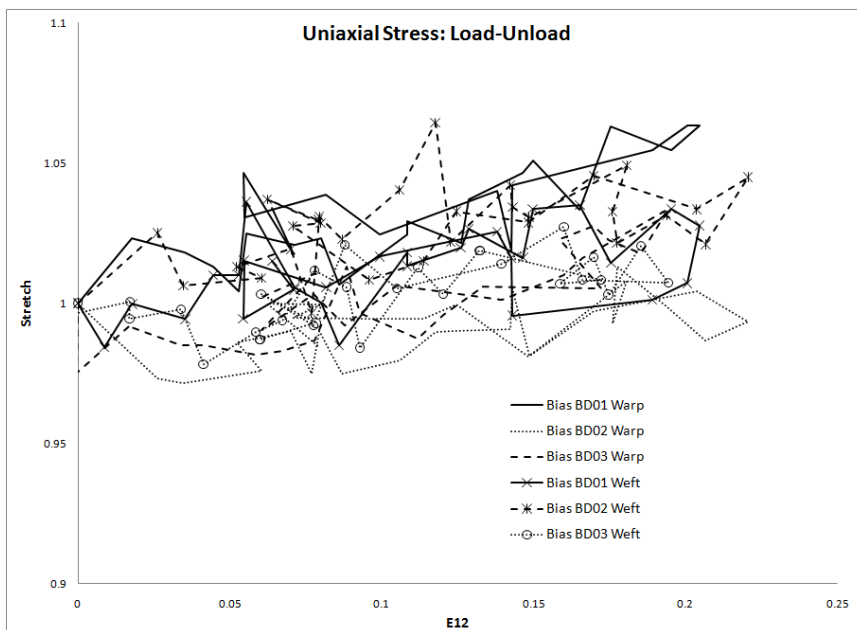


Figure 3-58. Measured stretch ratios for warp and weft yarns of cotton denim fabric during bias tension tests.



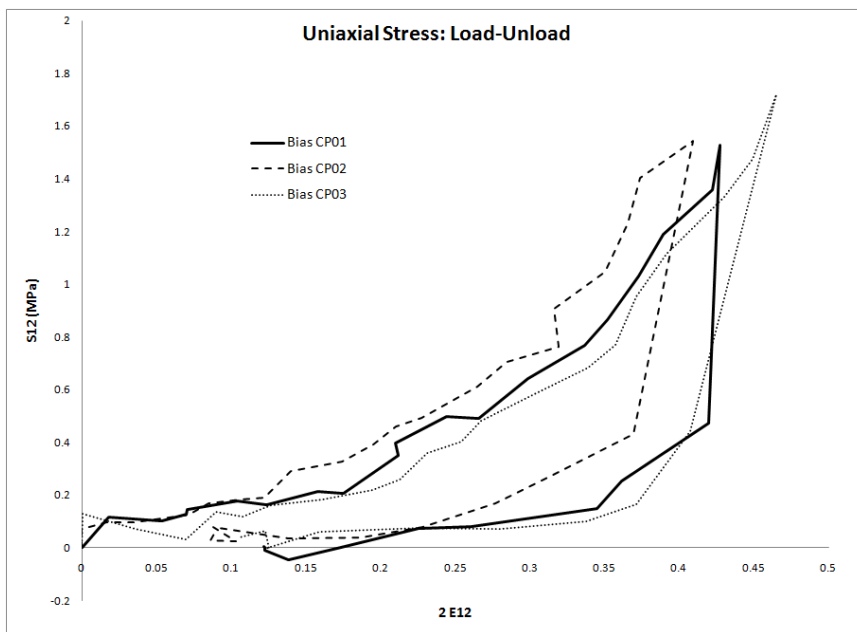


Figure 3-59. Measured shear stress-shear strain data for cotton-polyester blend.



Figure 3-60. Measured shear stress-shear strain data for cotton duck.

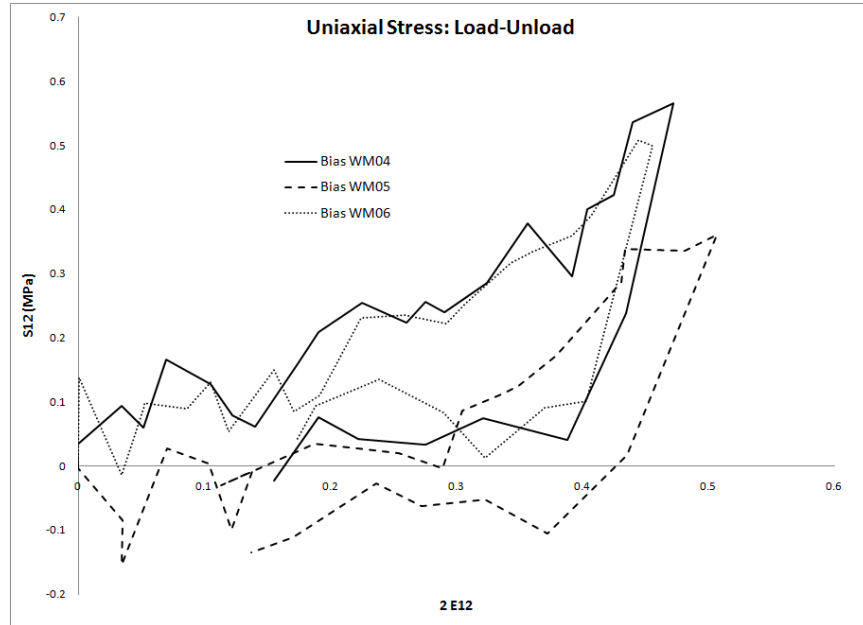


Figure 3-61. Measured shear stress-shear strain data for cotton muslin.

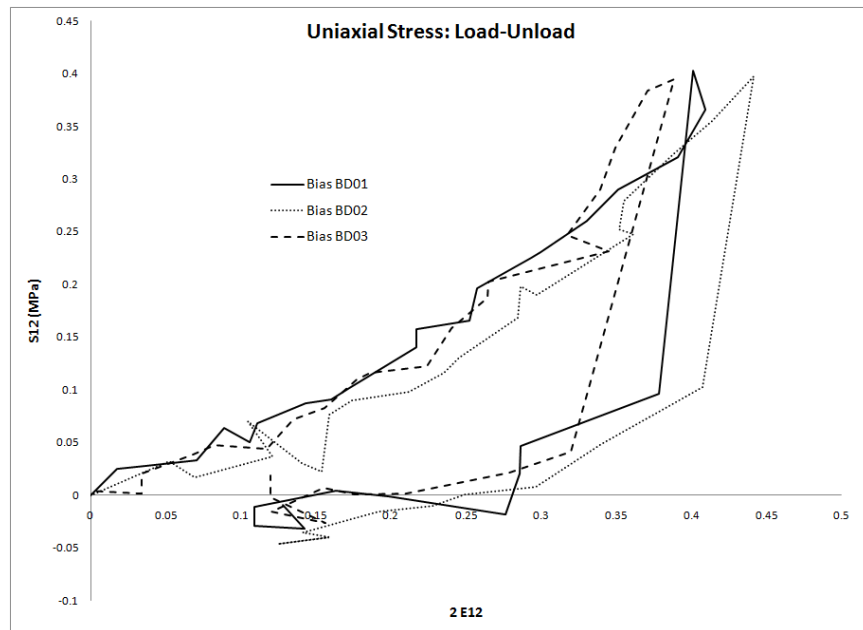


Figure 3-62. Measured shear stress-shear strain data for cotton denim.

### 3.4 Summary of Measured Fabric Behaviors

Several experimental tests have been performed in order to evaluate the in-plane behavior of four woven fabrics. Uniaxial tensile tests have shown that all the tested fabrics exhibit nonlinear decrimping behavior, anisotropy and hysteresis. Using a novel approach, bias extension tests were used to determine the shear behavior, which was also found to be nonlinear and hysteretic. To add mechanical realism to clothing simulations, constitutive models for woven fabrics should include these essential features, namely anisotropy, nonlinearity and hysteresis. The experimental results of this section are used to guide the development of such a constitutive model and then for both material parameter estimation and model verification.

## CHAPTER 4. REVIEW OF FABRIC CONSTITUTIVE MODELS

Since the 1930s, much work has been done in modeling the mechanical behavior of woven fabrics. Early analytical work by such authors as Peirce [27, 51], Hearle *et al* [26], and Grosberg and Kedia [52], focused on simple stretching and shearing of fabrics based on the weave geometry of a unit cell. More recently, there has been an increasing interest in computational modeling of the behavior of fabrics, where more complicated loadings can be considered. Much of the latter work was pioneered by the computer graphics industry in the 1980s; where the overall aim was visual realism, meaning that a simulation of the fabric should simply “look” real with no regard to the mechanical realism of the resulting behavior [10, 11]. In an attempt to address mechanical realism of fabric simulations, several approaches have been developed in regards to macroscopic behavior, which include yarn models, particle-spring models, and continuum models. In this chapter, all three are discussed with emphasis on continuum models. From the structural hierarchy present in woven fabrics, it is evident that their overall behavior is complex and is a function of many variables. While work is ongoing in the mechanical behavior at each length scale such as fibers and yarns [11], we concern ourselves here with behavior at the fabric scale, namely in-plane tensile and shear behavior and out-of-plane bending.

### 4.1 Yarn Models

Analytical yarn models have evolved from the work of Peirce, who defined the standard for the geometry of woven yarns [27, 51], which was shown in Figure 2-6. These models characterize the behavior of fabrics by studying the interactions of the yarns that make up the unit cell, or repeating pattern, of the weave. Essentially, extensions and rotations of yarns were used to determine corresponding tensile, shear and contact forces acting on the yarns. Once these forces in the yarns were calculated, they could be multiplied by the number of ends or picks per unit length to determine the force

per unit length of a fabric. Grosberg and Kedia [52] derived an analytical solution for the initial load extension moduli due to decrimping in a plain-weave fabric. For this decrimping region, they assumed the yarns to be inextensible and thin beams. The shape of the yarn between two neighboring intersecting yarns was determined by the reactions at each intersection: the force applied to extend the yarn, and the contact force between the two yarns at an intersection. Grosberg and Kedia [52] used initial geometric parameters and yarn bending rigidity to determine how the shape of the yarn changed when a load at the end of the yarn was applied for cases in which crossing yarns were present and absent.

In the early 1970s, Kawabata *et al* [33, 34, 44] presented seminal work investigating the deformation of fabrics under biaxial, uniaxial, and shear loads. For all aspects of their theory, they assumed elastic bodies, but noted that this assumption does not require the properties to be linear. For biaxial tension, they constructed a geometric model with parameters that included yarn densities, yarn crimp, and yarn spacing in the warp and weft directions, the angle between the yarn axis and the out-of-plane axis, yarn length in the unit cell, distance between the neutral line and the yarn axis along the out-of-plane axis in the undeformed state, the deflection of yarn along the out-of-plane axis in the deformed state as well as the warp and weft yarn extension properties.

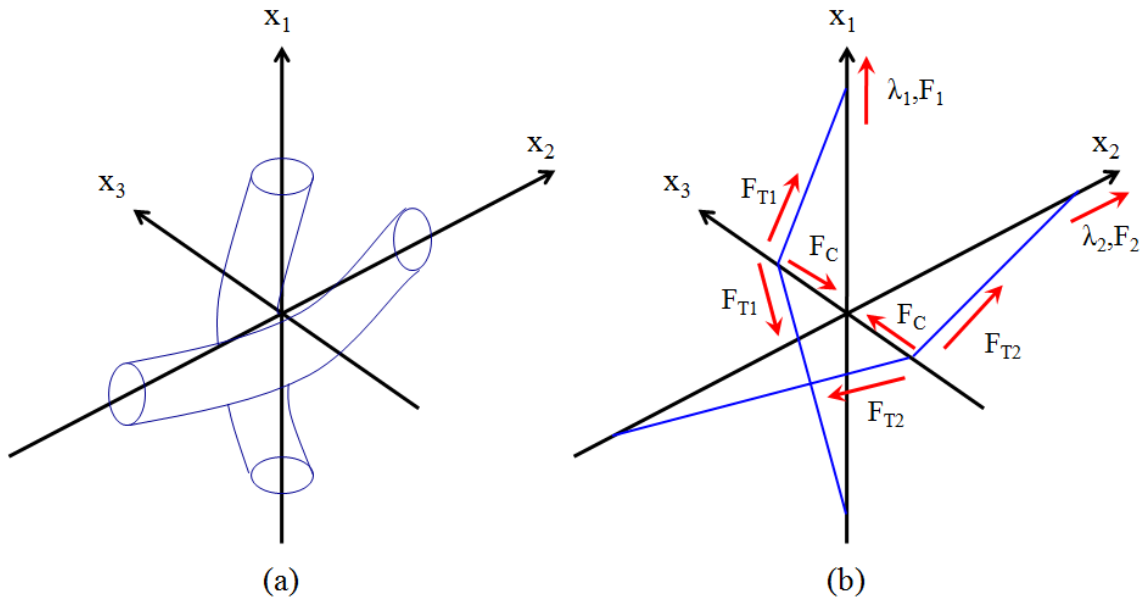


Figure 4-1. Yarn interaction: (a) the crossover point of two yarns and (b) the corresponding stretches and forces during loading.

Based upon the original and deformed geometries, they formulated a procedure to calculate the tensile forces in the warp and weft yarns and the contact force at the intersection of the two yarn families from the stretch ratios of the fabric in the warp and weft directions as shown in Figure 4-1. After initially assuming that the yarn thickness was inextensible, they then modified the procedure to include changes in yarn cross-section. To verify their model, they compared their theoretical results to experimental results under two loading conditions: uniform biaxial extension, where the stretch ratios,  $\lambda_1$  and  $\lambda_2$  were equal; and strip biaxial extension, where, while one stretch ratio was increased ( $\lambda_{1/2} > 1.0$ ), the other was held constant ( $\lambda_{2/1}=1.0$ ). The stretch ratio was defined as

$$\lambda = \frac{\text{length in the stretched state}}{\text{length in the unstretched state}} = 1 + \text{strain} \quad (4.1)$$

Examples of the results of both tests are shown in Figure 4-2.

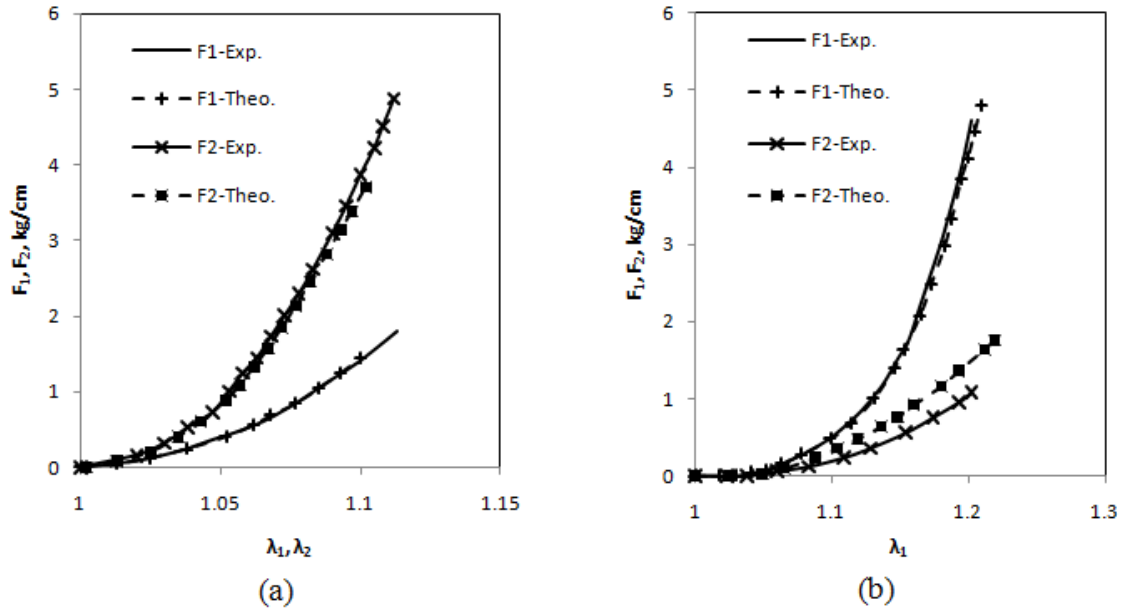


Figure 4-2. Comparison of Kawabata *et al's* [33] theory for a plain-weave cotton fabric versus experimental data for (a) uniform biaxial tension and (b) strip biaxial tension.

For uniaxial tension, they note that according to their biaxial theory, since the tensile force in the transverse direction was zero, the contact force would also be zero, which was in contrast to the experimental results. The biaxial theory was modified to include uniaxial tension by using a first-order approximation for the contact force, where the constants for the approximation were based upon material and geometric properties. The contact force was also shown to be the summation of the bending and shearing forces of the yarns at the crossover point. Since this shear term can have positive or negative values depending on a state of loading or unloading, the model was able to capture the

hysteresis present in experimental data as shown in Figure 4-4a. Finally, they further extended their theory to include shear deformation by using a linear approximation to estimate the torque required to change yarn intersection angle by an angle,  $\phi$ , and as a function of contact force (Figure 4-3). These torques, along with any present extensions, were then used to calculate the shear forces. Again, the increase or decrease of the shear angle allowed for the modeling of the hysteretic behavior. They modified their biaxial test machine to test for shear and an example of their experimental results was compared to their theory in Figure 4-4b. Overall, the models developed by Kawabata *et al* give very realistic behavior for uniaxial, biaxial, and shear deformation by including nonlinearity and hysteresis. The models, however, are not very conducive for clothing simulations in that number of parameters and computations is restrictive for the computational time that would be necessary.

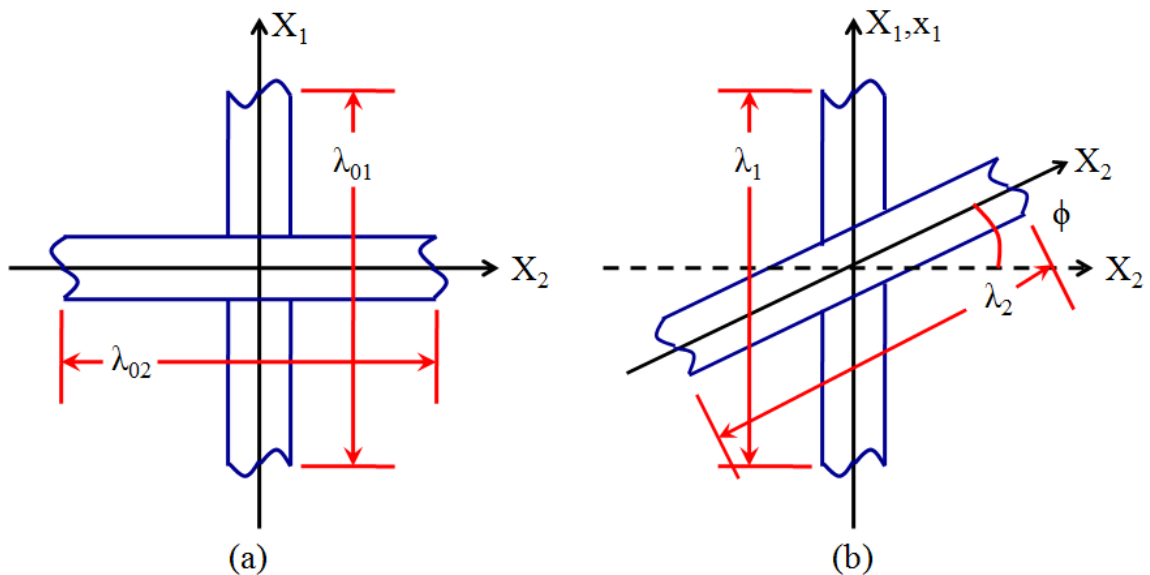


Figure 4-3. Yarn shear interaction: (a) the original configuration of a crossover point of two yarns and (b) the resulting deformation due to a shear load.



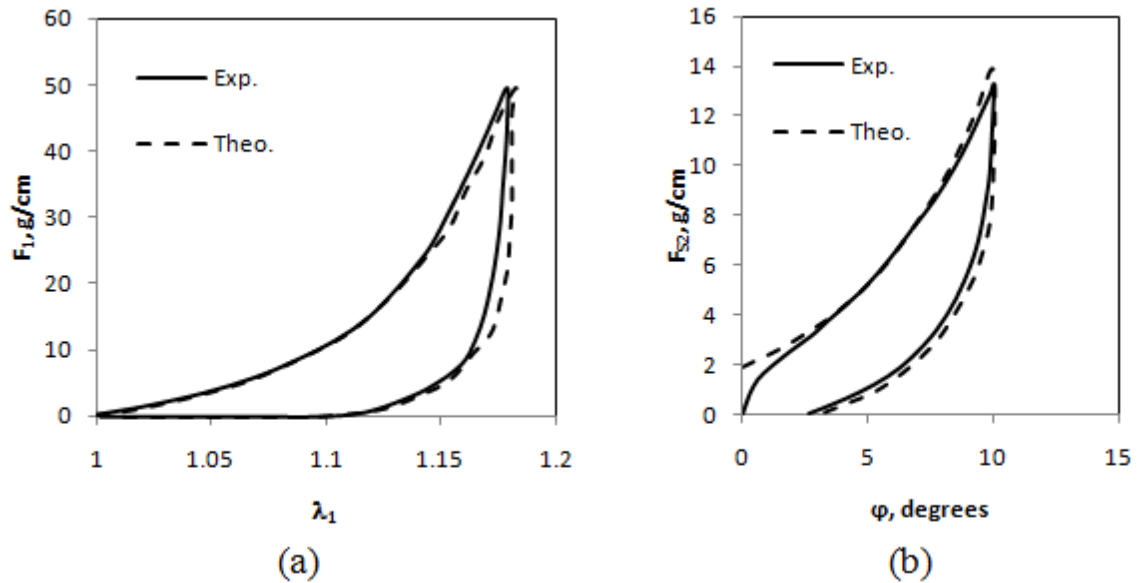


Figure 4-4. Comparison of Kawabata *et al's* [34, 44] theory for a plain-weave cotton fabric versus experimental data for (a) uniaxial tension and (b) shear.

More recently, Anandjiwala and Leaf [36, 53] developed a generalized yarn-geometry model that was able to include hysteresis evident in cyclic loadings of fabrics, which they note was the result of the viscoelastic nature of fibers and the friction between fibers and yarns. The model consisted of determining the curvature of a yarn in the deformed state using the yarn's bending, extension, and compression properties. To produce the hysteretic effect, a recovered state was defined when the applied load was less than the maximum load of a given cycle, thereby changing the parameters used to determine the curvature. Comparisons between their theoretical results and experimental results (Figure 4-5) showed generally good agreement during extension, but during recovery, their model greatly underestimates and amount of hysteresis.

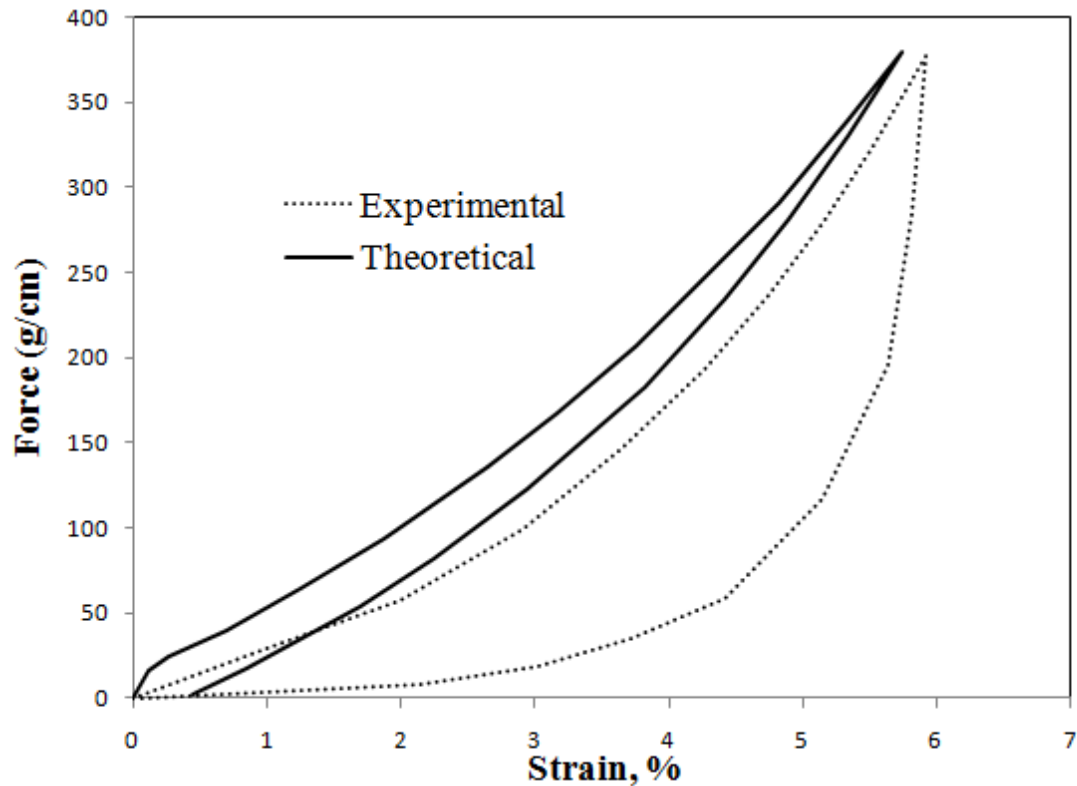


Figure 4-5. Comparison between hysteric model and experimental data [36].

In addition to the previously mentioned analytical models, unit cell finite element analyses have also proven to be a very effective tool. Cavallaro *et al* [54] used yarn unit cell finite element analysis to study the effects on mechanical properties due to plain-weave yarn structure and various shear and biaxial loadings. Unit cell studies of shear deformation were also presented by Sun and Pan [43] and Lin *et al* [45]. Hivet and Boisse [55] used unit cell analysis to study the behavior of different types of weaves.

#### 4.2 Particle-Spring Models

Since the early 1990s, the computational modeling of fabric and clothing at the macroscale has evolved into two main approaches: particle-based modeling and continuum-based modeling. Pioneered by Breen [9, 56], particle-based methods are

derived from the geometry of yarn models and essentially treat the intersections of warp and weft yarns as point masses, or particle nodes, connected to the surrounding nodes by springs and dashpots that can account for the stretching, shearing and bending of cloth as shown in Figure 4-6. In terms of macroscopic deformation, particle-spring models are able to accurately predict fabric behavior by varying the spring and dashpot parameters until the results correlate with experimental data, usually determined by means of the Kawabata Evaluation System (KES) [12]. Boubaker *et al* have used particle-spring models to study the interaction between yarns and their effect on fabric behavior [57, 58] and extended their work to the macroscopic study of drape [59]. Zhou *et al* [60] recently used this method to simulate the out-of-plane buckling due to in-plane shear loads. This method has been used extensively in drape and clothing simulations, especially in computer graphics applications due to its ease of implementation and visual realism of the results [12].

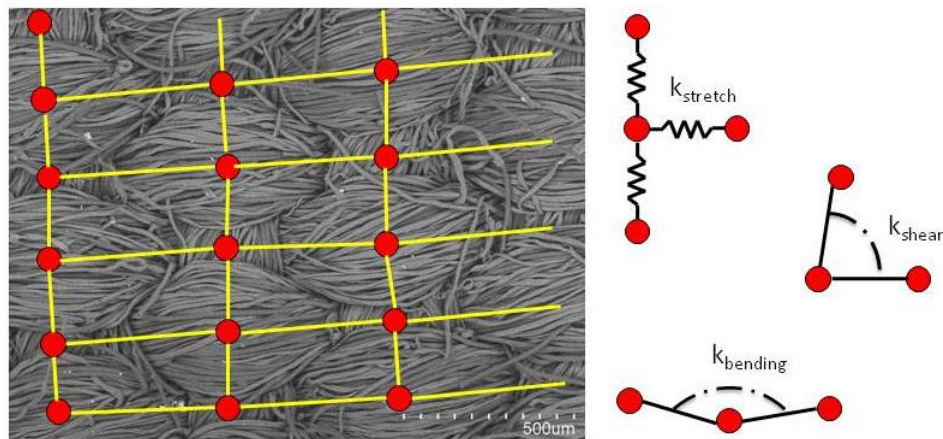


Figure 4-6. Example of a particle-spring model for a plain-weave fabric showing three types of springs.

### 4.3 Continuum Models

As has been demonstrated, woven fabrics are a discontinuous and heterogeneous material. Continuum models, however, homogenize fabrics into a thin, continuous, and homogenous sheet. For simulations of woven fabrics, many researchers have turned to finite element models. Because the thickness of fabrics is so much smaller in relation to the other, in-plane dimensions, it is convenient to develop constitutive equations that utilize shell elements. Figure 4-7 illustrates this homogenization where the material directors  $\mathbf{g}_1$  and  $\mathbf{g}_2$  correspond to the orientations of the warp and weft yarns, respectively.

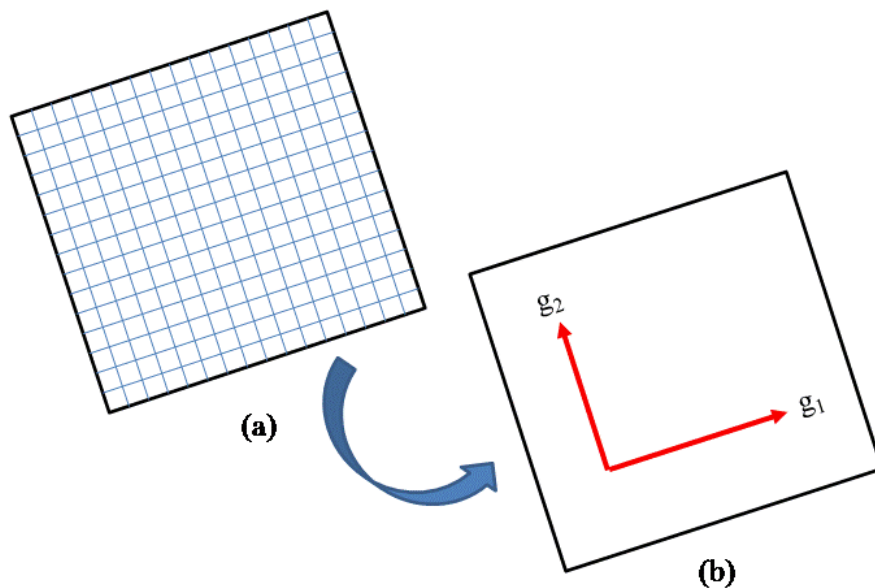


Figure 4-7. Homogenization of (a) a fabric of woven yarns to (b) a corresponding anisotropic continua.

Many continuum-based finite element models have been developed. Collier *et al* [15] modeled the draping behavior of fabrics using a four-node shell element. Noting that

woven textiles are not easily stretched yet will bend through large displacements, membrane and bending strains were derived that included linear and nonlinear terms. Assuming that the fabric had a linear stress-strain relationship, their numerical and experimental analysis consisted of draping a circular fabric over a circular metal plate of a smaller area where the only external load was gravity. Using three material parameters: the elastic moduli in the warp and weft directions and an assumed Poisson's ratio, they compared the drape coefficient (the ratio of the difference between the projected area and the area of the metal plate to the difference between the original fabric area and the area of the metal plate) they found using their model to experimental values and determined that there was close agreement between the drape coefficients, though the deformed shape was highly dependent upon the Poisson's ratio.

Chen and Govindaraj [13] developed a shell formulation that included the coupling of the stretching and bending within each element. Their model focused on calculating surface membrane shears, curvature change, and transverse shears and neglected any change in the shell's thickness. The model assumed a small strain linear-elastic orthotropic constitutive relationship.

$$\begin{Bmatrix} \sigma_{11} \\ \sigma_{22} \\ \sigma_{23} \\ \sigma_{13} \\ \sigma_{12} \end{Bmatrix} = \begin{bmatrix} \frac{E_1}{1-\nu^2} & \frac{E_2}{1-\nu^2} & 0 & 0 & 0 \\ \frac{E_2}{1-\nu^2} & \frac{E_1}{1-\nu^2} & 0 & 0 & 0 \\ 0 & 0 & G_{23} & 0 & 0 \\ 0 & 0 & 0 & G_{13} & 0 \\ 0 & 0 & 0 & 0 & G_{12} \end{bmatrix} \begin{Bmatrix} \varepsilon_{11} \\ \varepsilon_{22} \\ \varepsilon_{23} \\ \varepsilon_{13} \\ \varepsilon_{12} \end{Bmatrix} \quad (4.2)$$

Where  $E_1$  is the elastic modulus in the warp direction,  $E_2$  is the elastic modulus in the weft direction,  $G_{12}$ ,  $G_{13}$ , and  $G_{23}$  are shear moduli, and  $\nu$  is the Poisson's ratio.

Simulations of their model showed a realistic 3D rendering of a square fabric draped over a square base of smaller area, shown in Figure 4-8. Deformation and folds were in very close agreement with experimental results. They followed this up by

investigating the influence of material parameters on fabric drape [14]. They found that (1) materials with higher elastic moduli have less drape, (2) higher shear moduli induce an orthotropic effect, (3) changes in fabric thickness have a large influence on bending stiffness, and (4) in contrast to Collier's results, changes in Poisson's ratio have little influence on the drape.

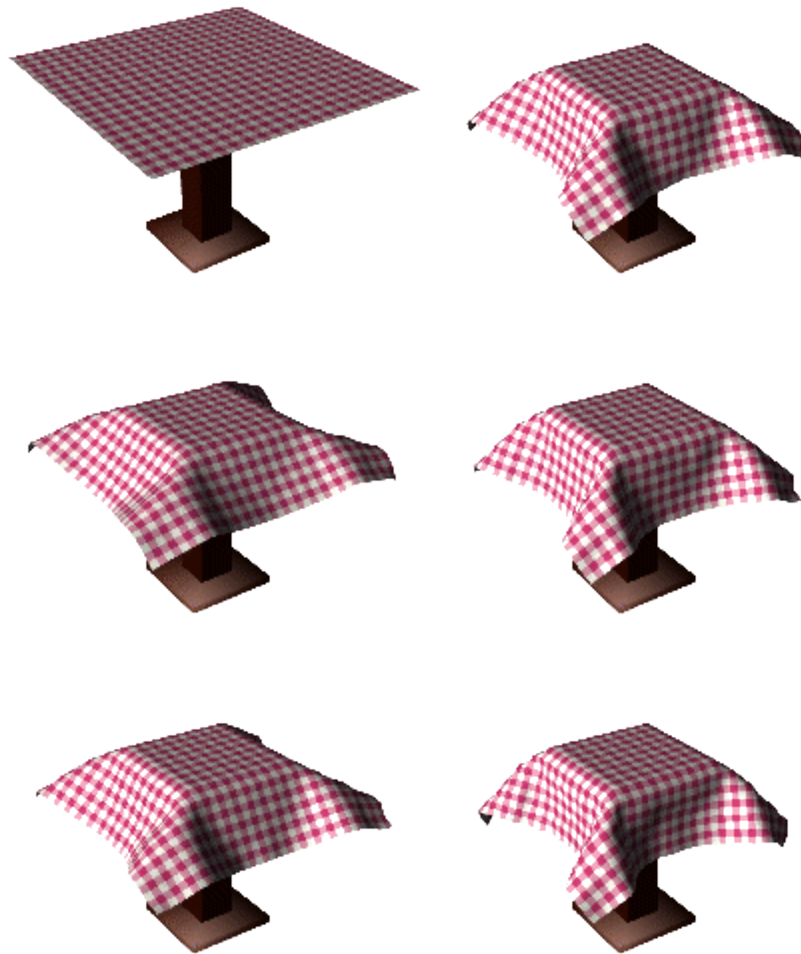


Figure 4-8. Animation of simulated fabric drape by Chen and Govindaraj [13].

Similarly, Kang and Yu [16] derived a large deformation, anisotropic method to simulate the drape of woven fabrics. Their shell model was formulated using Green-Lagrange strain that was broken down into three parts that accounted for membrane strain, bending strain, and transverse shear strain. The constitutive equations simplified down to the St. Venant-Kirchhoff model, which is an extension of the linear-elastic orthotropic constitutive model (4.2) to large deformation. The internal work was calculated using these strains along with their corresponding 2<sup>nd</sup> Piola-Kirchhoff stresses via an orthotropic elastic constitutive model and the external work was due to gravity. They verified their model against experimental results from deflection curves of fabric strips and drape results circular fabrics and found good agreement.

Wu *et al* [17] developed a constitutive model for dynamic drape simulations that included collision detections for fabrics. Their work mainly consisted of defining elastic moduli tensors for stretching and bending deformation in terms of the elastic, shear, bending, and twisting moduli, the Poisson's ratios, and bending quantities analogous to the Poisson's ratios. Most of the parameters were measured for a particular fabric using the KES tests, while the remaining parameters were estimated using the known quantities. Once these quantities were known, the strain energy density was found and the total energy was minimized to find the equilibrium state. The acceleration was then computed in order to find the next state of deformation, while correcting for any possible collisions.

While the preceding studies assumed anisotropic linear elasticity, others have aimed to include more of the material non-linearity in the constitutive modeling. Peng and Cao [61] developed a continuum mechanics-based constitutive model that allowed for non-orthogonal material directors that correspond to the local orientation of warp and weft yarns. They used a convected coordinate system in which the in-plane axes coincided with the warp and weft yarns of a woven composite fabric embedded in a shell element. With the convected coordinate system, they were able to transform stresses,

strains, and elastic moduli from one set of coordinates to another, using basic rotation matrices. Looking at load-strain curves from real fabric tests, they observed that there were three stages in the tension test: a stage with very small tensile modulus due to the decrimping of yarns, a stage with an approximately linear high tensile modulus, and finally a stage where damage was taking place evident by a non-linear curve with a smaller tensile modulus than that of the second stage; and two stages in shear tests: initial compliance due to the decrimping and rotation of yarns followed by a dramatic increase in stiffness due to shear lock. Using results from a specific test, they were able to form the components of the orthotropic elastic moduli by fitting a curve, which resulted in close agreement with that particular test as shown in Figure 4-9.

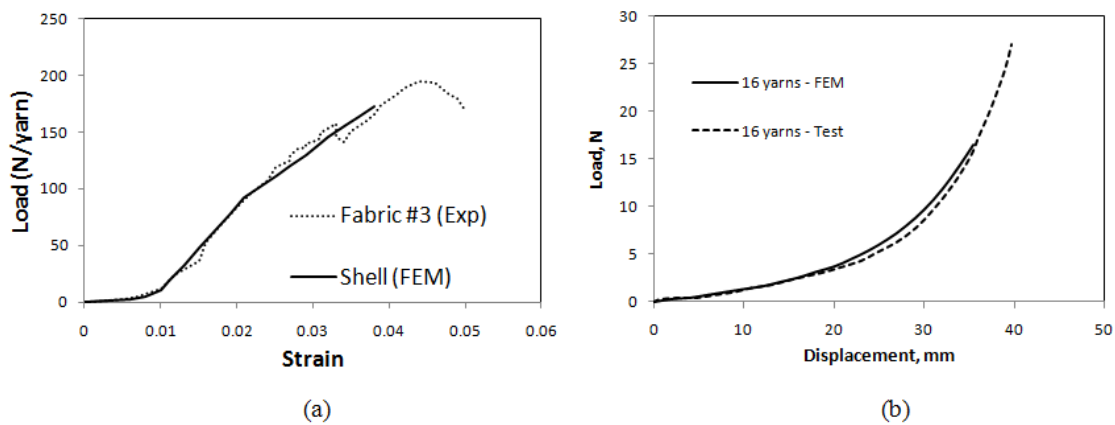


Figure 4-9. Comparison of (a) uniaxial warp/weft results and (b) bias  $45^\circ$  results for a woven composite fabric. In both cases, moduli were developed by fitting a curve to the experimental data [61].

Ruiz and Gonzalez [62] investigated the use of different hyperelastic strain energy functions in the modeling of fabrics. They considered several hyperelastic strain energy functions that were expressed as functions of the principle stretches of the strain tensor. In trying to minimize the number of experimental parameters, they considered two cases:



one in which only uniaxial tension test data were considered, and one including uniaxial tension, shear and biaxial tension test data. Their methodology included selection a hyperelastic model, introducing the experimental data from either of the cases, employing a nonlinear regression scheme to determine the coefficients of the selected model and then utilizing a finite element analysis to solve a test problem. They found that for the case considering only uniaxial tension test data, the Mooney-Rivlin, Yeoh, and Arruda-Boyce models produced the best fit with the initial experimental data; however, only the Yeoh and Arruda-Boyce models were able to converge to solutions in the finite element analysis. In the other case, only the Mooney-Rivlin model produced results that fit the experimental data well.

A promising extension of continuum models is that of a multiscale analysis. In this approach, the fabric is considered a continuum subjected to the applied macroscopic loads and boundary conditions. Through the use of continuum mechanics and finite element modeling, the calculated deformation gradient at a particular integration point is used as input into a unit cell analysis. There, methods such as those described earlier in the yarn modeling approach or the particle-spring approach are used to calculate the various forces acting on the yarns. These forces are then averaged and used to determine the stress at the continuum, or macroscopic, scale. Some interested work in this area has been done by King *et al* [63, 64] and Nadler *et al* [65].

Work by Reese [66] considered the anisotropic elastoplastic deformation of pneumatic membranes. The membranes were modeled as woven fibers embedded in a rubber-like matrix. A strain energy function that included a Neo-Hookean term for the matrix and anisotropic term for the woven fibers was proposed. Noting that the plastification was limited to the fibers, an anisotropic yield function, hardening law, and flow rule were introduced that were based upon a multiplicative split of the deformation gradient. Finite element results were compared to “experimental” data that was generated using a unit cell computer model and the results are shown in Figure 4-10. This

approach shows promise, however, they assumed that the behavior in the warp and weft directions was decoupled and the algorithm is computationally expensive.

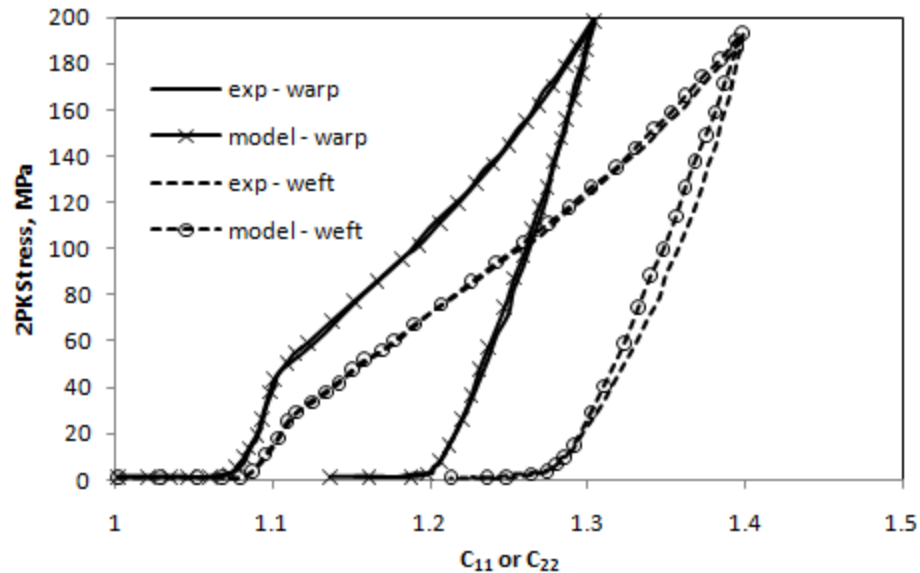


Figure 4-10. Comparison of biaxial response of experiments and model. Initially, behavior is controlled by the rubber matrix, resulting in very low stress. As the load is taken up by the yarns, stress increases rapidly until it yields, where plastic behavior dominates [66].

#### 4.4 Discussion

In terms of general fabric modeling, all the described approaches have their advantages and disadvantages. As the ultimate goal of this research is to develop constitutive models that will be used with dynamic clothing-wearer interactions, computational efficiency and stability as well as mechanical accuracy are crucial. Although the realism of fabric behavior demonstrated by yarn and multiscale models are very high, the computational expense of dynamic simulations at that resolution is just too great, and thus their use is not feasible at this time. Particle-spring models have seen widespread use in computer graphics and have proven to be mechanically realistic;

however, the coefficients of the various springs and dashpots are set for particular mesh size and changing the mesh would require resetting all parameters. While continuum-based models are more computationally involved, they are resolution independent and are better suited to capture the physics of the clothing using constitutive equations [3, 67].

Many current continuum models by researchers such as Collier *et al* [15], Chen and Govindaraj [13, 14], and Kang and Yu [16] assume linear elastic behavior, where the elastic and shear moduli are taken to be the initial moduli from experiments. In order to determine the suitability of these models, we use a St. Venant-Kirchhoff (SVK) constitutive model with linear elastic and shear moduli that are estimated from the initial linear slope of the cotton-polyester blend experimental data shown in Chapter 3. The results from the SVK model are compared to experimental data in Figure 4-11. The St. Venant-Kirchhoff model would be sufficient in simulations where the strains are small, say less than 5%, such as drape studies where the only load is that due to gravity; however, for clothing simulations where the local tensile strains may be as high as 25% [20] to 50% [19] the SVK model is clearly deficient.

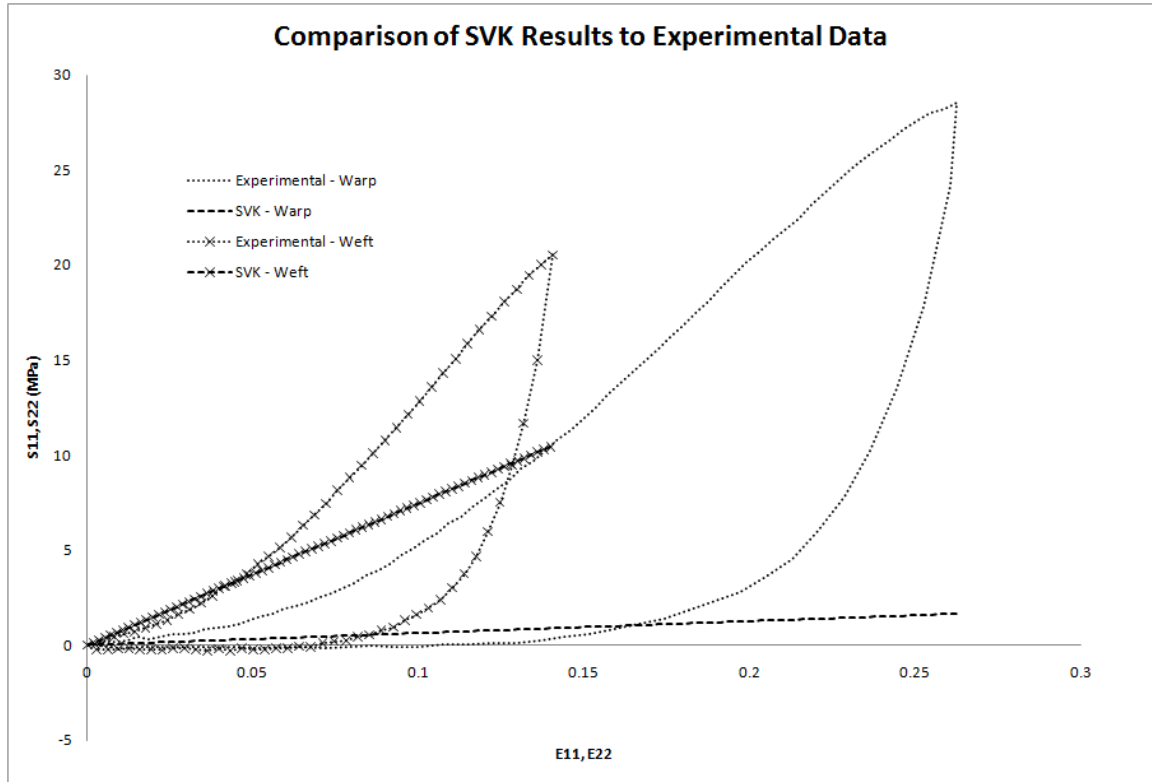


Figure 4-11. Comparison of SVK and experimental results for a monotonic uniaxial stress tensile test in the warp and weft directions for cotton-polyester blend fabric.

Therefore, it is seen as advantageous to develop a continuum-based constitutive model to be incorporated with a 3-D bilinear degenerated continuum shell element. Continuing on the recent fabric modeling direction, the model developed in this research will be an incrementally elastic, orthotropic model whose moduli are functions of the current strain tensor. In addition, a novel approach will be taken to include the substantial amount of hysteresis observed upon unloading of the fabric.

## CHAPTER 5. FINITE ELEMENT BACKGROUND

In this chapter, the finite element analysis framework for fabric modeling is presented. Since the thickness is much smaller than the other two physical dimensions of a textile, a macroscopic geometrically nonlinear shell element is a clear choice for modeling the behavior of fabrics. Currently, a three-dimensional bilinear degenerated continuum shell element, modified for use with finite deformations by Man [3] is employed. This shell element is degenerated, meaning that it must satisfy the vanishing normal stress condition.

### 5.1 Problem Statement

In order to develop a nonlinear shell formulation, the general problem statement is formulated through the use of energy methods following [68, 69]. In the energy approach, the equations of motion are derived by applying virtual displacements,  $\delta u_i$ , to the body that are consistent with the geometric constraints that the body is subjected to. This derivation not only provides the equations of motion, but also sets up the natural and essential boundary conditions. The use of virtual displacements can lead the body to take on an infinite number of configurations; however, of these, the only admissible configurations are those that satisfy the natural and essential boundary conditions. Finally, the true configuration is the one that satisfies the force equilibrium.

To begin, the momentum equation for the original, or reference, configuration  $\Omega_0$  is given as:

$$P_{iJ,J} + \rho_0 b_i = \rho_0 \ddot{u}_i \quad (5.1)$$

where  $\rho_0$  is the initial mass density,  $b_i$  is the body force,  $\ddot{u}_i$  is the acceleration, and  $P_{iJ}$  is the 1<sup>st</sup> PK stress. Natural (applied tractions) and essential (prescribed displacements) boundary conditions are prescribed, respectively, as:

$$\begin{aligned} P_{ij}n_j^0 &= \bar{t}_i^0 \text{ on } \Gamma_{t_i}^0 \\ u_i &= \bar{u}_i \text{ on } \Gamma_{u_i}^0 \end{aligned} \quad (5.2)$$

Where  $\Gamma_{t_i}^0$  and  $\Gamma_{u_i}^0$  are the locations on the boundary of  $\Omega_0$  where the tractions  $\bar{t}_i^0$  and displacements  $\bar{u}_i$  are prescribed, respectively, and  $n_j^0$  is the outward normal to the boundary of  $\Omega_0$ .

The weak form is developed by multiplying the momentum equation in (5.1) by a test function, in this case a virtual displacement,  $\delta u_i$ , and then integrating over the initial configuration as follows:

$$\int_{\Omega_0} \delta u_i (P_{ij,j} + \rho_0 b_i - \rho_0 u_i) d\Omega_0 = 0. \quad (5.3)$$

Distributing in the virtual displacement,

$$\int_{\Omega_0} [\delta u_i P_{ij,j} + \delta u_i \rho_0 b_i - \delta u_i \rho_0 u_i] d\Omega_0 = 0. \quad (5.4)$$

The derivative of the stress in the first term of the right hand side of (5.4) requires that the virtual displacement to be  $C^2$  (the second derivative of the virtual displacement is continuous). For the weak form of the momentum equation, the virtual displacements need only be  $C^0$ . Therefore, the derivative of the stress can be eliminated using the derivative product rule:

$$\int_{\Omega_0} \delta u_i \frac{\partial P_{ij}}{\partial X_j} d\Omega_0 = \int_{\Omega_0} \frac{\partial(\delta u_i P_{ij})}{\partial X_j} d\Omega_0 - \int_{\Omega_0} \frac{\partial \delta u_i}{\partial X_j} P_{ij} d\Omega_0. \quad (5.5)$$

Using the divergence theorem, the first term on the left hand side of (5.5) is converted to a surface integral:

$$\int_{\Omega_0} \frac{\partial(\delta u_i P_{ij})}{\partial X_j} d\Omega_0 = \int_{\Gamma_0} \delta u_i n_j^0 P_{ij} d\Gamma_0 + \int_{\Gamma_{\text{int}}^0} \delta u_i \langle n_j^0 P_{ij} \rangle d\Gamma_0. \quad (5.6)$$

The interior continuity condition states that on  $\Gamma_{\text{int}}^0, \langle n_j^0 P_{ij} \rangle = 0$ . Using (5.2), (5.6) can be rewritten as

$$\int_{\Omega_0} \frac{\partial(\delta u_i P_{ij})}{\partial X_j} d\Omega_0 = \int_{\Gamma_i^0} \delta u_i \bar{t}_i^0 d\Gamma_0 . \quad (5.7)$$

Substituting (5.5) and (5.7) into (5.4) and including a sign change, the weak form is:

$$\int_{\Omega_0} \delta F_{ij} P_{ij} d\Omega_0 = \int_{\Gamma_i^0} \delta u_i \bar{t}_i^0 d\Gamma_0 + \int_{\Omega_0} \delta u_i \rho_0 b_i d\Omega_0 - \int_{\Omega_0} \delta u_i \rho_0 \ddot{u}_i d\Omega_0 . \quad (5.8)$$

where  $\delta F_{ij} = \partial u_i / \partial X_j$ .

For completeness, the strong form may be derived by eliminating the derivative of the test function on the left hand side. Using (5.5) and (5.6), the left hand side of (5.8) may be rewritten as

$$\int_{\Omega_0} \delta F_{ij} P_{ij} d\Omega_0 = \int_{\Gamma_i^0} \delta u_i n_j^0 P_{ij} d\Gamma_0 + \int_{\Gamma_{\text{int}}^0} \delta u_i \langle n_j^0 P_{ij} \rangle d\Gamma_0 - \int_{\Omega_0} \delta u_i \bar{t}_i^0 d\Omega_0 . \quad (5.9)$$

The strong form can now be written as

$$\int_{\Omega_0} \delta u_i (P_{ij,j} + \rho_0 b_i - \rho_0 \ddot{u}_i) d\Omega_0 + \int_{\Gamma_i^0} \delta u_i (n_j^0 P_{ij} - \bar{t}_i^0) d\Gamma_0 + \int_{\Gamma_{\text{int}}^0} \delta u_i \langle n_j^0 P_{ij} \rangle d\Gamma_0 = 0, \quad (5.10)$$

where the first term is the momentum equation, the second term is the traction boundary condition and the last term is the interior continuity condition.

Since each term in (5.8) contains a virtual work increment (virtual displacement), the weak form may be rewritten in terms of the principle of virtual work:

$$\delta W^{\text{int}}(\delta u_i, u_i) = \delta W^{\text{ext}}(\delta u_i, u_i) - \delta W^{\text{kin}}(\delta u_i, u_i) \quad (5.11)$$

where:

$$\delta W^{\text{int}} = \int_{\Omega_0} \delta F_{ij} P_{ij} d\Omega_0 \quad (5.12)$$

$$\delta W^{\text{ext}} = \int_{\Gamma_i^0} \delta u_i \bar{t}_i^0 d\Gamma_0 + \int_{\Omega_0} \delta u_i \rho_0 b_i d\Omega_0 \quad (5.13)$$

$$\text{and } \delta W^{\text{kin}} = \int_{\Omega_0} \delta u_i \rho_0 \ddot{u}_i d\Omega_0 . \quad (5.14)$$

Because  $P_{ij}$  is not symmetric, it is advantageous to transform it to the symmetric second Piola-Kirchhoff tensor,  $S_{IJ}$ . Using the transformation rule

$$S_{IJ} = F_{Ik}^{-1} P_{kJ} \quad (5.15)$$

and the virtual Green-Lagrange strain

$$\delta E_{IJ} = \frac{1}{2} \left( \delta F_{IK}^T F_{KJ} + F_{IK}^T \delta F_{KJ} \right), \quad (5.16)$$

the internal virtual work in (5.12) is rewritten as

$$\delta W^{\text{int}} = \int_{\Omega_0} \delta E_{IJ} S_{JI} d\Omega_0. \quad (5.17)$$

## 5.2 Coordinate Systems

Currently, four coordinate systems are utilized in the shell implementation: (1) a global Cartesian coordinate system  $(X_1, X_2, X_3)$  with orthonormal basis vectors  $(\mathbf{e}_1, \mathbf{e}_2, \mathbf{e}_3)$ ; (2) a shell coordinate system  $(\xi, \eta, \zeta)$  that describes the physical domain of the shell element; (3) a lamina coordinate system defined at each integration point; and (4) a fiber Cartesian coordinate system at each node that is used as a reference frame for rotations.

In general, shells are highly non-planar in form. Each integration point in the element has a tangent plane with respect to the lamina. The lamina Cartesian coordinate system that is constructed at each integration point and is defined by the orthonormal basis vectors  $\mathbf{e}_1^l, \mathbf{e}_2^l$  and  $\mathbf{e}_3^l$ . To define these basis vectors, the tangent vectors for the  $\xi$  and  $\eta$  directions are constructed as:

$$\mathbf{e}_\xi = \frac{x_{i,\xi}}{\|x_{i,\xi}\|} \text{ and } \mathbf{e}_\eta = \frac{x_{i,\eta}}{\|x_{i,\eta}\|} \quad (5.18)$$

The normal basis vector is then constructed as:

$$\mathbf{e}_3^l = \frac{\mathbf{e}_\xi \times \mathbf{e}_\eta}{\|\mathbf{e}_\xi \times \mathbf{e}_\eta\|}, \quad (5.19)$$

and the tangent basis vectors are constructed as:

$$\mathbf{e}_1^l = \frac{\sqrt{2}}{2} (\mathbf{e}_\alpha - \mathbf{e}_\beta) \text{ and } \mathbf{e}_2^l = \frac{\sqrt{2}}{2} (\mathbf{e}_\alpha + \mathbf{e}_\beta), \quad (5.20)$$



where

$$\mathbf{e}_\alpha = \frac{\frac{1}{2}(\mathbf{e}_\xi + \mathbf{e}_\eta)}{\left\| \frac{1}{2}(\mathbf{e}_\xi + \mathbf{e}_\eta) \right\|} \text{ and } \mathbf{e}_\beta = \frac{\mathbf{e}_3^l \times \mathbf{e}_\alpha}{\left\| \mathbf{e}_3^l \times \mathbf{e}_\alpha \right\|}. \quad (5.21)$$

In general,  $\mathbf{e}_3^l$  is not tangent to the fiber direction. It is used to invoke the plane stress condition at each integration point. By enforcing the stress in the  $\mathbf{e}_3^l$  direction to be zero, a reduced constitutive equation is derived where five independent components for the stress and strain tensors is all that is needed as is shown in Chapter 6.

The fiber Cartesian coordinate system is constructed at each node with orthonormal basis vectors  $\mathbf{e}_1^f, \mathbf{e}_2^f$  and  $\mathbf{e}_3^f$ , with the requirement that  $\mathbf{e}_3^f$  is chosen to coincide with the fiber direction  $\hat{\mathbf{X}}_A$ , which is defined in the next section. An algorithm for calculating the fiber basis vectors is given by Hughes [70]. The global, lamina, and fiber coordinate systems are shown in Figure 5-1.

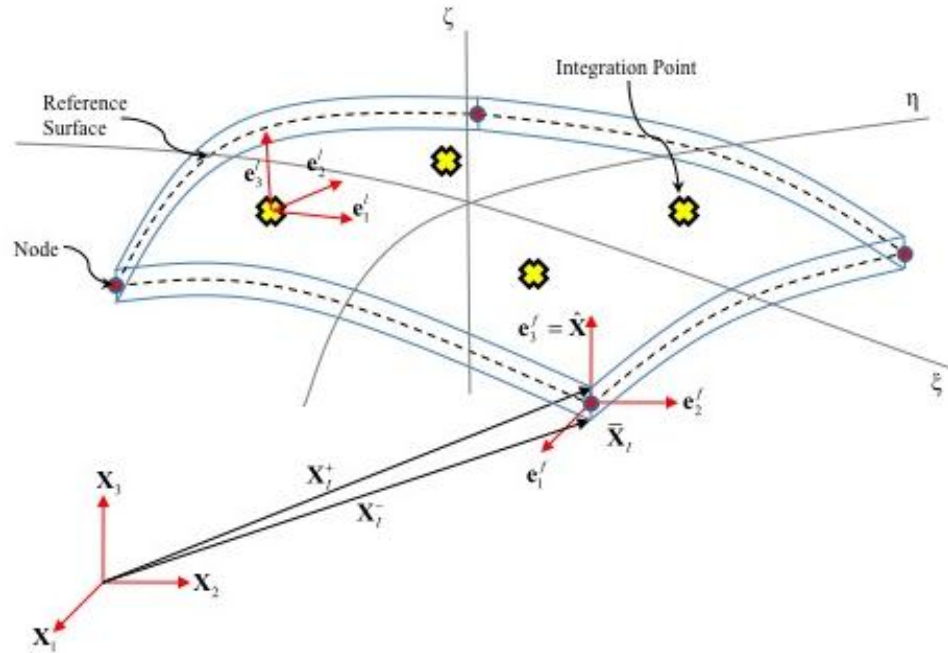


Figure 5-1. Geometric description of the shell element.

### 5.3 Shell Geometry and Kinematics

Using the approach of Hughes [70], Man [3, 8] developed a geometrical description for the initial and current configurations with respect to the lamina coordinate system according to the following relations, respectively:

$$\begin{aligned} \mathbf{X}(\xi, \eta, \zeta) &= \sum_{A=1}^{nen} N_A(\xi, \eta) \bar{\mathbf{X}}_A + \sum_{A=1}^{nen} N_A(\xi, \eta) z_A(\zeta) \hat{\mathbf{X}}_A \\ \mathbf{x}(\xi, \eta, \zeta) &= \sum_{A=1}^{nen} N_A(\xi, \eta) \bar{\mathbf{x}}_A + \sum_{A=1}^{nen} N_A(\xi, \eta) z_A(\zeta) \hat{\mathbf{x}}_A \end{aligned} ; \quad (5.22)$$

where  $\bar{\mathbf{X}}_A$  and  $\bar{\mathbf{x}}_A$  are the initial and current position vectors of mid-surface node  $A$ , respectively;  $\hat{\mathbf{X}}_A$  and  $\hat{\mathbf{x}}_A$  are the initial and current fiber directors emanating from node  $A$  in the fiber direction, respectively;  $z_A(\zeta)$  is a thickness function;  $N_A(\xi, \eta)$  is a two dimensional shape function associated with node  $A$  and  $nen$  is the number of element

nodes. The shell geometry is shown in Figure 5-1. Individual terms in (5.22) are defined as:

$$\begin{aligned}\bar{\mathbf{X}}_A &= \frac{1}{2}(1-\bar{\zeta})\mathbf{X}_A^- + \frac{1}{2}(1+\bar{\zeta})\mathbf{X}_A^+ \\ \bar{\mathbf{x}}_A &= \frac{1}{2}(1-\bar{\zeta})\mathbf{x}_A^- + \frac{1}{2}(1+\bar{\zeta})\mathbf{x}_A^+\end{aligned}\quad (5.23)$$

$$\begin{aligned}\hat{\mathbf{X}}_A &= \frac{\mathbf{X}_A^+ - \mathbf{X}_A^-}{\|\mathbf{X}_A^+ - \mathbf{X}_A^-\|} \\ \hat{\mathbf{x}}_A &= \frac{\mathbf{x}_A^+ - \mathbf{x}_A^-}{\|\mathbf{x}_A^+ - \mathbf{x}_A^-\|}\end{aligned}\quad (5.24)$$

$$\begin{aligned}z_A(\zeta) &= \frac{1}{2}(1+\zeta)z_A^+ + \frac{1}{2}(1-\zeta)z_A^- \\ z_A^+ &= \frac{1}{2}(1-\bar{\zeta})\|\mathbf{X}_A^+ - \mathbf{X}_A^-\| \\ z_A^- &= -\frac{1}{2}(1+\bar{\zeta})\|\mathbf{X}_A^+ - \mathbf{X}_A^-\|\end{aligned}\quad (5.25)$$

where  $\bar{\zeta} \in [-1,+1]$  is the natural coordinate of the reference surface ( $\bar{\zeta} = 0$  if the middle surface of the shell is chosen), and  $\mathbf{X}_A^+$  and  $\mathbf{X}_A^-$  are the coordinates of the top and bottom surfaces of the shell along each nodal fiber, respectively. This shell element has five parameters: three translational components in a Cartesian coordinate system and two rotations about the in-plane coordinate axes. The rotation about the out-of-plane coordinate axis is neglected as explained later in this section.

As a material deforms from the initial to the current configuration, the displacement vector for finite deformations is

$$\mathbf{u} = \mathbf{x} - \mathbf{X} \quad (5.26)$$

Using this relation, the current nodal position for node A is:

$$\bar{\mathbf{x}}_A = \bar{\mathbf{X}}_A + \bar{\mathbf{u}}_A, \quad (5.27)$$

where  $\bar{\mathbf{u}}_A$  is the displacement of a nodal point on the reference surface; and the fiber director is updated as:

$$\hat{\mathbf{x}}_A = \mathbf{R} \cdot \hat{\mathbf{X}}_A, \quad (5.28)$$

where  $\mathbf{R}$  is an orthogonal matrix describing the finite rotations of the nodal fiber director.

The matrix  $\mathbf{R}$  is derived using Euler's theorem, which states that in any rigid body rotation, there exists a line which remains fixed, about which the body rotates.

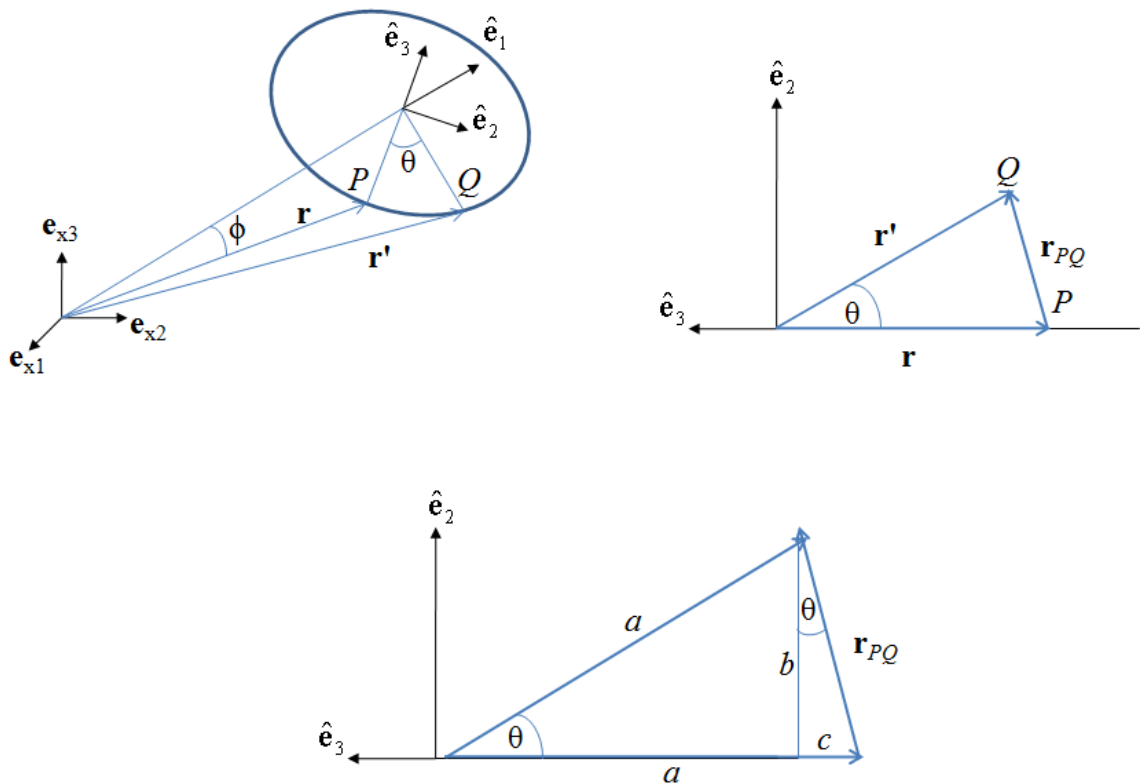


Figure 5-2. Finite rotation of a vector  $\mathbf{r}$  about the axis  $\hat{\mathbf{e}}_1$ .

To illustrate and derive the rotation matrix  $\mathbf{R}$ , we refer to Figure 5-2. The vector  $\mathbf{r}$  rotates about the unit vector  $\mathbf{e}$  to  $\mathbf{r}'$  by

$$\mathbf{r}' = \mathbf{R} \cdot \mathbf{r}, \quad (5.29)$$

and  $\mathbf{e}$  is defined as  $\hat{\mathbf{e}}_1$ . Using vector addition, (5.29) may be expressed as

$$\mathbf{r}' = \mathbf{r} + \mathbf{r}_{PQ}. \quad (5.30)$$

In the bottom diagram in Figure 5-2, the in-plane magnitude of both  $\mathbf{r}$  and  $\mathbf{r}'$  is  $a$ , where

$$a = r \sin \phi \quad (5.31)$$

and  $r$  is the magnitude of  $\mathbf{r}$ . Using geometry and trigonometry, we find that

$$b = r \sin \phi \sin \theta \quad (5.32)$$

$$c = r \sin \phi (1 - \cos \theta). \quad (5.33)$$

Using (5.32) and (5.33), (5.30) is expressed as

$$\mathbf{r}' = \mathbf{r} + r \sin \phi \sin \theta \hat{\mathbf{e}}_2 + r \sin \phi (1 - \cos \theta) \hat{\mathbf{e}}_3. \quad (5.34)$$

From the definition of the cross product, we can write

$$r \sin \phi \hat{\mathbf{e}}_2 = \mathbf{e} \times \mathbf{r} \quad (5.35)$$

$$r \sin \phi \hat{\mathbf{e}}_3 = \mathbf{e} \times (\mathbf{e} \times \mathbf{r}). \quad (5.36)$$

and express (5.34) as

$$\mathbf{r}' = \mathbf{r} + \sin \theta \mathbf{e} \times \mathbf{r} + (1 - \cos \theta) \mathbf{e} \times (\mathbf{e} \times \mathbf{r}). \quad (5.37)$$

To express (5.37) in matrix form, a skew-symmetric tensor is defined as

$$\begin{aligned} \boldsymbol{\Omega}(\mathbf{a}) &= \Omega_{ij}(a_k) \\ &= -e_{ijk} a_k, \end{aligned} \quad (5.38)$$

where  $e_{ijk}$  is the permutation symbol. Equations (5.35) and (5.36) are now expressed, respectively, as

$$\mathbf{e} \times \mathbf{r} = \boldsymbol{\Omega}(\mathbf{e})\mathbf{r} \quad (5.39)$$

$$\mathbf{e} \times (\mathbf{e} \times \mathbf{r}) = \boldsymbol{\Omega}^2(\mathbf{e})\mathbf{r}, \quad (5.40)$$

so that

$$\mathbf{r}' = \mathbf{r} + \sin \theta \boldsymbol{\Omega}(\mathbf{e})\mathbf{r} + (1 - \cos \theta) \boldsymbol{\Omega}^2(\mathbf{e})\mathbf{r}. \quad (5.41)$$

For the rotation matrix, it is convenient to define a column matrix of rotations  $\theta$ , with  $\boldsymbol{\theta} = \theta \mathbf{e}$ . Substituting  $\boldsymbol{\theta}$  into (5.41), yields

$$\mathbf{r}' = \mathbf{r} + \frac{\sin \theta}{\theta} \boldsymbol{\Omega}(\boldsymbol{\theta})\mathbf{r} + \frac{(1 - \cos \theta)}{\theta^2} \boldsymbol{\Omega}^2(\boldsymbol{\theta})\mathbf{r}. \quad (5.42)$$

Thus, the rotation matrix is defined as

$$\mathbf{R}(\boldsymbol{\theta}) = I + \frac{\sin \theta}{\theta} \boldsymbol{\Omega}(\boldsymbol{\theta}) + \frac{(1 - \cos \theta)}{\theta^2} \boldsymbol{\Omega}^2(\boldsymbol{\theta}), \quad (5.43)$$

where

$$\boldsymbol{\Omega}(\boldsymbol{\theta}) = \begin{bmatrix} 0 & -\theta_3 & \theta_2 \\ \theta_3 & 0 & -\theta_1 \\ -\theta_2 & \theta_1 & 0 \end{bmatrix} \text{ and } \theta = (\boldsymbol{\theta} \cdot \boldsymbol{\theta})^{1/2}. \quad (5.44)$$

In shell kinematics, the drilling degree of freedom,  $\theta_3$ , is usually excluded.

Therefore, the new orientation of the normalized fiber director is dependent only upon nodal rotations about the two in-plane axes of the fiber basis, or  $\boldsymbol{\theta}_A = \theta_{A1}^f \mathbf{e}_{A1}^f + \theta_{A2}^f \mathbf{e}_{A2}^f$ .

The current normalized fiber director can now be defined as

$$\hat{\mathbf{x}}_A = \hat{\mathbf{X}}_A + \frac{\sin \theta}{\theta} (\theta_{A2}^f \mathbf{e}_{A1}^f - \theta_{A1}^f \mathbf{e}_{A2}^f) + (1 - \cos \theta) \mathbf{e}_{A3}^f, \quad (5.45)$$

and the rotation of the fiber director tip is:

$$\begin{aligned} \hat{\mathbf{u}}_A &= \hat{\mathbf{x}}_A - \hat{\mathbf{X}}_A \\ &= \frac{\sin \theta}{\theta} (\theta_{A2}^f \mathbf{e}_{A1}^f - \theta_{A1}^f \mathbf{e}_{A2}^f) + (1 - \cos \theta) \mathbf{e}_{A3}^f, \end{aligned} \quad (5.46)$$

Therefore, given a nodal displacement vector

$$\mathbf{d}_A = (\bar{\mathbf{u}}_A \quad \boldsymbol{\theta}_A)^T, \quad (5.47)$$

the current nodal configuration is expressed as:

$$\begin{aligned}
\mathbf{x} &= \mathbf{x}(\mathbf{d}_A) \\
&= \sum_{A=1}^{nen} N_A (\bar{\mathbf{x}}_A + \bar{\mathbf{u}}_A) + \sum_{A=1}^{nen} N_A z_A \mathbf{R}(\boldsymbol{\theta}_A) \hat{\mathbf{X}}_A
\end{aligned} \tag{5.48}$$

#### 5.4 Explicit Linearized Kinematics

Because the problem is geometrically nonlinear, it needs to be solved iteratively.

In order to do this, (5.48) is linearized as

$$L[\mathbf{x}]_{\mathbf{d}_A^*} = \mathbf{x}^* + \Delta \mathbf{x}, \tag{5.49}$$

where  $\mathbf{x}^*$  is the trial displacement and  $\Delta \mathbf{x}$  is the directional derivative of  $\mathbf{x}$  along an incremental nodal displacement  $\Delta \mathbf{d}_A = (\Delta \mathbf{u}_A \quad \Delta \boldsymbol{\theta}_A)$ . The directional derivative is defined as

$$\begin{aligned}
\Delta \mathbf{x} &= \left. \frac{d}{d\varepsilon} [\mathbf{x}(\mathbf{d}_A^* + \varepsilon \Delta \mathbf{d}_A)] \right|_{\varepsilon \rightarrow 0} \\
&= \sum_{A=1}^{nen} N_A \Delta \bar{\mathbf{u}}_A + \sum_{A=1}^{nen} N_A z_A \left[ \left. \frac{\partial \mathbf{R}}{\partial \boldsymbol{\theta}_A} \right|_{\boldsymbol{\theta}_A = \boldsymbol{\theta}_A^*} \Delta \boldsymbol{\theta}_A \right] \hat{\mathbf{X}}_A
\end{aligned} \tag{5.50}$$

In general, the fiber basis vectors  $\mathbf{e}_i^f$  differ from the global basis vectors  $\mathbf{e}_i$ ; therefore, a transformation matrix relating the two bases is defined as

$$T_{mn} = (e_i^f)_m (e_j)_n. \tag{5.51}$$

The second term on the RHS in (5.50) is now transformed as

$$\begin{aligned}
\left[ \frac{\partial \mathbf{R}}{\partial \boldsymbol{\theta}_A} \Delta \boldsymbol{\theta}_A \right] \cdot \hat{\mathbf{X}}_A &= \frac{\partial R_{ij}}{\partial \theta_{A\alpha}^f} \Delta \theta_{A\alpha}^f \hat{X}_{Aj} \\
&= \left( T_{mi} \frac{\partial R_{mn}^f}{\partial \theta_{A\alpha}^f} T_{nj} \right) \Delta \theta_{A\alpha}^f (T_{rj} \hat{X}_{Ar}^f) \\
&= T_{mi} \left( \frac{\partial R_{mn}^f}{\partial \theta_{A\alpha}^f} \hat{X}_{An}^f \right) \Delta \theta_{A\alpha}^f,
\end{aligned} \tag{5.52}$$

where  $\alpha = 1, 2$ . Equation (5.52) leads to two auxiliary vectors  $D\hat{\mathbf{u}}_\alpha^A$  ( $\alpha = 1, 2$ ) defined as

$$D\hat{\mathbf{u}}_{\alpha i}^A = T_{mi} \frac{\partial \mathbf{R}_{mn}^f}{\partial \theta_{A\alpha}^f} \hat{\mathbf{X}}_{An}^f \quad (5.53)$$

and is the linearized displacement of the fiber director tip and

$$\frac{\partial \mathbf{R}^f}{\partial \theta_{A1}^f} \hat{\mathbf{X}}_A^f = \begin{bmatrix} \frac{\theta_{A1}^f \theta_{A2}^f \cos \theta}{\theta^2} - \frac{\theta_{A1}^f \theta_{A2}^f \sin \theta}{\theta^3} \\ -\frac{(\theta_{A1}^f)^2 \cos \theta}{\theta^2} - \frac{(\theta_{A2}^f)^2 \sin \theta}{\theta^3} \\ -\frac{\theta_{A1}^f \sin \theta}{\theta} \end{bmatrix} \quad (5.54)$$

$$\frac{\partial \mathbf{R}^f}{\partial \theta_{A2}^f} \hat{\mathbf{X}}_A^f = \begin{bmatrix} \frac{(\theta_{A2}^f)^2 \cos \theta}{\theta^2} + \frac{(\theta_{A1}^f)^2 \sin \theta}{\theta^3} \\ -\frac{\theta_{A1}^f \theta_{A2}^f \cos \theta}{\theta^2} + \frac{\theta_{A1}^f \theta_{A2}^f \sin \theta}{\theta^3} \\ -\frac{\theta_{A2}^f \sin \theta}{\theta} \end{bmatrix}. \quad (5.55)$$

The directional derivative can be written as

$$\Delta \mathbf{x} = \mathbf{H}^A \cdot \Delta \mathbf{d}_A \quad (5.56)$$

where the incremental displacement is

$$\Delta \mathbf{d}_A = \{\Delta \bar{u}_{A1} \quad \Delta \bar{u}_{A2} \quad \Delta \bar{u}_{A3} \quad \Delta \theta_{A1}^f \quad \Delta \theta_{A2}^f\}^T \quad (5.57)$$

and the generalized interpolation matrix is

$$\mathbf{H}^A = \begin{bmatrix} N_A & 0 & 0 & N_A z_A D\hat{\mathbf{u}}_{11}^A & N_A z_A D\hat{\mathbf{u}}_{21}^A \\ 0 & N_A & 0 & N_A z_A D\hat{\mathbf{u}}_{12}^A & N_A z_A D\hat{\mathbf{u}}_{22}^A \\ 0 & 0 & N_A & N_A z_A D\hat{\mathbf{u}}_{13}^A & N_A z_A D\hat{\mathbf{u}}_{23}^A \end{bmatrix}. \quad (5.58)$$

### 5.5 Force Vectors and Tangential Matrices

Since  $D\hat{\mathbf{u}}_{\alpha}^A$  is a nonlinear function of  $\boldsymbol{\theta}_A$ , the generalized interpolation matrix for the degenerated shell element is deformation dependent, unlike a continuous element.

Therefore, the variation of the shell configuration due to a virtual nodal displacement is



$$\delta x_i = H_i^{A\chi} \delta d_{A\chi} \quad (5.59)$$

$$\delta F_{IJ} = \delta x_{i,J} \quad (5.60)$$

$$\begin{aligned} \delta E_{IJ} &= \frac{1}{2} (\delta F_{kl} F_{kj} + F_{kl} \delta F_{kj}) \\ &= \frac{1}{2} (\delta x_{k,I} x_{k,J} + x_{k,I} \delta x_{k,J}) \end{aligned} \quad (5.61)$$

$$\Delta \delta E_{IJ} = \frac{1}{2} (\delta x_{k,I} \Delta x_{k,J} + \Delta x_{k,I} \delta x_{k,J}) \quad (5.62)$$

Using the linearized kinematics, the linearized variations, and the principle of virtual work described in section 5.1, the linearized force vectors are derived.

Linearizing the internal virtual work in (5.17), we get

$$L[\delta W^{\text{int}}]_{\mathbf{d}^*} = \int_{\Omega_0} \delta E_{IJ} S_{JI} d\Omega_0 + \int_{\Omega_0} \Delta \delta E_{IJ} S_{JI} d\Omega_0 + \int_{\Omega_0} \delta E_{IJ} \Delta S_{JI} d\Omega_0. \quad (5.63)$$

The first term on the RHS of (5.63) leads to the internal force by

$$\begin{aligned} \int_{\Omega_0} \delta E_{IJ} S_{JI} d\Omega_0 &= \delta d_{A\chi} \int_{\Omega_0} B_{IJ}^{A\chi} S_{JI} d\Omega_0 \\ &= \delta d_{A\chi} f_{A\chi}^{\text{int}}, \end{aligned} \quad (5.64)$$

such that internal force is defined as

$$f_{A\chi}^{\text{int}} = \int_{\Omega_0} B_{IJ}^{A\chi} S_{JI} d\Omega_0, \quad (5.65)$$

where

$$B_{IJ}^{A\chi} = H_{k,I}^{A\chi} F_{kj}. \quad (5.66)$$

The second term on the RHS of (5.63) geometric stiffness by

$$\begin{aligned} \int_{\Omega_0} \Delta \delta E_{IJ} S_{JI} d\Omega_0 &= \int_{\Omega_0} \delta x_{k,I} \Delta x_{k,J} S_{JI} d\Omega_0 \\ &= \delta d_{A\chi} \left( \int_{\Omega_0} H_{k,I}^{A\chi} H_{k,J}^{B\mu} S_{JI} d\Omega_0 \right) \Delta d_{B\mu} \\ &= \delta d_{A\chi} K_{A\chi B\mu}^G \Delta d_{B\mu} \end{aligned} \quad (5.67)$$

such that the geometric stiffness is defined as

$$K_{A\lambda B\mu}^G = \int_{\Omega_0} H_{k,I}^{A\lambda} H_{k,J}^{B\mu} S_{JI} d\Omega_0 \quad (5.68)$$

Assuming an incremental constitutive model

$$\Delta S_{IJ} = C_{IJKL} : \Delta E_{KL} \quad (5.69)$$

where  $C_{IJKL}$  is the tangent material operator, the third term on the RHS of (5.63) leads to the material stiffness by

$$\begin{aligned} \int_{\Omega_0} \delta E_{IJ} \Delta S_{JI} d\Omega_0 &= \int_{\Omega_0} (\delta x_{m,I} F_{mJ}) C_{IJKL} (\Delta x_{n,K} F_{nL}) d\Omega_0 \\ &= \delta d_{A\lambda} \left( \int_{\Omega_0} B_{IJ}^{A\lambda} C_{IJKL} B_{KL}^{B\mu} d\Omega_0 \right) \Delta d_{B\mu} \\ &= \delta d_{A\lambda} K_{A\lambda B\mu}^M \Delta d_{B\mu} \end{aligned} \quad (5.70)$$

such that the material stiffness is defined as

$$K_{A\lambda B\mu}^M = \int_{\Omega_0} B_{IJ}^{A\lambda} C_{IJKL} B_{KL}^{B\mu} d\Omega_0 \quad (5.71)$$

The external virtual work is not linearized and from (5.13),

$$\begin{aligned} \delta W^{\text{ext}} &= \int_{\Gamma_i^0} \delta u_i \bar{t}_i^0 d\Gamma_0 + \int_{\Omega_0} \delta u_i \rho_0 b_i d\Omega_0 \\ &= \delta d_{A\lambda} \int_{\Gamma_i^0} H_i^{A\lambda} \bar{t}_i^0 d\Gamma_0 + \delta d_{A\lambda} \int_{\Omega_0} H_i^{A\lambda} \rho_0 b_i d\Omega_0 \\ &= \delta d_{A\lambda} f_{A\lambda}^{\text{ext}} \end{aligned} \quad (5.72)$$

such that the external work is defined as

$$f_{A\lambda}^{\text{ext}} = \int_{\Gamma_i^0} H_i^{A\lambda} \bar{t}_i^0 d\Gamma_0 + \int_{\Omega_0} H_i^{A\lambda} \rho_0 b_i d\Omega_0 \quad (5.73)$$

Finally, the kinetic virtual work from (5.14) is

$$\begin{aligned} \delta W^{\text{kin}} &= \int_{\Omega_0} \delta u_i \rho_0 \ddot{u}_i d\Omega_0 \\ &= \delta d_{A\lambda} \left( \int_{\Omega_0} \rho_0 H_i^{A\lambda} H_i^{B\mu} d\Omega_0 \right) \Delta \ddot{d}_{B\mu} \\ &= \delta d_{A\lambda} M_{A\lambda B\mu} \Delta \ddot{d}_{B\mu} \end{aligned} \quad (5.74)$$

such that the mass matrix is defined as

$$M_{A\lambda B\mu} = \int_{\Omega_0} \rho_0 H_i^{A\lambda} H_i^{B\mu} d\Omega_0 \quad (5.75)$$

and the assumption that  $\ddot{u}_i = H_i^{A\chi} \Delta \ddot{d}_{A\chi}$  is due to the fact that the actual acceleration is complicated due to the shell kinematics, which is discussed by Man in [3]. In the preceding equations,  $A$  and  $B$  are node numbers, and the indices  $i, k, m, I, J, K$ , and  $L = 1, 2, 3$  and  $\chi$  and  $\mu = 1, 2, 3, 4, 5$ .

### 5.6 Solution Algorithms

The following global system of equations is then established for a dynamic system:

$$\mathbf{f}^{\text{int}}(\mathbf{d}^*) + [\mathbf{K}^G(\mathbf{d}^*) + \mathbf{K}^M(\mathbf{d}^*)] \cdot \Delta \mathbf{d} = \mathbf{f}^{\text{ext}} - \mathbf{M} \cdot \ddot{\mathbf{d}} \quad (5.76)$$

where  $\mathbf{d}^*$  is the trial displacement,  $\Delta \mathbf{d}$  is the incremental displacement, and  $\ddot{\mathbf{d}}$  is the corresponding nodal acceleration. For quasi-static problems, the inertial term on the RHS can be neglected. The solution algorithms are discussed in great detail in [3] and are summarized here. Box 1 shows the algorithm that solves for the quasi-static displacement using Newton iterations. Newmark's method, used to solve dynamic problems, is shown in Box 2.

#### Box 5-1: Newton's Method

1. Initialize:  $n = 0$ ,  $\mathbf{d}^* = \mathbf{0}$
2. Solve for load/time increment  $n+1$ 
  - a. Initial trial displacement:  $\mathbf{d}^* = \mathbf{d}^n$
  - b. Calculate the residual:  $\mathbf{r} = \mathbf{f}^{\text{int}}(\mathbf{d}^*) - \mathbf{f}^{\text{ext}}$
  - c. Calculate the tangential stiffness matrix:  $\mathbf{K}(\mathbf{d}^*)$
  - d. Calculate the incremental displacement:  $\Delta \mathbf{d} = -\mathbf{K}(\mathbf{d}^*)^{-1} \cdot \mathbf{r}$
  - e. Update the trial displacement:  $\mathbf{d}^* = \mathbf{d}^* + \Delta \mathbf{d}$
  - f. Check for convergence:
    - i. Update residual:  $\mathbf{r} = \mathbf{f}^{\text{int}}(\mathbf{d}^*) - \mathbf{f}^{\text{ext}}$
    - ii. If  $|\mathbf{r}(\mathbf{d}^*)| \geq RTOL$  then go to 2(c)
3. Update final displacement:  $\mathbf{d}^{n+1} = \mathbf{d}^*$

## Box 5-1: Continued

4. Set  $n = n+1$  and go to 2

## Box 5-2: Newmark's Method

1. Initialize: set  $n = 0$  and state  $\mathbf{d}^0, \mathbf{v}^0$  and  $\mathbf{a}^0$
  2. Solve for load/time increment  $n+1$ 
    - a. Form predictors:
 
$$\mathbf{a}^* = 0$$

$$\mathbf{v}^* = \mathbf{v}^n + (1 - \alpha)\Delta t \mathbf{a}^n + \alpha \Delta t^2 \mathbf{a}^*$$

$$\mathbf{d}^* = \mathbf{d}^n + \Delta t \mathbf{v}^n + (1 - 2\beta)\frac{\Delta t^2}{2} \mathbf{a}^n + \beta \Delta t^2 \mathbf{a}^*$$
    - b. Calculate the residual:
 
$$\tilde{\mathbf{r}}^* = \mathbf{f}^{\text{ext}} - \mathbf{f}^{\text{int}}(\mathbf{d}^*) - \mathbf{M} \cdot \mathbf{a}^* - a\mathbf{M} \cdot \mathbf{v}^* - b\mathbf{K}_M(\mathbf{d}^n) \cdot \mathbf{v}^*$$
    - c. Calculate the tangential stiffness matrix:
 
$$\tilde{\mathbf{K}}^* = \mathbf{M} + \beta \Delta t^2 \mathbf{K}(\mathbf{d}^*) + \alpha \Delta t a \mathbf{M} + \alpha \Delta t b \mathbf{K}_M(\mathbf{d}^n)$$
    - d. Calculate the incremental displacement:  $\Delta \mathbf{a} = -(\tilde{\mathbf{K}}^*)^{-1} \cdot \tilde{\mathbf{r}}^*$
    - e. Update the predictors:
 
$$\mathbf{a}^* = \mathbf{a}^* + \Delta \mathbf{a}; \mathbf{v}^* = \mathbf{v}^* + \alpha \Delta t \Delta \mathbf{a}; \mathbf{d}^* = \mathbf{d}^* + \beta \Delta t^2 \Delta \mathbf{a}$$
    - f. Check for convergence:
      - i. Update residual:  $\tilde{\mathbf{r}}^*$
      - ii. If  $|\tilde{\mathbf{r}}^*| \geq RTOL$  then go to 2(c)
  3. Update incremental solution:  $\mathbf{a}^{n+1} = \mathbf{a}^*; \mathbf{v}^{n+1} = \mathbf{v}^*; \mathbf{d}^{n+1} = \mathbf{d}^*$
  4. Set  $n = n+1$  and go to 2
- 
- $\alpha$  and  $\beta$  are Newmark's parameters, and  $a$  and  $b$  are coefficients from the damping matrix:  $\mathbf{C} = a\mathbf{M} + b\mathbf{K}_M(\mathbf{d}^n)$  as discussed in [3].

## CHAPTER 6. INCREMENTAL CONSTITUTIVE MODEL FOR FABRICS

The behavior of woven clothing and its relationship with a digital human model is quite complex. Areas of contact such as the knees, elbows, and the backside cause fabric to experience high strains where the deformation is highly anisotropic, hysteretic and nonlinear. Here, we use large deformation continuum mechanics to describe the kinetics and kinematics required for a finite element analysis. From a macroscopic perspective, there are two levels of motion that occur: (1) rigid body translations and rotations of the clothing due to the human model being able to move in the global reference frame; and (2) deformation of the clothing due to gravity, applied loads and the process of conforming to the moving body. The two levels of motion are demonstrated in Figure 6-1, where an element on an initially straight cylindrical sleeve of clothing, shown on the left, has a local coordinate system with one particular orientation to that of the global coordinate system and, shown on the right, the same element has rotated and deformed so that the current local coordinate system now has a different orientation with respect to the global coordinate system. The strain tensor at a point in the element is computed using the deformation. The corresponding stress is a nonlinear function of the strain. In this chapter, an anisotropic constitutive model featuring incremental loading and unloading is developed to model the fabric behavior.

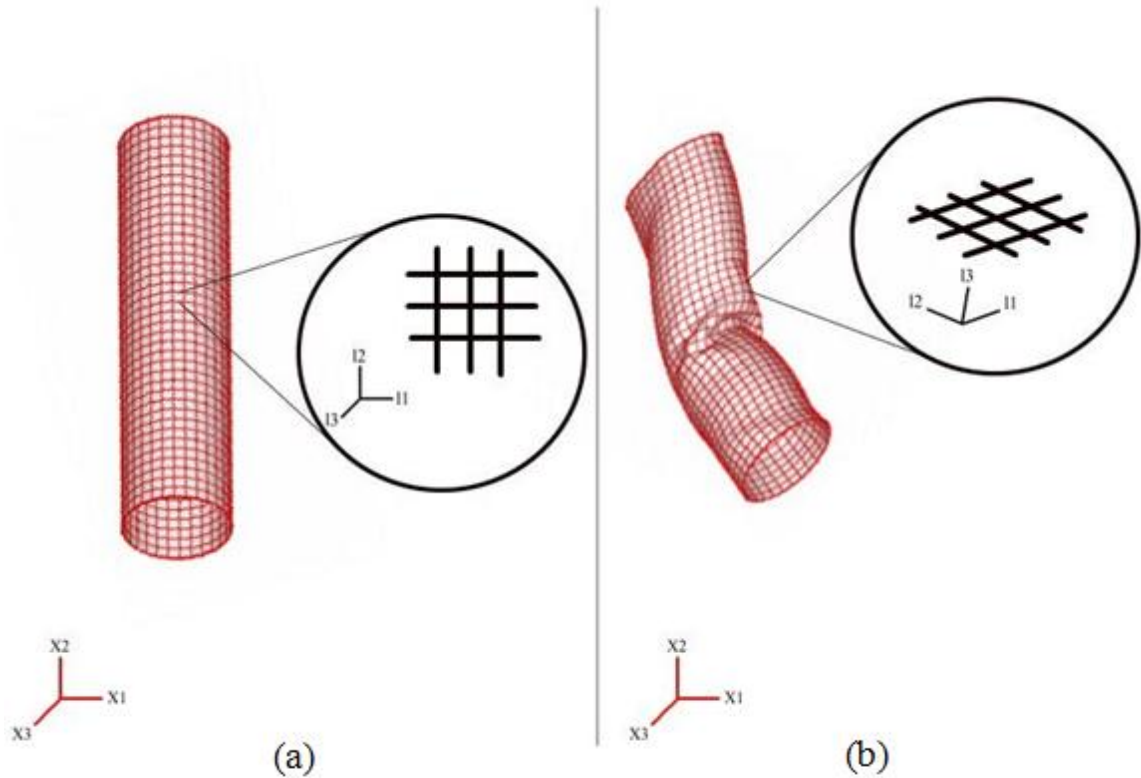


Figure 6-1. Model of a sleeve at (a) the original configuration and (b) the current configuration in relation to a global coordinate Cartesian coordinate system.

### 6.1 Initial Computations

The model is derived using a Lagrangian description of motion at each point in the continuum fabric model. The reference and current configurations are denoted as  $X_I$  and  $x_j$ , respectively. Using the shell kinematics from the previous chapter, an incremental trial displacement,  $(u_i^{n+1})^{trial}$  at the current  $(n+1)^{th}$  load/time step is used to compute the current configuration of the shell. From this updated configuration, the deformation gradient at each integration point is calculated with respect to the lamina coordinate system by

$$F_{ij}^{n+1} = \frac{\partial (u_i^{n+1})^{trial}}{\partial X_j} + \delta_{ij}. \quad (6.1)$$

The deformation gradient is used to calculate the right Cauchy-Green deformation tensor at the point as

$$C_{IJ}^{n+1} = F_{iI}^{n+1} F_{kJ}^{n+1} ; \quad (6.2)$$

from which the current and incremental Green-Lagrange strain tensors are calculated, respectively, as

$$E_{IJ}^{n+1} = \frac{1}{2} (C_{IJ}^{n+1} - \delta_{IJ}) \quad (6.3)$$

$$\Delta E_{IJ}^{n+1} = E_{IJ}^{n+1} - E_{IJ}^n . \quad (6.4)$$

It is noted here that the commonly used symbol for the right Cauchy-Green deformation tensor,  $\mathbf{C}$ , is also often used to denote the stiffness modulus in the mechanics literature. Care is taken to make clear in which context the symbol  $\mathbf{C}$  is used.

## 6.2 Global to Material Frame Transformations

It is assumed that at the  $n^{\text{th}}$  equilibrium configuration of the model, the strain in the lamina coordinate system  $\mathbf{E}^n$ , the stress in the material coordinate system  $\hat{\mathbf{S}}^n$ , maximum values of yarn stretch ratios,  $\lambda_{warp}^{\max}$  and  $\lambda_{weft}^{\max}$ , a shear strain correction term in the material coordinate system  $\hat{E}_5^*$ , and a state variable used to determine the form of the shear modulus  $|\hat{E}_5^{n+1} - \hat{E}_5^*|^{peak}$  are known at each integration point. The previous stress and strain tensors are referenced to the local lamina coordinate system of the shell element in which the point resides. In the original configuration (i.e. the  $0^{\text{th}}$  configuration), the warp and weft material directors, assumed to be orthogonal, may have any orientation with respect to the lamina coordinates in the plane of the shell element as shown in Figure 6-2.

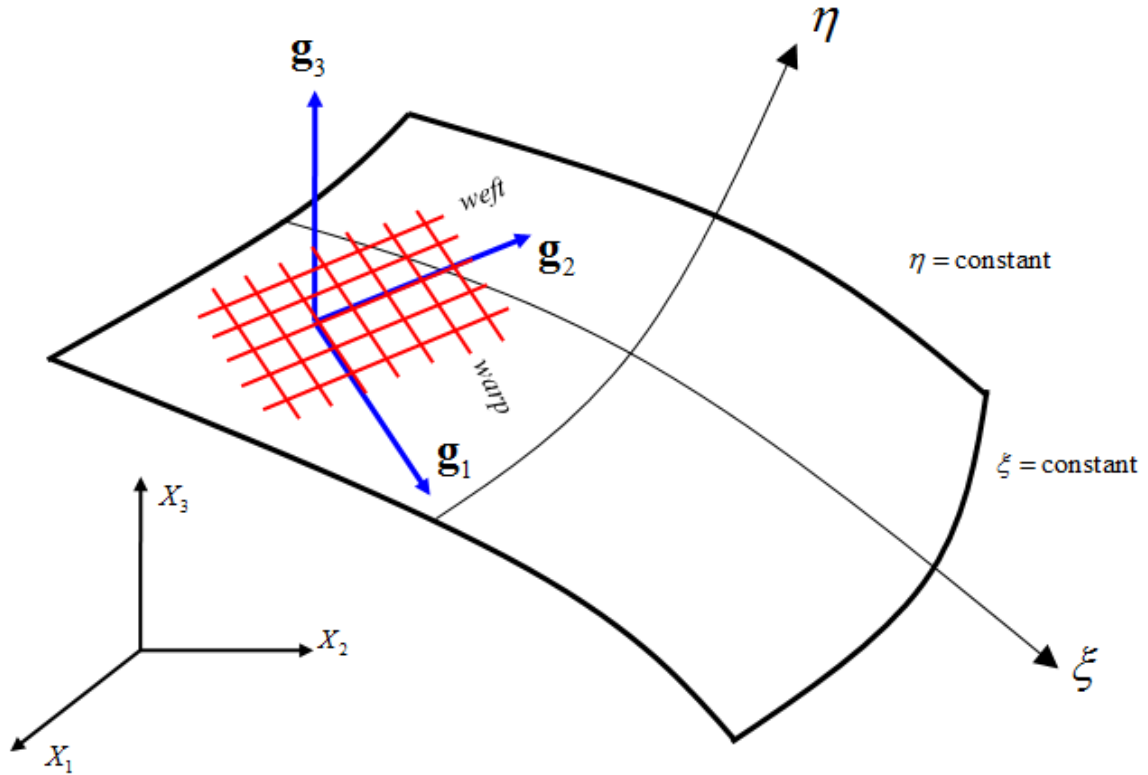


Figure 6-2. General orientation of the warp and weft material directors  $\mathbf{g}_1$ ,  $\mathbf{g}_2$ , and  $\mathbf{g}_3$  relative to the lamina coordinates of the shell element.

An orthogonal transformation matrix  $\mathbf{Q}$  is constructed using the direction cosines between the lamina and material coordinate systems in the original configuration as

$$\begin{aligned} Q_{IJ} &= \cos(x_I^{lam}, x_J^{mat}) \\ &= \begin{bmatrix} Q_{11} & Q_{12} & Q_{13} \\ Q_{21} & Q_{22} & Q_{23} \\ Q_{31} & Q_{32} & Q_{33} \end{bmatrix} \end{aligned} \quad (6.5)$$

In what follows, tensors that are referenced to the material coordinate system will be designated with a '^'; whereas, corresponding tensors in the lamina coordinate system will not. The  $(n+1)^{\text{th}}$  current and incremental strain tensors in the lamina coordinate system are transformed to the material coordinate system as

$$\hat{\mathbf{E}}_{IJ}^{n+1} = Q_{KI} Q_{LJ} \mathbf{E}_{KL}^{n+1} \quad (6.6)$$



$$\Delta \hat{E}_{IJ}^{n+1} = Q_{KI} Q_{LJ} \Delta E_{KL}^{n+1}. \quad (6.7)$$

For use with the finite element equations, it is advantageous to convert the strain and stress tensors to vectors, respectively, using Voigt notation. The Voigt notation for the stress and strain tensors for the degenerated shell element is, respectively,

$$\begin{Bmatrix} S_1 \\ S_2 \\ S_3 \\ S_4 \\ S_5 \end{Bmatrix} = \begin{Bmatrix} S_{11} \\ S_{22} \\ S_{23} \\ S_{13} \\ S_{12} \end{Bmatrix} \text{ and } \begin{Bmatrix} E_1 \\ E_2 \\ E_3 \\ E_4 \\ E_5 \end{Bmatrix} = \begin{Bmatrix} E_{11} \\ E_{22} \\ 2E_{23} \\ 2E_{13} \\ 2E_{12} \end{Bmatrix}. \quad (6.8)$$

The stress and strain vectors are length five due to the vanishing normal stress,  $S_{33}$ . For clarification, it is possible to compute the through-thickness strain,  $E_{33}$ , but at this time, it is not used in the shell kinematics. On the other hand, for computations requiring the strain and stress to be in tensor form, such as transformations, the strain and stress tensors are recovered as

$$\begin{bmatrix} S_{11} & S_{12} & S_{13} \\ S_{21} & S_{22} & S_{23} \\ S_{31} & S_{32} & S_{33} \end{bmatrix} = \begin{bmatrix} S_1 & S_5 & S_4 \\ S_5 & S_2 & S_3 \\ S_4 & S_3 & 0 \end{bmatrix} \text{ and } \begin{bmatrix} E_{11} & E_{12} & E_{13} \\ E_{21} & E_{22} & E_{23} \\ E_{31} & E_{32} & E_{33} \end{bmatrix} = \begin{bmatrix} E_1 & \frac{E_5}{2} & \frac{E_4}{2} \\ \frac{E_5}{2} & E_2 & \frac{E_3}{2} \\ \frac{E_4}{2} & \frac{E_3}{2} & 0 \end{bmatrix}. \quad (6.8)$$

The derivation in the rest of this chapter will use Voigt notation unless otherwise noted.

### 6.3 Construction of Moduli

Once the strain tensors are referenced with respect to the material coordinates, the challenge is to construct a tangent stiffness matrix,  $\hat{\mathbf{C}}^{n+1}$ , for the fabric that accounts for the nonlinear, anisotropic and hysteretic behavior. The general form for the condensed stiffness matrix used for the incremental constitutive model shown in (5.69) is

$$\hat{\mathbf{C}}^{n+1} = \begin{bmatrix} \hat{C}_{11}^{n+1} & \hat{C}_{12}^{n+1} & \hat{C}_{13}^{n+1} & \hat{C}_{14}^{n+1} & \hat{C}_{15}^{n+1} \\ \hat{C}_{21}^{n+1} & \hat{C}_{22}^{n+1} & \hat{C}_{23}^{n+1} & \hat{C}_{24}^{n+1} & \hat{C}_{25}^{n+1} \\ \hat{C}_{31}^{n+1} & \hat{C}_{32}^{n+1} & \hat{C}_{33}^{n+1} & \hat{C}_{34}^{n+1} & \hat{C}_{35}^{n+1} \\ \hat{C}_{41}^{n+1} & \hat{C}_{42}^{n+1} & \hat{C}_{43}^{n+1} & \hat{C}_{44}^{n+1} & \hat{C}_{45}^{n+1} \\ \hat{C}_{51}^{n+1} & \hat{C}_{52}^{n+1} & \hat{C}_{53}^{n+1} & \hat{C}_{54}^{n+1} & \hat{C}_{55}^{n+1} \end{bmatrix}. \quad (6.9)$$

We assume that the material behaves as a nonlinear anisotropic material, so that the number of nonzero components is reduced to

$$\hat{\mathbf{C}}^{n+1} = \begin{bmatrix} \hat{C}_{11}^{n+1} & \hat{C}_{12}^{n+1} & 0 & 0 & 0 \\ \hat{C}_{21}^{n+1} & \hat{C}_{22}^{n+1} & 0 & 0 & 0 \\ 0 & 0 & \hat{C}_{33}^{n+1} & 0 & 0 \\ 0 & 0 & 0 & \hat{C}_{44}^{n+1} & 0 \\ 0 & 0 & 0 & 0 & \hat{C}_{55}^{n+1} \end{bmatrix}. \quad (6.10)$$

The individual components of (6.10) are explicitly stated as

$$\hat{\mathbf{C}}^{n+1} = \begin{bmatrix} \frac{\hat{D}_1^{n+1}}{1 - \nu_{12}\nu_{21}} & \frac{\nu_{21}\hat{D}_1^{n+1}}{1 - \nu_{12}\nu_{21}} & 0 & 0 & 0 \\ \frac{\nu_{12}\hat{D}_2^{n+1}}{1 - \nu_{12}\nu_{21}} & \frac{\hat{D}_2^{n+1}}{1 - \nu_{12}\nu_{21}} & 0 & 0 & 0 \\ 0 & 0 & \hat{G}_{23}^{n+1} & 0 & 0 \\ 0 & 0 & 0 & \hat{G}_{13}^{n+1} & 0 \\ 0 & 0 & 0 & 0 & \hat{G}_{12}^{n+1} \end{bmatrix}, \quad (6.11)$$

where, for the current time-step,  $\hat{D}_i^{n+1}$  ( $i = 1, 2$ ) are the elastic moduli in the warp and weft directions, respectively,  $\hat{G}_{12}^{n+1}$  is the in-plane shear modulus,  $\hat{G}_{23}^{n+1}$  and  $\hat{G}_{13}^{n+1}$  are the transverse shear moduli, and  $\nu_{12}$  and  $\nu_{21}$  are the Poisson's ratios. The construction of the moduli in (6.11) that will produce the nonlinear and anisotropic behavior is discussed in the following subsections.

### 6.3.1 Axial Moduli

In order to produce nonlinear loading and hysteresis, the elastic loading moduli in the warp and weft directions are functions of the current Green-Lagrange strain in the material coordinate system for each respective yarn and state variables that determine if a

yarn direction is in tension or compression and loading or unloading. The stretch ratios in the warp and weft directions are used in order to define when a particular yarn at a quadrature point is in a state of loading or unloading. The current stretch ratios in the warp and weft yarn directions are defined as

$$\lambda_{warp}^{n+1} = \sqrt{1 + 2(\hat{E}_1)^{n+1}} \quad (6.12)$$

$$\lambda_{weft}^{n+1} = \sqrt{1 + 2(\hat{E}_2)^{n+1}} \quad (6.13)$$

With respect to the yarn direction, the fabric is said to be in a state of compression when the respective stretch ratio is less than 1.00 and in a state of tension when the stretch ratio is greater to or equal to 1.00. To induce the hysteretic effects, the stretch ratios are compared to the maximum value each has experienced:  $\lambda_{warp}^{\max}$  and  $\lambda_{weft}^{\max}$ ; which are both initially set to 1.00.

When a particular yarn direction is subjected to a tensile load and the stretch ratio is larger than its previous maximum value, it is proposed that the elastic loading modulus in the corresponding direction be a function of the current state of strain by using a polynomial fit of the experimental data presented in Chapter 3. The stress in the warp (1) and weft (2) directions are related to their respective strains (in tensor notation) by

$$\hat{S}_{11} = a(\hat{E}_{11})^4 + b(\hat{E}_{11})^3 + c(\hat{E}_{11})^2 + d(\hat{E}_{11}) + e \quad (6.14)$$

$$\hat{S}_{22} = f(\hat{E}_{22})^4 + g(\hat{E}_{22})^3 + h(\hat{E}_{22})^2 + k(\hat{E}_{22}) + l \quad (6.15)$$

By taking the derivative of each stress component by the respective strain, we are able to determine the corresponding loading moduli at the current time-step as

$$\hat{D}_1^{n+1} = \frac{d\hat{S}_{11}}{d\hat{E}_{11}} = 4a(\hat{E}_{11})^3 + 3b(\hat{E}_{11})^2 + 2c(\hat{E}_{11}) + d \quad (6.16)$$

$$\hat{D}_2^{n+1} = \frac{d\hat{S}_{22}}{d\hat{E}_{22}} = 4f(\hat{E}_{22})^3 + 3g(\hat{E}_{22})^2 + 2h(\hat{E}_{22}) + k \quad (6.17)$$

Additional adjustments to the warp and weft moduli must be made when either the warp or weft yarn is in compression ( $\lambda_i^{n+1} < 0$ ) or when it is being unloaded or reloaded ( $\lambda_i^{n+1} < \lambda_i^{\max}$ ). When either yarn is in compression, it buckles almost immediately. Therefore, the elastic moduli are set to the initial moduli when the respective strain is zero.

$$\hat{D}_1^{n+1} = d \quad (6.18)$$

$$\hat{D}_2^{n+1} = k \quad (6.19)$$

When the current stretch ratio is less than the maximum and greater than zero (see Figure 3-18), the associated yarn direction is in a state of either unloading or reloading. The behavior of fabrics shows a much stiffer response in this case and the corresponding unloading modulus is determined by fitting a linear trend line through the first three points upon unload from the experimental data (Figures 3-13 through 3-16) as

$$\hat{D}_1^{n+1} = \hat{D}_1^{\text{unload}} \quad (6.20)$$

$$\hat{D}_2^{n+1} = \hat{D}_2^{\text{unload}} \quad (6.21)$$

One issue that arises in the model is that when a fabric transitions from a state of loading to a state of unloading, the elastic modulus is discontinuous. This is addressed by using a linear interpolation between the unload modulus and the previous loading modulus when  $\lambda_i^{n+1} \geq 0.999\lambda_i^{\max}$ . The diagonal in-plane components of the stiffness matrix can now be constructed as

$$\hat{C}_{11}^{n+1} = \frac{\hat{D}_1^{n+1}}{1 - \nu_{12}\nu_{21}} \quad (6.22)$$

$$\hat{C}_{22}^{n+1} = \frac{\hat{D}_2^{n+1}}{1 - \nu_{12}\nu_{21}} \quad (6.23)$$

Justification of equations (6.20) and (6.21) is based upon the following assumption: when a material is loaded in uniaxial tension and then unloaded, no matter

the presence of residual strain, the slope of the stress-strain curve upon unloading is assumed to be the elastic modulus of the material. Acknowledging the complex interaction between the fibers and yarns that make up woven fabric, we take the unloading slope to be the theoretical elastic modulus of the fabric in terms of warp, weft, and shear. When the fabric is in a state of being loaded, the yarns are either trying to straighten out or rotate. We assume that, for a particular load (i.e. uniaxial tension, shear), if the fabric were to continually decrimp, the loading modulus would approach the unloading modulus. However, as can be seen in Figures 3-9 through 3-12, this will never be case because the fabric will either begins to yield, exhibiting elastoplastic behavior, or fail.

### 6.3.2 Off-diagonal Moduli

By definition, an orthotropic stiffness matrix is symmetric. However, for fabrics, the deformation includes both material and geometric behavior, which means that, in general, the transverse behavior associated with the off-diagonal terms is not the same when loaded in the warp and weft directions. As an example, the loading moduli of representative samples for the warp and weft monotonic tests of cotton-polyester blend were approximated using a quadratic fit. Assuming constant warp and weft Poisson's ratios (discussed in detail in section 3.3.3), the off-diagonal components of the stiffness matrix,  $\hat{C}_{21}^{n+1}$  and  $\hat{C}_{12}^{n+1}$  were estimated and plotted against one another as a function of axial strain as shown in Figure 6-3. It is clear that the two lines do not lie upon one another as they would if they were truly symmetric. Further, if one or both the yarn directions were in a state of unloading, where the stiffness is much higher and assumed to be linear, the disparity could be even greater. Therefore, we allow the incremental stiffness tensor to be non-symmetric with the off-diagonal terms defined as

$$\begin{aligned}\hat{C}_{12}^{n+1} &= \nu_{21}\hat{C}_{11}^{n+1} \\ \hat{C}_{21}^{n+1} &= \nu_{12}\hat{C}_{22}^{n+1}\end{aligned}\tag{6.24}$$

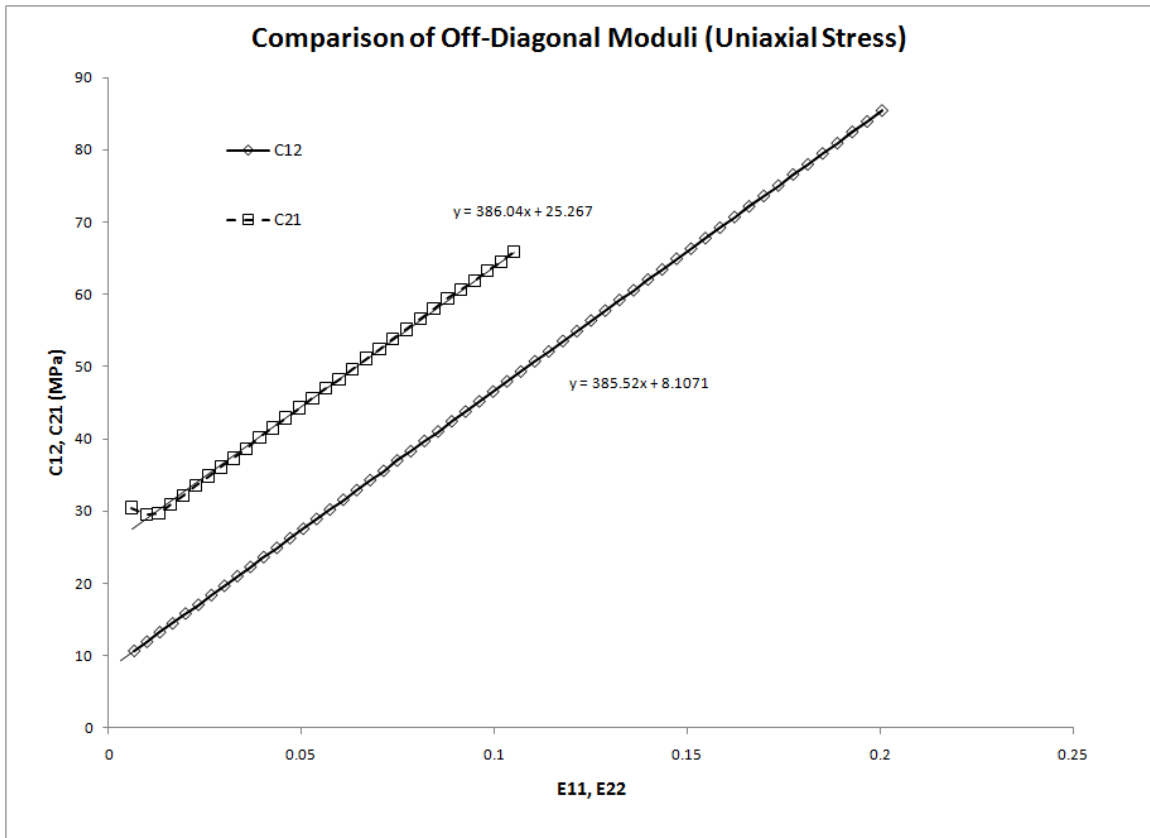


Figure 6-3. Comparison of  $\hat{C}_{21}^{n+1}$  and  $\hat{C}_{12}^{n+1}$  for cotton-polyester blend subjected to monotonic loading (uniaxial stress) using curve fit.

### 6.3.3 Shear Moduli

Like the axial behavior, shear behavior exhibits nonlinear loading and hysteresis. Additionally, fabrics are susceptible to cycles where stresses and strains may be positive and/or negative, as shown in Figure 6-4. In order to approximate this behavior in the model, the in-plane shear modulus is constructed in a manner similar to the elastic moduli, where the nonlinear loading shear modulus is computed from a polynomial fit of the shear stress:

$$\hat{S}_{12} = m(2\hat{E}_{12})^4 + n(2\hat{E}_{12})^3 + p(2\hat{E}_{12})^2 + q(2\hat{E}_{12}) + r \quad (6.25)$$

$$\hat{G}_{12}^{n+1} = \frac{d\hat{S}_{12}}{d2\hat{E}_{12}} = 4m(2\hat{E}_{12})^3 + 3n(2\hat{E}_{12})^2 + 2p(2\hat{E}_{12}) + q \quad (6.26)$$

and the unloading modulus to induce hysteresis is a linear approximation of the unloading behavior shown in Figures 3-28 through 3-31:

$$\hat{G}_{12}^{n+1} = \hat{G}_{12}^{unload} \quad (6.27)$$

The challenge here is to determine which modulus is appropriate for the current state of strain. First, the previous in-plane shear stress is multiplied by the current shear strain increment ( $\hat{S}_5^n \cdot \Delta\hat{E}_5^{n+1}$ ). If this product is positive, then there is a loading condition; otherwise, it is in a state of unloading. Further, if there is a state of loading, it must be determined if it is in “virgin” territory, where the behavior is nonlinear, or if it is being reloaded with a linear assumption. This is accomplished by an additional state variable:

$$SV = |\hat{E}_5^{n+1} - \hat{E}_5^*| \quad (6.28)$$

The value  $\hat{E}_5^*$  (initially set to zero) is used to determine the relative shear strain so that the behavior may become nonlinear whenever the sign of the shear stress changes during any cyclic loadings. The state variable in (6.28) is then the magnitude of the current relative shear strain. If  $SV$  is greater than the peak value for that particular cycle, then nonlinear loading is taking place; otherwise, the fabric is reloading with the constant modulus (6.27). When the state of loading/unloading/reloading is determined, the in-plane shear component of the stiffness matrix is then defined as

$$\hat{C}_{55}^{n+1} = \hat{G}_{12}^{n+1} \quad (6.29)$$

For out-of-plane bending, parameters have yet to be experimentally determined.

Therefore, the transverse shear moduli are estimated in accordance with Timoshenko beam theory using a correction factor of 5/6 so that:

$$\hat{C}_{33}^{n+1} = \hat{C}_{44}^{n+1} = \frac{5}{6} \hat{G}_{12}^{n+1} \quad (6.30)$$

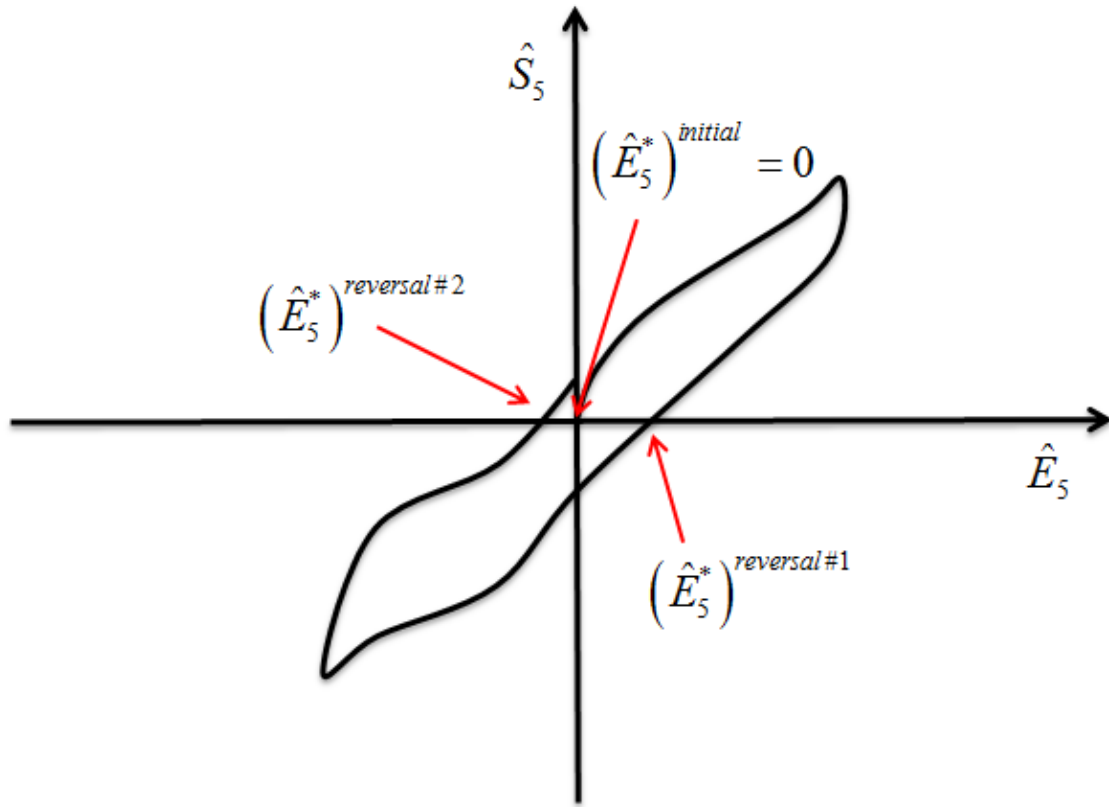


Figure 6-4. Typical fabric behavior due to shear and different locations of values of  $\hat{E}_5^*$  depending on the cyclic loading.

#### 6.4 Stress Update

Once the current stiffness matrix is constructed, the current stress is calculated as

$$\hat{S}_I^{n+1} = \hat{S}_I^{n+1} + \hat{C}_{II}^{n+1} : \Delta \hat{E}_J^{n+1} \quad (6.31)$$



$$\begin{Bmatrix} \hat{S}_1^{n+1} \\ \hat{S}_2^{n+1} \\ \hat{S}_3^{n+1} \\ \hat{S}_4^{n+1} \\ \hat{S}_5^{n+1} \end{Bmatrix} = \begin{Bmatrix} \hat{S}_1^n \\ \hat{S}_2^n \\ \hat{S}_3^n \\ \hat{S}_4^n \\ \hat{S}_5^n \end{Bmatrix} + \begin{bmatrix} \hat{C}_{11}^{n+1} & \hat{C}_{12}^{n+1} & 0 & 0 & 0 \\ \hat{C}_{21}^{n+1} & \hat{C}_{22}^{n+1} & 0 & 0 & 0 \\ 0 & 0 & \hat{C}_{33}^{n+1} & 0 & 0 \\ 0 & 0 & 0 & \hat{C}_{44}^{n+1} & 0 \\ 0 & 0 & 0 & 0 & \hat{C}_{55}^{n+1} \end{bmatrix} \begin{Bmatrix} \hat{E}_1^{n+1} \\ \hat{E}_2^{n+1} \\ 2\hat{E}_3^{n+1} \\ 2\hat{E}_4^{n+1} \\ 2\hat{E}_5^{n+1} \end{Bmatrix}. \quad (6.32)$$

As mentioned in the previous section, when the fabric is subjected to cyclic shear loadings, we assume that the behavior is nonlinear upon its initial loading. When the fabric is unloaded in shear, it is assumed that the behavior is linear until the sign of the shear stress changes. When that happens,  $\hat{E}_5^*$  is set to the current values of shear strain,  $\hat{E}_5^{n+1}$ ; and the peak value of SV is reset to zero for storage.

### 6.5 Material to Global Frame Transformations

As derived in Chapter 5, the material stiffness matrix,  $\mathbf{K}^m$ , is computed using the stiffness modulus. Since the model is incremental and nonlinear, the consistent tangent operator (6.33) is computed to increase computational speed by increasing the rate of convergence.

$$\left(\hat{\mathbf{C}}^{cons}\right)^{n+1} = \frac{d\hat{\mathbf{S}}^{n+1}}{d\hat{\mathbf{E}}^{n+1}} = \hat{\mathbf{C}}^{n+1} + \frac{d\hat{\mathbf{C}}^{n+1}}{d\hat{\mathbf{E}}^{n+1}} : \Delta\hat{\mathbf{E}}^{n+1} \quad (6.33)$$

The formulation of the finite element equations requires that the stress tensor and the tangent moduli be in the lamina coordinate system. Therefore, these values must be transformed from the material coordinate system back to the lamina coordinate system using the same transformation matrix,  $Q_{IJ}$ , as before. These transformations are computed as followed:

$$S_{IJ}^{n+1} = Q_{IK} Q_{JL} \hat{S}_{KL}^{n+1} \quad (6.34)$$

$$C_{IJKL}^{n+1} = Q_{IM} Q_{JN} Q_{KP} Q_{LQ} \hat{C}_{MNPQ}^{n+1} \quad (6.35)$$

## 6.6 Summary of Fabric Model

A simple constitutive model for the anisotropic, nonlinear and hysteretic behavior of woven fabrics has been presented. The algorithm for the fabric model described in the preceding sections is summarized in Box 2. The algorithm for the computation of the consistent tangent operator is summarized in Box 3.

Box 6-1: Algorithm for Fabric Model with Incremental Loading and Unloading

- In shell FEA subroutine
  - Read in  $\mathbf{E}^n$ ,  $\hat{\mathbf{S}}^n$ ,  $\lambda_{warp}^{\max}$ ,  $\lambda_{weft}^{\max}$ ,  $\hat{E}_5^*$ , and  $SV^{Peak}$  from storage
  - At  $(n+1)^{\text{th}}$  step:
    - Given a displacement,  $\mathbf{u}^{n+1}$
    - Compute deformation gradient:  $\mathbf{F}^{n+1} = \frac{\partial \mathbf{u}^{n+1}}{\partial \mathbf{X}} + \mathbf{1}$
    - Compute right Cauchy-Green deformation gradient:
 
$$\mathbf{C}^{n+1} = (\mathbf{F}^{n+1})^T \mathbf{F}^{n+1}$$
  - Send to fabric model:  $\mathbf{E}^n$ ,  $\hat{\mathbf{S}}^n$ ,  $\mathbf{C}^{n+1}$ ,  $\lambda_{warp}^{\max}$ ,  $\lambda_{weft}^{\max}$ ,  $\hat{E}_5^*$ , and  $SV^{Peak}$
- In fabric model subroutine
  - Compute the current Green-Lagrange strain:  $\mathbf{E}^{n+1} = \frac{1}{2}(\mathbf{C}^{n+1} - \mathbf{1})$
  - Compute the incremental strain:  $\Delta \mathbf{E}^{n+1} = \mathbf{E}^{n+1} - \mathbf{E}^n$
  - Transform the current and increment strain tensors from the lamina to the material coordinate system:
 
$$\hat{\mathbf{E}}^{n+1} = \mathbf{Q}^T \mathbf{E}^{n+1} \mathbf{Q}$$

$$\Delta \hat{\mathbf{E}}^{n+1} = \mathbf{Q}^T \Delta \mathbf{E}^{n+1} \mathbf{Q}$$
  - Compute stretches and state variables:
 
$$\lambda_{warp}^{n+1} = \sqrt{1 + 2(\hat{E}_1)^{n+1}}$$

$$\lambda_{weft}^{n+1} = \sqrt{1 + 2(\hat{E}_2)^{n+1}}$$

$$\hat{S}_5^n \cdot \Delta \hat{E}_5^{n+1}$$

$$SV = |\hat{E}_5^{n+1} - \hat{E}_5^*|$$

## Box 6-1: Continued

- Compute: the stiffness matrix  $\hat{\mathbf{C}}^{n+1}$  by equations (6.16) through (6.24), (6.26), (6.27), (6.29), and (6.30)
- Compute:  $\hat{\mathbf{S}}^{n+1} = \hat{\mathbf{S}}^n + \hat{\mathbf{C}}^{n+1} : \Delta \hat{\mathbf{E}}^{n+1}$
- Reset (if needed)  $\hat{E}_5^*$  and  $SV^{Peak}$
- Transform stress and tangent operator from material to lamina reference system:  

$$\mathbf{S}^{n+1} = \mathbf{Q} \hat{\mathbf{S}}^{n+1} \mathbf{Q}^T$$
- If computing the material stiffness,  $\mathbf{K}^m$ , need the consistent tangent operator in the lamina coordinate system:  

$$\left( \hat{\mathbf{C}}^{cons} \right)^{n+1} = \frac{d\hat{\mathbf{S}}^{n+1}}{d\hat{\mathbf{E}}^{n+1}} = \hat{\mathbf{C}}^{n+1} + \frac{d\hat{\mathbf{C}}^{n+1}}{d\hat{\mathbf{E}}^{n+1}} : \Delta \hat{\mathbf{E}}^{n+1}$$

$$\left( \mathbf{C}^{cons} \right)^{n+1} = \mathbf{Q}^T \mathbf{Q} \left( \hat{\mathbf{C}}^{cons} \right)^{n+1} \mathbf{Q}^T \mathbf{Q}$$
- If:
  - $\lambda_{warp}^{n+1} > \lambda_{warp}^{max} \Rightarrow \lambda_{warp}^{max} = \lambda_{warp}^{n+1}$
  - $\lambda_{weft}^{n+1} > \lambda_{weft}^{max} \Rightarrow \lambda_{weft}^{max} = \lambda_{weft}^{n+1}$
- Return to shell FEA subroutine:  $\mathbf{S}^{n+1}$ ,  $\hat{\mathbf{S}}^n$ ,  $\left( \mathbf{C}^{cons} \right)^{n+1}$ ,  $\lambda_{warp}^{max}$ ,  $\lambda_{weft}^{max}$ ,  $\hat{E}_5^*$ , and  $SV^{Peak}$
- In shell FEA subroutine
  - Set  $(\square)^n = (\square)^{n+1}$ , where  $(\square)$  are the strain and stress tensors returned from the model.
  - Store  $\mathbf{E}^n$ ,  $\hat{\mathbf{S}}^n$ ,  $\lambda_{warp}^{max}$ ,  $\lambda_{weft}^{max}$ ,  $\hat{E}_5^*$ , and  $SV^{Peak}$

## Box 6-2: Routine for the computation of consistent tangent operator

- Do l = 1, nstress
  - Do I = 1, 5
    - Do j = 1, 5
      - $\left( \hat{\mathbf{C}}_{ij}^{cons} \right)^{n+1} = \left( \hat{\mathbf{C}}_{ij} \right)^{n+1}$
    - Enddo
  - Enddo
  - If  $((\lambda_{warp}^{n+1} < \lambda_{warp}^{max}) \text{ AND } (\hat{E}_1^{n+1} > 0))$  Then

## Box 6-2: Continued

- $(\hat{C}_{11}^{cons})^{n+1} = (\hat{C}_{11})^{n+1} + (12a(\hat{E}_1^{n+1})^2 + 6b(\hat{E}_1^{n+1}) + 2c)\Delta\hat{E}_1^{n+1}$
- $(\hat{C}_{12}^{cons})^{n+1} = (\hat{C}_{12})^{n+1} + \nu_{21}(12a(\hat{E}_1^{n+1})^2 + 6b(\hat{E}_1^{n+1}) + 2c)\Delta\hat{E}_2^{n+1}$
- Endif
- If( $(\lambda_{weft}^{n+1} < \lambda_{weft}^{max})$  AND ( $\hat{E}_2^{n+1} > 0$ ))Then
  - $(\hat{C}_{22}^{cons})^{n+1} = (\hat{C}_{22})^{n+1} + (12f(\hat{E}_2^{n+1})^2 + 6g(\hat{E}_2^{n+1}) + 2h)\Delta\hat{E}_2^{n+1}$
  - $(\hat{C}_{21}^{cons})^{n+1} = (\hat{C}_{21})^{n+1} + \nu_{12}(12f(\hat{E}_2^{n+1})^2 + 6g(\hat{E}_2^{n+1}) + 2h)\Delta\hat{E}_1^{n+1}$
- Endif
- If(nonlinear shear loading)Then
  - $(\hat{C}_{55}^{cons})^{n+1} = (\hat{C}_{55})^{n+1} + (12m|\hat{E}_5^{n+1} - \hat{E}_5^*|^2 + 6n|\hat{E}_5^{n+1} - \hat{E}_5^*| + 2p)\Delta\hat{E}_5^{n+1}$
  - $(\hat{C}_{33}^{cons})^{n+1} = (\hat{C}_{44}^{cons})^{n+1} = \frac{5}{6}(\hat{C}_{55}^{cons})^{n+1}$
- Endif
- Enddo

## CHAPTER 7. MODEL VERIFICATION AND APPLICATIONS

In this chapter, the incremental constitutive model developed in the previous chapter is employed in a 3D bilinear continuum degenerated shell finite element. In section 7.1, trend lines are fit to the tensile and shear cyclic experimental data for the four fabrics in order to determine elastic and shear loading and unloading moduli. The material parameters for the blend, duck, muslin and denim fabrics are then summarized. Computational results for cyclic uniaxial stress in a variety of material orientations using the incremental constitutive model are compared to corresponding experimental data in section 7.2. The model is also applied in section 7.3 to some scenarios for which there were no experimental data with which to compare. These include: biaxial strain tests and dynamic drape and poke tests. Finally, the determination of material parameters and the computational results are discussed in section 7.4.

### 7.1 Material Parameters

#### 7.1.1 Axial Moduli

While typical warp and weft stress-strain data for fabrics features a nonlinear relationship, the linear elastic constitutive models mentioned in Chapter 4 typically use the initial slopes (at very small strain values) as the elastic moduli in the respective directions. Here, to capture the nonlinearity, the loading and unloading moduli in the principle (warp and weft) directions are based upon fitting curves to the representative experimental data from single-cycle uniaxial stress tests. Figures 7-1 through 7-4 show the fitting of the warp and weft data for cotton-polyester blend, cotton duck, cotton muslin, and cotton denim, respectively. In each case, either a quadratic or quartic polynomial, whichever ensures an initial positive modulus and is the best fit curve, is used to relate the stress and strain. The first derivatives of these functions are the elastic loading moduli as a function of total strain in the corresponding warp or weft direction.

The unloading modulus is determined by fitting a linear trend line through the first three data points upon unloading. Table 7.1 shows the corresponding loading and unloading moduli for the warp and weft directions. The average Poisson's ratios for the warp and weft directions found in section 3.3.3 and are listed in Table 7.2 along with the mass density for each fabric.

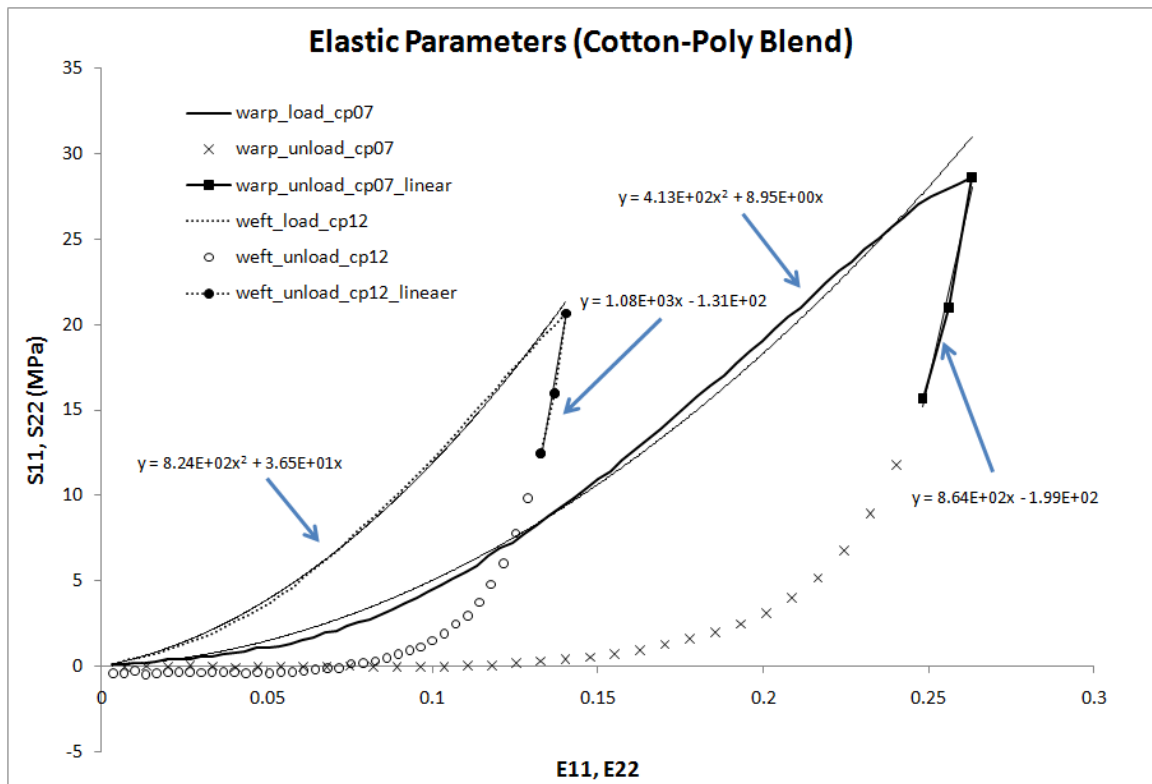


Figure 7-1. Curve fitting the loading and unloading behavior in order to determine tensile parameters in the warp and weft directions for cotton-polyester blend.

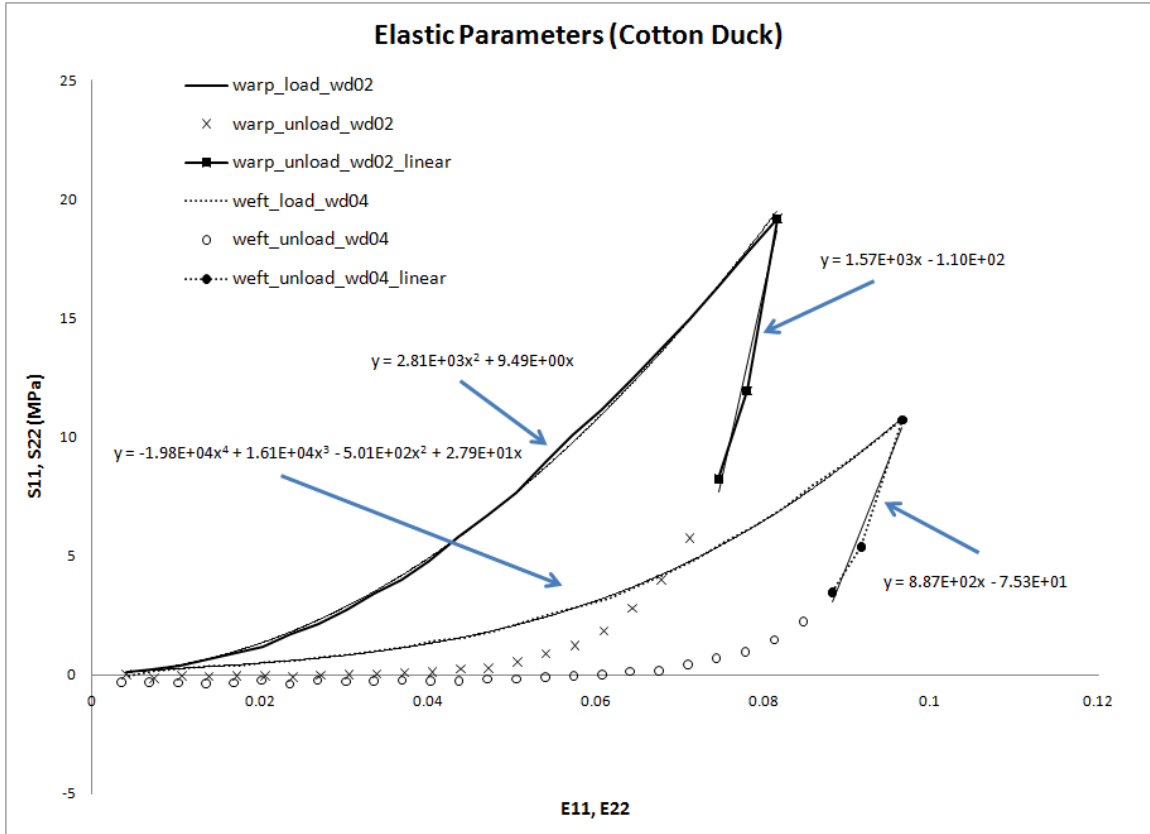


Figure 7-2. Curve fitting the loading and unloading behavior in order to determine tensile parameters in the warp and weft directions for cotton duck.

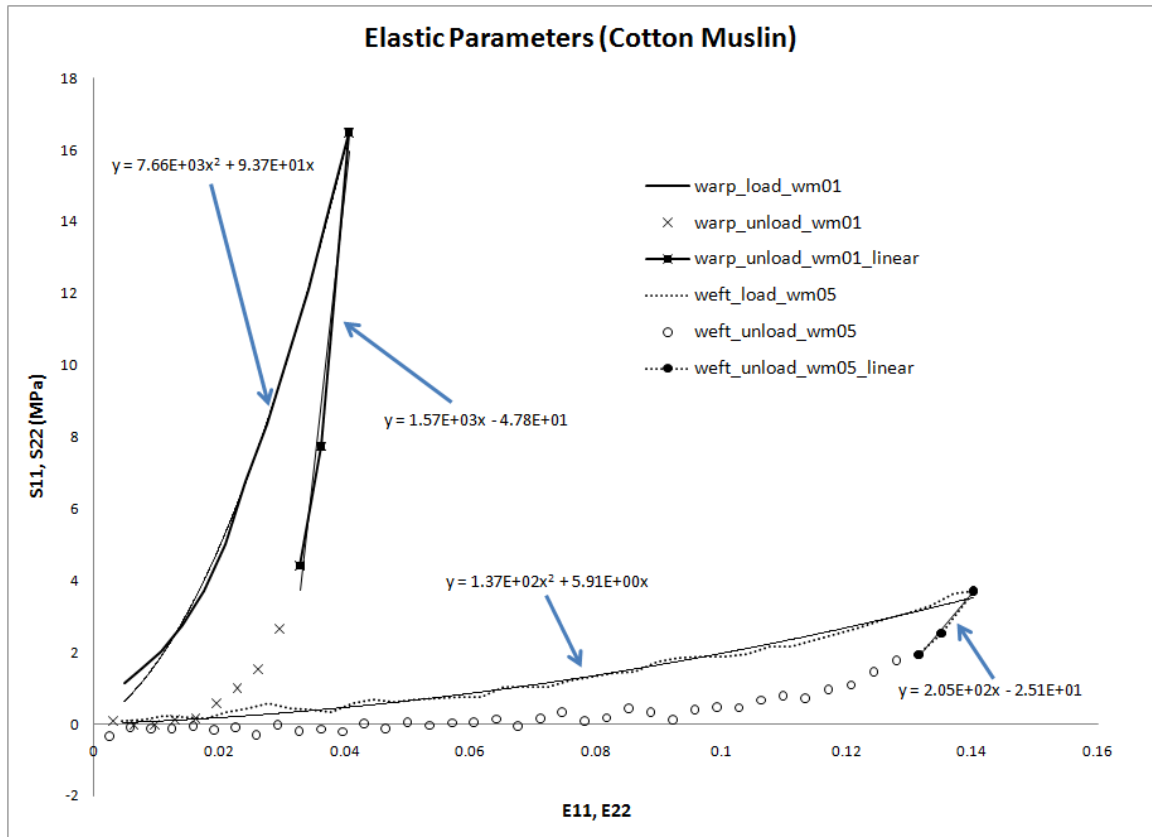


Figure 7-3. Curve fitting the loading and unloading behavior in order to determine tensile parameters in the warp and weft directions for cotton muslin.



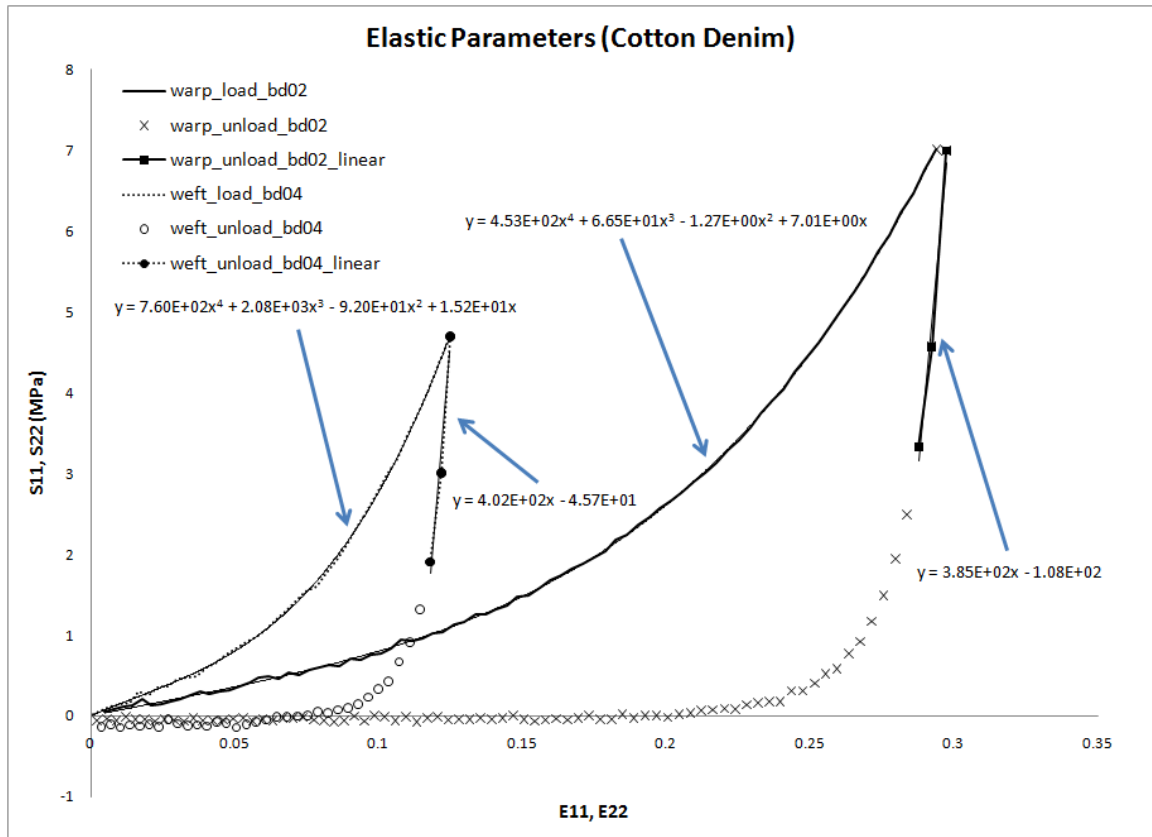


Figure 7-4. Curve fitting the loading and unloading behavior in order to determine tensile parameters in the warp and weft directions for cotton denim

Table 7.1. Tensile loading and unloading moduli for the four tested fabrics (tensor notation).

<i>Fabric</i>	$\hat{D}_1^{load} (MPa)$	$\hat{D}_1^{unload} (MPa)$	$\hat{D}_2^{load} (MPa)$	$\hat{D}_2^{unload} (MPa)$
C-P Blend	$8.26 \times 10^2 E_{11} + 8$	$8.64 \times 10^2$	$1.65 \times 10^3 E_{22} + 37$	$1.08 \times 10^3$
Cotton Duck	$5.62 \times 10^3 E_{11} + 9$	$1.57 \times 10^3$	$-7.92 \times 10^4 (E_{22})^3 + 4.83 \times 10^4 (E_{22})^2 - 1.00 \times 10^3 E_{22} + 28$	$8.87 \times 10^2$
Cotton Muslin	$1.53 \times 10^4 E_{11} + 9$	$1.57 \times 10^3$	$2.74 \times 10^2 E_{22} + 6$	$2.05 \times 10^2$
Cotton Denim	$1.81 \times 10^3 (E_{22})^3 - 2.00 \times 10^2 (E_{22})^2 + 3E_{22} + 7$	$3.85 \times 10^2$	$3.04 \times 10^3 (E_{22})^3 + 6.24 \times 10^3 (E_{22})^2 - 1.84 \times 10^2 E_{22} + 15$	$4.02 \times 10^2$

Table 7.2. Average Poisson's ratios and mass densities for the four tested fabrics.

<i>Fabric</i>	$\nu_{12}$	$\nu_{21}$	$\rho (kg/m^3)$
C-P Blend	0.25	0.42	590
Cotton Duck	0.99	0.68	470
Cotton Muslin	2.04	0.41	350
Cotton Denim	0.12	0.22	370

### 7.1.2 Shear Moduli

The in-plane shear moduli are determined using the shear stress and shear strain data, which themselves are calculated using results from the bias-45° tests. Nonlinearity is introduced by fitting a 4<sup>th</sup>-order polynomial curve to the loading shear stress-shear strain data and a linear trend line through the first few data points upon unloading .

Figures 7-5 through 7-8 show the fitting of the warp and weft data for cotton-polyester

blend, cotton duck, cotton muslin, and cotton denim, respectively. Table 7.3 shows the corresponding shear moduli, which are found by taking the first derivative of the shear stress with respect to the shear strain.

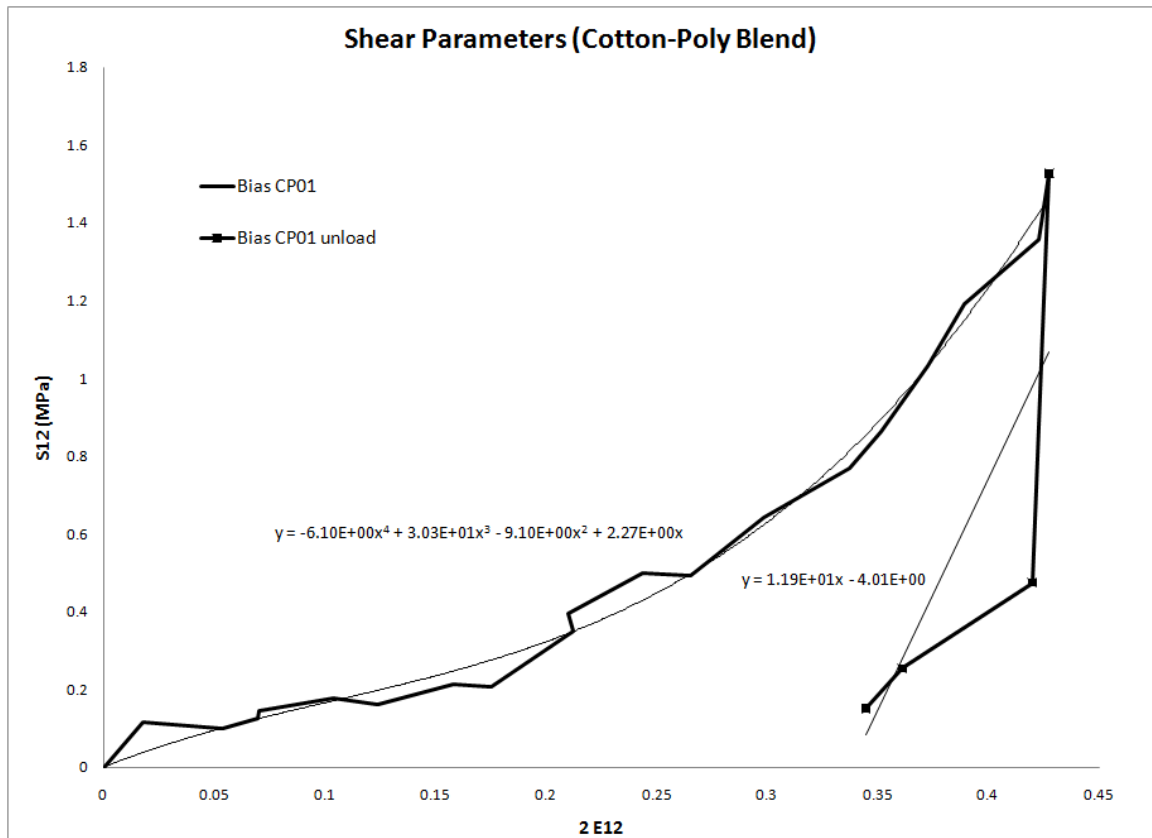


Figure 7-5. Curve fit of shear stress-strain data for loading and unloading behavior from representative cotton-polyester bias-45 test.

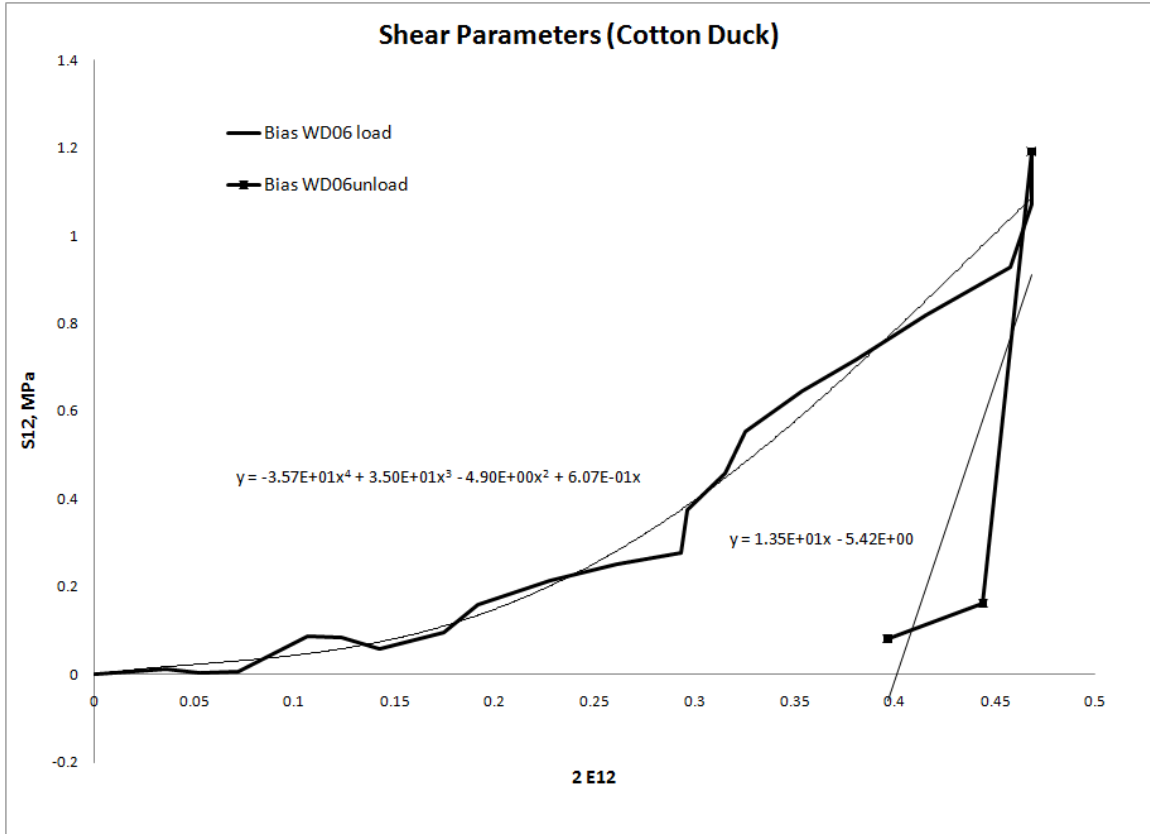


Figure 7-6. Curve fit of shear stress-strain data for loading and unloading behavior from representative cotton duck bias-45 test.

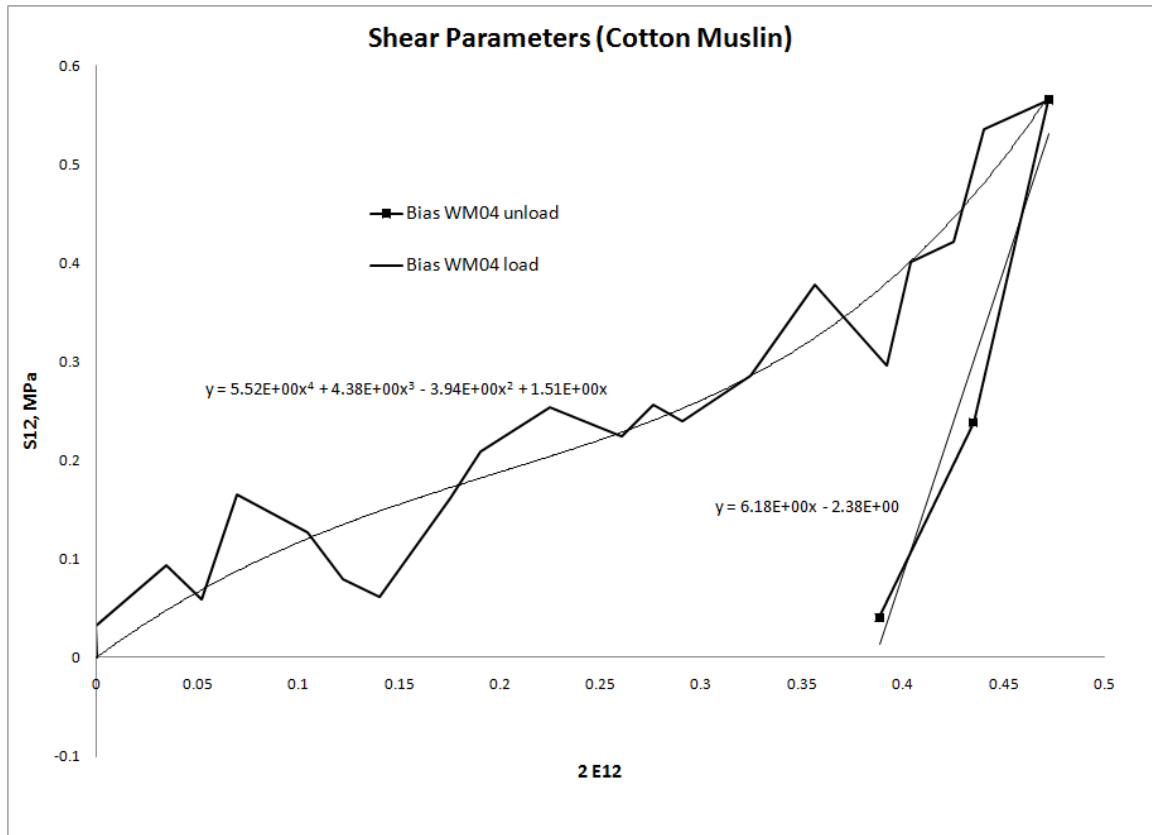


Figure 7-7. Curve fit of shear stress-strain data for loading and unloading behavior from representative cotton muslin bias-45 test.

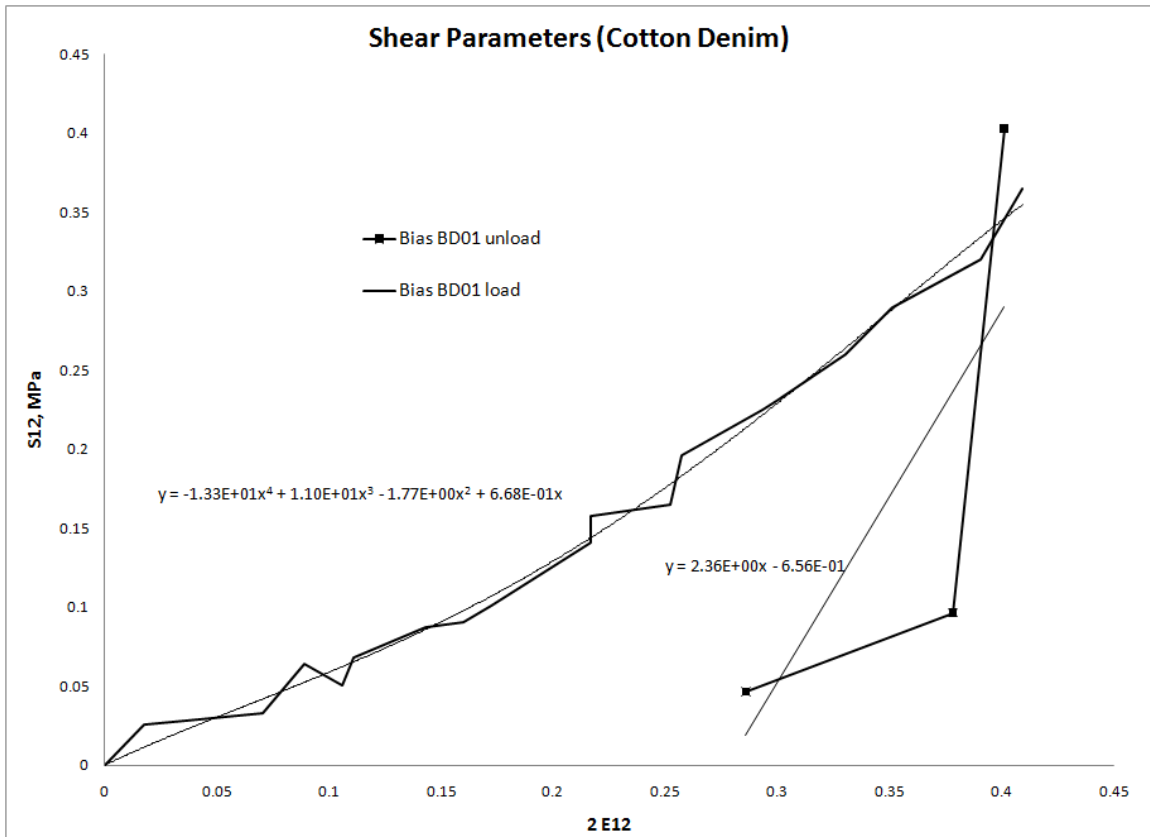


Figure 7-8. Curve fit of shear stress-strain data for loading and unloading behavior from representative cotton denim bias-45 test.

Table 7.3. In-plane loading and unloading shear moduli for the four tested fabrics.

<i>Fabric</i>	$\hat{G}_{12}^{load}$ (MPa)	$\hat{G}_{12}^{unload}$ (MPa)
C-P Blend	$-24(E_{12})^3 + 90(E_{12})^2 - 18E_{12} + 2$	12
Cotton Duck	$-143(E_{12})^3 + 105(E_{12})^2 - 10E_{12} + 1$	14
Cotton Muslin	$22(E_{12})^3 + 13(E_{12})^2 - 8E_{12} + 2$	6
Cotton Denim	$-53(E_{12})^3 + 33(E_{12})^2 - 4E_{12} + 1$	2

## 7.2 Verification of Fabric Model

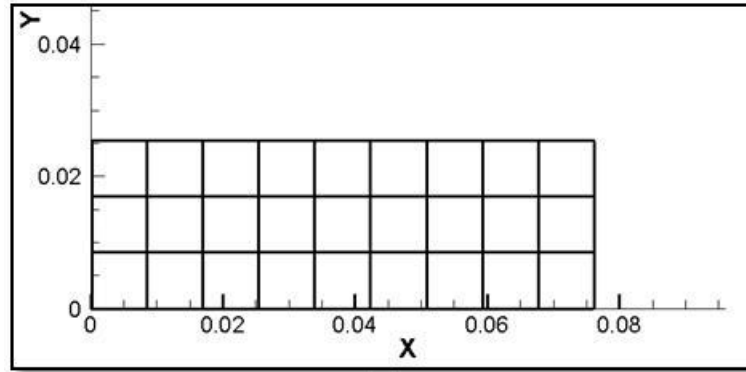
In order to verify the results of the fabric constitutive model, simulations replicating the cyclic uniaxial stress tests are compared to the experimental data. A finite element model was created to simulate the experimental tests described in section 3.3 for the tested fabrics. The geometry of the model was 1.0 inch by 3.0 inches and consisted of twenty-seven 3-D degenerated bilinear continuum shell elements. The boundary conditions were fixed on one end with a prescribed displacement on the opposite end to simulate the pin grips, with the out-of-plane displacements and rotations constrained for quasi-static simulations. The material parameters for the fabrics are listed in the previous section.

### 7.2.1 Axial Tests in Warp and Weft Directions

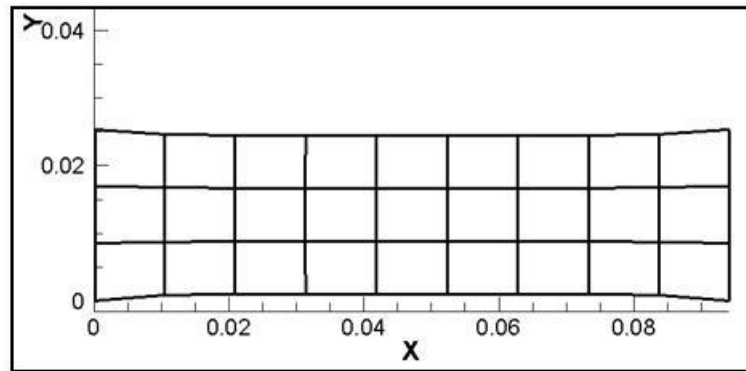
The prescribed maximum displacements for the cyclic tests in the warp and weft directions are the same as those used for the experimental tests, and are listed in Table 3.4. Material directors for loading in the warp and weft directions, respectively, are

$$Q_{II}^{warp} = \begin{bmatrix} 1 & 0 & 0 \\ 0 & 1 & 0 \\ 0 & 0 & 1 \end{bmatrix} \text{ and } Q_{II}^{weft} = \begin{bmatrix} 0 & 1 & 0 \\ -1 & 0 & 0 \\ 0 & 0 & 1 \end{bmatrix}. \quad (7.1)$$

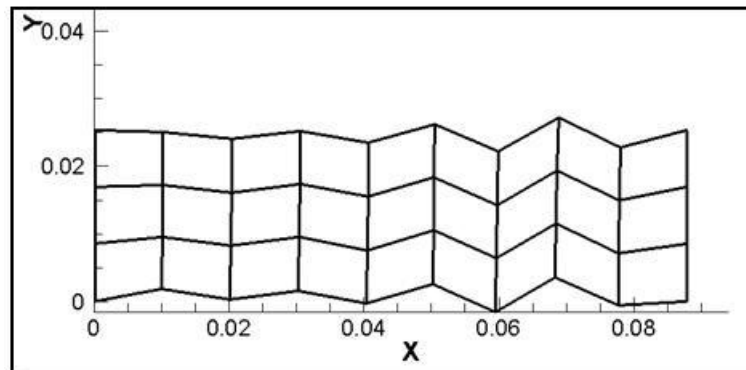
The finite element simulation of the cyclic uniaxial stress tests in the warp and weft directions produced visual results that were consistent with experiments in that there was a contraction in the transverse direction and the specimen experienced a buckling instability upon unloading as shown in Figure 7-9. The stress-strain results from cyclic uniaxial stress tests in the warp and weft directions for the four fabrics are shown in Figures 7-10 through 7-13. The cyclical results for the bias tests are also included in the figures to demonstrate the anisotropy of the fabric behavior.



(a)



(b)



(c)

Figure 7-9. Snapshots of cyclic simulation in the warp direction of cotton-polyester blend at (a) the initial configuration, (b) the maximum displacement, and (c) the compressive buckling instability upon unloading.

In each case, the fabric model exhibits nonlinear loading, linear hysteretic unloading and anisotropy as would be expected. The results for cotton-polyester blend



and denim compare very well to the experimental data as shown in Figures 7-10 and 7-11, respectively. As expected, the computational results are consistent with the curve fits used to determine the loading moduli from section 7.1. For the cotton-polyester blend, the greatest relative error in the warp direction during loading is 11% and occurs at the maximum strain. This occurs because the actual experimental specimen started to exhibit tensile yielding, whereas the present model does not feature yielding behavior. The maximum relative error in the weft direction is about 6% at a strain of approximately 0.10. The initial unloading behavior matches up with the linear unloading modulus estimated from the experiments and shows that the load decreases very rapidly leading to the eventual buckling instability seen in Figure 7-9c. For the denim results, there is no visually discernible error, as the loading curves for the model and the experimental data lie essentially on top of one another.

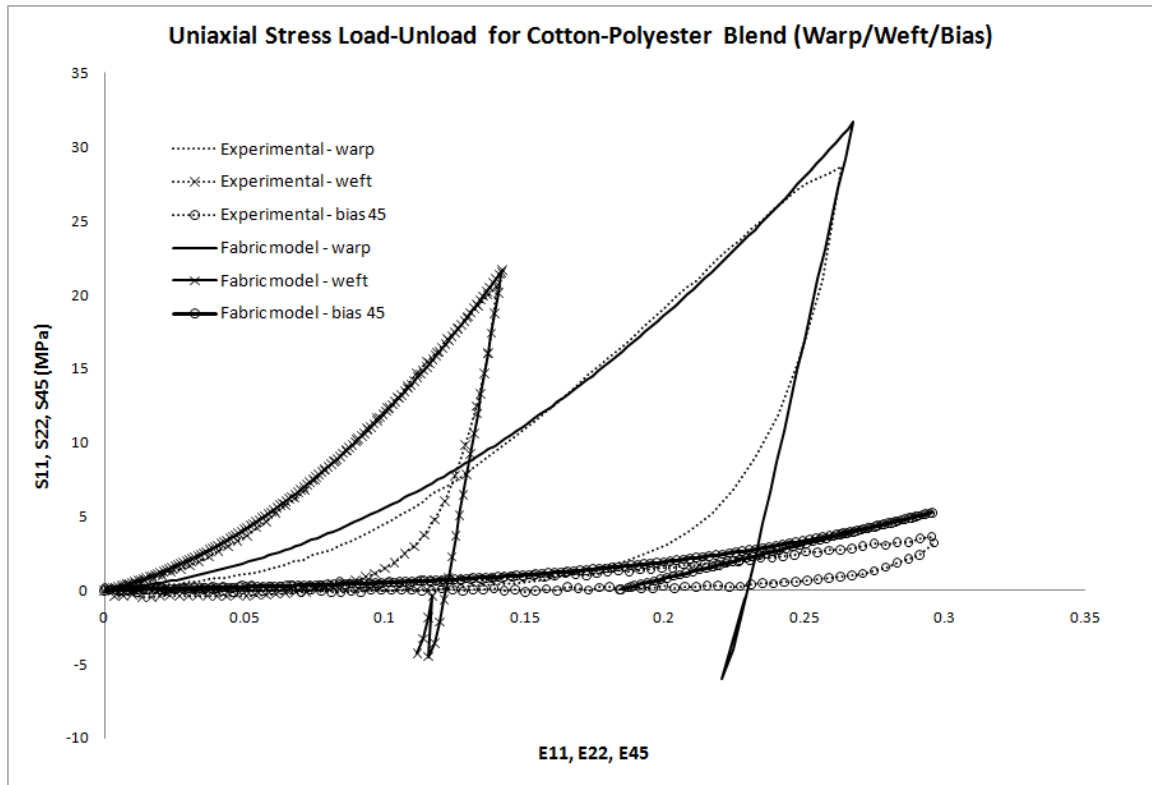


Figure 7-10. Comparison of computational and experimental results for cyclic uniaxial stress tensile tests loaded in the warp, weft and bias 45 directions for cotton-polyester blend fabric.

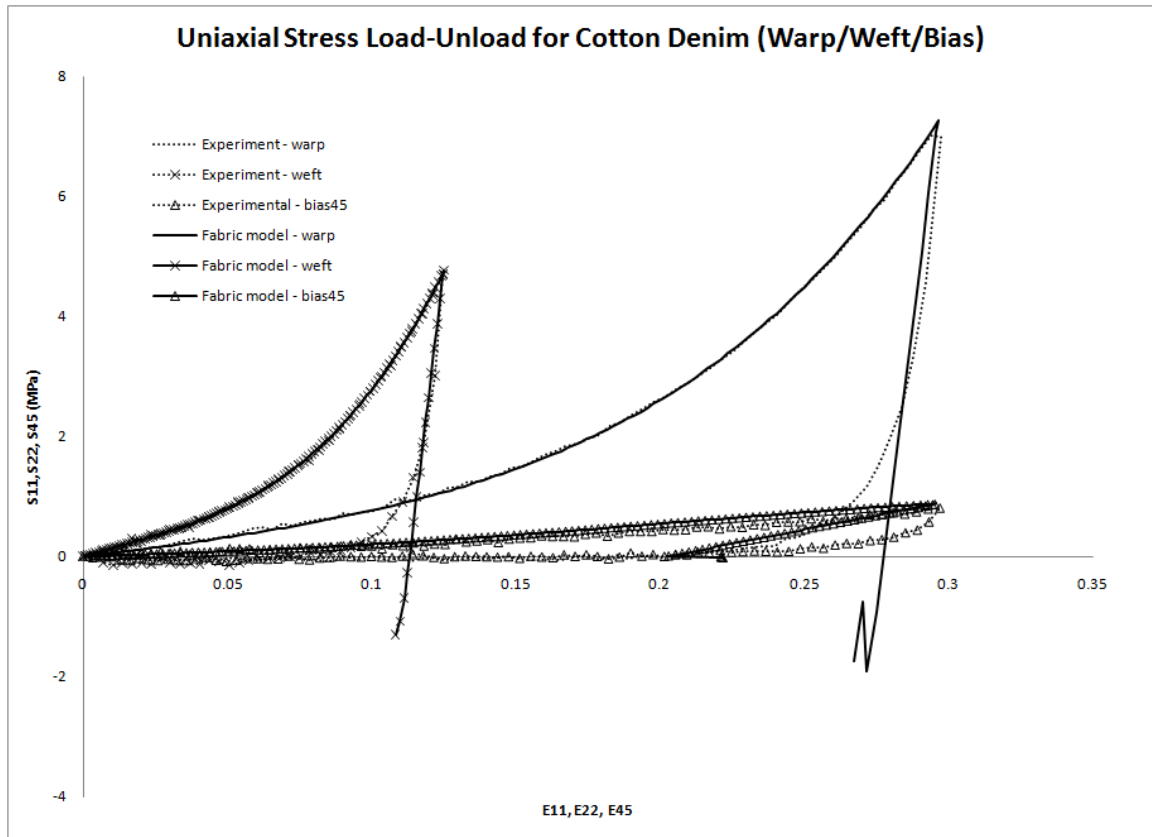


Figure 7-11. Comparison of computational and experimental results for cyclic uniaxial stress tensile tests loaded in the warp, weft and bias 45 directions for cotton denim fabric.

Using the twenty-seven element model, shell finite element simulations for duck and muslin either experienced convergence issues or greatly over-estimated the stress. In order to test the material model alone, a single element was loaded to the equivalent strain and the uniaxial stresses were calculated. The results using the single-element model match the experimental data very well and are shown in Figures 7-12 and 7-13 (denoted without an asterisk).

It is hypothesized that the simulation issues for these two fabrics are due to the extremely large apparent Poisson's ratios. In order to test this hypothesis, a parametric study was conducted to determine the upper bounds for apparent Poisson's ratios of these

two fabrics for this particular constitutive model and solution algorithm. These bounds are shown in Table 7.4. Using the modified Poisson's ratios, simulations using the twenty-seven element model were executed and the obtained results (denoted with an asterisk) demonstrated much more reasonable stress-strain relationships in the warp and weft directions for both fabrics with maximum percent errors of 3% and 15% in the warp direction and 1% and 9% in the weft direction for duck and muslin, respectively. If larger values of Poisson's ratios than those listed in Table 7.4 are used, the stress at any given strain during loading is much greater than the corresponding experimental value.

Table 7.4. Upper bound for modified Poisson's ratios for Duck and Muslin.

<i>Fabric</i>	$\nu_{12}^*$	$\nu_{21}^*$
Cotton Duck	0.40	0.40
Cotton Muslin	0.40	0.40

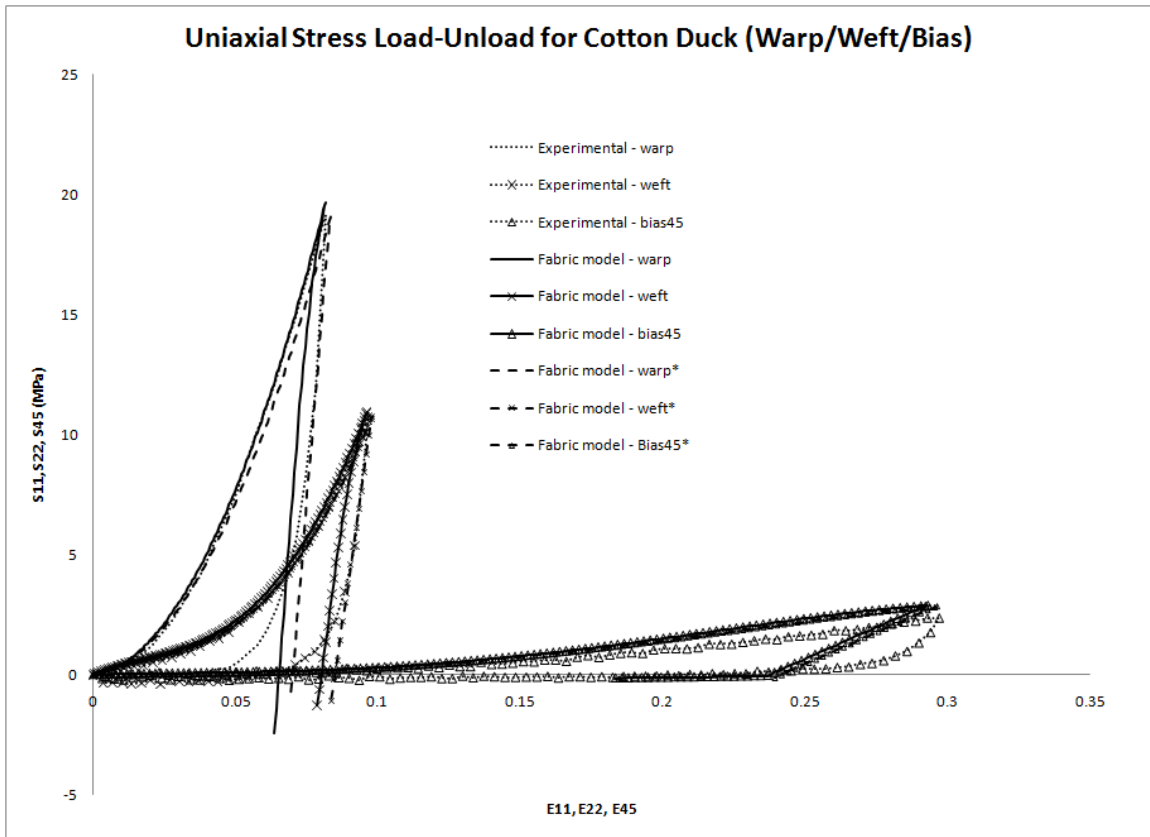


Figure 7-12. Comparison of computational and experimental results for cyclic uniaxial stress tensile tests loaded in the warp, weft and bias 45 directions for cotton duck fabric. The model results without an asterisk are for a single-element simulation and the model results with the asterisk are the 27 element simulation with modified Poisson's ratios.

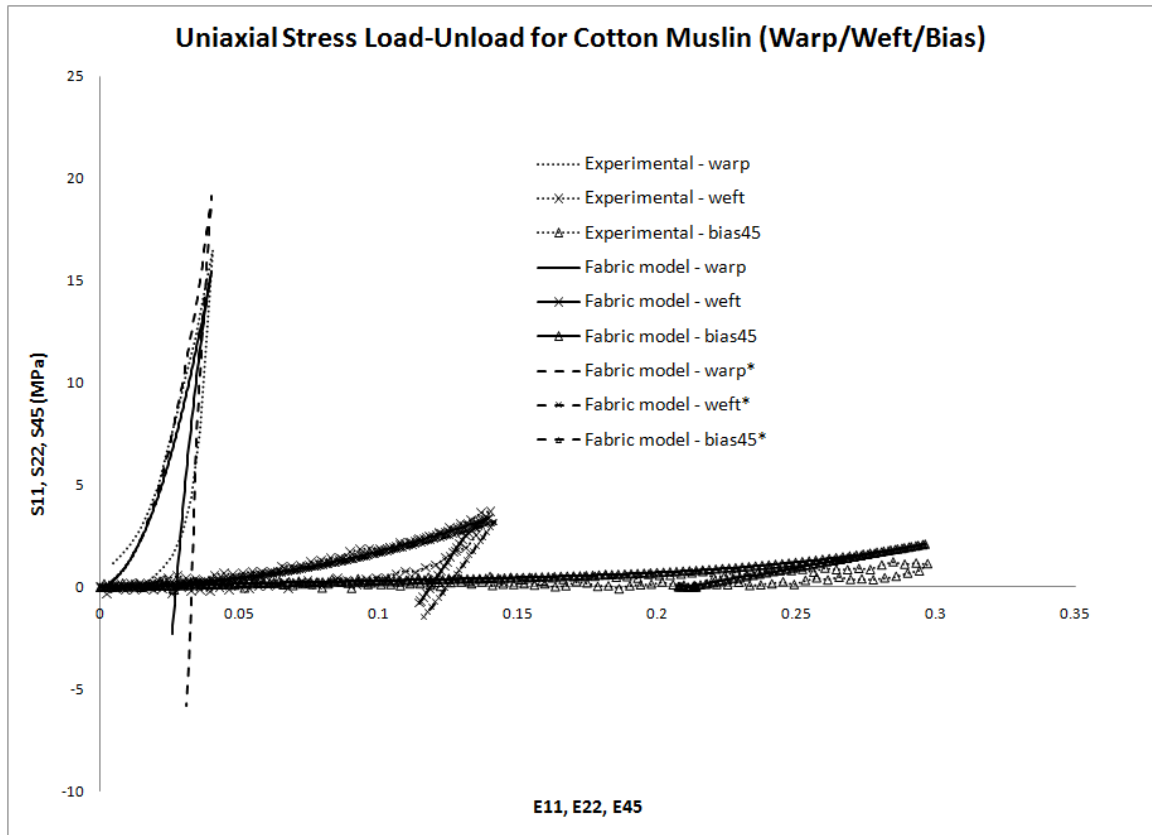


Figure 7-13. Comparison of computational and experimental results for cyclic uniaxial stress tensile tests loaded in the warp, weft and bias 45 directions for cotton muslin fabric. The model results without an asterisk are for a single-element simulation and the model results with the asterisk are the 27 element simulation with modified Poisson's ratios.

Since the experiments and the simulations were subjected to uniaxial stress, the fabrics contracted in the direction transverse to that of the loading to ensure zero transverse stress. Comparisons of the lateral strain as a function of longitudinal strain between the fabric model results and experimental data are shown in Figures 7-14 through 7-17. The computational strain results for the cotton-polyester blend and cotton denim compare well to the measured experimental strains. For cotton muslin and cotton denim, the computational strain results for the single-element simulations also compare well to the measured experimental data; however, the results for the twenty-seven element models feature large disagreements between the model and the experimental data due to the use of modified Poisson's ratios.

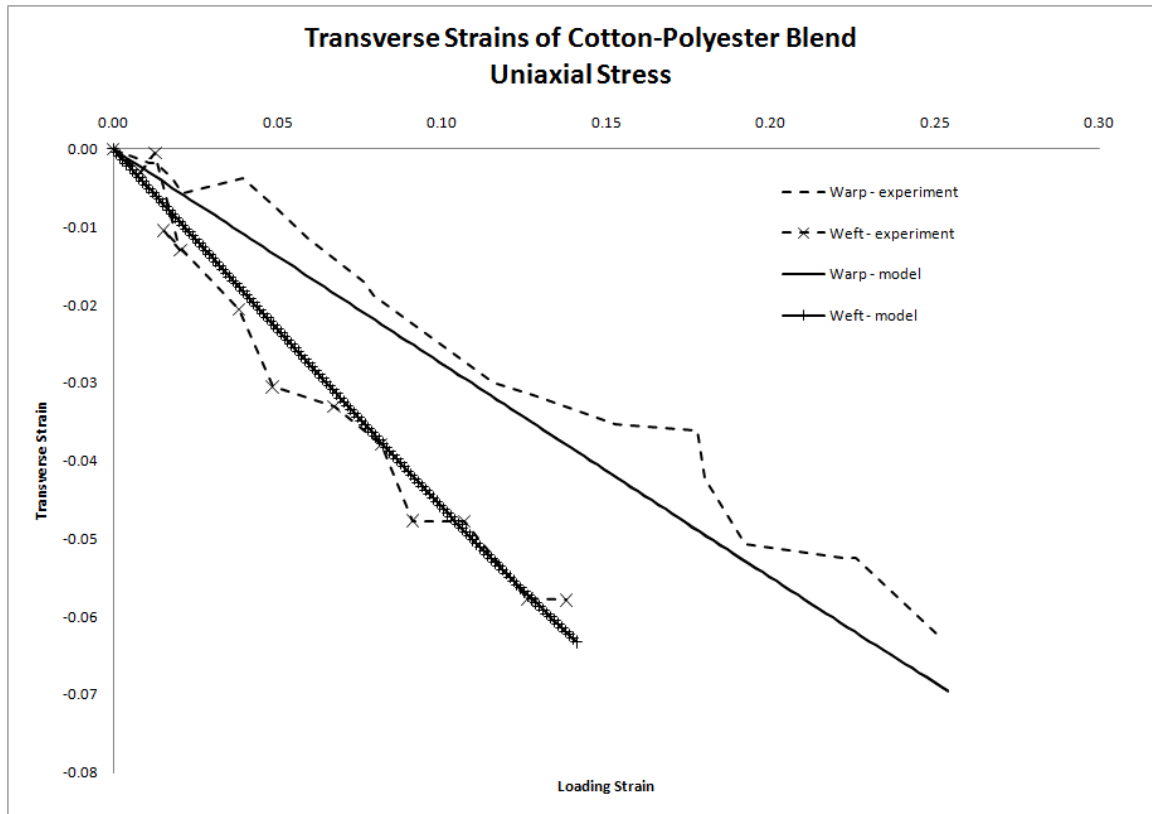


Figure 7-14. Comparison of the computational and experimental transverse strains as a function of loading strain for cotton-polyester blend fabric.

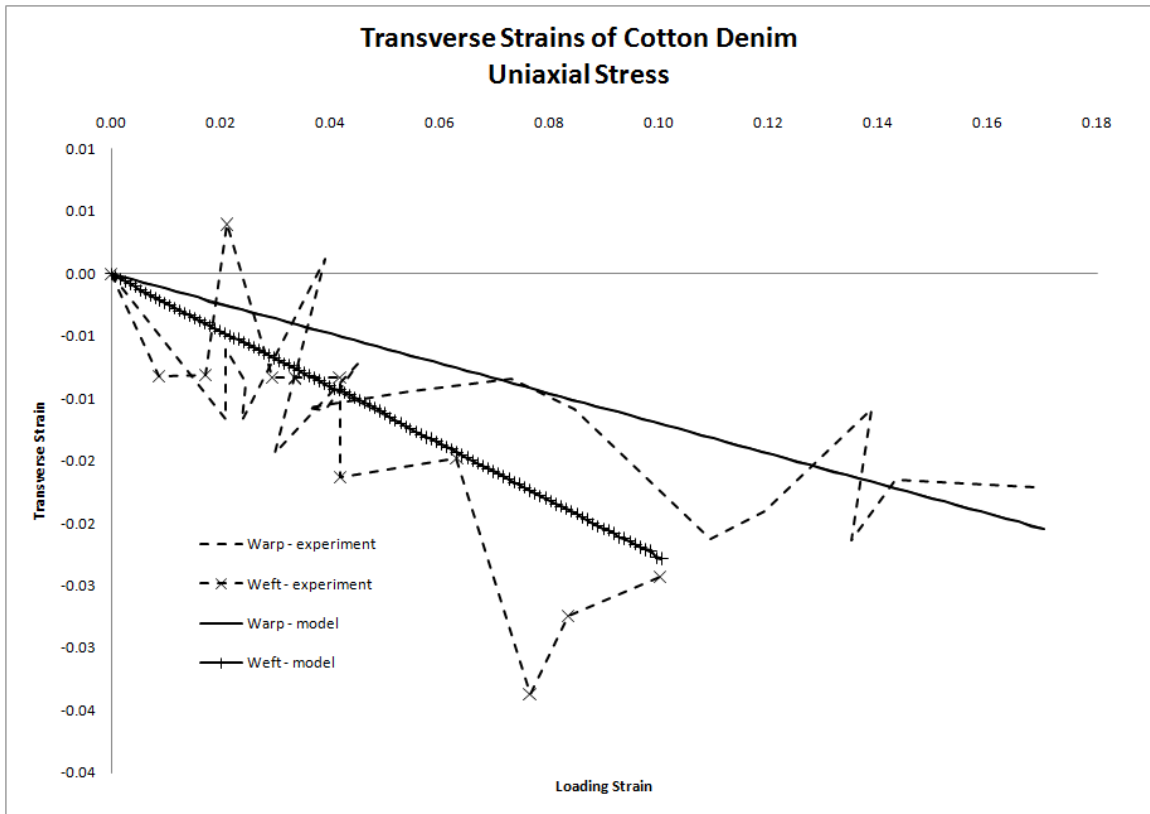


Figure 7-15. Comparison of the computational and experimental transverse strains as a function of loading strain for cotton denim fabric.



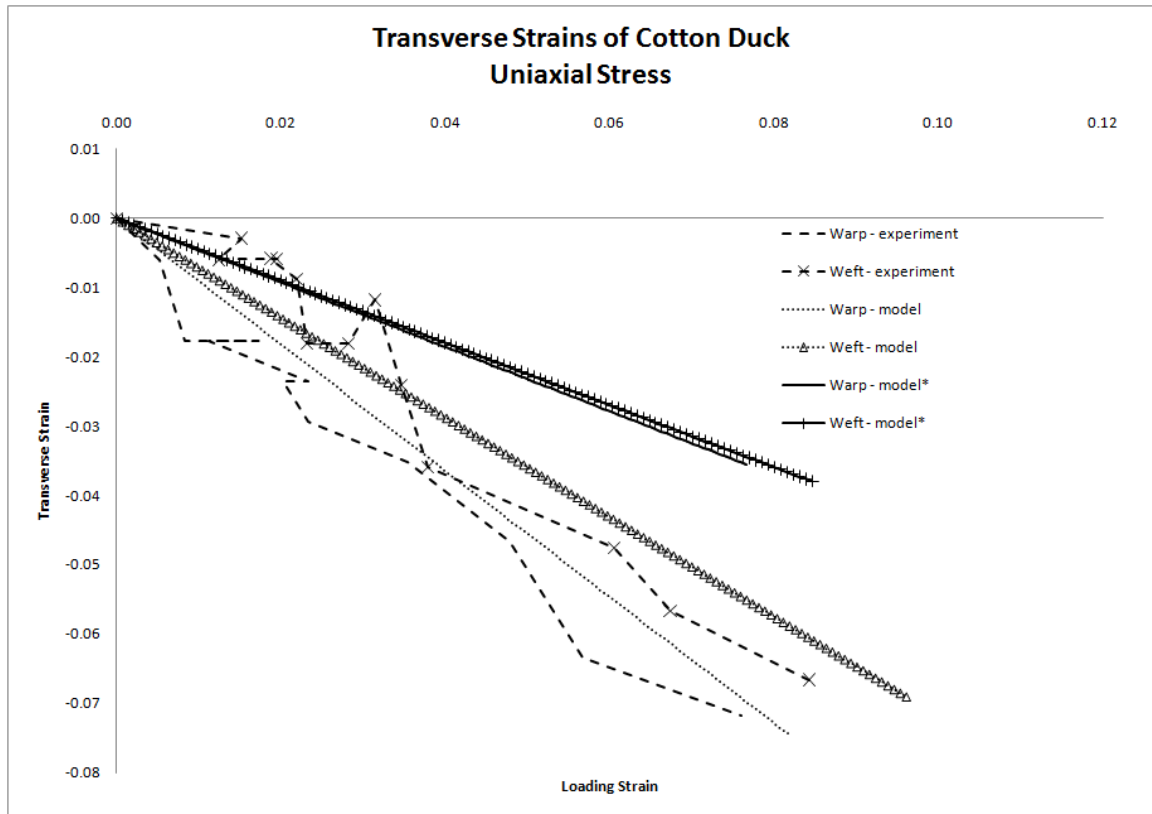


Figure 7-16. Comparison of the computational and experimental transverse strains as a function of loading strain for cotton duck fabric. The model results without an asterisk are for a single-element simulation and the model results with the asterisk are the 27 element simulation with modified Poisson's ratios.

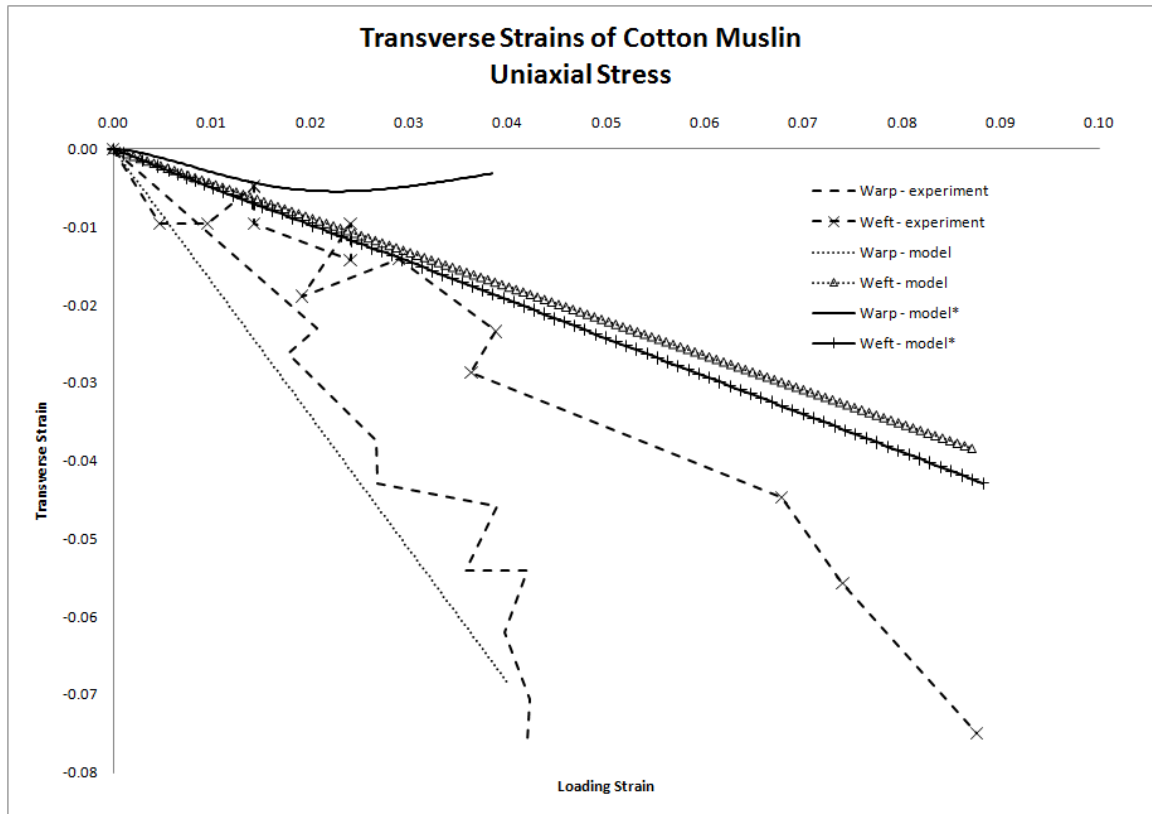


Figure 7-17. Comparison of the computational and experimental transverse strains as a function of loading strain for cotton muslin fabric. The model results without an asterisk are for a single-element simulation and the model results with the asterisk are the 27 element simulation with modified Poisson's ratios.

As mentioned in section 3.3.2, when a fabric is loaded in tension, the behavior is nonlinear so long as the current strain value is greater than the previous maximum strain value. When the fabric is unloaded and subsequently reloaded, the behavior is assumed to be linear if the current strain is less than the maximum value, which is supported by Figure 3-18. To verify the fabric model with this assumption, a simulation of a cotton-polyester blend specimen subjected to a cyclic uniaxial stress in the warp direction was carried out. The specimen was loaded to 75% of the prescribed maximum displacement, unloaded to 70% of the maximum displacement and then reloaded to 100%. The results of this test are shown in Figure 7-18 and are consistent with the expected behavior.

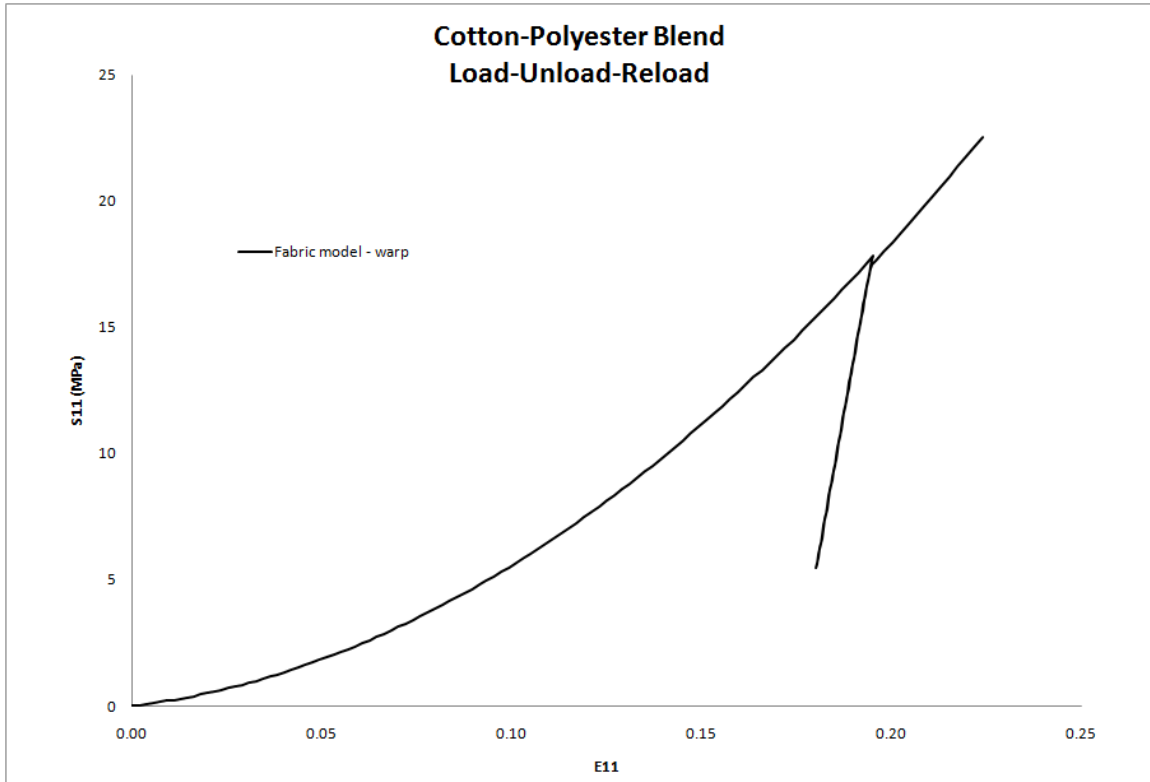


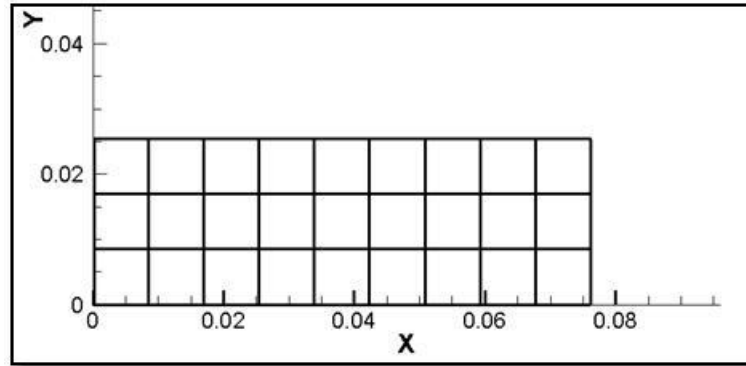
Figure 7-18. Uniaxial stress loading, unloading and reloading of a cotton-polyester blend fabric in the warp direction.

### 7.2.2 Bias and Simple Shear Tests

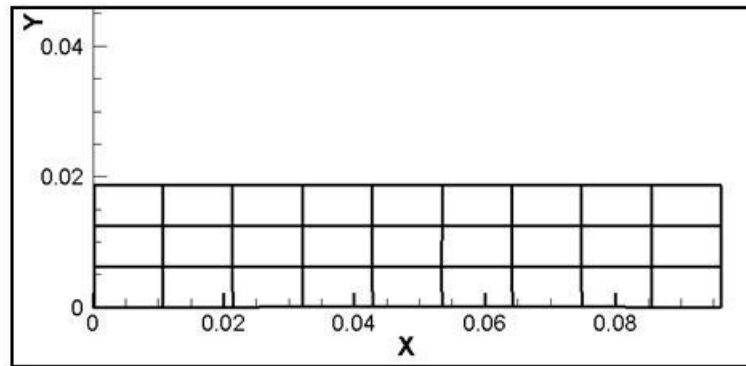
Simulations to replicate the bias 45 tests were conducted to compare with the experimental data. The geometry of the specimens and loading conditions were the same as those of the axial tests in the warp and weft directions, except that the boundary conditions were relaxed at the ends of the specimen to allow contraction in the lateral direction while experiencing uniaxial stress. The prescribed displacement for each test was 20.0 mm. The material directors for these tests are set as

$$Q_{IJ}^{bias45} = \begin{bmatrix} \frac{\sqrt{2}}{2} & \frac{\sqrt{2}}{2} & 0 \\ -\frac{\sqrt{2}}{2} & \frac{\sqrt{2}}{2} & 0 \\ 0 & 0 & 1 \end{bmatrix}. \quad (7.2)$$

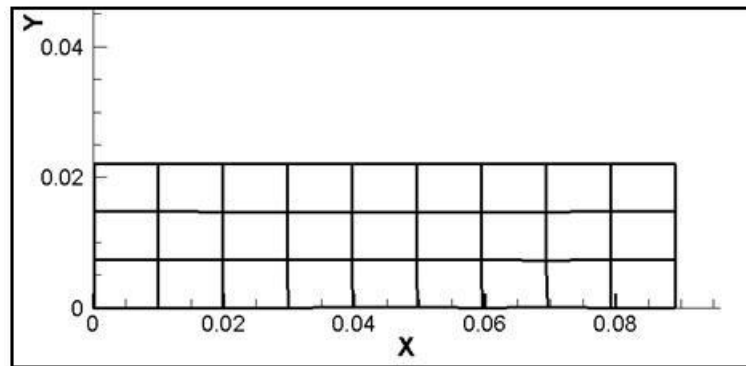
Snapshots of a representative simulation at the initial configuration, maximum displacement and onset of buckling shown in Figure 7-19 and the stress-strain results for the four fabrics are shown in Figures 7-20 through 7-23. The results for cotton-polyester blend show close agreement up to a strain of 0.15. Beyond that strain level, the model gradually over-predicts the experimental data up to 44% at a strain of 0.30. The results for cotton denim agree up to a strain of 0.10 with the model over-predicting the experimental stress by 13% at a strain of 0.25. Similarly, the results for cotton denim agree up to a strain of 0.10 with a maximum percent error of 26% at a strain of 0.25. Finally, the results for cotton muslin are in agreement up to a strain of 0.15 with a maximum percent error of 75% at the maximum strain value of 0.30. In each case, the model is also able to exhibit the hysteresis upon unloading.



(a)



(b)



(c)

Figure 7-19. Snapshots of cyclic simulation in the bias 45 direction of cotton-polyester blend at (a) the initial configuration, (b) the maximum displacement, and (c) unloading.

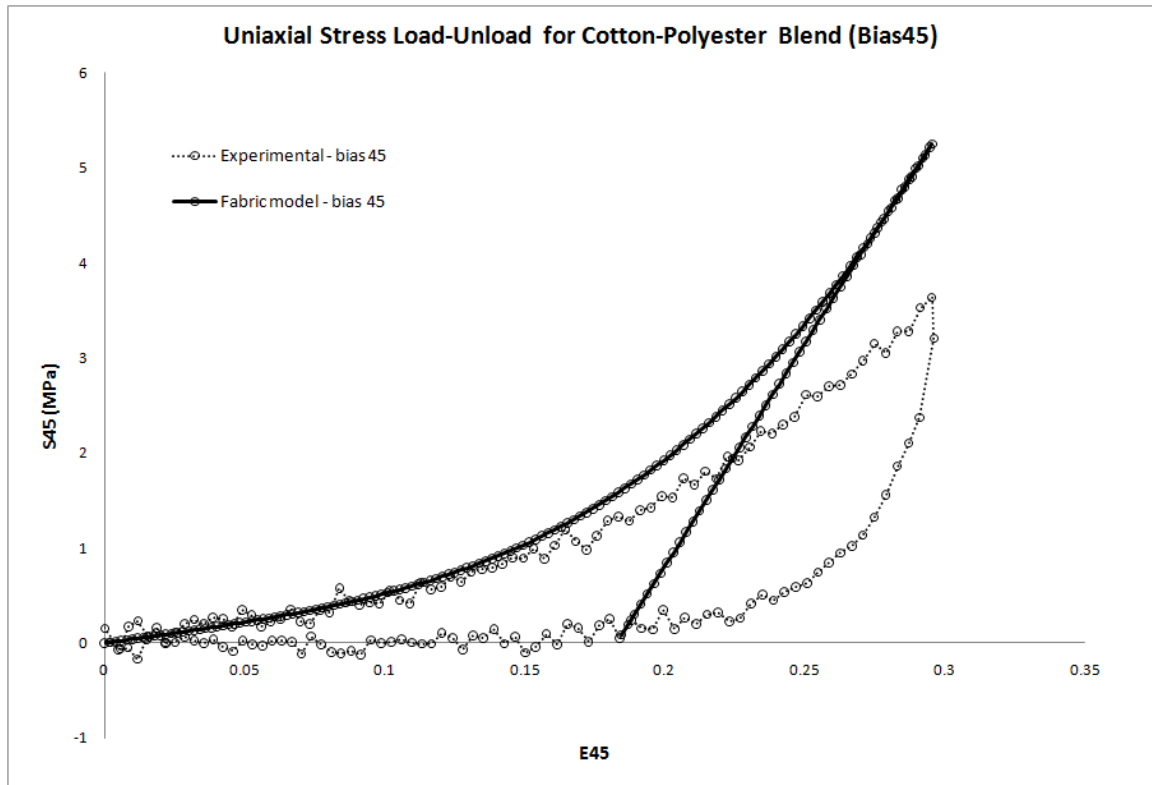


Figure 7-20. Comparison of the fabric model results of a bias 45 tension test to the experimental data for cotton-polyester blend.

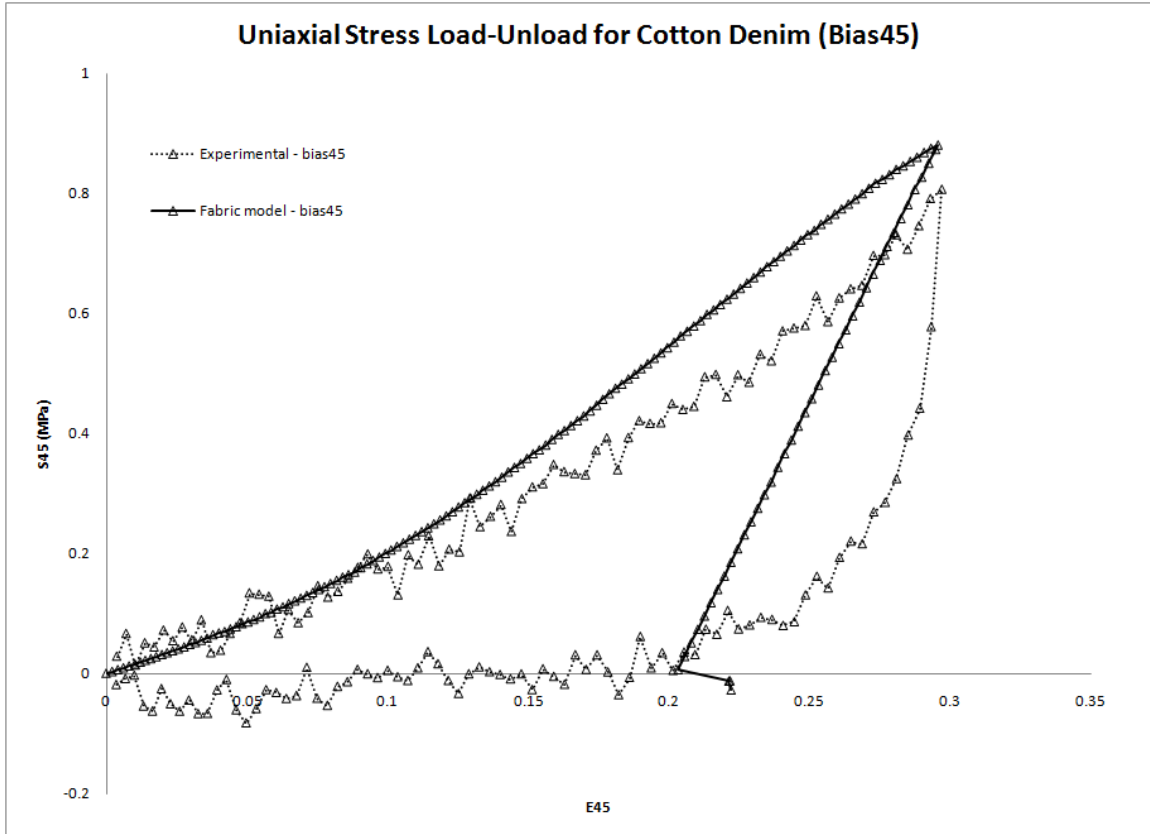


Figure 7-21. Comparison of the fabric model results of a bias 45 tension test to the experimental data for cotton denim.

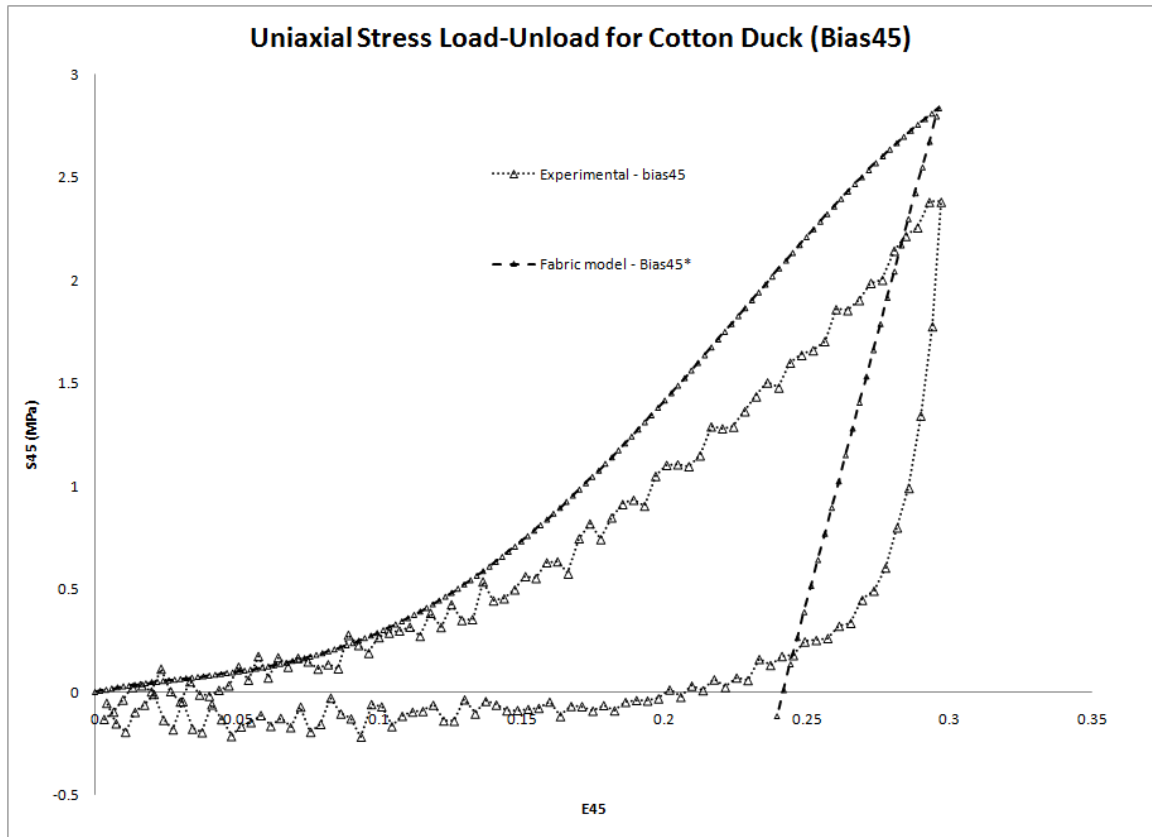


Figure 7-22. Comparison of the fabric model results of a bias 45 tension test to the experimental data for cotton duck.



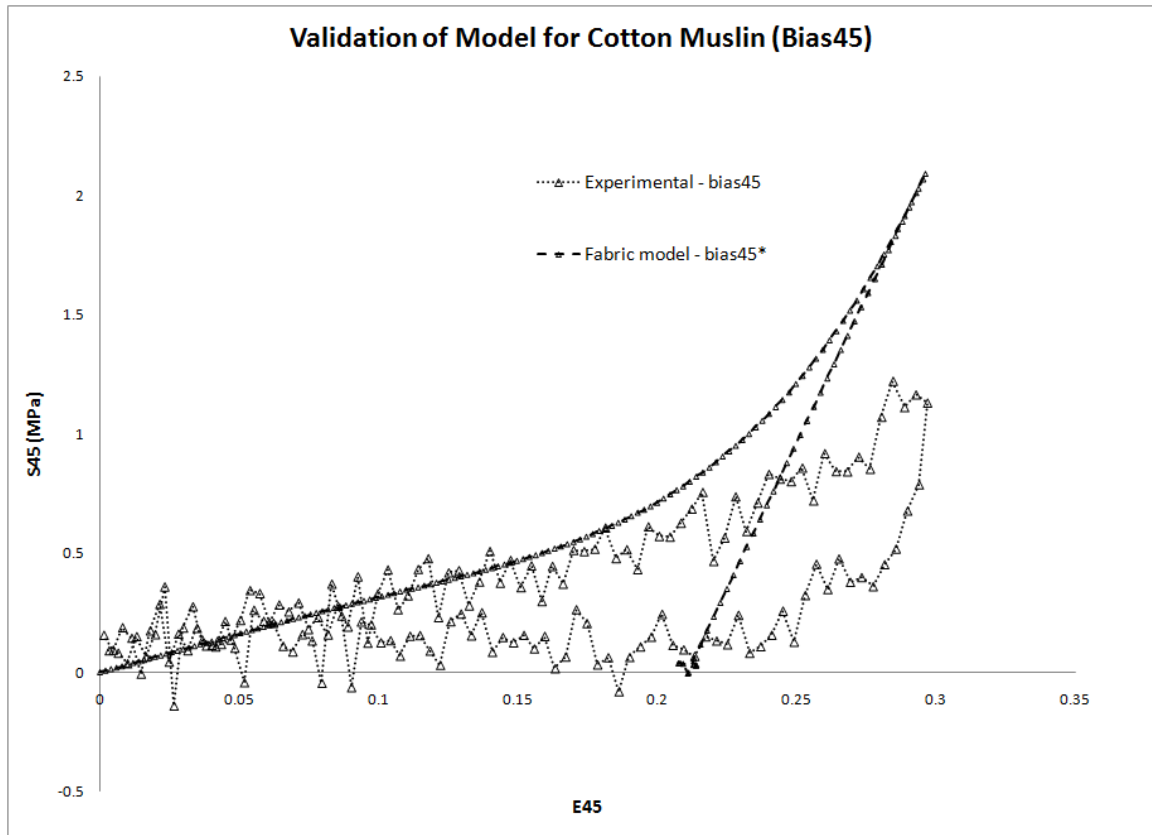


Figure 7-23. Comparison of the fabric model results of a bias 45 tension test to the experimental data for cotton muslin.

In order to test the model in situations where the yarn directors are in more general orientations, experimental and computational tests were conducted for cotton-polyester blend and cotton denim for two cases: (1) the warp yarn is at an angle of  $30^\circ$  to the loading direction; and (2) the warp yarn is at an angle of  $60^\circ$  to the loading direction.

$$Q_{IJ}^{warp30} = \begin{bmatrix} \frac{\sqrt{3}}{2} & \frac{1}{2} & 0 \\ -\frac{1}{2} & \frac{\sqrt{3}}{2} & 0 \\ 0 & 0 & 1 \end{bmatrix} \text{ and } Q_{IJ}^{warp60} = \begin{bmatrix} \frac{1}{2} & \frac{\sqrt{3}}{2} & 0 \\ \frac{\sqrt{3}}{2} & \frac{1}{2} & 0 \\ 0 & 0 & 1 \end{bmatrix}. \quad (7.3)$$

The duck and muslin fabrics are not included since the modified Poisson's ratios used in the simulations lead to behavior that doesn't necessarily correlate to the experiments. Displayed in Figures 7-24 and 7-25, the results show that the computational results compare reasonably well with the experimental data. Discrepancies can be attributed to the experimental data consisting of stresses and strains in the loading direction only, whereas the computational simulation shows that the complex membrane behavior, due to the bias angle and the anisotropy (see Figure 7-26), results in additional lateral and shear stresses and strains that are not taken into account for this comparison; and which, when averaged over the whole domain, also exhibit small stress fluctuations in the loading directions.

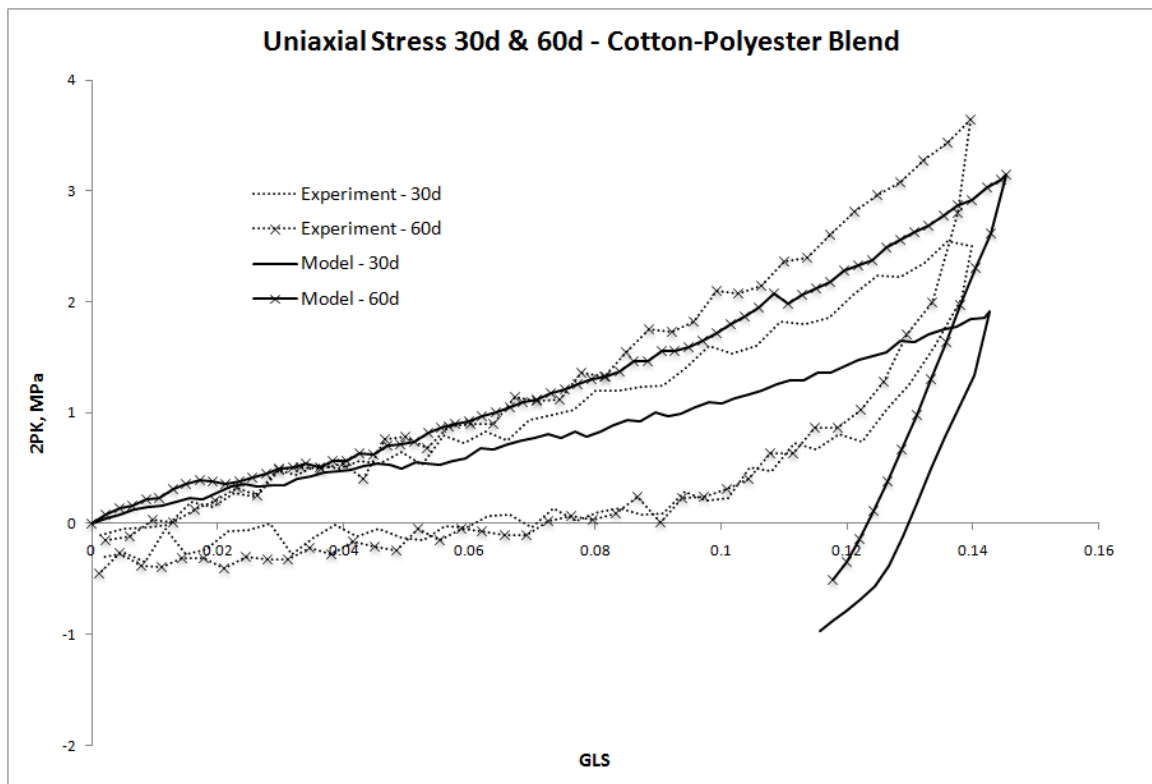


Figure 7-24. Experimental and computational uniaxial stress results for cotton-polyester blend for warp yarn orientations of  $30^\circ$  and  $60^\circ$  to the loading direction.

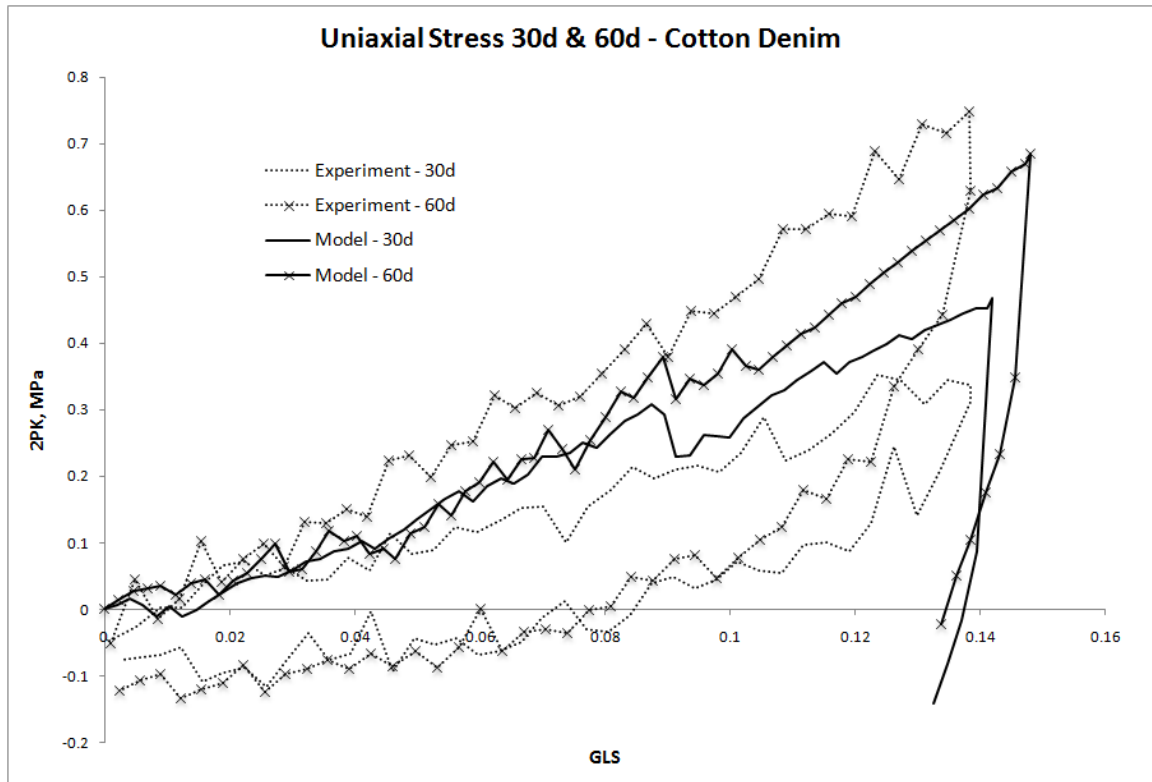
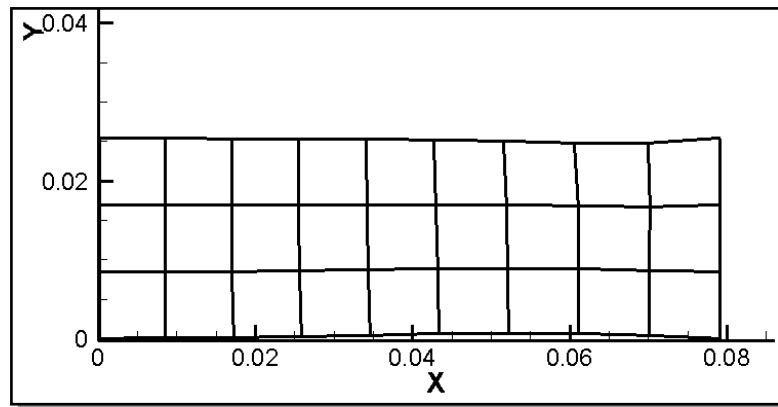
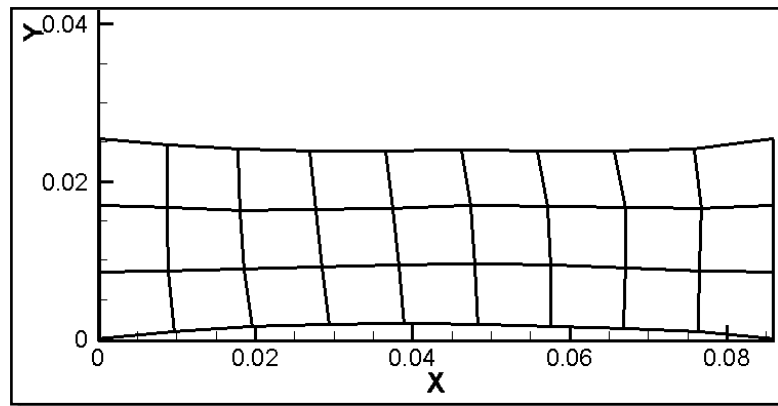


Figure 7-25. Experimental and computational uniaxial stress results for cotton denim for warp yarn orientations of 30° and 60° to the loading direction.



(a)



(b)

Figure 7-26. Simulation results showing non-uniform behavior at (a) the beginning and (b) near the maximum displacement for cotton-polyester blend with the warp yarn oriented  $30^\circ$  to the loading direction.

As discussed in section 2.3, the behavior of fabrics is further complicated in that trellising of the yarns can lead to cyclic shear behavior. To see how the model handles cyclic shear loading, a square specimen consisting of nine elements was subjected to a simple shear test. In this case, the model results are as expected and are shown in Figure 7-27. The initial loading of the specimen exhibits nonlinear behavior up to the point where unloading occurs. The unloading is linear until the shear stress changes signs, at which point, nonlinear behavior is reintroduced using a relative shear strain value. Another simulation tested the loading, unloading and subsequent reloading of the simple

shear model. For this test, the unloading was small so that the sign of the shear stress did not change, allowing to see if the reloading modulus was linear until the previous maximum relative strain. Figure 7-28 shows the results of a simple shear test in which a cotton-polyester blend fabric was loaded, unloaded a small amount and reloaded producing the expected behavior.

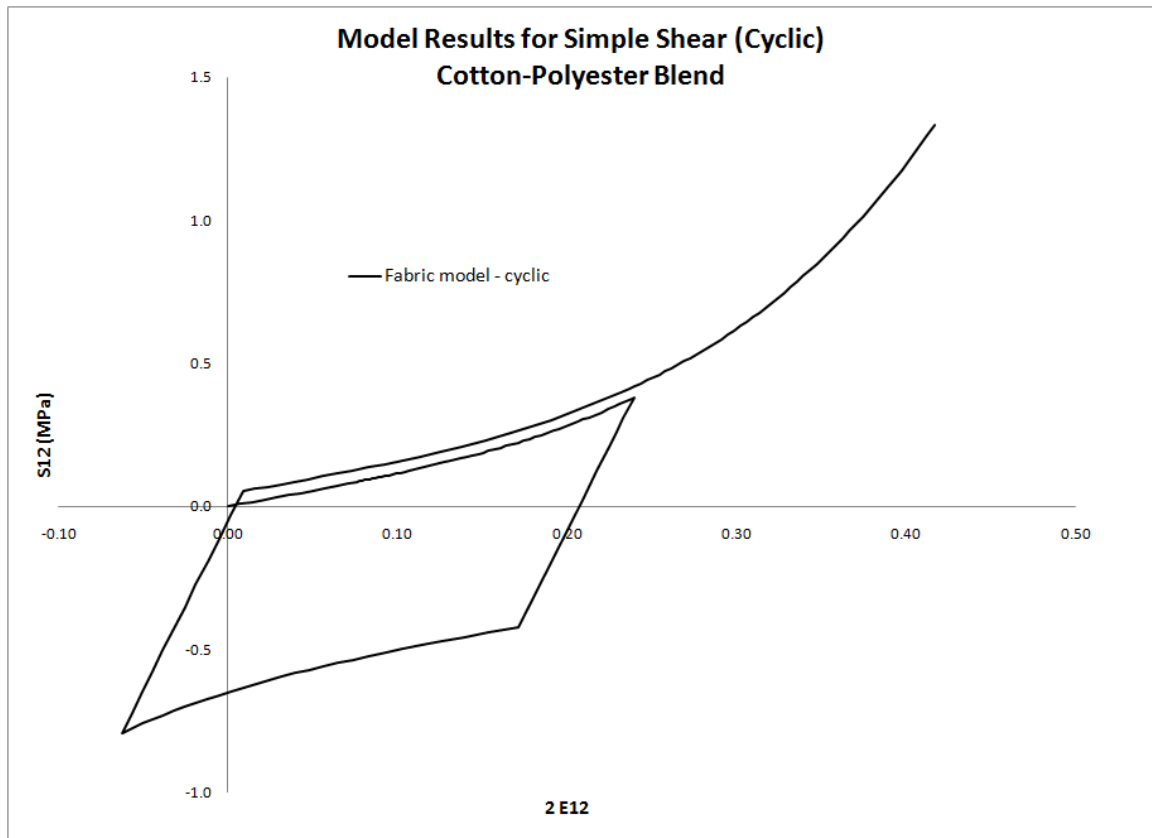


Figure 7-27. Modeling the shear stress and strain behavior of a cotton-polyester blend fabric subjected to a cyclic simple shear test.

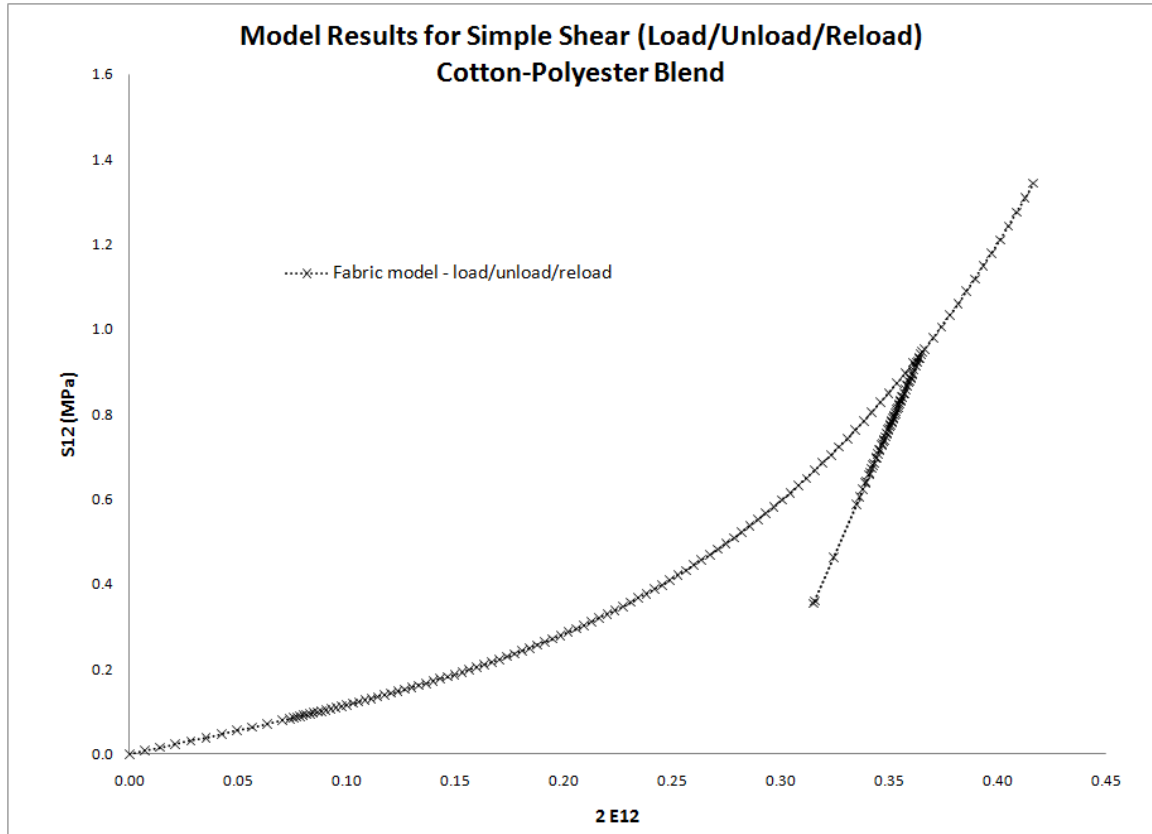


Figure 7-28. Modeling the shear stress and strain behavior of a cotton-polyester blend fabric subjected to a simple shear test where the specimen is loaded, unloaded and then reloaded.

### 7.3 Applications

#### 7.3.1 Biaxial Strain

The presence of a biaxial strain, in which both the warp and weft yarns are extended, leads to a stiffer response since as both yarns are straightening, less decrimping takes place [33]. Here, the fabric model is tested in a quasi-static simulation in which 25.4 cm by 25.4 cm fabric sheets of cotton-polyester blend and cotton denim are subjected to a single-cycle biaxial load. The load consisted of a 1:1 strain ratio in which the maximum displacement was 3.0 cm. The results, shown in Figures 7-29 and 7-30, affirm that the presence of transverse strains have a tremendous affect on the stress in

either yarn direction. This suggests that biaxial loads would lead to fabric damage, such as tearing, at lower strains than if the fabric were only subjected to a uniaxial load.

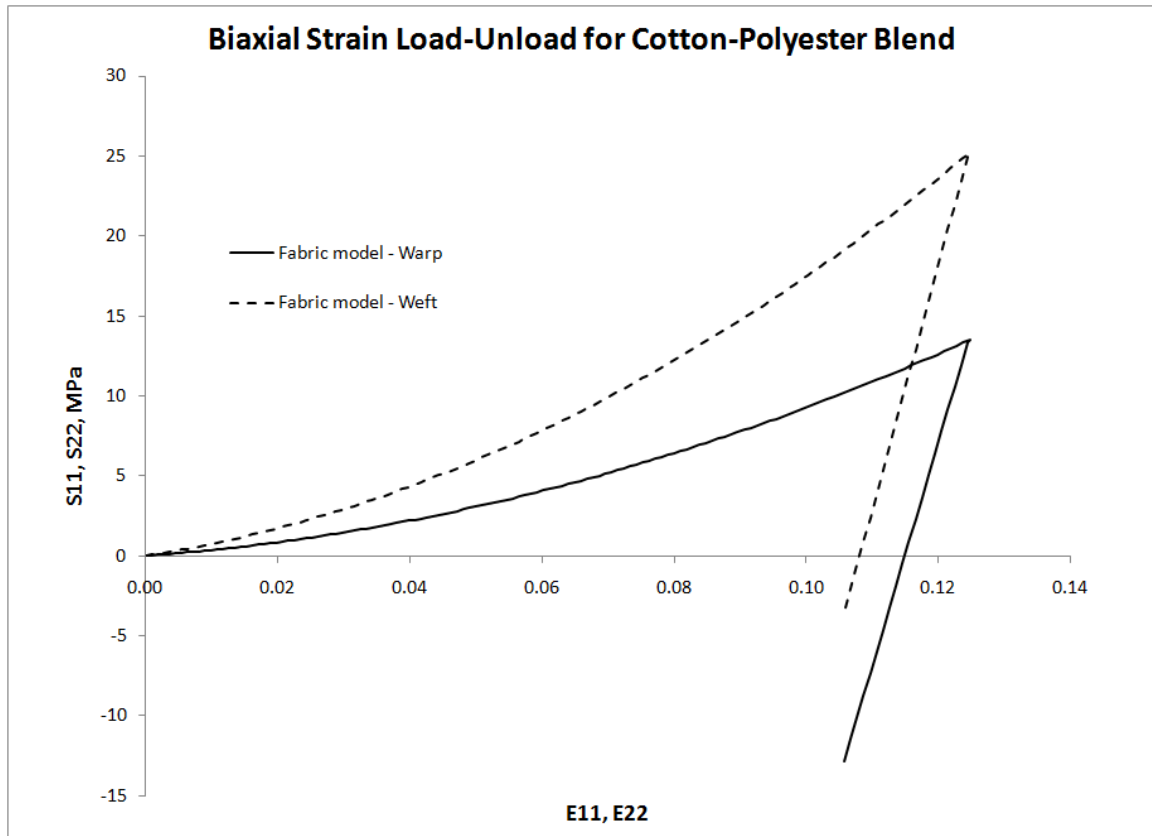


Figure 7-29. Computational results for 1:1 biaxial strain of cotton-polyester blend.

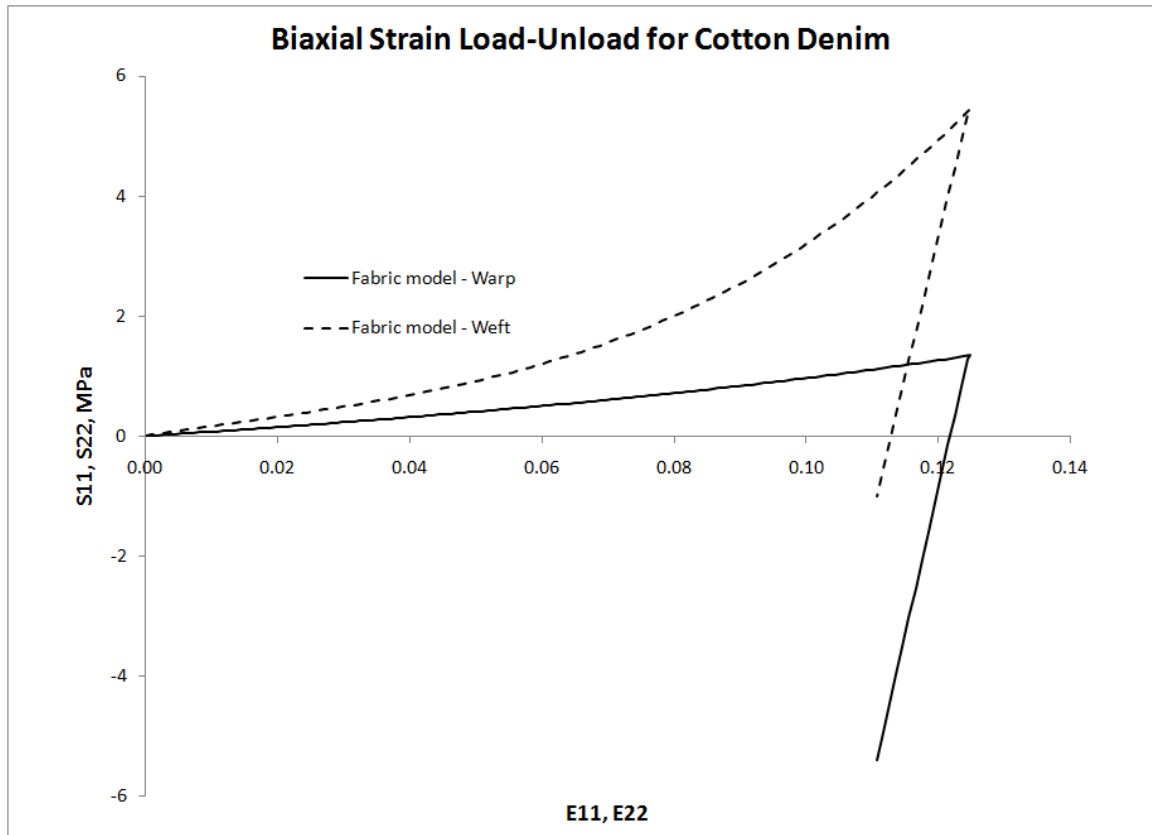


Figure 7-30. Computational results for 1:1 biaxial strain of cotton denim.

### 7.3.2 Draping Fabric From Four Corners

In order to test the fabric model in a dynamic simulation, a simple test problem is introduced in which a square piece of fabric is pinned at its four corners and held horizontally. The load is that due to gravity and allows the fabric to deform into a concave shape. The fabric is comprised of the cotton-polyester blend, for which the material properties are listed in section 7.1 and the dimensions are 2.0 meters by 2.0 meters with the warp and weft directions aligned with the x and y axes, respectively. The initial configuration of the dynamic test problem is shown in Figure 7-31(a). The problem is solved explicitly using Newmark's method where  $\alpha = \frac{1}{2}$  and  $\beta = 0$  and the time step is  $1 \times 10^{-5}$  seconds.



The visual results for the dynamic simulation are shown in Figure 7-31. The simulation comes to equilibrium within 0.5 seconds, which seems well within reason. In order to achieve these results, the shear hysteresis had to be switched off, otherwise the problem became unstable. However, the dynamic simulation does utilize the fabric model in which the behavior is anisotropic, nonlinear and includes hysteresis in the warp and weft yarn directions.

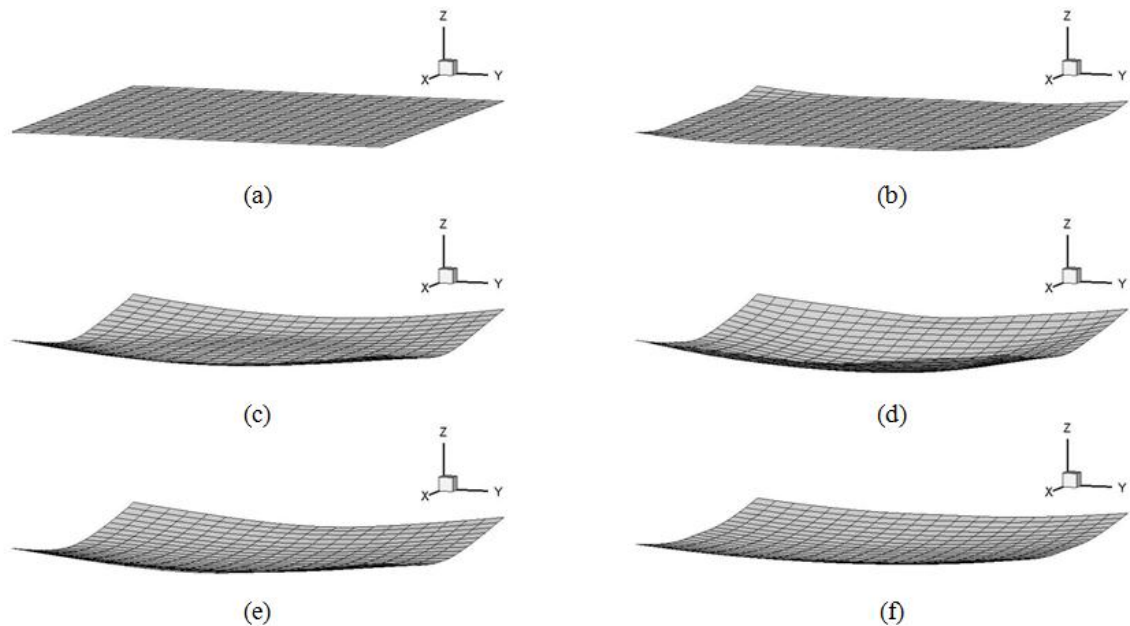


Figure 7-31. The dynamics response of a cotton-polyester blend fabric falling with gravity but pinned at the four corners at (a) 0.0 seconds, (b) 0.1 seconds, (c) 0.2 seconds, (d) 0.3 seconds, (e) 0.4 seconds, and (f) 0.5 seconds.

### 7.3.3 Poking Fabric

Another dynamic simulation consists of poking the center of a fabric. For this problem, the central 16 elements of a 2.0 meter by 2.0 meter cotton-polyester blend fabric are displaced in the z-direction by 0.40 meters and then returned to zero displacement in

0.5 seconds. All nodes along the boundary of the fabric are constrained and the warp and weft direction are aligned with the x and y axes, respectively. The initial configuration of the poking problem with the element numbers is shown in Figure 7-32. The problem is solved explicitly using Newmark's method where  $\alpha = 1/2$  and  $\beta = 0$  and the time step is  $1 \times 10^{-5}$  seconds.

1	21	41	61	81	101	121	141	161	181	201	221	241	261	281	301	321	341	361	381
2	22	42	62	82	102	122	142	162	182	202	222	242	262	282	302	322	342	362	382
3	23	43	63	83	103	123	143	163	183	203	223	243	263	283	303	323	343	363	383
4	24	44	64	84	104	124	144	164	184	204	224	244	264	284	304	324	344	364	384
5	25	45	65	85	105	125	145	165	185	205	225	245	265	285	305	325	345	365	385
6	26	46	66	86	106	126	146	166	186	206	226	246	266	286	306	326	346	366	386
7	27	47	67	87	107	127	147	167	187	207	227	247	267	287	307	327	347	367	387
8	28	48	68	88	108	128	148	168	188	208	228	248	268	288	308	328	348	368	388
9	29	49	69	89	109	129	149	169	189	209	229	249	269	289	309	329	349	369	389
10	30	50	70	90	110	130	150	170	190	210	230	250	270	290	310	330	350	370	390
11	31	51	71	91	111	131	151	171	191	211	231	251	271	291	311	331	351	371	391
12	32	52	72	92	112	132	152	172	192	212	232	252	272	292	312	332	352	372	392
13	33	53	73	93	113	133	153	173	193	213	233	253	273	293	313	333	353	373	393
14	34	54	74	94	114	134	154	174	194	214	234	254	274	294	314	334	354	374	394
15	35	55	75	95	115	135	155	175	195	215	235	255	275	295	315	335	355	375	395
16	36	56	76	96	116	136	156	176	196	216	236	256	276	296	316	336	356	376	396
17	37	57	77	97	117	137	157	177	197	217	237	257	277	297	317	337	357	377	397
18	38	58	78	98	118	138	158	178	198	218	238	258	278	298	318	338	358	378	398
19	39	59	79	99	119	139	159	179	199	219	239	259	279	299	319	339	359	379	399
20	40	60	80	100	120	140	160	180	200	220	240	260	280	300	320	340	360	380	400

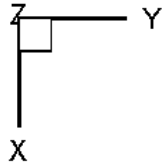


Figure 7-32. Original configuration of a square cotton-polyester blend fabric. The elements in the blue square are displaced in the z-direction. The stress-strain data for the SVK model and the present model are compared for the elements highlighted in red.

The poking problem was solved using both the St. Venant-Kirchhoff (SVK) model and the fabric model developed in this dissertation. It is noted that the shear behavior in this test did not include any hysteresis. Visual results from the SVK model and the present fabric model are presented in Figures 7-33 and 7-34, respectively. These visual results show that the simulation using the SVK model recovers the original configuration upon removal of the load, whereas the simulation using the present fabric model shows that the fabric has permanently stretched and thus wrinkles/buckles upon unloading, which is what one would expect. The stress-strain data for both models were compared at two elements: 207 and 271, and are shown in Figures 7-35 and 7-36, respectively. For both elements, there is little shear deformation. For element 207, a majority of the deformation was in the warp direction and the corresponding stress using the present fabric model is nonlinear and a higher magnitude than that found using the SVK model. Similar results are found for element 271, where the deformation was mostly in the weft direction. For the simulation using the fabric model, the shear strains transverse to the loading direction for both elements are roughly zero, but still lead to significant stress values. For unloading, the stress-strain graphs only show one data point for the present model due to the subsequent buckling of the fabric.

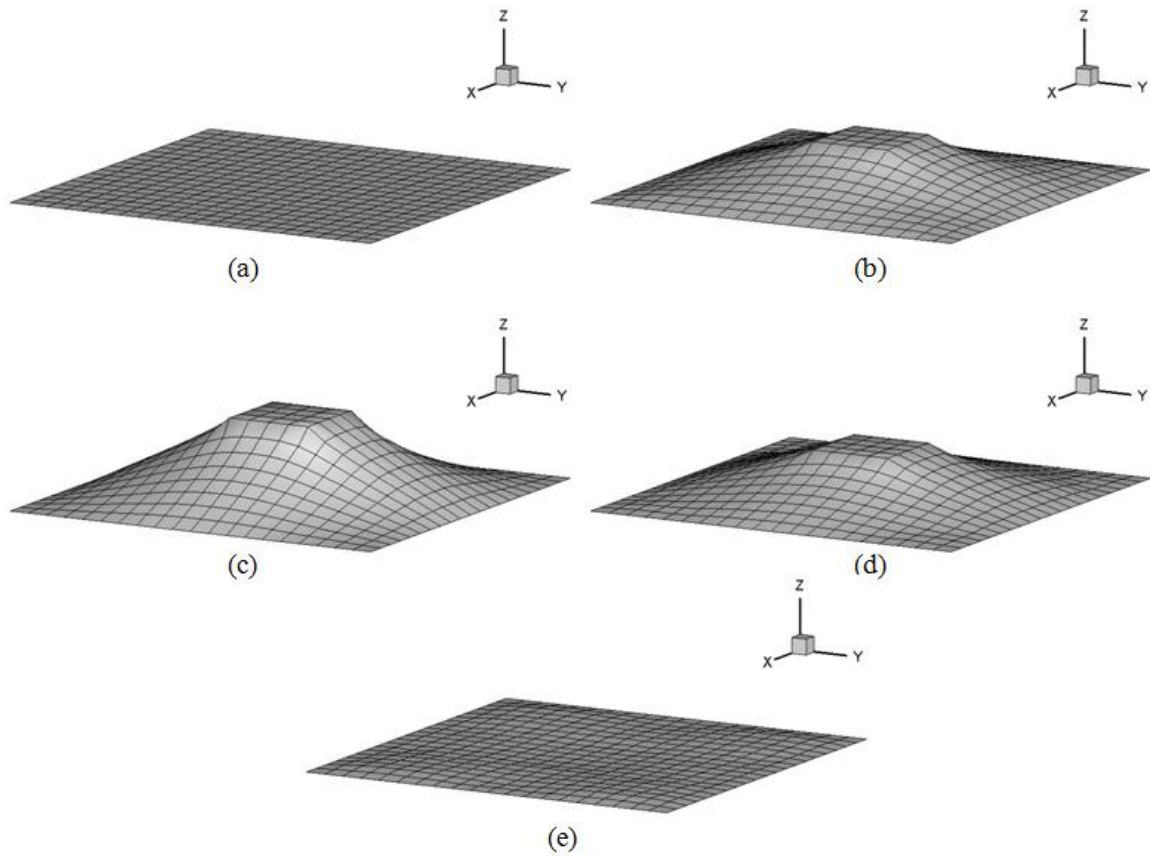


Figure 7-33. The dynamics response of a cotton-polyester blend fabric poke test using the SVK model at (a) 0.0 seconds, (b) 0.15 seconds, (c) 0.25 seconds, (d) 0.35 seconds, and (e) 0.50 seconds.

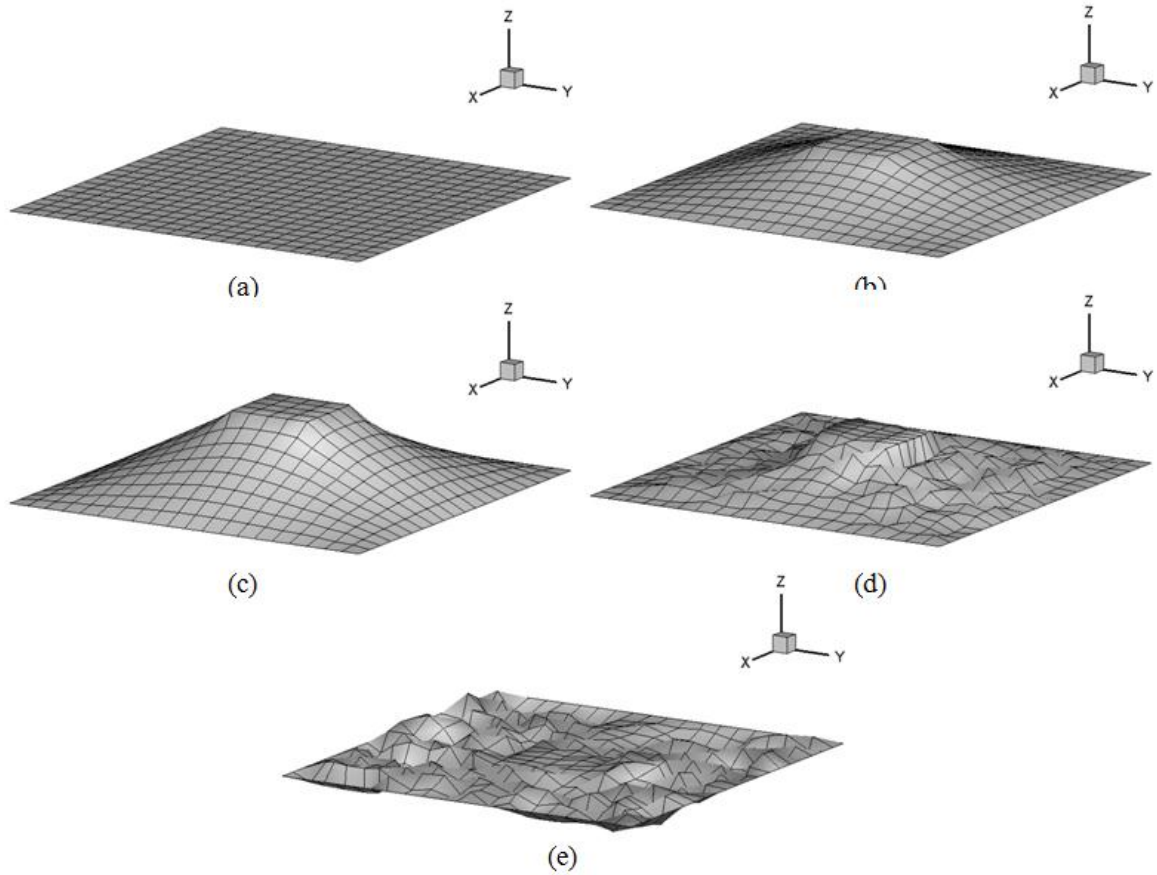


Figure 7-34. The dynamics response of a cotton-polyester blend fabric poke test using the present fabric model at (a) 0.0 seconds, (b) 0.15 seconds, (c) 0.25 seconds, (d) 0.35 seconds, and (e) 0.50 seconds.

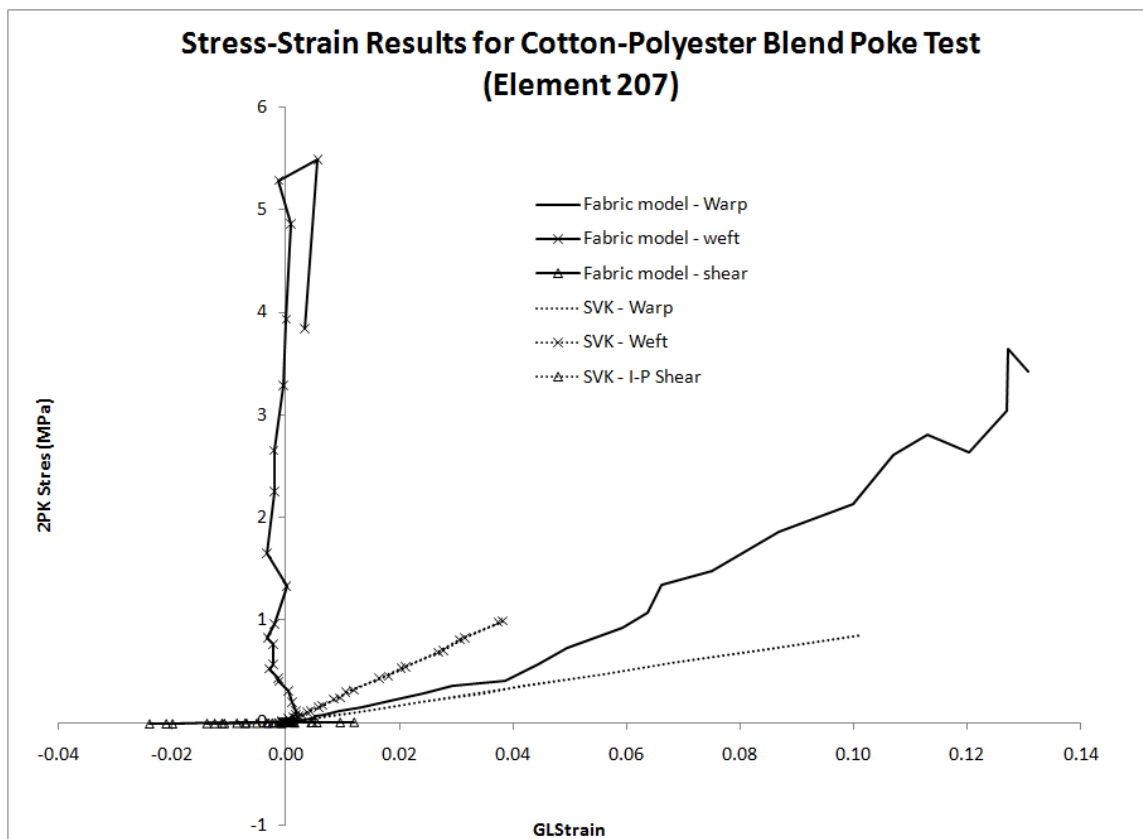


Figure 7-35. Poke test stress-strain results for element 207.

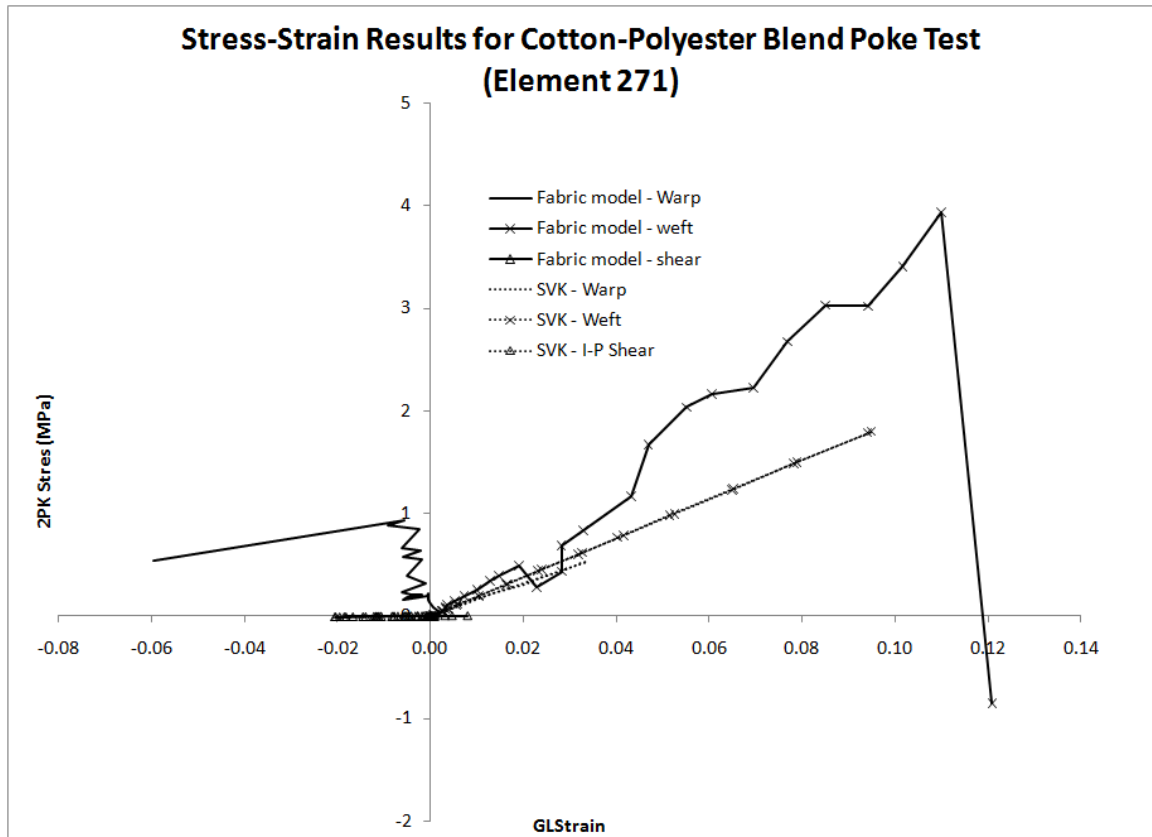


Figure 7-36. Poke test stress-strain results for element 271.

#### 7.4 Discussion

This dissertation research has involved measuring the mechanical behavior of woven fabrics and developing an incremental constitutive model with parameters gleaned from experimental data. For measuring the mechanical behavior, a uniaxial load frame, a digital camera and a computer were used to determine loading/unloading Young's moduli, shear moduli and Poisson's ratios using monotonic and cyclic uniaxial stress tests. The experiments themselves were simple to setup and execute; and the data collected features the expected behaviors for woven fabrics in that they contain strong anisotropy, nonlinearity, and hysteresis

In this research, the use of photogrammetry was found to be a moderately effective way to determine macroscopic fabric strains. Although the procedure developed here is simple, the data analysis is cumbersome due to the manual nature of measuring the displacements of markers located on the fabrics. Furthermore, the relatively low photograph resolution led to data that had a high signal-to-noise ratio, especially at low strain levels. In order to fully utilize this procedure, the following recommendations are made: (1) a higher resolution digital SLR camera should be used so that measurements are more precise and random errors stemming from slight movements of the camera due to shutter actuation and focusing are minimized; and (2) more precise markers that can be tracked more accurately with computer software should be used. This procedure would be a natural choice for capturing macroscopic strain behavior for both uniaxial and biaxial tests in that it is simple and non-invasive, so long as the markers themselves do not affect the stiffness of the fabric.

Using photogrammetry and a bias 45 tensile test, a novel method for determining the shear modulus of woven fabrics was developed. This method involved measuring the stretch and the angle between two marked lines that coincide with the warp and weft directions using a series of digital photos. These measurements were used to determine the shear strain present in the center of the fabric specimens. A transformation of the tensile stress from the bias experiments produced the corresponding shear stress. Taking the first derivative of the polynomial trend line fitted to the loading shear stress-strain data for each fabric led to the loading shear modulus. In order to validate the shear moduli used in the new fabric model, the moduli from this new procedure are compared to the shear moduli estimated using the approach derived by Kilby and introduced in section 3.3.4. The equation is restated here for convenience:

$$G_{12} = \frac{1}{\frac{4}{E_{45^\circ}} - \frac{1}{E_1} - \frac{1}{E_2} + \left( \frac{\nu_{21}}{E_1} + \frac{\nu_{12}}{E_2} \right)} \quad (7.3)$$



An immediate issue that arises when trying to compare the two sets of values is that the loading shear modulus developed here is a nonlinear function of shear strain whereas the moduli estimated using (7.3) are constant values. To circumvent this issue, the elastic moduli in the warp, weft, and bias 45 directions are assumed to be the initial tangent moduli from the experimental stress-strain curves. The estimated shear moduli for the four fabrics using Kilby's approach and the initial tangent shear moduli determined from the present approach are listed in Table 7.5 along with and the percent difference between the two. The moduli determined using the two methods compare very well with one another for cotton-polyester blend and cotton duck; however, there is a large difference between the two estimates for cotton muslin and cotton denim. For these last two fabrics, the behavior is much more compliant than the blend and the duck, which could lead to more potential errors, such as pre-load, when installing the specimens into the grips and also less precise measurements due to the available load cell. From the results, it is concluded that the present approach for estimating the in-plane shear modulus is valid and more applicable for determining a function for a nonlinear shear modulus, especially since the modulus relates directly to the experimental data instead of an estimate.

Table 7.5. Estimates of the constant shear modulus using Kilby's equation and the corresponding estimate from the present approach.

<i>Fabric</i>	$G_{12}$ (Kilby)	$G_{12}$ (present) <sup>†</sup>	% Difference
C-P Blend	1.08	1.09	1.0
Cotton Duck	0.87	0.82	5.5
Cotton Muslin	0.29	0.76	62.2
Cotton Denim	0.24	0.43	45.2

<sup>†</sup>Using initial moduli (zero shear strain) as constants

The constitutive model developed in this work has captured the anisotropic, nonlinear, and hysteretic behavior of woven fabrics, as shown in section 7.2. Compared to the isotropic or orthotropic linear elastic models discussed in Chapter 4 [13-16], the present model is much more mechanically realistic. To highlight these comparisons, results for cyclic uniaxial-stress tests in the warp and weft directions from the SVK model, using the initial moduli from the material parameters listed in section 7.1 for cotton-polyester blend, were plotted against the warp and weft results from the present incremental model and the experimental data and are shown in Figure 7-37. In the warp direction, the stress values at 1%, 5%, and 10% strain for the present model differ from the experimental data by 14%, 45%, and 3%, respectively; compared to 67%, 75%, and 94% for the SVK model. The data in the weft direction shows a similar trend, where at the same strain values, the present model differs by 13%, 2%, and 6%, respectively, from the experimental data; and the SVK model differs by 33%, 10%, and 42%. It would be possible to obtain more accurate results in the small strain region using a linear elastic model if the moduli were obtained using a secant method, but overall, since the state of strain in the critical areas mentioned in Chapter 1 undergo large strains, these models are not well suited for clothing modeling.

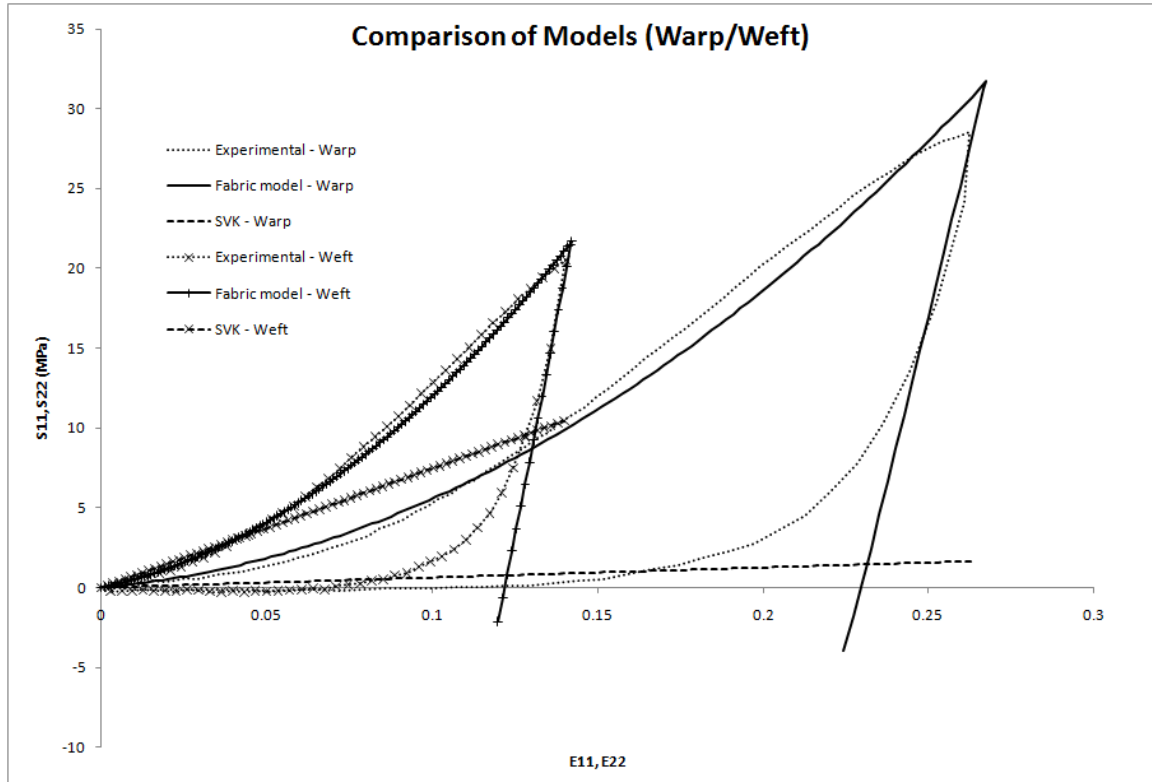


Figure 7-37. Comparison of experimental, SVK and the present fabric model results in the warp and weft directions for cotton-polyester blend.

Like the present fabric model, Peng and Cao [61] included non-linearity by determining the axial and shear moduli directly by fitting curves to the experimental load-strain data. Their computational results for uniaxial warp, weft and bias 45 compare well to their data (see Figure 4-9); however, they do not consider any unloading behavior as we do here. Further, their model assumes a very weak interaction between the two yarn families such that a biaxial load would not lead to significantly higher stress. As was shown in section 7.3.1, the present model does account for this coupling behavior. Compared to multiscale analyses [63-65], the present model does not achieve the level of mechanical detail, but is better suited for dynamic analyses as it requires fewer computations.

One significant limitation of the model that has arisen is that fabrics with excessively large Poisson's ratios (around 0.4 or greater, depending on the fabric) can lead to an over-prediction of stress or numerical instabilities. In these cases, the Poisson's ratios can be modified so that more reasonable stress-strain behavior is produced; however, this comes at the cost of accurate lateral strains. Further, the experimental tests as well as the 3D degenerate shell elements neglect the through-the-thickness deformation; so that it is unknown what affect the corresponding Poisson's ratio would have on the parameters or the results.

The hysteresis observed in the experimental data is present when fabrics are unloaded from any state of stress due to friction between fibers and/or yarns. The model developed here has accounted for this hysteresis by assuming a constant "stiff" elastic modulus whenever a state of unloading or reloading is present. The present model has assumed an "elastic" nature for simplicity and does not account for yielding, inelastic behavior, or damage from a theoretical standpoint. As discussed in the first chapter, the large states of strain that fabrics may be subjected to could lead to inelastic behavior during loading, as evident in Figure 3-9, or breaking of yarns and the subsequent tearing of fabrics, such as in Figures 3-10 through 3-12. Further development of fabric constitutive models could include plastic deformation and damage, which would surely have an effect on clothing-wearer interaction in terms of comfort, range-of-motion, and service life.

Finally, the fabric model was tested in three applications. In the first, cotton-polyester blend and cotton denim fabrics were subjected to a biaxial strain. While experimental data is not available to compare, the results did exhibit the expected behavior in that the presence of a lateral strain causes a stiffer response. The second application consisted of a dynamic simulation where a cotton-polyester blend fabric, pinned horizontally at the four corners, was subjected to a gravity load. The dynamic response of that hanging fabric was as expected, though the shear hysteresis in the model

had to be neglected. The third application consisted of poking the center of a cotton-polyester blend fabric using both the SVK model and the present fabric model (neglecting shear hysteresis). The results of this poke test show that compared to the SVK model; the present model exhibited the expected nonlinear behavior and permanently deformed fabric upon unloading. Work continues to include the shear hysteresis in dynamics simulations. Further, the dynamic test problems are very simple and do not include any sort of contact, which is another significant aspect of the clothing-wearer modeling framework. In order to fully employ the present fabric model, more comprehensive dynamic testing must be carried out.

## CHAPTER 8. CONCLUSION AND FUTURE WORK

### 8.1 Conclusion

In this dissertation, the mechanical behavior of woven fabrics has been measured and a phenomenological constitutive model developed to capture the anisotropic, nonlinear and hysteretic behavior observed in experimental observations. The research included a series of monotonic and cyclic experimental tests to study the behavior of four woven fabrics when subjected to uniaxial stress in the warp, weft, and bias 45 directions. The four fabrics were cotton-polyester blend, cotton duck, cotton muslin, and cotton denim. The force and grip displacement data for each test was used to compute the Green-Lagrange strain and the 2<sup>nd</sup> Piola-Kirchhoff stress in the loading direction. Results from tests in the warp and weft directions led to stress-strain graphs from which loading and unloading elastic moduli were derived by taking the first derivative of trend lines fit to the experimental data. Series of photographs from the warp and weft monotonic tests were used to determine longitudinal and lateral strains along the fabric specimen. These strain values were used to estimate apparent Poisson's ratios in the respective yarn directions of each fabric. The tests in the bias 45 direction led to a new procedure that determined the shear behavior by taking a series of photographs from which the stretches and rotations of the warp and weft yarns could be measured. The stretches and rotations of the yarns were then used to calculate the shear strain, whereas the shear stress was computed by a transformation of the stress in the loading direction. The loading and unloading shear moduli were found by taking the first derivative of the trend line fit to shear stress-strain data. Initial loading shear moduli from the new procedure were compared to shear moduli estimated using Kilby's equation and were found to be appropriate values. The new procedure is a better way to determine the shear moduli from bias tests in that it is a direct measurement and is able to capture nonlinear shear behavior since they are functions of shear strain.

Using the material parameters from the experimental data, simulations replicating the experimental tests were conducted in the warp, weft and bias 45 directions for the four fabrics. The stress and strain behavior produced by the fabric model in the warp and weft directions for cotton-polyester blend and cotton denim compared well with the experimental data; however, the Poisson's ratios for the duck and muslin fabrics had to be greatly reduced in order to obtain realistic stress-strain behavior, which came at the cost of realistic lateral strains. Simulations of the four fabrics in the bias 45 direction were realistic below certain levels of strain, but gradually over-estimated the bias stress above the respective levels. A biaxial strain simulation showed that the presence of a transverse strain has a tremendous affect on stiffness. Dynamic simulations of a fabric draped from its four corners and a fabric being poked in the center both produced visually realistic results, though shear hysteresis was neglected in the model.

Compared to the continuum models presented in Chapter 4, the fabric model developed in this dissertation has several advantages. Many researches assumed linear elastic behavior, which can greatly under-estimate the stress at larger strains, whereas the present model is able to capture more realistic nonlinear fabric behavior. While the model by Peng and Cao and the hyperelastic models investigated by Ruiz and Gonzalez are able to produce nonlinear results, they only considered fabric loading, so that the hysteresis evident upon unloading is not considered. The current model accounts for this hysteresis by using a larger elastic modulus whenever the point of interest in the fabric is in a state of unloading or reloading. While results from multiscale and elastoplastic models also produce realistic fabric behavior, the model developed here requires less computational effort. The current model also comes with some limitations. Due to the complex nature of woven fabrics, homogenizing them into a continuum and determining appropriate material parameters and developing a constitutive model that exhibits realistic behavior proves challenging, particularly when biaxial loads are present and when the apparent Poisson's ratios are very large. In the end, a fabric model was

developed that demonstrates stress-strain behavior that is much more realistic than the linear elastic constitutive models that have been used by many researchers.

## 8.2 Future Work

In order to further develop more realistic fabric and clothing simulations, there are many opportunities for future research. For the current research, work continues in order to apply the fabric model to a variety of dynamics simulations so that more accurate clothing-wearer interaction studies may eventually be conducted. In particular, dynamic simulations that include contact need to be performed. Additional experimental tests should be conducted in order to verify the computational results. A simple test would be to drop a ball onto the center of a square piece of fabric clamped along all sides. Video showing the displacements of the fabric due the dropping ball could then be compared to the computational results. Fabrics are also susceptible to plastic deformation and tearing at high strains. The current model could be modified to account for plastic deformation, one of the challenges being how to construct an appropriate yield surface.

Any macroscopic fabric model should be made as general as possible to accommodate a wide variety of fabrics and their respective properties. Since much of the complex behavior of fabrics is due to geometrical effects of the weaving process and friction, multiscale modeling could be used to estimate additional fabric properties that are either difficult or currently impossible to determine experimentally. Further, this work did not investigate the out-of-plane behavior of fabrics. Additional tests should be developed to study the transverse shear behavior through the thickness of the fabric, which could then be incorporated into the model. Procedures and equipment to study the mechanical behavior of fabrics subjected to multi-axial loads should be further developed so that appropriate moduli may be derived from the overall state of strain instead of being a function of strain in associated yarn direction.



## REFERENCES

1. Docter, P. and B. Peterson, *Up*. 2009, Disney-Pixar: USA.
2. OptiTex, *OptiTex 3D Runway*. 2010, OptiTex International: Petach-Tikva, Israel.
3. Man, X., *A Mathematical and Computational Multiscale Clothing Modeling Framework*, in *Civil and Environmental Engineering*. 2006, The University of Iowa: Iowa City. p. 144.
4. Terzopoulos, D., et al., *Elastically Deformable Models*. Computer Graphics (ACM), 1987. **21**(4): p. 205-214.
5. Terzopoulos, D. and K. Fleischer, *Modeling inelastic deformation: viscoelasticity, plasticity, fracture*. Computer Graphics (ACM), 1988. **22**(4): p. 269-278.
6. Kadolph, S.J., *Textiles*. 10th ed. 2007, Upper Saddle River, NJ: Pearson Prentice Hall. 496.
7. Man, X. and C.C. Swan. *Mathematical clothing modeling in a digital human environment*. 2004. Anaheim, CA, United States: American Society of Mechanical Engineers, New York, NY 10016-5990, United States.
8. Man, X., C.C. Swan, and S. Rahmatalla. *A clothing modeling framework for uniform and armor system design*. 2006. Kissimmee, FL, United States: International Society for Optical Engineering, Bellingham WA, WA 98227-0010, United States.
9. House, D.H. and D.E. Breen, eds. *Cloth Modeling and Animation*. 2000, A K Peters: Natick, MA. 344.
10. Choi, K.-J. and H.-S. Ko, *Research problems in clothing simulation*. Computer Aided Design, 2005. **37**(6): p. 585-92.
11. Hearle, J.W.S., *From Biological Macromolecules to Drape of Clothing: 50 Years of Computing for Textiles*, in *Computational Textile*, X.L. Zeng, Y.; Ruan, D.; Koehl, L., Editor. 2007, Springer: Berlin. p. 1-19.
12. HU, J., *Structure and mechanics of woven fabrics*. 2004, Boca Raton, FL: CRC Press LLC. 305.
13. Chen, B. and M. Govindaraj, *Physically based model of fabric drape using flexible shell theory*. Textile Research Journal, 1995. **65**(6): p. 324-330.
14. Chen, B. and M. Govindaraj, *Parametric study of fabric drape*. Textile Research Journal, 1996. **66**(1): p. 17-24.
15. Collier, J.R., et al., *Drape prediction by means of finite-element analysis*. Journal of the Textile Institute, 1991. **82**(1): p. 96-107.
16. Kang, T.J. and W.R. Yu, *Drape simulation of woven fabric by using the finite-element method*. Journal of the Textile Institute, 1995. **86**(4): p. 635-648.

17. Wu, Z., C.K. Au, and M. Yuen, *Mechanical properties of fabric materials for draping simulation*. International Journal of Clothing Science and Technology, 2003. **15**: p. 56-68.
18. Volino, P., F. Cordier, and N. Magnenat-Thalmann, *From early virtual garment simulation to interactive fashion design*. Computer-Aided Design, 2005. **37**(6): p. 593-608.
19. Kirk, J.W. and S.M. Ibrahim, *Fundamental relationship of fabric extensibility to anthropometric requirements and garment performance*. Textile Research Journal, 1966. **36**(1): p. 37-47.
20. Bassett, R.J., R. Postle, and N. Pan, *Experimental methods for measuring fabric mechanical properties: A review and analysis*. Textile Research Journal, 1999. **69**(11): p. 866-875.
21. Adanur, S., *Wellington Sears Handbook of Industrial Textiles*. 1995, Lancaster, PA: Technomic Publishing Co, Inc.
22. Collier, B.J., M.J. Bide, and P.G. Tortora, *Understanding Textiles*. 7th ed. 2009, Upper Saddle River, New Jersey: Pearson Prentice Hall.
23. Li, Y. and X.-Q. Dai, *Biomechanical Engineering of Textiles and Clothing*. 2006, Boca Raton: CRC PRESS.
24. Bauer-Kurz, I., *Fiber Crimp and Crimp Stability in Nonwoven Fabric Process*, in *Fiber and Polymer Science*. 2000, North Carolina State University: Raleigh. p. 125.
25. Collier, B.J. and H.H. Epps, *Textile Testing and Analysis*. 1999, Upper Saddle River, New Jersey: Merrill.
26. Hearle, J.W.S., P. Grosberg, and S. Backer, *Structural Mechanics of Fibers, Yarns, and Fabrics*. Vol. 1. 1969, New York: Wiley-Interscience. 469.
27. Peirce, F.T., *The Geometry of Cloth Structure*. Journal of the Textile Institute, 1937. **28**: p. 45-96.
28. Dhingra, R.C., S. de Jong, and R. Postle, *LOW-STRESS MECHANICAL PROPERTIES OF WOOL AND WOOL-BLEND WOVEN FABRIC*. Textile Research Journal, 1981. **51**(12): p. 759-768.
29. Bruniaux, P., A. Ghith, and C. Vasseur, *Modeling and Parametric Study of a Fabric Drape*. Advances in Complex Systems, 2003. **6**(4): p. 457-476.
30. ASTM, *D5025-95 Standard Test Method for Breaking Force and Elongation of Textile Fabrics (Strip Method)*. 2006, ASTM International: West Conshohocken.
31. ASTM, *D1777-96 Standard Test Method for Thickness of Textile Materials*. 2007, ASTM International: West Conshohocken.
32. ASTM, *D3776-09 Standard Test Methods for Mass Per Unit Area (Weight) of Fabric*. 2009, ASTM International: West Conshohocken, PA.

33. Kawabata, S., M. Niwa, and H. Kawai, *The Finite Deformation Theory of Plain-Weave Fabrics Part I: The Biaxial-Deformation Theory*. Journal of the Textile Institute, 1973. **64**(1): p. 21-46.
34. Kawabata, S., M. Niwa, and H. Kawai, *The Finite Deformation Theory of Plain-Weave Fabrics Part II: The Uniaxial-Deformation Theory*. Journal of the Textile Institute, 1973. **64**(2): p. 47-61.
35. Sun, H., N. Pan, and R. Postle, *On the Poisson's ratios of a woven fabric*. Composite Structures, 2005. **68**(4): p. 505-10.
36. Anandjiwala, R.D. and G.A.V. Leaf, *Large-scale extension and recovery of plain woven fabrics. Part II. Experimental and discussion*. Textile Research Journal, 1991. **61**(12): p. 743-754.
37. Pan, N., S.H. Zeronian, and H.-S. Ryu, *Alternative approach to the objective measurement of fabrics*. Textile Research Journal, 1993. **63**(1): p. 33-43.
38. ASTM, *D5035-06 Standard Test Method for Breaking Force and Elongation of Textile Fabrics (Strip Method)*. 2008, ASTM International: West Conshohocken.
39. ASTM, *D5034-09 Standard Test Method for Breaking Force and Elongation of Textile Fabrics (Grab Method)*. 2009, ASTM International: West Conshohocken, PA.
40. Zheng, J., et al., *Relationship between uniaxial and strip biaxial tensile properties of fabrics*. Textile Research Journal, 2008. **78**(3): p. 224-231.
41. Kilby, W.F., *Planar stress-strain relationships in woven fabrics*. Journal of the Textile Institute, 1963. **54**(1): p. 9-27.
42. Raftenberg, M.N., et al., *Plain-Woven, 600-Denier Kevlar KM2 Fabric Under Quasistatic, Uniaxial Tension*, A.R. Laboratory, Editor. 2005.
43. Sun, H. and N. Pan, *Shear deformation analysis for woven fabrics*. Composite Structures, 2005. **67**(3): p. 317-22.
44. Kawabata, S., M. Niwa, and H. Kawai, *The Finite-Deformation Theory of Plain-Weave Fabrics Part III: The Shear-Deformation Theory*. Journal of the Textile Institute, 1973. **64**(2): p. 62-85.
45. Lin, H., et al., *Finite element modelling of fabric shear*. Modelling and Simulation in Materials Science and Engineering, 2009. **17**(1).
46. Lo, W.M. and J.L. Hu, *Shear properties of woven fabrics in various directions*. Textile Research Journal, 2002. **72**(5): p. 383-390.
47. Morozov, E.V. and V.V. Vasiliev, *Determination of the shear modulus of orthotropic materials from off-axis tension tests*. Composite Structures, 2003. **62**(3-4): p. 379-382.
48. Shanahan, W.J., D.W. Lloyd, and J.W.S. Hearle, *CHARACTERIZING THE ELASTIC BEHAVIOR OF TEXTILE FABRICS IN COMPLEX DEFORMATIONS*. Textile Research Journal, 1978. **48**(9): p. 495-505.

49. Wu, H.-C., *Continuum Mechanics and Plasticity*. CRC Series: Modern Mechanics and Mathematics, ed. D.G.a.R.W. Ogden. 2005, Boca Raton: Chapman & Hall/CRC. 684.
50. Sidhu, R.M.J.S., et al., *Finite element analysis of textile composite preform stamping*. *Composite Structures*, 2001. **52**(3-4): p. 483-497.
51. Peirce, F.T., *Geometrical Principles Applicable to the Design of Functional Fabrics*. *Textile Research Journal*, 1947. **17**(3): p. 123-147.
52. Grosberg, P. and S. Kedia, *Mechanical properties of woven fabrics -- I*. *Textile Research Journal*, 1966. **36**(1): p. 71-79.
53. Anandjiwala, R.D. and G.A.V. Leaf, *Large-scale extension and recovery of plain woven fabrics. Part I. Theoretical*. *Textile Research Journal*, 1991. **61**(11): p. 619-634.
54. Cavallaro, P.V., A.M. Sadegh, and C.J. Quigley, *Decrimping behavior of uncoated plain-woven fabrics subjected to combined biaxial tension and shear stresses*. *Textile Research Journal*, 2007. **77**(6): p. 403-416.
55. Hivet, G. and P. Boisse, *Consistent 3D geometrical model of fabric elementary cell. Application to a meshing preprocessor for 3D finite element analysis*. *Finite Elements in Analysis and Design*, 2005. **42**(1): p. 25-49.
56. Breen, D.E., *A Particle-Based Model for Simulating the Draping Behaviour of Woven Cloth*. 1993, Rensselaer Polytechnic Institute: Troy, NY.
57. Boubaker, B.B., B. Haussy, and J.-F. Ganghoffer, *Consideration of the yarn-yarn interactions in meso/macro discrete model of fabric. Part II: Woven fabric under uniaxial and biaxial extension*. *Mechanics Research Communications*, 2007. **34**(4): p. 371-378.
58. Boubaker, B.B., B. Haussy, and J.F. Ganghoffer, *Consideration of the yarn-yarn interactions in meso/macro discrete model of fabric. Part I: Single yarn behaviour*. *Mechanics Research Communications*, 2007. **34**(4): p. 359-70.
59. Boubaker, B., B. Haussy, and J.F. Ganghoffer, *Discrete models of woven structures. Macroscopic approach*. *Composites Part B: Engineering*, 2007. **38**(4): p. 498-505.
60. Zhou, C., X. Jin, and C.C.L. Wang, *Shear buckling and dynamic bending in cloth simulation*. *Computer Animation and Virtual Worlds*, 2008. **19**(3-4): p. 493-503.
61. Peng, X.Q. and J. Cao, *A continuum mechanics-based non-orthogonal constitutive model for woven composite fabrics*. *Composites Part A (Applied Science and Manufacturing)*, 2005. **36**(6): p. 859-74.
62. Ruiz, M.J.G. and L.Y.S. Gonzalez, *Comparison of hyperelastic material models in the analysis of fabrics*. *International Journal of Clothing Science and Technology*, 2006. **18**(5): p. 314-25.

63. King, M.J., P. Jearanaisilawong, and S. Socrate, *A continuum constitutive model for the mechanical behavior of woven fabrics*. International Journal of Solids and Structures, 2005. **42**(13): p. 3867-96.
64. King, M.J. and S. Socrate. *A shell formulation to model the three-dimensional deformation response of woven fabrics*. 2004. Anaheim, CA, United States: American Society of Mechanical Engineers, New York, NY 10016-5990, United States.
65. Nadler, B., P. Papadopoulos, and D.J. Steigmann, *Multiscale constitutive modeling and numerical simulation of fabric material*. International Journal of Solids and Structures, 2006. **43**(2): p. 206-221.
66. Reese, S., *Meso-macro modelling of fibre-reinforced rubber-like composites exhibiting large elastoplastic deformation*. International Journal of Solids and Structures, 2003. **40**(4): p. 951-980.
67. Etmuss, O., M. Keckeisen, and W. Strasser. *A fast finite element solution for cloth modelling*. 2003. Canmore, Alta., Canada: IEEE Comput. Soc.
68. Reddy, J.N., *Theory and Analysis of Elastic Plates and Shells*. Second ed. 2007, Boca Raton: CRC Press. 547.
69. Belytschko, T., W.K. Liu, and B. Moran, *Nonlinear Finite Elements for Continua and Structures*. 2000, Chichester, UK: John Wiley & Sons, LTD. 650.
70. Hughes, T.J.R., *The Finite Element Method: Linear Static and Dynamic Finite Element Analysis*. 1987, Englewood Cliffs, New Jersey: Prentice-Hall, Inc.

## APPENDIX A

In order to interpret the experimental data using large deformation continuum mechanics, expressions for the Green-Lagrange strain and the 2<sup>nd</sup> Piola-Kirchhoff stress need to be derived according to the experimental procedure described in chapter 3. Figure A-1 summarized the uniaxial tensile test where the initial gage length,  $l_0$ , between the two pins is 3.0 inches. The square scribed into the center of the specimen has initial dimensions  $X_1$  and  $X_2$ . Since deformation in the out-of-plane dimension is not measured, the corresponding strain is neglected. As the test commences, the two pins are separated in displacement control where the distance between the pins is  $l(t)$ , therefore creating the load  $P(t)$ . As the load increases, the scribed square becomes increasingly distorted into a roughly rectangular shape with current dimensions of  $x_1(t)$  and  $x_2(t)$ . The test program directly gives values of  $P(t)$  and  $\Delta l(t)$ , where  $\Delta l(t) = l(t) - l_0$ . Dimensions of the scribed square,  $X_i$  and  $x_i(t)$  ( $i = 1, 2$ ) are measured from the digital photographs taken throughout each test.

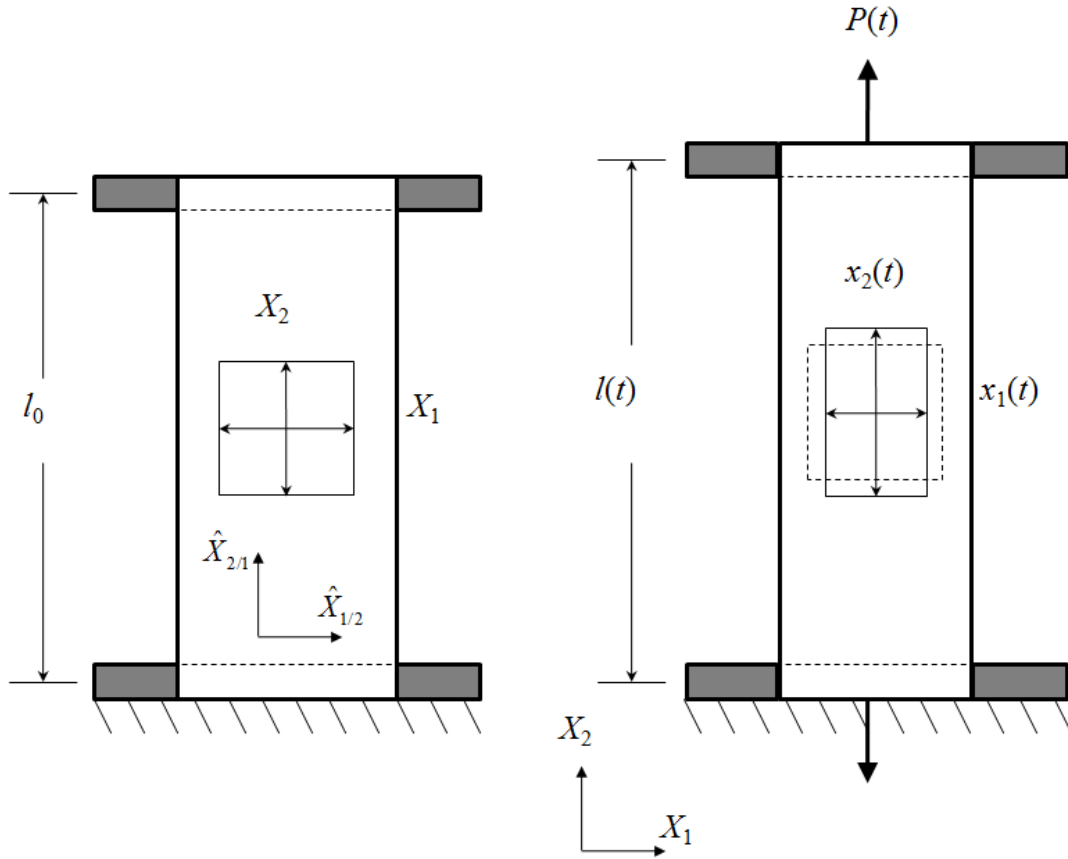


Figure A-1. Uniaxial tensile test schematic.

Green-Lagrange strain is defined by the expression

$$\mathbf{E} = \frac{1}{2}(\mathbf{F}^T \mathbf{F} - \mathbf{1}) \quad (\text{A1})$$

The deformation gradient is defined as

$$\mathbf{F} = F_{ij} = \frac{\partial x_i}{\partial X_j} = \begin{bmatrix} \frac{\partial x_1}{\partial X_1} & \frac{\partial x_1}{\partial X_2} & \frac{\partial x_1}{\partial X_3} \\ \frac{\partial x_2}{\partial X_1} & \frac{\partial x_2}{\partial X_2} & \frac{\partial x_2}{\partial X_3} \\ \frac{\partial x_3}{\partial X_1} & \frac{\partial x_3}{\partial X_2} & \frac{\partial x_3}{\partial X_3} \end{bmatrix} \quad (\text{A2})$$

For the uniaxial tensile test and neglecting any through-thickness changes, the deformation gradient is

$$\mathbf{F}(t) = \begin{bmatrix} \lambda_1(t) & 0 & 0 \\ 0 & \lambda_2(t) & 0 \\ 0 & 0 & 1 \end{bmatrix} \quad (\text{A3})$$

where

$$\lambda_i(t) \equiv \text{stretch ratio} = 1 + \frac{u_i(t)}{X_I}, \quad (\text{A4})$$

with  $u_i(t) = x_i(t) - X_I$ . By inserting (A3) into (A1) and simplifying, we get

$$\begin{aligned} E(t) &= \frac{1}{2} \left\{ \begin{bmatrix} \lambda_1(t) & 0 & 0 \\ 0 & \lambda_2(t) & 0 \\ 0 & 0 & 1 \end{bmatrix}^T \begin{bmatrix} \lambda_1(t) & 0 & 0 \\ 0 & \lambda_2(t) & 0 \\ 0 & 0 & 1 \end{bmatrix} - \begin{bmatrix} 1 & 0 & 0 \\ 0 & 1 & 0 \\ 0 & 0 & 1 \end{bmatrix} \right\} \\ &= \frac{1}{2} \left\{ \begin{bmatrix} \lambda_1^2(t) & 0 & 0 \\ 0 & \lambda_2^2(t) & 0 \\ 0 & 0 & 1 \end{bmatrix} - \begin{bmatrix} 1 & 0 & 0 \\ 0 & 1 & 0 \\ 0 & 0 & 1 \end{bmatrix} \right\} \\ &= \begin{bmatrix} \frac{1}{2}[\lambda_1^2(t) - 1] & 0 & 0 \\ 0 & \frac{1}{2}[\lambda_2^2(t) - 1] & 0 \\ 0 & 0 & 0 \end{bmatrix} \\ &= \begin{bmatrix} E_{11}(t) & 0 & 0 \\ 0 & E_{22}(t) & 0 \\ 0 & 0 & 0 \end{bmatrix} \end{aligned} \quad (\text{A5})$$

Using (A4),  $E_{ii}(t)$  can be further simplified as



$$\begin{aligned}
E_{ii}(t) &= \frac{1}{2} [\lambda_i^2(t) - 1] \\
&= \frac{1}{2} \left[ \left( 1 + \frac{u_i(t)}{X_I} \right) \left( 1 + \frac{u_i(t)}{X_I} \right) - 1 \right] \\
&= \frac{1}{2} \left[ 1 + \frac{2u_i(t)}{X_I} + \left( \frac{u_i(t)}{X_I} \right)^2 - 1 \right] \\
&= \frac{u_i(t)}{X_I} + \frac{1}{2} \left( \frac{u_i(t)}{X_I} \right)^2
\end{aligned} \tag{A6}$$

Since the experimental tests are uniaxial tension, the stress tensor will consist of all zeros except for the component corresponding to the loading direction. For the uniaxial 2<sup>nd</sup> Piola-Kirchhoff (2PK) stress, we first define the Cauchy stress as

$$\boldsymbol{\sigma}(t) = \begin{bmatrix} 0 & 0 & 0 \\ 0 & \frac{P(t)}{A} & 0 \\ 0 & 0 & 0 \end{bmatrix}, \tag{A7}$$

where  $P(t)$  is the uniaxial force at time  $t$  and  $A$  is the cross-sectional area in the current configuration. Next, we express the 2PK stress as

$$\mathbf{S} = J\mathbf{F}^{-1} \cdot \boldsymbol{\sigma} \cdot \mathbf{F}^{-T}, \tag{A8}$$

Where  $\mathbf{S}$  is the 2PK stress,  $\mathbf{F}$  is the deformation gradient and  $J$  is the Jacobian, which is defined as

$$J = \det(\mathbf{F}). \tag{A9}$$

For the measured deformations, the current cross-sectional area (neglecting out-of-plane deformation) is related to original as

$$A = A_0 \lambda_1. \tag{A10}$$

In the case of these experiments, the inverse of the deformation gradient is

$$\mathbf{F}(t)^{-1} = \begin{bmatrix} \frac{1}{\lambda_1(t)} & 0 & 0 \\ 0 & \frac{1}{\lambda_2(t)} & 0 \\ 0 & 0 & 1 \end{bmatrix}. \quad (\text{A11})$$

By plugging (A7), (A10), and (A11) into (A8), we get

$$\begin{aligned} \mathbf{S}(t) &= [\lambda_1(t)\lambda_2(t)] \begin{bmatrix} \frac{1}{\lambda_1(t)} & 0 & 0 \\ 0 & \frac{1}{\lambda_2(t)} & 0 \\ 0 & 0 & 1 \end{bmatrix} \cdot \begin{bmatrix} 0 & 0 & 0 \\ 0 & \frac{P(t)}{A_0\lambda_1(t)} & 0 \\ 0 & 0 & 0 \end{bmatrix} \cdot \begin{bmatrix} \frac{1}{\lambda_1(t)} & 0 & 0 \\ 0 & \frac{1}{\lambda_2(t)} & 0 \\ 0 & 0 & 1 \end{bmatrix} \\ &= \lambda_2(t) \begin{bmatrix} 0 & 0 & 0 \\ 0 & \frac{P(t)}{A_0} \frac{1}{\lambda_2^2(t)} & 0 \\ 0 & 0 & 0 \end{bmatrix} \\ &= \begin{bmatrix} 0 & 0 & 0 \\ 0 & \frac{P(t)}{A_0} \frac{1}{\lambda_2(t)} & 0 \\ 0 & 0 & 0 \end{bmatrix} \\ &= \begin{bmatrix} 0 & 0 & 0 \\ 0 & \frac{P(t)}{A_0 \left[ 1 + \frac{u_2(t)}{X_2} \right]} & 0 \\ 0 & 0 & 0 \end{bmatrix} \end{aligned} \quad (\text{A12})$$